Faculty of Aerospace Engineering

Tuning of a Haptic Collision Avoidance System for UAV Teleoperation

Using Neuromuscular Admittance Measurements

Emmanuel Sunil

January 16, 2014

TU Delft Delft University of Technology

Challenge the future

Tuning of a Haptic Collision Avoidance System for UAV Teleoperation

Using Neuromuscular Admittance Measurements

Master of Science Thesis

For obtaining the degree of Master of Science in Aerospace Engineering
at Delft University of Technology

Emmanuel Sunil

January 16, 2014

Faculty of Aerospace Engineering · Delft University of Technology

Delft University of Technology

Delft University Of Technology
Department Of
Control and Simulation

The undersigned hereby certify that they have read and recommend to the Faculty of Aerospace Engineering for acceptance a thesis entitled **"Tuning of a Haptic Collision Avoidance System for UAV Teleoperation"** by **Emmanuel Sunil** in partial fulfillment of the requirements for the degree of **Master of Science**.

Dated: January 16, 2014

Readers:

J. Smisek, MSc.

dr.ir. M. M. van Paassen

prof.dr.ir. M. Mulder

S. Kimmer, MSc.

Contents

List of Figures

List of Tables

Acronyms

AFF	Artificial Force Field
CNS	Central Nervous System
FOV	Field of View
FT	Force Task
GCS	Ground Control Station
GPF	Generalized Potential Field
GTO	Golgi Tendon Organ
HA	Haptic feedback Acceptance
HCAS	Haptic Collision Avoidance System
HSC	Haptic Shared Control
NHF	No Haptic Feedback
NMS	Neuromuscular System
PRF	Parametric Risk Field
PT	Position Task
RMS	Root Mean Square
RT	Relax Task
RTB	Relative To Baseline
SA	Situational Awareness
STD	Standard Deviation
TLX	Task Load Index
UAV	Unmanned Aerial Vehicle

Thesis Outline

This report is divided into three parts:

I Journal Paper: Paper summarizing entire work including results and analysis of offline simulation and human-in-the-loop experiment

II Preliminary Report: Report containing thesis objectives, literature study, offline simulation (modeling and results) and experiment proposal

III Experiment Appendices: Supplementary documents related to the human-in-the-loop experiment

A bibliography is provided at the end of the report.

Part I

PAPER

Tuning of a Haptic Collision Avoidance System for Unmanned Aircraft Teleoperation

Emmanuel Sunil, Jan Smisek, Marinus M. van Paassen, *Member, IEEE,* and Max Mulder

***Abstract*—This research investigates a neuromuscular analysis based tuning algorithm for haptic cues that has been hypothesized to simultaneously improve safety and workload when compared to heuristic tuning, applied to a haptic collision avoidance system for unmanned aircraft teleoperation. This novel tuning method considers the combined stiffness of the human arm and the control inceptor when computing ideal haptic cues. The 'relaxed' setting of the neuromuscular system, for which neural reflexes are suppressed, is chosen as the design point for tuning haptic cues as it is expected to lead to the lowest workload, contrary to the 'force' and 'position' settings. Theoretical investigations using offline simulations verified the novel approach and the selection of the 'relaxed' setting. Subsequently, a teleoperation experiment ($n = 12$) in an obstacle laden urban environment was conducted with six different tuning profiles, including a manual control condition. Results showed that safety, workload and situational awareness was substantially improved over conditions that ignored the neuromuscular system. Additionally, over-tuning haptic cues was found to be worse than manual control for user acceptance of the system. No significant differences were found between the 'relaxed' and 'force' settings, suggesting that selection between these two options depends on the specific application of haptic cues. The admittance-trajectory relationship during teleoperation was studied, without haptic cues, to further improve the tuning method. Here, no statistical differences in admittance were observed between different obstacles. However, a significant effect was found for admittance variations within obstacles, and an inverse relationship was established between admittance and UAV velocity/yaw rate.**

***Index Terms*—Tuning haptic feedback, neuromuscular admittance, unmanned aerial vehicle (UAV), teleoperation, collision avoidance, haptic shared control.**

I. Introduction

UNMANNED aerial vehicles (UAVs) have become increasingly popular due to their ability to act as versatile sensor platforms for relatively low development and operational costs. Despite numerous commercial applications, at present, UAVs are mainly used in the military domain [1]. However, recent industry-wide efforts are pushing towards introducing UAVs in civilian airspace. In fact, in 2013 the FAA has awarded restricted type certificates for two UAVs, the AeroVironment Puma and the Insitu ScanEagle, to operate over civilian airspace in the arctic circle [2]. These developments have raised safety related concerns, particularly if UAVs are to fly over populated areas in the near future.

Previous studies have shown that UAVs are up to 50 times more accident prone than their manned counterparts [3], and up to 70% of all UAV accidents are attributed to human error [4]. Although UAVs are 'unmanned aircraft', there is significant human involvement in the planning and operation of UAV missions [5]. UAVs are typically controlled from ground control stations (GCS) which predominantly supply only visual information to the UAV teleoperator. This visual feedback suffers from time delays and has low resolution, contrast and field of view (FOV) [6]. In addition, the physical separation between the aircraft and the teleoperator leads to a lack of auditory, kinesthetic and vestibular sensory inputs which are normally available to pilots of manned aircraft [7]. These shortcomings in the design of GCS can overload the visual channel of teleoperators, resulting in situations with poor situational awareness (SA) and high workload.

To address these issues, and to improve the safety of UAV teleoperation, a novel control interface that augments visual feedback with kinesthetic, or haptic cues, for collision avoidance in obstacle laden environments has been developed by Boschloo et al. and Lam et al. [8] [9]. The interface, termed haptic collision avoidance system (HCAS), is based on the principles of haptic shared control (HSC). The HCAS has been extensively evaluated through multiple human-in-the-loop experiments [10]–[12]. These experiments have shown that the HCAS significantly improves the safety of UAV teleoperation, but at the cost of increased physical workload. Studies investigating the relationship between the human arm's neuromuscular properties and the tuning of HSC systems have revealed that 'trial and error' tuning of haptic moments, as used by early iterations of the HCAS, can result in poor haptic interaction between the automation and the teleoperator [13]. This poor interaction has been attributed to the large adaptation range of the human arm neuromuscular system (NMS) which is able to adapt its properties such that performance and stability are satisfactory, regardless of the specific tuning used [14]. However, adaptations to non-optimal settings of the NMS can lead to physical discomfort over time, as well as increased frustration with the system [14].

An alternative approach is to tune haptic cues to match a 'design neuromuscular setting', where the properties of the NMS, namely end-point admittance/stiffness, are desirable for the control task under consideration. It is hypothesized that the novel tuning method will reduce high teleoperator workload levels observed in previous experiments by taking into account the response of the NMS to haptic feedback moments. Using experimental measurements of the NMS taken by Smisek et. al [15], this research aims to verify and validate the proposed neuromuscular analysis based tuning paradigm through an offline simulation and a human-in-the-loop experiment. To investigate additional factors that may affect optimal tuning of the HCAS, a secondary goal of this

The authors are with the Control and Simulation division, Faculty of Aerospace Engineering, TU Delft, Kluyverweg 1, 2629HS Delft, The Netherlands. Email: e.sunil@student.tudelft.nl, j.smisek@tudelft.nl, m.m.vanpaassen@tudelft.nl, m.mulder@tudelft.nl

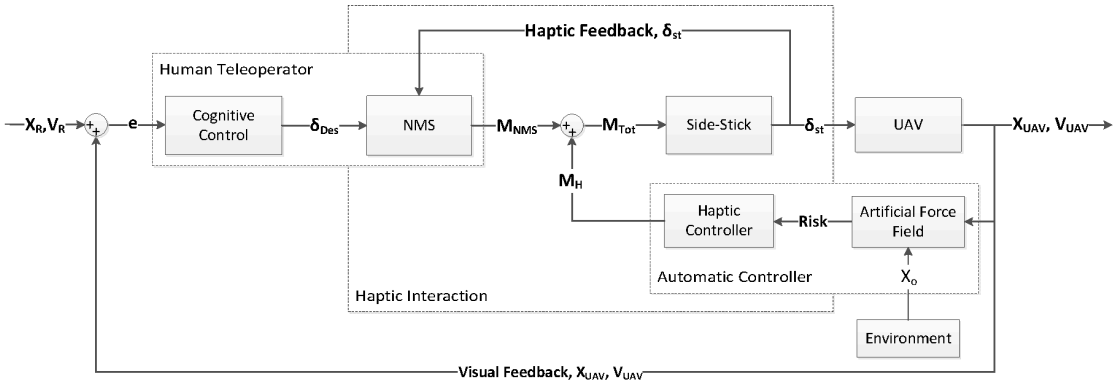

Fig. 1. Haptic collision avoidance system (HCAS) architecture. The system, based on the design philosophy of haptic shared control (HSC), supplements visual feedback with haptic cues generated by an automatic controller to help teleoperators avoid collisions with obstacles in the environment.

work is to investigate the relationship between the adaptation of neuromuscular admittance and the trajectory to be flown by the UAV teleoperator.

This paper begins with a description of the HCAS and provides the theoretical framework of the neuromuscular analysis based tuning method in Sec. II and Sec. III respectively. This is followed in Sec. IV with the setup and results of the offline simulation used to verify the novel tuning method. In Sec. V, the design of the human-in-the-loop experiment used to validate the tuning law is elaborated. The results of the experiment are presented and discussed in terms of the two research goals in Sec. VI and Sec. VII respectively. Finally, the main conclusions are listed in Sec. VIII.

II. Haptic Collision Avoidance System

The haptic collision avoidance system (HCAS) aims at increasing the safety and performance of UAV teleoperation, whilst seeking to improve teleoperator situational awareness (SA) and workload. To meet these conflicting requirements, Boschloo and Lam [8] [9], the original designers of the HCAS, adopted the principles of haptic shared control (HSC) [16] [17].

A. System Architecture

A block diagram schematic of the HCAS is depicted in Fig. 1. Here it can be seen that the outer visual feedback loop of the UAV teleoperator is complemented with an inner haptic feedback loop originating from an automatic controller. Similar to other HSC systems, the automatic controller can be subdivided into two distinct components or 'mappings' [18]. The first mapping, which replicates the visual/cognitive control task of the teleoperator, is performed by a so called 'artificial force field' (AFF). The AFF, see Sec. II-B, scans the environment for obstacles and computes the risk of collisions. This risk is converted to a haptic moment, M_H, by the 'haptic controller' which constitutes the second mapping, and its function is comparable to that of the human neuromuscular system (NMS). The haptic moment, M_H, and the moment generated by the teleoperator NMS, M_{NMS}, acts together on the side-stick, and its resulting position dictates the sole steering commands issued to the UAV. This distinct characteristic of HSC systems guarantees that the teleoperator can always overrule the automation, as long as the haptic controller is designed to ensure that $M_{H_{max}} < M_{NMS_{max}}$ [14].

The haptic feedback perceived by the teleoperator is a result of side-stick neutral position shifts caused by M_H, and the usefulness of the haptic feedback provided is twofold. First, the presence of haptic moments informs the teleoperator of potential collisions with the environment. Second, the magnitude and direction of M_H indicates a collision avoidance steering maneuver that the teleoperator can follow to safely navigate around obstacles. This is particularly helpful when visual information from onboard cameras is not in the direction of motion of the UAV. In this way, the HCAS can improve the SA of UAV teleoperators for an otherwise pure manual control task (i.e., when no obstacles are detected).

The primary advantage of the HCAS over autonomous collision avoidance systems is that the teleoperator is constantly aware of the intentions of the automation. Moreover, the continuous communication between the two parties allows the teleoperator to be actively involved in the decision making process through intuitive haptic interactions [17]. This also allows for faster detection of automation failures, improving the fault detection and resolution ability of teleoperators. For these reasons, the HCAS has the potential to overcome many of the human-machine issues reported for pure automatic control systems [19] [20].

It should be noted that in Fig. 1, only moment feedback haptic cues are supplied by the haptic controller as it is the only haptic configuration of interest in this research. Additionally, haptic feedback is only provided for longitudinal and lateral (horizontal) control of the UAV, and communication time delays are not considered.

B. Artificial Force Field

The artificial force field (AFF) is the first of two components of the automatic controller in the HCAS architecture, see

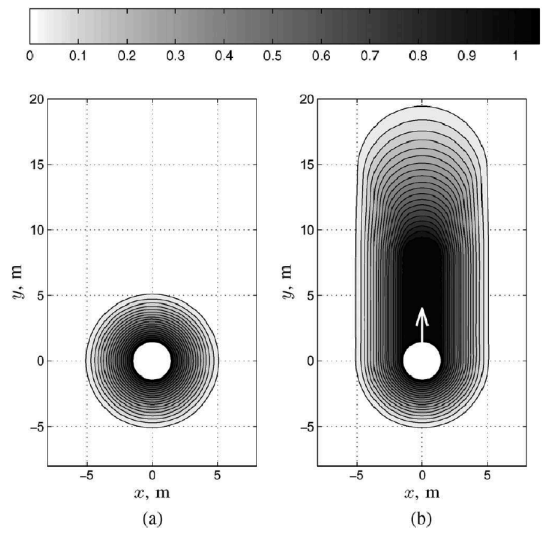

Fig. 2. The parametric risk field (PRF) adjusts its shape and size based on the instantaneous UAV velocity and maximum UAV deceleration [21]. The color-bar indicates the risk/probability of collision. (a) $\mathbf{v} = 0m/s$. (b) $\mathbf{v} = 4m/s$.

Fig. 1. The AFF moves with the UAV, and is used to compute the risk (i.e., probability) of collisions for obstacles detected within the area scanned by it. Based on this risk, repulsive haptic moments are applied on the side-stick by the haptic controller to guide the teleoperator away from danger.

Boschloo et al. designed an AFF specifically for UAV teleoperation known as the parametric risk field (PRF) [8]. The shape and size of the PRF is proportional to the instantaneous UAV velocity, $\mathbf{v}$, and inversely proportional to its maximum deceleration, a_{max}. If the UAV is not moving, the PRF scans a relatively small circular region around the UAV as in Fig. 2a. For non-zero velocities, the PRF extends in the direction of motion to provide sufficient time for the teleoperator to react to haptic feedback moments as in Figure 2b. Offline simulations and human-in-the-loop experiments have revealed that the PRF is more stable, and results in smaller haptic moments, thus allowing for higher UAV velocities, when compared to other AFFs discussed in literature, such as the generalized potential field (GPF) designed for ground robot obstacle avoidance [10] [21] [22].

Fig. 3 displays the parameters and 'zones' that define the PRF. Parameters d_{stop} and d_{ahead} are responsible for extending the size of the PRF when the UAV is moving and are defined using simple kinematic relations for rigid body motion [8]:

$$d_{stop} = \frac{|\mathbf{v}|^2}{2a_{max}} \quad (1)$$

$$d_{ahead} = |\mathbf{v}|\, t_{ahead} \quad (2)$$

From Fig. 3 and the above equations, it is clear that the PRF geometry is completely defined by four constant parameters: r_{pz}, d_{min}, t_{ahead} and a_{max}. The values of these parameters were refined through simulations for the UAV model used in this research by Lam and are listed in Table I [21].

AFFs typically compute the risk of collision based on the relative distance between the UAV and an obstacle,$\mathbf{p}$. For the PRF, risk is also dependent on the zone in which an obstacle is located and the instantaneous UAV velocity, $\mathbf{v}$:

$$risk\,(\mathbf{p},\mathbf{v}) = \begin{cases} 1 & \text{if } \mathbf{p} \text{ in Zone 1} \\ \cos\left(\frac{d}{d_0}180^o + 180^o\right) + 1 & \text{if } \mathbf{p} \text{ in Zone 2} \\ 0 & \text{if } \mathbf{p} \text{ in Zone 3} \end{cases} \quad (3)$$

Here, the shifted cosine function for risk computation in zone 2 enables a smooth transition in risk values between zones, thus ensuring that there are no sudden changes in the corresponding haptic moments. To evaluate the shifted cosine function at a point $\mathbf{p}$, distances d and d_0 need to be computed and are defined in Fig. 3.

The PRF is also used to compute a collision avoidance steering vector. The magnitude of this vector is equal to the risk value computed using equation (3), and its direction is defined from the obstacle to the center of the UAV. If multiple obstacles are detected, the final collision avoidance steering vector can be computed using a so called 'max-min' method [8]. In this method, the largest and smallest collision avoidance steering vectors are summed vectorially.

C. Previous Experimental Results

The HCAS has been tested extensively by Lam in multiple human-in-the-loop experiments during which teleoperator subjects were required to perform reconnaissance tasks in obstacle laden urban environments. These experiments tested multiple AFF designs and haptic feedback configurations, as well as the use of so called 'wave variable' transformations to counteract communication time delays [10]–[12], [23]. In all these experiments, it was found that haptic feedback considerably reduced the number of collisions and thereby increased the safety of teleoperation when compared to pure

TABLE I
HEURISTICALLY OPTIMIZED CONSTANT PARAMETERS THAT DEFINE THE GEOMETRY OF THE PARAMETRIC RISK FIELD

Parameter	Value	Description
r_{pz}	1.5	Radius of protection zone [m]
d_{min}	1.5	Distance between zone 1 and zone 2 [m]
t_{ahead}	2	Maximum available reaction time [s]
a_{max}	1	Maximum UAV deceleration $[m/s^2]$

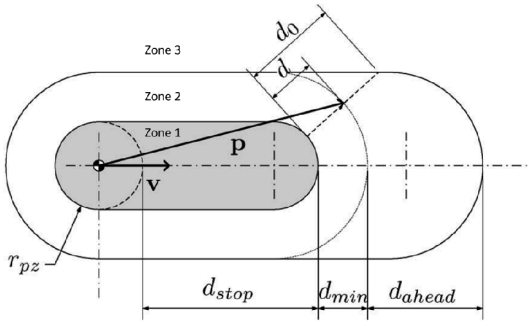

Fig. 3. Variables used to describe the shape of the parametric risk field (PRF) [8].

manual control, see Fig. 4. Additionally, haptic feedback was also found to improve performance, resulting in higher average UAV velocities.

However, the overall subjective workload measured using the NASA Task Load Index (TLX) was always greater with haptic feedback. Fig. 5 shows error-bar charts for the various components of the NASA TLX, including overall Z-scores, for the same experiment as depicted in Fig. 4. Lam attributed the increased overall workload (Fig. 5a) to the increased physical workload (Fig. 5b) and frustration (Fig. 5c) exhibited for haptic feedback configurations [10]. Furthermore, Lam reported that some subjects described haptic moments as 'too strong', making it difficult to overrule the automation [10]. To improve the realism of the experiment, in his latest research Lam included a time penalty for each collision [12]. Despite this change in the experiment protocol, subjective physical workload and measured control activity continued to be much higher for haptic feedback configurations.

The source of this increased physical workload for haptic configurations can be understood by considering the tuning procedure used for the haptic controller. Equation (4) shows that the haptic moment, M_H, is computed as the product of the haptic gain, K_H, and the risk vector magnitude, $|\mathbf{R}|$. In essence, the form of the haptic moment control law corresponds to that of a proportional controller in which the haptic gain, K_H, has to be optimized:

$$M_H = K_H \cdot |\mathbf{R}| \tag{4}$$

In initial implementations of the system, K_H was tuned using a 'trial and error' process, and in doing so Lam accepted that a tradeoff had to be made between safety and workload. As safety was given a higher priority, the haptic controller was 'overturned' using a 'high' value for K_H. This caused haptic moments to be perceived as 'too strong', leading to increased physical workload and higher frustration levels over time. To compensate for these problems and deliver the theoretical benefits of the HCAS described in Sec. II-A, a new 'human-centered' tuning procedure is introduced in the following section.

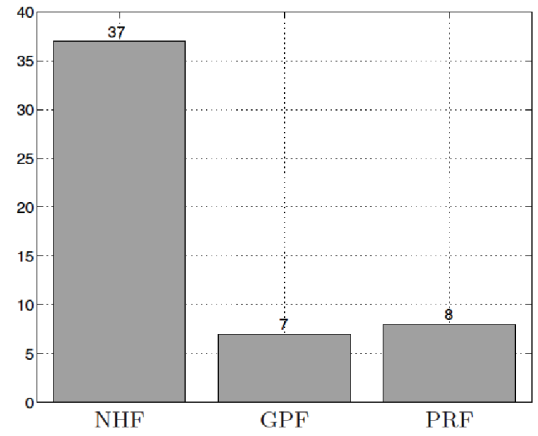

Fig. 4. Total number of collisions for all subjects [10]. Here 'NHF' stands for no haptic feedback; 'GPF' and 'PRF' are haptic feedback configurations using different artificial force fields (AFFs). Haptic feedback improves teleoperation safety by significantly reducing the number of collisions.

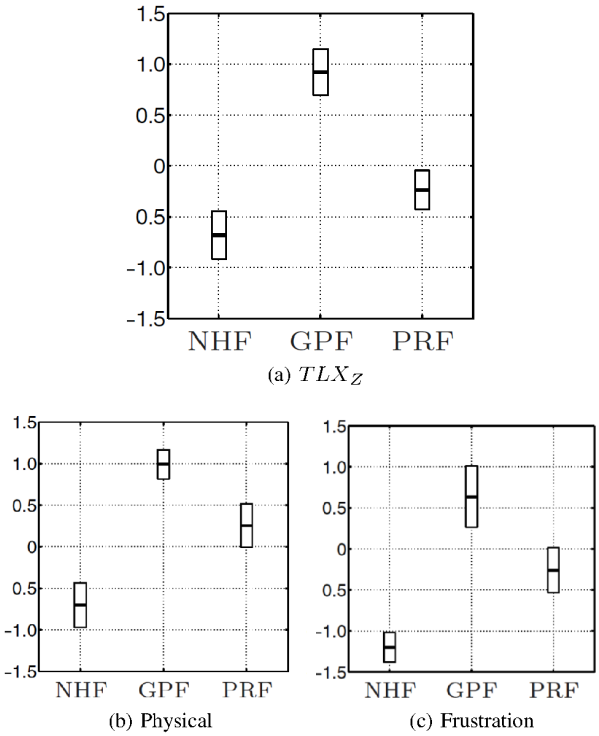

Fig. 5. Mean and 95% confidence intervals of the overall subjective workload and two (of six) workload sources measured using the NASA TLX [10]. Haptic feedback configurations (GPF & PRF) result in higher overall Z-scores compared to pure manual control (NHF) due to increased physical workload and frustration.

III. Tuning Haptic Feedback

Haptic moments applied on the side-stick are transmitted to the teleoperator via the human arm neuromuscular system (NMS). Therefore, by taking into account the NMS response when tuning haptic moments, the high physical workload and frustration levels reported for heuristic tuning methods may be reduced. This novel tuning approach makes use of models and measurements of the NMS.

A. Human Arm Neuromuscular System

The human arm neuromuscular system (NMS) resembles a closed loop feedback control system, see Fig. 6. The central nervous system (CNS), which consists of the brain and spinal cord, determines appropriate motor commands based on feedback from sensors, as well as goal directed feedforward control signals originating from 'higher brain centers' [24]. These motor commands trigger specific muscles to apply moments, causing or restricting motion of the skeleton. The magnitude of muscle moments is determined by its level of activation, which in turn affects its spring-damper characteristics [25]. The skeleton provides a rigid structure for the NMS components, and its mass and inertia properties also affect the kinematics of the system. The NMS is much quicker in detecting and responding to stimuli when compared to the visual system: $40ms$ vs. $200ms$ [24]. This fast reaction time is thanks to subconscious reflexive feedback paths through the spinal cord

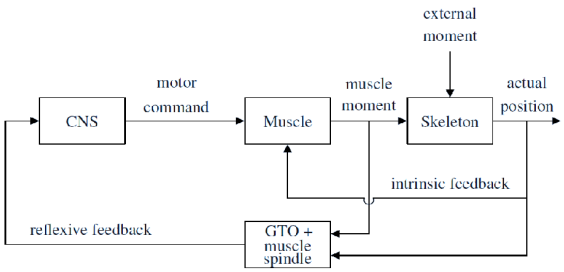

Fig. 6. Closed loop block diagram of the human arm neuromuscular system (NMS) [25]. The system resembles a classic feedback control system.

provided by force and position feedback of the Golgi tendon organ (GTO) and muscle spindles respectively.

With respect to the tuning of the haptic controller, an important dynamic property of the NMS is its endpoint admittance. Endpoint admittance is defined as the "causal relationship between moment (input) and hand position (output)" [24]. Therefore admittance is practically equal to the inverse stiffness of the system. Moreover, admittance has been found to be dependent on the magnitude and direction of the voluntary feed-forward or 'bias' moments commanded by the CNS [15] [25].

The NMS is highly adaptive and endpoint admittance can be varied over a large range of values by modulating the stiffness and damping parameters of the muscles through two physiological mechanisms. The first mechanism involves the adjustment of the relative strengths of the aforementioned reflexive feedback paths. Greater force feedback from the GTO results in high admittance. On the other hand, larger position feedback using muscle spindles results in low admittance. At a setting where both feedback paths are suppressed, admittance is characterized by relatively constant intrinsic muscle stiffness and damping values caused by a constant level of activation [25]. The second mechanism entails co-contraction of muscle pairs resulting in low admittance, and it is often used to reject external disturbances [24]. When comparing the two mechanisms, reflexive feedback is a more energy efficient process, leading to lower physical workload [24].

Using these two mechanisms, humans can be instructed to respond to haptic moments in three distinct ways known in literature as the force (FT), relax (RT) and position tasks (PT). Each task instruction is described in Table II along with their associated relative admittances.

B. Neuromuscular Admittance Based Tuning Paradigm

Experimental evidence has shown that the NMS varies its admittance/stiffness over a large range of values to match a particular tuning setting of the haptic controller [13] [18]. Therefore it is difficult to determine an optimal tuning setting as most settings result in adequate stability and performance of the combined human-machine system [13] [15]. However, an adaptation to a non-optimal tuning setting has been found to cause increased physical workload and frustration, as reported by Lam for heuristic tuning of the HCAS, see Sec. II-C.

A possible solution to this problem is to tune the haptic controller to match a so called 'design neuromuscular admittance' setting [14] [15]. In this way, the NMS will adapt to a tuning setting that is based on its own properties, possibly reducing conflicts between the human operator and the automation on a neuromuscular level. This is approach illustrated below for the HCAS:

$$M_H = \underbrace{[K_{NMS} + K_{st}]}_{combined\ system\ stiffness} \cdot |\mathbf{R}| \tag{5}$$

Here K_{NMS} is the design neuromuscular stiffness (i.e., inverse admittance) and K_{st} is the stiffness of the side-stick control interface. When comparing equations (4) and (5), the main difference in the new approach is that the haptic moment, M_H, is computed based on the 'combined' stiffness of the NMS and the side-stick. The rationale behind this new tuning paradigm can be better understood by considering Fig. 7

Three possible design points for tuning haptic moments corresponds to the neuromuscular admittance/stiffness settings of FT, RT and PT, see Table II. Each of these tasks are characterized by different, but relatively constant admittance values at low (haptic moment) frequencies. Therefore neuromuscular admittance/stiffness can be included in the haptic moment control law as a simple gain, just as in equation (5).

TABLE II
DESCRIPTION AND RELATIVE ADMITTANCES OF THE THREE NEUROMUSCULAR TASK INSTRUCTIONS

Task	Admittance	Description
Force Task (FT)	High	Actively follow haptic forces and give way to the motion of the control interface
Relax Task (RT)	Medium	Do not react to haptic forces and follow motion of control interface
Position Task (PT)	Low	Resist haptic forces and maintain position of control interface

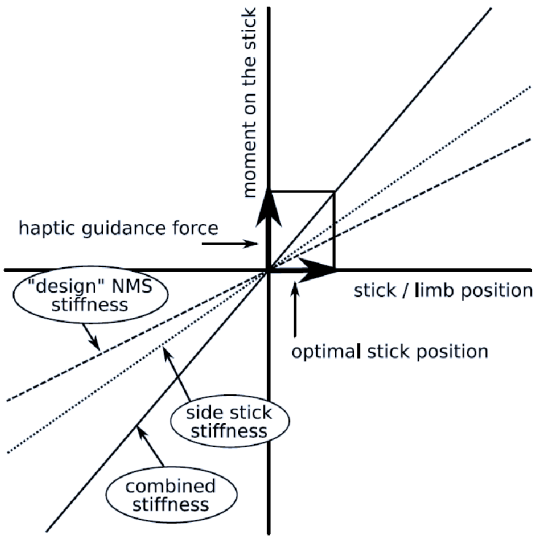

Fig. 7. Rationale behind the novel tuning procedure [15]. Here it is proposed that a haptic moment corresponding to the combined system stiffness i.e., stiffness of stick + design neuromuscular stiffness, has to be provided by the haptic controller to obtain the desired stick deflection.

In this study, the relax task stiffness is selected as the design point for tuning the haptic controller. This is because reflexes are naturally suppressed when performing the RT and the properties of the NMS are mainly dependent on its intrinsic mass-spring-damper characteristics. Consequently, the RT leads to the lowest physical activity of the three possible design points, thus the selection of the RT is aligned with the goal of reducing physical workload for the HCAS. Additionally, as the teleoperator can both increase and decrease his/her admittance relative to the RT, the control authority of the automation can be varied as desired during flight. This two-way variation of control authority is not easily possible for PT and FT as the teleoperator can only increase or decrease admittance, respectively, relative to these two settings.

Since neuromuscular admittance is dependent on the magnitude and direction of feedforward bias moments, M_{NMS}, the haptic moment control law is defined separately for the longitudinal (X) and lateral (Y) axes:

$$M_{H_X}\left(M_{NMS_X}\right) = \left[K_{NMS_X}\left(M_{NMS_X}\right) + K_{st_X}\right] \cdot \mathbf{R}_X \quad (6)$$

$$M_{H_Y}\left(M_{NMS_Y}\right) = \left[K_{NMS_Y}\left(M_{NMS_Y}\right) + K_{st_X}\right] \cdot \mathbf{R}_Y \quad (7)$$

C. Experimental Measurement of Neuromuscular Admittance

Admittance can be measured experimentally by applying small stochastic disturbance torques, T_{dist}, on the control interface to excite the NMS, and by measuring resulting hand displacements, δ_{NMS}, and handling moments, M_{NMS}. T_{dist} is designed in the frequency domain as a stochastic multi-sine signal that contains power at logarithmically spaced frequencies, typically up to $20Hz$ [26]. The phase of the sine components are randomized to ensure an unpredictable signal that

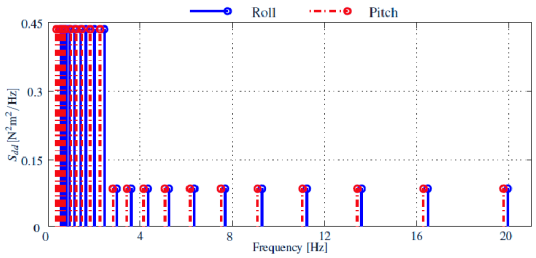

(a) Frequency domain representation

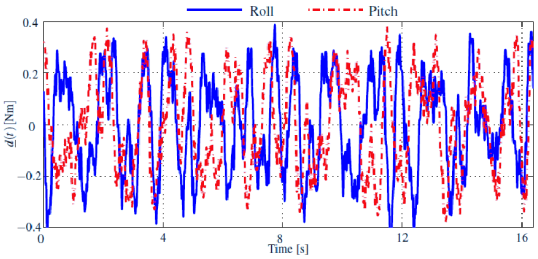

(b) Time domain realization for 1 period

Fig. 8. Frequency and time domain representations of the disturbance torques designed by Smisek et. al to suppress reflexive activity and thereby measure relax task admittance, whilst applying feedforward bias moments [15].

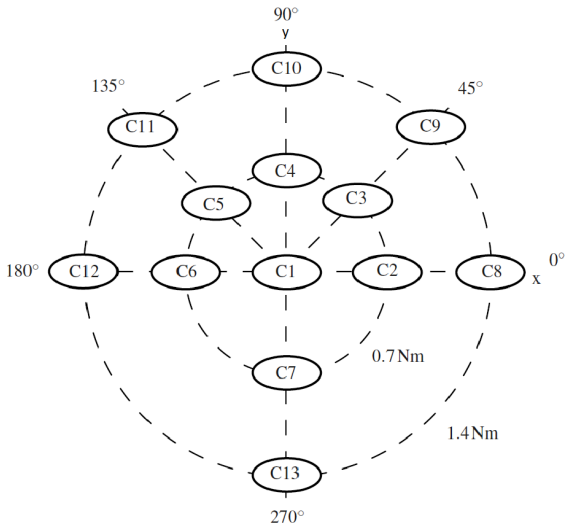

Fig. 9. Thirteen bias moment conditions of the experiment used by Smisek et. al to measure RT admittance [15].

cannot be anticipated by experiment subjects [24]. Admittance along the longitudinal and lateral hand axes can be measured simultaneously by applying two different disturbance torques which are separated in the frequency domain [27]. In this way, the response to each disturbance can be separated when identifying admittance from the measured data.

From experimental data, admittance can be estimated at the frequencies of the disturbance torque by computing the cross-spectral density between T_{dist} and δ_{NMS}, and the cross-spectral density between T_{dist} and M_{NMS}:

$$\hat{H}_{adm}\left(f_{dist}\right) = \frac{\hat{S}_{\delta_{NMS}T_{dist}}\left(f_{dist}\right)}{\hat{S}_{M_{NMS}T_{dist}}\left(f_{dist}\right)} \quad (8)$$

Note that equation (8) has to be evaluated separately along the longitudinal and lateral directions to estimate the admittance along these two axes.

In this study, two disturbance torques are used to measure admittance for different applications, and are discussed in the following paragraphs.

1) Disturbance Torque for Relax Task Admittance Measurement:

A human-in-the-loop experiment with ten subjects was conducted by Smisek et. al to measure RT admittance to implement the neuromuscular analysis based tuning algorithm described by equations (6) and (7). To measure RT admittance whilst applying feedforward bias moments, neural reflexes have to be artificially suppressed. Smisek et. al proposed a wide bandwidth disturbance torque with full power up to $2.5Hz$ and 20% of full power at higher frequencies [15]. This principle was used to design two uncorrelated disturbance torques, each with power at twenty logarithmically spaced frequencies (from $0.4 - 20Hz$), to measure RT admittance along the roll and pitch axes, see Fig. 8. Additionally, subjects were required to apply bias moments of thirteen different magnitudes and directions to obtain a complete set of admittance

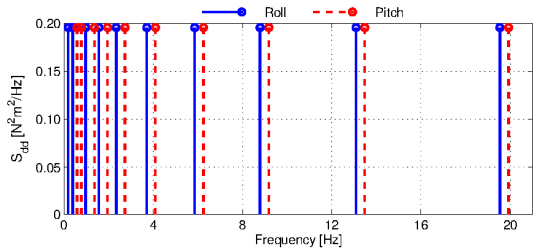

(a) Frequency domain representation

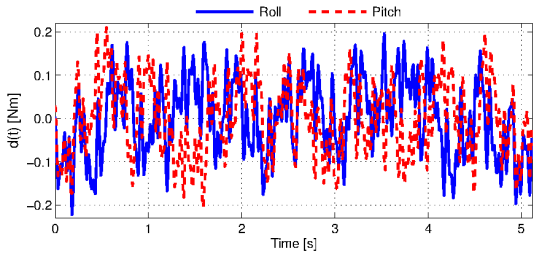

(b) Time domain realization for 1 period

Fig. 10. Frequency and time domain representations of the disturbance torques used to investigate the relationship between adaptation of admittance and the trajectory to be flown. This disturbance torque permits neural reflexes.

measurements for tuning the haptic controller, see Fig. 9.

Results from the experiment performed by Smisek et al. indicated that the new measurement method succeeded in suppressing reflexive activity, and data from that experiment is averaged over all subjects for tuning the RT haptic controller in this study (see condition EC4 in Table VI). Furthermore, the disturbance torque developed by Smisek et. al is used to measure the RT admittance of the subjects that took part in this research to design haptic controllers tuned to match each subject's specific neuromuscular properties (see condition EC3 in Table VI).

2) Disturbance Torque for Admittance-Trajectory Relationship Investigation:

Experimental admittance measurements are also needed to evaluate whether admittance adapts to the trajectory flown. For this purpose, the inherent neuromuscular admittance of the subject has be measured whilst performing a teleoperation task, see Sec. V. Consequently, a wide bandwidth disturbance torque is designed with equal power at ten logarithmically spaced frequencies between $0.5 - 20Hz$, see Fig. 10. To prevent this disturbance torque from affecting manual control of the UAV, it's power has been scaled such that the resulting side-stick motion is limited to 30% of the maximum stick deflection (when the teleoperator is not holding the stick).

IV. Offline Simulation

Offline simulations are used to verify the neuromuscular analysis based tuning procedure described in Sec. III-B. Additionally the sensitivity of the HCAS to varying teleoperator NMS and haptic controller tuning settings is also investigated.

A. Simulation Architecture

The simulation is used to study the teleoperator-automation haptic interaction alone. Therefore, the visual feedback teleoperators receive in reality is intentionally neglected. By doing so, the simulated teleoperator has to rely solely on the haptic feedback to avoid collisions, thus isolating the effects of the haptic interaction when analyzing the simulation results. These considerations result in the simulation architecture given in Fig. 11. The following paragraphs describe the models used to implement the simulation components.

1) Cognitive Control:

The simulated teleoperator behavior is modeled assuming he/she has a perfect internal representation of the side-stick and UAV dynamics. Based on this assumption, the longitudinal side-stick moment, M_{C_X}, needed to maintain a constant desired UAV velocity, V_{des}, is equal to:

$$M_{C_X} = \delta_{st_X} K_{st_X} \qquad \text{where} \qquad \delta_{st_X} = \left[\frac{\delta_{st_{X_{max}}}}{V_{max}}\right] V_{des} \tag{9}$$

Here, δ_{st_X} and $\delta_{st_{X_{max}}}$ are the required and maximum longitudinal side-stick deflections, K_{st_X} is the side-stick stiffness and V_{max} is the maximum UAV velocity. The same principle is applied to determine the lateral side-stick moment, M_{C_Y}, needed to maintain a constant desired UAV yaw rate, $\dot{\psi}_{des}$. In the simulation V_{des} =5 [m/s] and $\dot{\psi}_{des}$ =0 [rad/s].

2) Neuromuscular Model:

The dynamics of the muscles and skeletal bones of the human arm and hand are simulated using the NMS model developed by de Vlugt [28]. A block diagram of this model, including transfer functions of its components, can be visualized in Fig. 12. In the figure, ω_0 and β represent the natural frequency and the damping ratio of the muscles and equals 13.82 [rad/s] and $\sqrt{2}/2$ respectively [29]. By varying the model parameters, it is possible to simulate the teleoperators's response to the three neuromuscular task instructions i.e., the response to FT, RT and PT. The inertia of the arm [Nms^2/rad], I_i, as well as the stiffness [Nm/rad] and damping [Nms/rad] of the intrinsic feedback, K_i and B_i, and grip dynamics, K_g and B_g, were measured experimentally by Lasschuit for RT [25]:

$$I_i = \begin{bmatrix} I_{iX} & 0 \\ 0 & I_{iY} \end{bmatrix} = \begin{bmatrix} 0.015 & 0 \\ 0 & 0.008 \end{bmatrix}$$

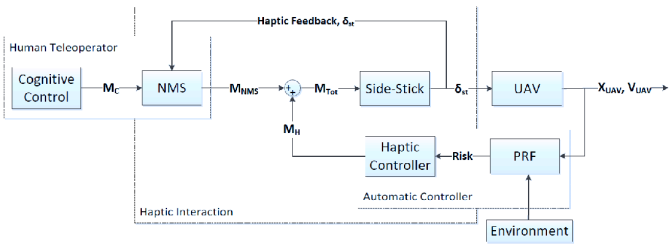

Fig. 11. Overall simulation architecture. This scheme is similar to reality, however the visual feedback loop is deliberately removed to isolate the effects of teleoperator-automation haptic interaction.

$$B_i = \begin{bmatrix} B_{i_P} & 0 \\ 0 & B_{i_Y} \end{bmatrix} = \begin{bmatrix} 0.51 & 0 \\ 0 & 0.06 \end{bmatrix}$$

$$B_g = \begin{bmatrix} B_{g_P} & 0 \\ 0 & B_{g_Y} \end{bmatrix} = \begin{bmatrix} 2.50 & 0 \\ 0 & 2.03 \end{bmatrix}$$

$$K_i = \begin{bmatrix} K_{i_X} & 0 \\ 0 & K_{i_Y} \end{bmatrix} = \begin{bmatrix} 9.20 & 0 \\ 0 & 1.21 \end{bmatrix}$$

$$K_g = \begin{bmatrix} K_{g_P} & 0 \\ 0 & K_{g_Y} \end{bmatrix} = \begin{bmatrix} 298.48 & 0 \\ 0 & 163.25 \end{bmatrix}$$

To simulate the NMS model for FT and PT, the above stiffness and damping parameters of RT are multiplied by a gain of 0.5 and 7.0 respectively. The rationale for this is explained in the 'Haptic Controller' paragraph below.

3) Side-Stick and UAV Dynamics:
A simple linear spring, with stiffness K_{st} equal to 2.0 [Nm/rad] in both longitudinal and lateral directions, models the side-stick dynamics:

$$\delta_{st} = \frac{M_{Tot}}{K_{st}} \tag{10}$$

The UAV is modeled as a control augmented helicopter with a rotor radius of 1.5 [m]. Longitudinal side-stick inputs are mapped to velocity commands along the body X axis, and lateral side-stick inputs are mapped to yaw rate commands around the body Z axis:

$$H_{X_{UAV}}(s) = \frac{V_X}{\delta_X} = \frac{1}{(0.3s+1)(0.18s+1)} \tag{11}$$

$$H_{Y_{UAV}}(s) = \frac{\dot{\psi}}{\delta_Y} = \frac{1}{(0.2s+1)} \tag{12}$$

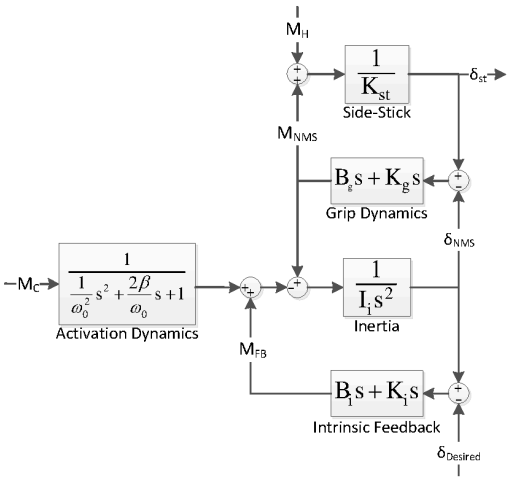

Fig. 12. Pilot neuromuscular system model adopted from de Vlugt [28]. Note that reflexive feedback paths have been neglected due to the constant level of activation of muscles in the simulation.

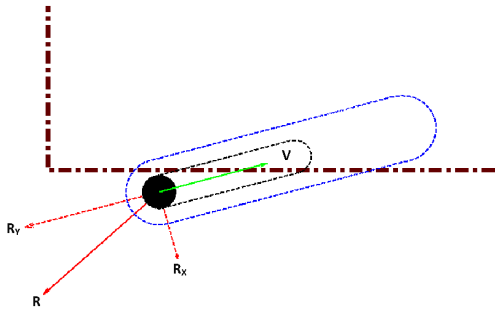

Fig. 13. Discrete parametric risk field (PRF) implementation with velocity vector, V, and final collision avoidance vector, R . The direction and magnitude of R_X and R_Y indicates how the UAV has to be steered to avoid obstacles.

In addition to the above dynamics, the UAV has a maximum velocity, V_{max}, and acceleration, a_{max}, of 5.0 [m/s] and 1.0 [m/s^2] in the longitudinal direction, and a maximum yaw rate, $\dot{\psi}_{max}$, and yaw acceleration, $\ddot{\psi}_{max}$, of 0.32 [rad/s] and 2.0 [rad/s^2] in the lateral direction.

4) Parametric Risk Field:
A sensor model with a resolution of 3^0 and a range of 50 [m] is used to detect obstacles 360^0 around the UAV in the virtual environment of the simulation. The parametric risk field is mapped on to the 'sensor rays' such that its geometry is discretized along each ray. The size of the PRF used is determined by the constant parameters listed in Table I. By comparing the distance of an obstacle to the distance of the PRF zone boundaries, the risk of collision can be computed for each sensor ray using equation (3). Subsequently, the total risk vector for all rays can be computed using the 'max-min' method outlined in Sec. II-B. The discretized PRF, as well as the resultant collision avoidance steering vector, **R**, is pictured in Fig. 13.

5) Haptic Controller:
Based on the instantaneous risk of collision and the stiffness of the NMS, haptic feedback moments are applied on the side-stick using the neuromuscular admittance based control laws given by equations (6) and (7). In the simulation, the control strategy and consequently the bias moments applied by the simulated teleoperator remains constant. Using experimental data measured by Smisek et. al, the corresponding neuromuscular stiffness values along the longitudinal and lateral axes, K_{NMS_X} and K_{NMS_Y}, for RT are listed in Table III.

To tune the haptic controller for FT and PT stiffness settings, data from published literature presenting stiffness/admittance

TABLE III
EXPERIMENTALLY DERIVED NMS STIFFNESS OF THE RELAX TASK FOR THE SIMULATION CONDITIONS

	Control Strategy	M_C [Nm]	$K_{NMS_{RT}}$ [Nm/rad]
X'	$V_{des} = 5.0m/s$	0.7	5.051
Y'	$\dot{\psi}_{des} = 0.0rad/s$	0.0	0.455

measurements of the human arm were consulted [30] [27]. This literature review revealed that the NMS stiffness for FT and PT were approximately 0.5 and 7 times that of RT, respectively:

$$K_{NMS_{FT}} = G_{FT} \cdot K_{NMS_{RT}} = 0.5 \cdot K_{NMS_{RT}} \tag{13}$$

$$K_{NMS_{PT}} = G_{PT} \cdot K_{NMS_{RT}} = 7.0 \cdot K_{NMS_{RT}} \tag{14}$$

'Gains' G_{FT} and G_{PT} are also used to determine the NMS model parameters for FT and PT from those of RT.

6) Environment:

A tunnel shaped obstacle, see Fig. 16, represents the virtual environment of the simulation. Due to the constant control strategy of the simulated teleoperator, haptic moments generated when the UAV gets too close to tunnel walls indirectly guides the teleoperator from the starting location to the target point. To perturb the motion of the UAV through the tunnel, a 30^o turn (to force a 'chicane' like maneuver), a sudden change in the tunnel diameter (from 18 [m] to 12 [m]), and a dead-end (to stop the UAV completely) are included in the geometry of the tunnel. These additional elements cause variations in the haptic feedback that is generated.

B. Simulation Setup

1) Independent Variables and Conditions:

The neuromuscular task instruction and the setting of the haptic controller make up the two independent variables of the simulation. Twelve simulation conditions arising from different combinations of the two independent variables, as well as a 'Baseline' condition, are defined in Table IV.

The 'Stick Tuning' haptic controller, HC_{ST}, considers only the stick stiffness, K_{st}, when computing haptic moments. By comparing HC_{ST} to controllers that take into account the combined stiffness of the NMS and the side-stick, the novel neuromuscular analysis based tuning method can be verified. The 'Baseline' condition is used to enable a fair comparison between the twelve simulation conditions. For this condition, no NMS is modeled and it uses HC_{ST}. In effect the 'Baseline' condition simulates a quasi-automatic collision avoidance system in which there are no physical interactions between the teleoperator NMS and the side-stick.

TABLE IV
SIMULATION CONDITIONS ARISING FROM DIFFERENT COMBINATIONS OF NEUROMUSCULAR TASK INSTRUCTION & HAPTIC CONTROLLER SETTING

Condition	NMS Task	Haptic Controller
SC1	NMS_{FT}	HC_{FT}
SC2		HC_{RT}
SC3		HC_{PT}
SC4		HC_{ST}
SC5	NMS_{RT}	HC_{FT}
SC6		HC_{RT}
SC7		HC_{PT}
SC8		HC_{ST}
SC9	NMS_{PT}	HC_{FT}
SC10		HC_{RT}
SC11		HC_{PT}
SC12		HC_{ST}
Baseline	No NMS	HC_{ST}

TABLE V
DEPENDENT VARIABLES OF THE SIMULATION

Measure	Variable	Description
Performance	RMS_{V_X}	Root mean square error of velocity RTB[1] [%]
	σ_{V_X}	Standard deviation of velocity RTB [%]
	d_{target}	Distance to target RTB [%]
Control Activity	$\sigma_{\delta_{st}}$	Standard deviation of stick deflection RTB [%]
	$\sigma_{\dot{\delta}_{st}}$	Standard deviation of stick deflection rate RTB [%]
	$CRR_{\delta_{st}}$	Control reversal rate of stick deflection RTB [%]
Safety	$\overline{d}_{obstacle}$	Mean distance to obstacle RTB [%]
	$n_{collisions}$	Number of collisions [-]
Haptic Controller Accuracy	$RMS_{(\lvert M_{NMS}\rvert - \lvert M_H\rvert)}$	RMS error between absolute NMS moment and absolute haptic moment [Nm]

2) Dependent Variables:

The dependent variables used to evaluate the teleoperator-automation haptic interaction in terms of performance, control activity, safety and haptic controller accuracy are listed in Table V. Here, haptic controller accuracy measures how well the controller predicted moments generated by the NMS.

As no haptic feedback is generated outside the tunnel and as safety is of prime importance in teleoperation, dependent variables are only computed up to the first collision. To allow for fairer comparisons between simulation conditions, for a particular condition, dependent variables are calculated relative to the same distance traveled by the 'Baseline' condition up to the first collision (RTB[1]). For instance, if the UAV traveled 30 [m] before the first collision, dependent variables for that condition are computed relative to the baseline results till 30 [m].

For each simulation condition, a 'Combined Score', S_C, is computed as the summation of the simulation dependent variables to easily quantify differences between conditions through a single numerical value:

$$S_C = RMS_{V_X} + \sigma_{V_X} + d_{target} + \sigma_{\delta_{st}} + \sigma_{\dot{\delta}_{st}} + CR_{\delta_{st}} + \overline{d}_{obstacle} + 100\ n_{collisions} + 100\ RMS_{(M_H - M_{NMS})} \tag{15}$$

As the number of collisions, $n_{collisions}$, and the haptic controller accuracy, $RMS_{(\lvert M_H\rvert - \lvert M_{NMS}\rvert)}$, are not computed

[1]RTB stands for 'Relative to Baseline'

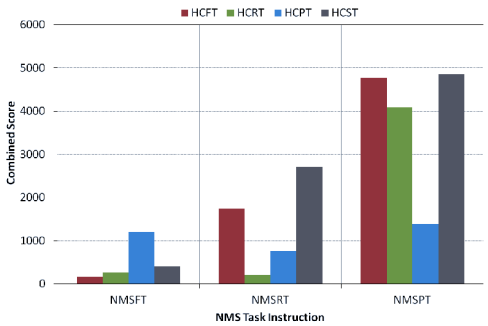

Fig. 14. Combined scores for all four haptic controllers for the three neuromuscular task instructions. A low value indicates better overall response.

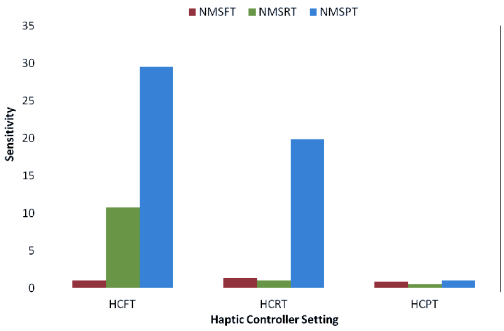

Fig. 15. Sensitivity of each haptic controller to variations in the neuromuscular task instruction. A large value indicates a high controller sensitivity.

RTB[1], their values are multiplied by a gain of 100 such that all components of S_C are within the same order of magnitude. Similar to the individual dependent variables, smaller values of S_C indicate a better overall system response.

C. Simulation Results and Analysis

1) Overall Simulation Results:

Fig. 14 displays a bar chart of the combined scores of all twelve simulation conditions categorized according to neuromuscular task instruction. The figure shows that for all three neuromuscular settings, the haptic controller tuned to the same admittance/stiffness as the NMS model has the lowest combined score, and therefore the best overall system response. For instance, the best overall response for all conditions is for HC_{FT} when tuned for NMS_{FT}. When neuromuscular admittance is neglected in the tuning of the haptic controller, as for the 'Stick Tuning' controller HC_{ST}, the system response degrades progressively with increasing NMS stiffness, and produces the worst system response for NMS_{RT} and NMS_{PT}. Additionally, HC_{ST} resulted in the most collisions for all three neuromuscular tasks.

It can also be noted from Fig. 14 that for a particular task instruction, the value of the combined score increases significantly when the haptic controller is under-tuned as opposed to an over-tuned controller. This is clearly evident for NMS_{RT} where the combined score of HC_{FT} (1750) is almost two and a half times that of HC_{PT} (760), indicating a greater deterioration of the overall system response with an under-tuned controller. Finally, it is clear from Figure 14 that all four controllers perform the worst for NMS_{PT}, indicating that PT should not be chosen as the tuning setting for the haptic controller.

A sensitivity analysis of the three admittance based controllers is computed from changes in the combined score when neuromuscular task instruction is varied to an off-design point and is pictured in Figure 15. Here a large value indicates high sensitivity.

It is clear from Fig. 15 that HC_{PT} has the lowest sensitivity of all the controllers. This is expected for this controller as large moments need to be applied to prevent overshoots of the UAV for all three neuromuscular settings. On the other hand, HC_{FT}, which was found to have the best overall response from Figure 14, is the most sensitive to changes in admittance. The sensitivity of HC_{RT} is between that of HC_{PT} and HC_{FT}.

These results agree with those found experimentally by Cleij [18], and they also demonstrate the necessity of taking into account the 'combined' system stiffness when tuning the haptic controller. Furthermore, the results show that the HC_{RT} controller, tuned to the relax task stiffness, is an ideal middle ground when considering actual system response, as well as controller sensitivity.

2) 'Relaxed' Neuromuscular System Results:

As mentioned in Sec. III-B, this research selects the relax task (RT) as the design point for tuning haptic moments. Differences between the haptic controllers for the 'relaxed' NMS can be analyzed in detail through Fig. 16. Here, the trajectories traced by the UAV, as well as the magnitude and direction of the haptic collision avoidance moments supplied per second are shown. Additionally, the UAV protection zone per second is depicted as black dashed circles, and the spacing between circles can be used to infer velocity changes of the UAV.

Fig. 16 shows that the under-tuned controllers, HC_{ST} and HC_{FT}, follow erratic trajectories, and as a result are more susceptible to collisions. In addition, the under-tuned controllers seem to apply relatively large lateral haptic moments at close proximity to tunnel walls. On the other hand, when the haptic controller is tuned to the same stiffness as the NMS as for HC_{RT}, or is over-tuned as in the case of HC_{PT}, the UAV appears to decelerate faster and at greater distances from tunnel walls. Furthermore, haptic moments supplied tend to be aligned along the UAV trajectory, with less lateral moments.

This difference in control strategy between under and over-tuned controllers can be explained by considering the form of the haptic moment control law given by equation (5). The maximum haptic moment that can be supplied is numerically equal to the combined system stiffness $(K_{NMS} + K_{st})$ when the risk of collision is one, i.e., when the probability of collision is 100%. Therefore, when the combined system stiffness is underestimated, as for under-tuned controllers, adequate haptic collision avoidance moments are generated only when the UAV is extremely close to obstacles such that the risk of collision is relatively high. This insufficient deceleration of the UAV longitudinal velocity requires high lateral haptic moments to induce large heading changes in an

attempt to steer the UAV away from danger. However for both HC_{ST} and HC_{FT}, the delayed haptic guidance results in a number of collisions and oscillatory UAV motion.

Safety improves considerably when the haptic controller overestimates the combined system stiffness as for HC_{PT}. For this controller, it can be seen in Fig. 16d that longitudinal haptic moments build up in magnitude from larger distances to obstacles. This causes the UAV to decelerate to very low velocities at close proximity to tunnel walls, thus requiring relatively small lateral haptic moments to steer it safely without collisions. When the controller is tuned to match the stiffness of the NMS as with HC_{RT}, a mixture of the two control strategies is used, leading to higher average UAV velocities and no collisions.

Additional evidence for the differences in control strategy can be found by comparing the normalized side-stick deflections caused by haptic feedback, see Fig. 17. This figure shows that HC_{RT} and HC_{PT} have greater longitudinal side-stick deflections resulting in higher UAV decelerations, while HC_{ST} and HC_{FT} have greater lateral side-stick deflections causing increased yaw rates. The figure also shows that the control activity of the controllers rises with increasing assumed combined system stiffness and is the highest for HC_{PT}. Particularly in the longitudinal direction, HC_{PT} causes highly erratic side-stick deflections of extreme magnitudes and high deflection ratessee, Figure 17a,. Such haptic behavior has been found in previous experiments to contribute significantly to subjective physical workload and frustration, and thus should be avoided when tuning the haptic controller [23].

For a more quantitative analysis of the simulation results, the reader is referred to [31].

V. Human-In-The-Loop Experiment

The results of the offline simulation provide initial insights into the teleoperator-automation haptic interaction and verifies the novel neuromuscular analysis based tuning procedure. However, the trends found in the simulation are influenced by the intentional suppression of visual feedback to the teleoperator. In reality, the teleoperator is expected to manually steer away from obstacles in the visual field of view (FOV) and haptic cues are meant to improve safety and SA, particularly when obstacles are outside the FOV. To validate the novel tuning procedure, as well as to investigate the admittance-trajectory relationship (without haptic feedback), a human-in-

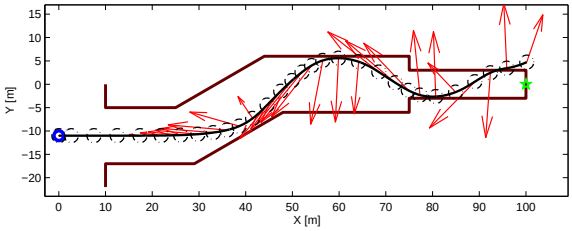

(a) Stick tuning haptic controller, HC_{ST}

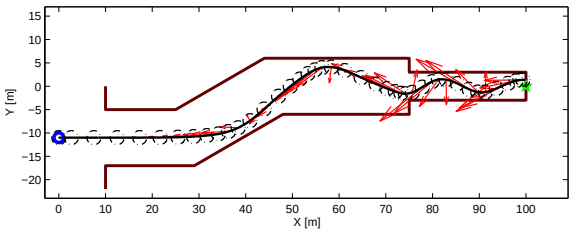

(b) Force task haptic controller, HC_{FT}

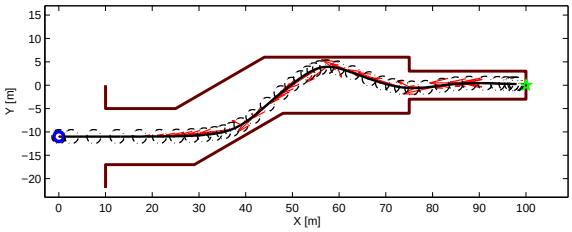

(c) Relax task haptic controller, HC_{RT}

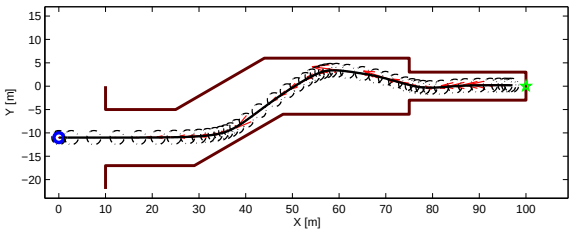

(d) Position task haptic controller, HC_{PT}

Fig. 16. Trajectories (black solid lines), haptic feedback per second (red arrows) and UAV protection zone per second (dashed black circles) of the four haptic controllers for relax task NMS setting, NMS_{RT}

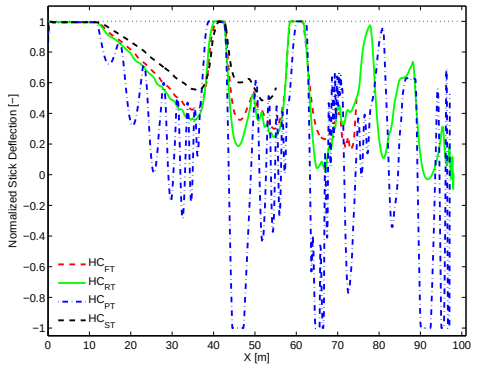

(a) Longitudinal

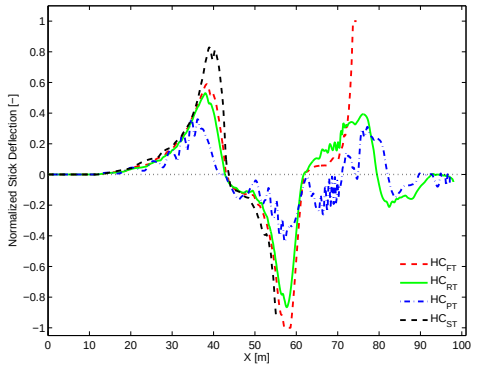

(b) Lateral

Fig. 17. Normalized stick deflection of the four haptic controllers for relax task NMS setting, NMS_{RT}. The dotted black horizontal lines represent the deflections necessary to maintain the desired velocity and yaw rate.

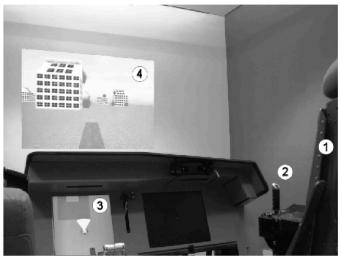

Fig. 18. Human-Machine Interaction lab with aircraft chair (1), hydraulic side-stick (2), navigation display (3) and onboard camera view (4)

the-loop experiment that replicated UAV teleoperation, with visual feedback, was conducted.

A. Method

The human-in-the-loop experiment is divided in two parts. To investigate whether it is beneficial to tune the haptic controller to match each individual subject's NMS properties, the relax task (RT) admittance of each subject is measured in experiment part A using the disturbance torque designed by Smisek et. al, see Sec. III-C1. Admittance was measured along the longitudinal and lateral axes for the thirteen conditions pictured in Fig. 9, and part A takes one hour and thirty minutes to complete. The procedure and analysis methods used in experiment part A are identical to those used by Smisek et. al, and the reader is referred to [15] for more details.

The novel tuning procedure is validated and the admittance-trajectory relationship is studied in experiment part B. In this part, subjects were required to perform a UAV teleoperation task in a virtual environment. The following subsections focuses on the design of experiment B.

1) Subjects and Task Instruction:

Twelve right handed male subjects from the graduate student population of the faculty of Aerospace Engineering, with an average age of 23.42 years ($\sigma = 0.67$ years), took part in the experiment. Participant consent and approval from the Human Research Ethics Committee of the TU Delft were obtained before conducting the experiment. No monetary compensation was provided.

In the experiment (part B), subjects were required to fly from waypoint to waypoint (represented as smoke plumes), in an obstacle laden urban environment containing buildings of various shapes and sizes. Subjects were instructed, in order of priority, to avoid collisions, fly as closely as possible through the center of waypoints, and to fly as fast as possible. Furthermore, subjects were asked to choose and maintain a constant arm-hand orientation and grip throughout the experiment.

Haptic feedback moments (derived from different haptic controller tuning profiles) were applied to the control loaded side-stick to help avoid collisions with the environment. To enhance the realism of the experiment if a collision occurred, a loud beep is sounded and a twenty second time penalty is applied during which the experiment is paused. Subsequently, the UAV is repositioned to the start of the subtask (see subsection V-A3) where the collision occurred and the experiment is continued.

2) Apparatus:

The fixed base flight simulator of the Human-Machine Interaction lab (HMI Lab) at TU Delft is used to conduct the experiment, see Fig. 18. Here the subject is seated in a aircraft chair (1), with an electro-hydraulic side-stick and arm rest (2) mounted on the right side. Visual feedback is provided by two displays. An 18 inch LCD screen with a resolution of 1280×1024 at 60 [Hz] is used as a navigation display (3). An onboard camera view (4) is projected onto a white wall 2.9 [m] in front of the subject with a resolution of 1024×768 at 60 [Hz]. The camera view of the 'outside world' has a field of view of 60^o horizontally and 45^o vertically, and is fixed to the longitudinal axis of the UAV.

The electro-hydraulic side-stick displayed in Fig. 18 is used for manual control of the UAV and to provide haptic collision avoidance moments. Second order dynamics with an inertia $I_{st} = 0.02$ [kgm^2], a damping coefficient $B_{st} = 0.2$ [Nms/rad], and a spring constant $K_{st} = 2.0$ [Nm/rad] are simulated on both stick axes. These values match those used by Smisek et. al for neuromuscular admittance identification [15]. Furthermore, stick motion is limited to 0.35 [rad] and 0.40 [rad] in the longitudinal and lateral directions respectively. The UAV helicopter dynamics used in the offline simulation, see Sec. IV-A3, is also used in the experiment. The parameters of the PRF used to detect obstacles and compute the risk of collision are listed in Table I.

3) Trajectories:

The trajectories used are the same as those designed by Lam for previous UAV teleoperation experiments [9]. The virtual environment for the remote sensing task consists of six different obstacles termed 'subtasks', see Fig. 19. In the 'outside world' camera view, subtasks are pictured as buildings and waypoints as smoke plumes, see Fig. 18.

Smoke plumes are intended to reduce visibility near obstacles and each subtask is designed to provoke a different control behavior. For instance, in subtask 3, the subject is required to hover and fly backwards into the building until a stop sign is visible (asterisk in Fig. 19c). Since the camera view is in the opposite direction of motion, the subject has to rely heavily on haptic feedback to complete the maneuver without collisions.

Trajectories are composed of the six subtasks arranged randomly, see Fig 20. To reduce boredom and learning effects, three different trajectories are designed for the experiment. A trajectory takes approximately two minutes and thirty seconds to complete (without collisions).

4) Haptic Controller Implementation:

Previous research has shown that neuromuscular admittance is dependent on the magnitude and direction of teleoperator bias moments [15] [25]. Unlike the offline simulation, the haptic controller used in the experiment takes this property into account by using nearest neighbor interpolation of the instantaneous bias moment magnitude and direction to determine the nearest measurement condition (of the thirteen conditions) visualized in Fig. 9. Subsequently, the measured

stiffness values (K_{NMS_X} and K_{NMS_Y}) for the 'nearest condition' are used to compute appropriate haptic moments using equations (6) and (7). Nearest-neighbor interpolation is adopted as it is an easy method to implement and resulted in stable haptic moments without the need for additional filters. It is hoped that this dynamic tuning approach will allow the haptic controller to better anticipate the real time stiffness of the NMS, and consequently improve the teleoperator's appreciation of haptic cues.

5) Independent Variables and Experiment Conditions: Two categories of independent variables are defined for the experiment. The first category is concerned with the tuning profile (TP) of the haptic controller (HC). In total six different tuning profiles are tested in the experiment and the resulting experiment conditions are listed in upper part of Table VI. Note that the over-tuned controller, OT, is based on a gain of '2' as opposed to the simulation where a gain of '7' was used. This is because a gain of 7 resulted in haptic moments that were deemed too high for safety reasons, and a gain of 2 was sufficient to perceive the magnitude difference between RT and OT controllers.

The second independent variable is subtask (SB), consisting of the six subtasks which make up the obstacles for the remote sensing task, see Fig. 19. The effect of the six subtasks on

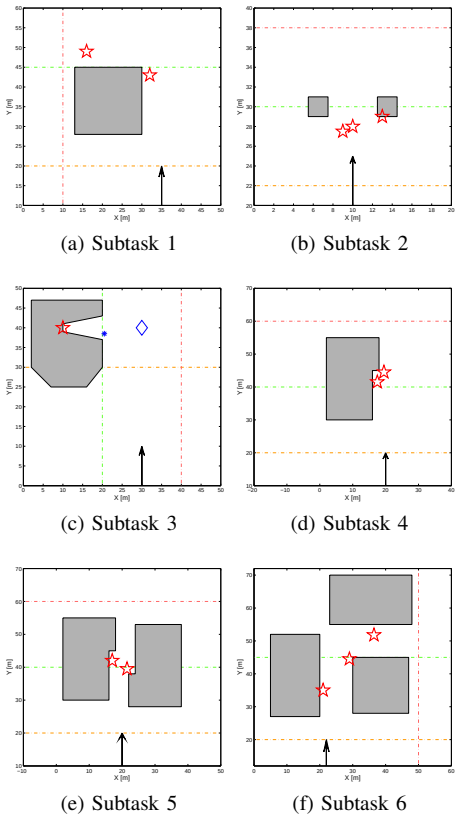

(a) Subtask 1 (b) Subtask 2

(c) Subtask 3 (d) Subtask 4

(e) Subtask 5 (f) Subtask 6

Fig. 19. Six obstacles or 'subtasks' used in the experiment. Waypoints are pictured as red stars and the UAV reset location and orientation after a collision are indicated with black arrows. The orange, green and pink lines are the 'beginning', 'middle' and 'end' locations at which admittance is identified during a 0.5s interval.

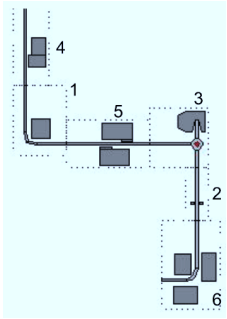

Fig. 20. An example trajectory consisting of the six 'subtasks' arranged randomly.

neuromuscular admittance is investigated in condition EC7. In this condition, continuous disturbance torques are applied on the side-stick to measure admittance whilst performing the teleoperation task with the same subject instructions as for conditions EC1-EC6. No collision avoidance haptic moments are provided whilst measuring admittance in condition EC7. The design of the disturbance torque used for this purpose is discussed in Sec. III-C2.

6) Dependent Variables: The dependent variables used to compare different haptic controllers can be divided into six categories: performance, control activity, haptic activity, safety, haptic controller accuracy and subjective questionnaires. Neuromuscular admittance is the only dependent variable for condition EC7. A complete list of dependent variables is listed in Table VII. Here 'RMS' stands for root mean square, 'STD' stands for standard deviation and 'SGN' is the sign of a variable (i.e., positive/negative).

A few dependent variables listed in Table VII need additional clarification. The haptic controller accuracy variables are used to determine the extent of agreement between the human teleoperator and the haptic controller (automation) on the magnitude and direction of haptic moments. Magnitude comparisons are based on the RMS error between the NMS moment and the haptic moment, $RMS_{(|M_{NMS}|-|M_H|)}$, with

TABLE VI
EXPERIMENT CONDITIONS

Condition	Symbol	Description
EC1	NHF	No haptic feedback. Pure manual control of UAV.
EC2	ST	HC tuned to match only stick stiffness
EC3	IRT	HC tuned to individual subject's relax task stiffness (f_{dist} = 0.5Hz)
EC4	RT	HC tuned based on average relax task stiffness of 10 subjects using data collected by Smisek et. al (f_{dist} = 0.5Hz)
EC5	UT	HC under-tuned relative to RT ($UT = RT \times 0.5$)
EC6	OT	HC over-tuned relative to RT ($OT = RT \times 2$)
EC7	ADM	No haptic cues. Disturbance torques applied to measure admittance.

TABLE VII
DEPENDENT VARIABLES OF THE EXPERIMENT

Measure	Symbol	Description
Safety	$n_{collisions}$	Number of collisions [-]
	$\overline{R}$	Mean risk magnitude [-]
Performance	$\overline{V}$	Mean velocity [m/s]
	d_{wp}	Min distance to waypoints [m]
Control Activity	$\overline{M}_{NMS}$	Mean NMS moment [Nm]
	$\sigma_{\dot{\delta}_{st}}$	STD stick rate [rad/s]
Haptic Activity	$\overline{M}_H$	Mean haptic moment [Nm]
	σ_{M_H}	STD haptic moment [Nm]
Haptic Controller Accuracy	$RMS_{(\lvert M_{NMS}\rvert - \lvert M_H\rvert)}$	RMS error between the NMS moment and the haptic moment [Nm]
	$SGN_{M_H \ \& \ M_{NMS}}$	SGN ratio of haptic and NMS moments [-]
Subjective	NASA TLX	Subjective workload assessment
	SA	Subjective situational awareness questionnaire
	HA	Subjective haptic feedback acceptance questionnaire
Admittance	$H_{ADM_{overall}}$	Overall/Mean admittance per subtask at 0.5 Hz [rad/Nm]
	$H_{ADM_{3Point}}$	Admittance at 'beginning', 'middle' and 'end' per subtask at 0.5 Hz [rad/Nm]

smaller values indicating higher magnitude agreement. A sign comparison ratio of the haptic moment and the neuromuscular moment, $SGN_{M_H \ \& \ M_{NMS}}$, is used to determine whether the teleoperator agrees with the direction of haptic moments. The higher the ratio (E[0,1]), the higher the agreement. Control activity, haptic activity and haptic accuracy variables are computed separately along the longitudinal (X) and lateral (Y) axes to investigate the control strategy differences between under and over-tuned haptic controllers observed in the offline simulation. In addition to computing the mean admittance per subtask, $H_{ADM_{overall}}$, admittance is also identified for 0.5 second intervals around the 'beginning', 'middle' and 'end' locations (LC) to investigate admittance variations within each subtask, $H_{ADM_{3Point}}$. These locations are illustrated in Fig. 19. Furthermore, the dependence of admittance on both velocity and trajectory are considered when analyzing the experiment data. It should be noted that admittance is also computed separately along the two side-stick axes.

Questionnaires are used to measure subjective workload, situational awareness (SA) and haptic feedback acceptance (HA) for conditions EC1-EC6. Workload is measured using the NASA Task Load Index (TLX) questionnaire [32]. The NASA TLX defines workload as the weighted average of six subjective subscales: mental demand, physical demand, temporal demand, performance, frustration and effort. The higher the resulting weighted average (E[0,100]), the higher the subjective workload. SA and HA are measured using questionnaires based on the Eurocontrol SASHA method [33]. These questionnaires aim at measuring the teleoperator's awareness of his/her surroundings and whether haptic feedback was helpful in completing the task, respectively. The SA and HA questions are answered on a five point likert scale (0-4), and the mean score of all the questions is taken as a measure of SA/HA, with higher scores indicating better SA/HA.

7) Procedure:

The experiment begins with a training session during which subjects are presented with two randomly chosen haptic feedback configurations, as well as the 'no haptic feedback' condition to gain familiarity with the task and the UAV dynamics. Subsequently, subjects perform (at least one) training and four measurement runs per haptic configuration. The experiment conditions listed in Table VII are performed by all subjects and are randomized using the 'Latin Square' approach to minimize unsystematic variation in the dependent variables. Subjects are not informed about the conditions they are performing and at the end of each condition, subjects are requested to fill in the aforementioned subjective questionnaires, see Table VII. Subjects are encouraged to take at least one break of five minutes between experiment conditions to avoid fatigue and prevent subjective opinions about prior conditions from affecting future measurements. The total duration of the experiment including training, breaks and the pre-experiment briefing is four hours.

B. Hypotheses

The five hypotheses of the human-in-the-loop experiment are listed below and are based on the simulation results as well as previous research:

1) Safety, SA and HA are expected to increase, and workload is expected to decrease when the haptic controller is tuned to take into account the combined system stiffness when compared to a controller which is tuned to only the stick stiffness (ST).
2) The over tuned controller (OT) will result in the least number of collisions and the lowest mean risk value. However, this increased safety is expected to come at the cost of increased control activity, particularly when compared to the under tuned controllers (UT and ST). Despite the improvements in safety, the increased control activity and accompanying increased physical effort are likely to lead to the lowest HA for OT.
3) Under tuned controllers (UT and ST) are likely to cause greater lateral haptic activity and comparatively higher mean risk values. On the other hand, over tuned controllers are expected to have greater longitudinal haptic activity, as well as lower mean risk values. This is based on the simulation results which showed differences in control strategies between over and under-tuned controllers.

4) Individual tuning is likely to improve haptic controller accuracy and reduce subjective physical workload, however this is not expected to be a highly significant effect.
5) Neuromuscular admittance is expected to decrease when the operator is subjected to trajectory elements that limit visibility and force a reduction of velocity

The first four hypotheses are concerned with the tuning of the haptic controller. The fifth hypothesis is related the to effect of trajectory and velocity on admittance variations.

VI. Results

All dependent variables, except subjective questionnaires, are computed per subtask to take into account the different order of subtasks in each trajectory. Dependent variables computed for multiple runs of the same subtask are averaged for each subject. Subsequently, the effects of the independent variables, TP (haptic controller tuning profile) and SB (subtask), on the dependent variables are analyzed using statistical methods. Interval/ratio dependent variables are studied using full-factorial repeated-measures ANOVA (analysis of variance), with pairwise Bonferroni corrected comparisons used as post-hoc tests. To comply with ANOVA assumptions, Greenhouse-Geisser corrections were applied to the degrees of freedom for non-spherical data. Additionally, interval data is visualized using error bar charts (means and 95% confidence intervals). Ordinal dependent variables ($n_{collisions}$ and subjective questionnaires) are inspected using the Friedman test followed with Wilcoxon matched signed rank tests for post-hoc analysis (also with Bonferroni corrections). Ordinal data is shown with the aid of box plots (median and interquartile range).

The results of the experiment are presented in three parts. First, the relax task (RT) admittance measurements collected in this research are qualitatively compared to the measurements made earlier by Smisek et. al. Thereafter, results concerning the validation of the novel tuning procedure are considered. Finally, results regarding the admittance-trajectory relationship are presented.

A. Comparison of Relax Task Neuromuscular Admittance Measurements

In the experiment, two haptic controller tuning profiles were based on the relax task admittance: the IRT controller is tuned to match each individual subject's relax task admittance, whereas the RT controller is tuned based on the average relax task admittance of ten subjects measured in an earlier identification experiment [15]. By comparing the effects of the two relax task controllers on the dependent variables of the experiment, it was planned to determine whether individual tuning is necessary for practical implementation of the novel tuning method. Fig. 21 shows admittance measurements using so called 'admittance ellipses' for a typical subject of the current research and for a typical subject from the earlier experiment. Here admittance for each bias moment condition is characterized by the magnitudes of the major and minor axes of the ellipses.

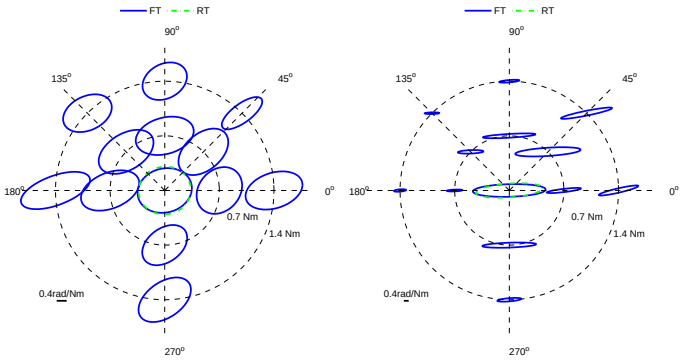

(a) Current Measurements (b) Previous Measurements

Fig. 21. Comparison of current and previous admittance measurements using 'admittance ellipses'. Each figure represents the admittance ellipse for one subject for $f_{dist} = 0.5Hz$. The admittance measured in this study is substantially higher for all measurement conditions.

By comparing the two measurement sets, it is immediately obvious that admittance measured in the current research is significantly higher for all bias moment conditions. Furthermore, admittance along both axes are similar in magnitude for the current research, whereas the previous measurements show large differences between the two axes, with substantially higher admittance along the lateral axis. These differences occur despite the fact that the same disturbance torque was used to measure admittance, as well as similar experiment protocols and analysis procedures.

A possible cause for these differences may be due to modifications applied to the electro-hydraulic side-stick of the HMI lab between the two experiments: the side-stick controller was updated with newer electronics and the internal update rate of the stick was increased to improve its stability. Physical differences between the two experiment subject populations may have also attributed to the variations observed between the two measurement sets. On a different note, the overlap of the RT and FT ellipses for the central conditions for both data sets strongly indicate that the wide bandwidth disturbance torque proposed by Smisek et. al is indeed an appropriate method to measure relax task admittance in the presence of bias moments.

Due to the above mentioned differences between the two measurement sets, experiment hypothesis 4 cannot be conclusively analyzed. None the less, the two relax task controllers are compared in subsequent sections to gain initial insights on the benefits of tuning the haptic controller to suit individual subjects.

B. Neuromuscular Admittance Based Tuning Law Validation

1) Safety:

Fig. 22a shows that the number of collisions, $n_{collisions}$, decreased with increasing strength of the haptic controller, agreeing with simulation results. A Friedman test revealed a significant effect of TP on $n_{collisions}$ (TP: $\chi^2(5) = 11.58$, $p \leq 0.05$). Post-hoc analysis using the Wilcoxon signed rank test found that the over-tuned controller, OT, resulted in significantly fewer collisions when compared to the pure manual

control condition (NHF) and the stick tuned controller (ST). No statistically significant differences were found between UT, IRT and RT despite the decreasing number of collisions observed for these controllers in Fig. 22a. Fig 22b shows that the highest number of collisions occurred for subtask 5; this subtask was reported by subjects to be the most difficult of all subtasks, followed by subtask 6. Contrastingly, subtasks 1 and 2 were found to cause no collisions. These differences lead to a highly significant effect of SB on $n_{collisions}$ (SB: $\chi^2(5) = 29.02$, $p \leq 0.01$).

The mean risk of collision, $\overline{R}$, is shown in Fig. 23. Subtasks 4, 5 and 6 were found to have similar and higher risk magnitudes when compared to subtasks 1, 2 and 3 leading to statistically highly significant effect of SB on $\overline{R}$ (SB: $F_{5,55} = 40.20, p \leq 0.01$). The higher risk for subtasks 4, 5 and 6 maybe due to the close vicinity of waypoints (smoke plumes) to building corners for these subtasks, see Fig 19. Fig. 23 shows that risk tends to decrease slightly for the stronger haptic controllers. However, as risk is mainly dependent on the trajectory flown by the teleoperator, which in turn is affected by the locations of waypoints, no significant effect of TP was found for $\overline{R}$. This is not in line with simulation results which showed that risk was inversely proportional to the strength of the haptic controller.

2) Performance:

The mean velocity of the UAV, $\overline{V}$, is shown in Fig. 24a. Here it can be seen that for a particular subtask, $\overline{V}$ is relatively constant for all haptic controllers, resulting in no statistical significance of TP on $\overline{V}$. On the contrary, $\overline{V}$ varies substantially with SB, causing a highly significant effect (SB: $F_{2.06,22.67} = 106.40, p \leq 0.01$). When comparing Fig 24a with Fig 22b, it can be seen that velocity tends to be lower for subtasks with the most number of collisions and vice-versa. This indicates that subjects decreased UAV velocity in an attempt to follow the primary task instruction of avoiding collisions.

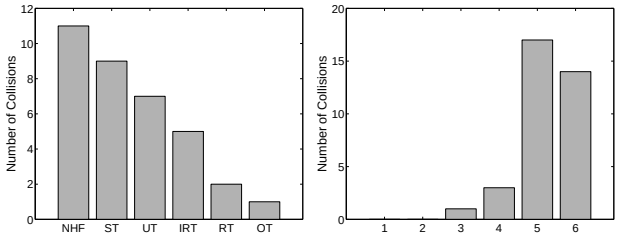

(a) Tuning Profile (b) Subtask

Fig. 22. Bar charts for the number of collisions, $n_{collisions}$, categorized according to TP (a) and ST (b). The numbers 1-6 on the horizontal axis of (b) correspond to the subtask number.

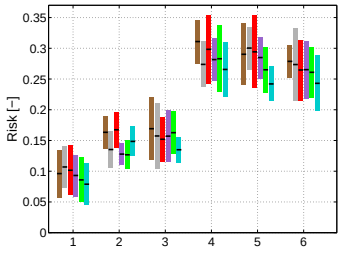

Fig. 23. Means and 95% confidence intervals of mean risk,$\overline{R}$. The numbers 1-6 on the horizontal axis correspond to the subtask number. NHF(brown), ST(gray), UT(red), IRT(violet), RT(green) and OT(cyan).

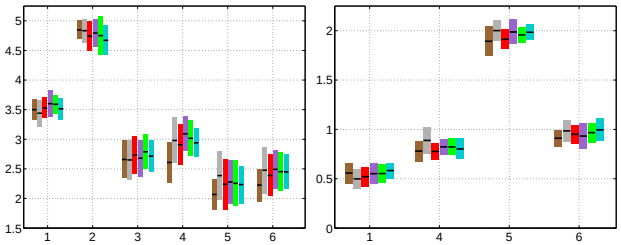

(a) $\overline{V}$, m/s (b) d_{wp}, m

Fig. 24. Means and 95% confidence intervals of performance related dependent variables. The numbers 1-6 on the horizontal axis correspond to the subtask number. NHF(brown), ST(gray), UT(red), IRT(violet), RT(green) and OT(cyan). Subtasks 2 and 3 did not have smoke plumes serving as waypoints and thus are not shown.

The minimum distance to waypoints, d_{wp}, is computed for subtasks 1, 4, 5 and 6, see Fig. 24b. For subtasks 2 and 3, the smoke plumes served to obscure the visual feedback supplied to the teleoperator and thus were not considered to be waypoints. Similar to $\overline{V}$, d_{wp} is not affected by the haptic controller tuning profile, thus a low statistical significance is observed between TP and d_{wp}. However Fig. 24b indicates that subtask had a high significance on d_{wp} (SB: $F_{3,33} = 295.17, p \leq 0.01$). Moreover, it can be seen that d_{wp} follows the same trend as $n_{collisions}$, and subtasks with more collisions have higher d_{wp}. This provides additional evidence that subjects employ a conservative control strategy when tackling difficult obstacles.

From the above discussion, it is clear that TP had no significance on the performance of UAV teleoperation. This indicates that subjects adapted their control strategies to ensure that task instructions were followed with similar performance for all haptic controller tuning profiles, even for the strong repulsive feedback applied by the OT controller.

3) Control Activity:

Fig. 25a shows that the mean longitudinal neuromuscular/bias moment, $\overline{M}_{NMS_X}$, applied by the subjects varied greatly to match the strength of the haptic controller, resulting in a highly significant effect of TP on $\overline{M}_{NMS_X}$ (TP: $F_{2.96,33.60} = 25.53, p \leq 0.01$). Post-hoc analysis revealed that OT and NHF caused considerably higher and lower $\overline{M}_{NMS_X}$ respectively, while no statistical differences were found between the other haptic controllers. This trend is reversed for subtask 3 where the UAV was required to fly backwards, suggesting that subjects relied more on haptic feedback when visual cues were not in the direction of motion, causing a highly significant two-way interaction (TP×SB: $F_{4.74,52.10} = 17.68, p \leq 0.01$). Subtask 2 resulted in much higher $\overline{M}_{NMS_X}$ compared to other subtasks, resulting in a highly significant effect of SB on $\overline{M}_{NMS_X}$ (SB: $F_{1.84,20.24} = 62.323, p \leq 0.01$).

The sign of the lateral bias moment, $\overline{M}_{H_Y}$, depends on

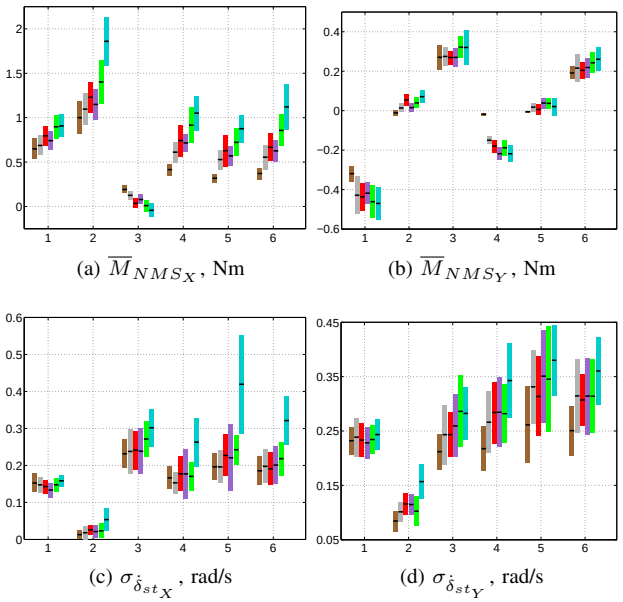

(a) $\overline{M}_{NMS_X}$, Nm (b) $\overline{M}_{NMS_Y}$, Nm

(c) $\sigma_{\dot{\delta}_{st_X}}$, rad/s (d) $\sigma_{\dot{\delta}_{st_Y}}$, rad/s

Fig. 25. Means and 95% confidence intervals of control activity related dependent variables. The numbers 1-6 on the horizontal axis correspond to the subtask number. NHF(brown), ST(gray), UT(red), IRT(violet), RT(green) and OT(cyan).

the direction of the turn required to navigate around an obstacle, thus subtask had a high significance on $\overline{M}_{H_Y}$ (SB: $F_{5,55} = 163.29, p \leq 0.01$). In terms of TP, smaller differences were found between the haptic controllers when compared to the longitudinal direction. However, OT caused higher (absolute value) $\overline{M}_{H_Y}$ than the other conditions, a significant effect (TP: $F_{2.81,30.93} = 3.55, p \leq 0.05$). For subtask 4, the NHF condition resulted in much lower (absolute value) $\overline{M}_{H_Y}$ when compared to the haptic controllers, leading to a highly significant two-way interaction (TP×SB: $F_{4.22,46.45} = 7.96, p \leq 0.01$). This difference is probably caused by the lowest directional agreement of lateral haptic moments, see Fig. 27d, which maybe turn is a result of the highest lateral haptic moments recorded for this subtask, see Fig. 26b.

The standard deviation of the longitudinal side-stick deflection rate, $\sigma_{\dot{\delta}_{st_X}}$, is displayed in Fig. 25c. For most subtasks, $\sigma_{\dot{\delta}_{st_X}}$ was the smallest for NHF and the highest for OT (TP: $F_{1.73,19.07} = 38.22, p \leq 0.01$), except for subtask 4 where $\sigma_{\dot{\delta}_{st_X}}$ was the smallest for ST (TP×SB: $F_{2.42,26.56} = 5.27, p \leq 0.01$). Fig. 25c also shows that $\sigma_{\dot{\delta}_{st_X}}$ was the lowest for subtask 2, a highly significant effect (SB: $F_{1.73,19.07} = 38.22, p \leq 0.01$).

In the lateral direction, similar trends were found for $\sigma_{\dot{\delta}_{st_Y}}$, see Fig. 25d. Although $\sigma_{\dot{\delta}_{st_Y}}$ was also the highest for OT, there were less variations between haptic controllers (TP×SB: $F_{5,55} = 11.94, p \leq 0.01$). As no turns are necessary to complete subtask 2, this obstacle resulted in the lowest $\sigma_{\dot{\delta}_{st_Y}}$, a highly significant effect (SB: $F_{1.66,18.22} = 29.53, p \leq 0.01$). Post-hoc analysis found no statistically relevant differences between the other subtasks. Additionally, no two-way interactions were observed between TP and SB.

It can be concluded from the above analysis that all four control activity related dependent variables increased with increasing strength of the haptic controller and is the highest for OT, agreeing with previously discussed simulation results (see Sec. IV-C2). Furthermore, the highest mean UAV velocity ($\overline{V}$) and teleoperator bias moments ($\overline{M}_{NMS_X}$ & $\overline{M}_{NMS_Y}$), along with the lowest side-stick deflection rates ($\sigma_{\dot{\delta}_{st_X}}$ & $\sigma_{\dot{\delta}_{st_Y}}$) for subtask 2 indicates that subjects found this obstacle the easiest and were able to fly straight though it without the need to slow down or make control corrections to avoid collisions.

4) Haptic Activity:

The absolute value of the mean longitudinal haptic moment, $\overline{M}_{H_X}$, shown in Fig. 26a, was the largest for OT and the smallest for NHF, resulting in high statistical significance of TP on $\overline{M}_{H_X}$ (TP: $F_{1.61,17.68} = 55.52, p \leq 0.01$). Despite the apparent differences between IRT and RT, particularly for subtasks 4-6, post-hoc comparisons revealed no statistical differences between the two relax task tuning profiles. By comparing Fig. 25a and Fig. 26a, it can be noted that haptic cues generally acted in the opposite direction of M_{NMS} such as to reduce UAV velocity to avoid collisions, and for most subtasks, $\overline{M}_{H_X}$ was directed along the negative longitudinal side-stick axis. However, for subtask 3 the trend was reversed as subjects were required to fly backwards into a building, resulting in haptic cues along the positive longitudinal side-stick axis. This difference led to a highly significant statistical effect of SB on $\overline{M}_{H_X}$ (SB: $F_{1.75,19.19} = 45.02, p \leq 0.01$), as well as a two-way interaction with high significance (TP×SB: $F_{3.51,38.61} = 21.387, p \leq 0.01$).

Unlike the longitudinal direction, no statistical significance of TP was observed for the mean lateral haptic moment, $\overline{M}_{H_Y}$, even for the strong repulsive moments provided by OT, see Fig. 26b. Regarding the dependency on SB, subtask 4 resulted in the highest $\overline{M}_{H_Y}$, a highly significant effect

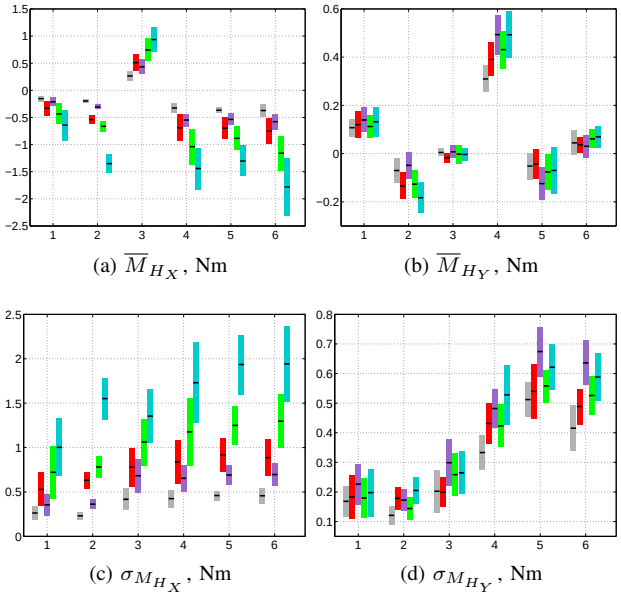

(a) $\overline{M}_{H_X}$, Nm (b) $\overline{M}_{H_Y}$, Nm

(c) $\sigma_{M_{H_X}}$, Nm (d) $\sigma_{M_{H_Y}}$, Nm

Fig. 26. Means and 95% confidence intervals of haptic activity related dependent variables. The numbers 1-6 on the horizontal axis correspond to the subtask number. ST(gray), UT(red), IRT(violet), RT(green) and OT(cyan).

(SB: $F_{5,55} = 78.40, p \leq 0.01$). As the direction of lateral haptic cues is dependent on the relative lateral position of obstacles to the UAV, which in turn varies between subtasks, a highly significant two-way interaction was observed for $\overline{M}_{H_Y}$ (TP×SB: $F_{20,220} = 5.98, p \leq 0.01$).

Fig 26c displays the standard deviation of the longitudinal haptic moment, $\sigma_{M_{H_X}}$, which was always highest for OT and generally increased with increasing strength of the haptic controller, a statistically highly significant difference (TP: $F_{1.68,18.47} = 78.95, p \leq 0.01$). Post-hoc tests showed a significant difference between IRT and RT ($p = 0.001$), with $\sigma_{M_{H_X}}$ considerably lower for IRT. Fig. 26c also shows that variations increased from subtask 1 to 6, resulting in a statistically significant effect of SB on $\sigma_{M_{H_X}}$ (SB: $F_{2.52,27.76} = 7.97, p \leq 0.01$). The differences between subtasks was most prominent for subtasks 2 and 6 where OT resulted in much higher $\sigma_{M_{H_X}}$ than the other haptic controllers, a two-way interaction of high significance (TP×SB: $F_{4.17,45.82} = 4.70, p \leq 0.01$).

The variations of the lateral haptic moment, $\sigma_{M_{H_Y}}$, shown in Fig 26d, are much greater for subtasks 4-6 when compared to subtasks 1-3, a highly significant effect (SB: $F_{5,55} = 48.36, p \leq 0.01$). This trend was also found for the mean risk of collision, see Fig 23, indicating that risk translates mainly into variations of $\sigma_{M_{H_Y}}$. Surprisingly, IRT produced the largest $\sigma_{M_{H_Y}}$ for all subtasks (TP: $F_{4,44} = 17.33, p \leq 0.01$), and significant differences were also found between IRT and RT ($p = 0.03$). Additionally, the difference between IRT and the other controllers was most pronounced for subtask 6, causing a significant two-way interaction (TP×SB: $F_{6.44,70.89} = 2.40, p \leq 0.05$).

The results for haptic activity match simulation results in the longitudinal direction, and 'stronger' haptic controllers were found to produce greater longitudinal haptic moments, encouraging subjects to reduce (longitudinal) UAV velocity near obstacles. Longitudinal and lateral variations in haptic cues were also found to increase as the strength of the controller increased for both simulation and experiment results. Furthermore, simulation results indicated greater lateral haptic moments for the under-tuned controllers. However, this trend was not seen in the experiment, in fact, the indifference in $\overline{M}_{H_Y}$ between the five haptic controllers suggests that subjects were more willing to accept lateral haptic feedback moments.

5) Haptic Controller Accuracy:

Longitudinal agreement of the haptic moment magnitude, $RMS_{(|M_{NMS_X}|-|M_{H_X}|)}$, is shown in Fig. 27a. Note that $\sigma_{M_{H_X}}$ displays the similar trends to $RMS_{(|M_{NMS_X}|-|M_{H_X}|)}$. OT was found to have the highest value for $RMS_{(|M_{NMS_X}|-|M_{H_X}|)}$, and consequently the lowest magnitude agreement of all controllers, a highly significant effect (TP: $F_{1.70,18.67} = 49.35, p \leq 0.01$). In addition, post-hoc tests uncovered significant differences between IRT and RT ($p = 0.011$), with much higher agreement for IRT. With respect to SB, subtask 1 resulted in highest magnitude agreement while it was lowest for subtask 6, resulting in a statistically significant effect of SB on

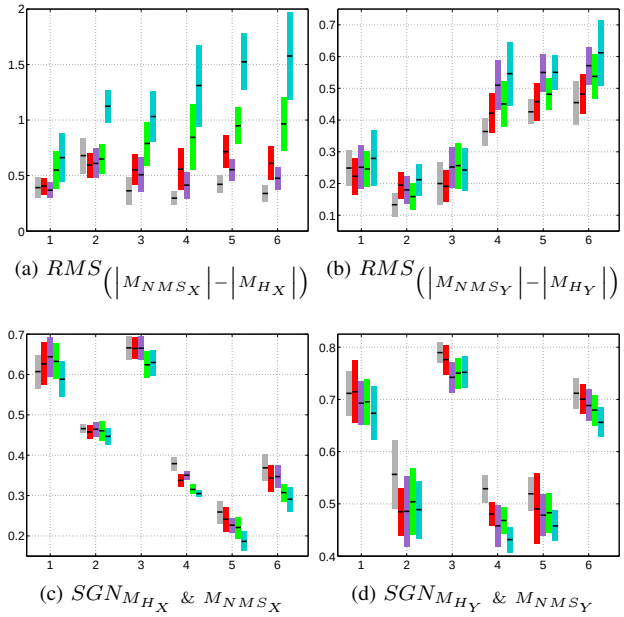

(a) $RMS_{(|M_{NMS_X}|-|M_{H_X}|)}$ (b) $RMS_{(|M_{NMS_Y}|-|M_{H_Y}|)}$

(c) $SGN_{M_{H_X}\ \&\ M_{NMS_X}}$ (d) $SGN_{M_{H_Y}\ \&\ M_{NMS_Y}}$

Fig. 27. Means and 95% confidence intervals of haptic controller accuracy related dependent variables. The numbers 1-6 on the horizontal axis correspond to the subtask number. ST(gray), UT(red), IRT(violet), RT(green) and OT(cyan).

$RMS_{(|M_{NMS_X}|-|M_{H_X}|)}$ (SB: $F_{2.24,24.55} = 5.45, p \leq 0.01$). As the differences between controllers is more evident for subtasks 4-6, a two-way interaction of high significance was also observed (TP×SB: $F_{3.59,39.53} = 10.99, p \leq 0.01S$).

Haptic moment magnitude agreement in the lateral direction, $RMS_{(|M_{NMS_Y}|-|M_{H_Y}|)}$, follows a similar trend to $\sigma_{M_{H_Y}}$. As a result, OT also had the lowest lateral magnitude agreement, resulting in a highly significant effect of TP (TP: $F_{4,44} = 13.17, p \leq 0.01$). When compared to the longitudinal direction, magnitude agreement is higher for $RMS_{(|M_{NMS_Y}|-|M_{H_Y}|)}$, and no statistical differences were found between IRT and RT in the lateral case. However, variations between controllers increase for subtasks 4-6 yielding a highly significant two-way interaction (TP×SB: $F_{20,220} = 2.124, p \leq 0.01S$), and as these three subtasks also caused much lower magnitude agreement, SB also caused high significance (SB: $F_{5,55} = 46.36, p \leq 0.01$).

Directional agreement of longitudinal haptic moments is accessed using $SGN_{M_{H_X}\ \&\ M_{NMS_X}}$, see Fig. 27c, with larger values implying greater agreement. Highest directional agreement was found for the under-tuned controllers (ST and UT) and the lowest for OT, resulting in a highly significant effect of TP on $SGN_{M_{H_X}\ \&\ M_{NMS_X}}$ (TP: $F_{4,44} = 26.35, p \leq 0.01$). Subtask 1 was an exception where IRT produced the highest directional agreement, producing a two-way interaction of high significance (TP×SB: $F_{20,220} = 2.71, p \leq 0.01S$). Furthermore, Bonfferoni corrected paired comparisons showed that IRT resulted in better longitudinal directional agreements than RT ($p = 0.005$). Subtasks 1 and 3 exhibited high longitudinal directional agreement, but agreement fell sharply for subtasks 4-6, a highly significant effect of SB (SB: $F_{5,55} = 231.75, p \leq 0.01$).

Lateral directional agreement, $SGN_{M_{H_Y}\ \&\ M_{NMS_Y}}$, is displayed in Fig. 27d. From the figure it is clear that lateral directional agreement is, on average, greater than for the longitudinal direction. Subtask 3 resulted in the highest lateral directional agreement as the UAV was required to fly backwards, forcing subjects to rely on haptic cues to avoid obstacles outside their (lateral) visual FOV. Subtasks 1 and 6 also resulted in much higher directional agreements than other subtasks as these two obstacles involved sharp 90^o turns which obscured visual position of obstacles (whilst making the turn). These findings yield a highly significant effect of SB on $SGN_{M_{H_Y}\ \&\ M_{NMS_Y}}$ (SB: $F_{5,55} = 76.813, p \leq 0.01$). Concerning the relationship with TP, lateral directional agreement deteriorated with increasing strength of the haptic controller, a statistically significant effect (TP: $F_{4,44} = 10.38, p \leq 0.01$). Additionally no significant differences were found between IRT and RT, and two-way interactions were nonexistent.

Haptic controller accuracy results show that agreement between then the teleoperator and the haptic controller, in terms of magnitude and direction of haptic moments, was better in the lateral direction. This provides strong additional evidence for the earlier mentioned conclusion that subjects found lateral haptic cues more helpful in performing the assigned tasks. This maybe due to insufficient lateral visual cues, forcing subjects to be reliant on lateral haptic moments, particularly for obstacles with sharp turns (subtasks 1, 4, 5 and 6) or when visual cues from the on board camera are not in the direction of motion (subtask 3). Furthermore, the decreasing magnitude agreement for controllers with high σ_{M_H} indicates that oscillatory haptic cues leads to lower user acceptance of the system.

6) Subjective Questionnaires:

Fig. 28 shows overall workload computed using the NASA TLX subjective questionnaire. Here, a lower subjective rating symbolizes lower workload. A Friedman test showed that there was a highly significant effect of TP on overall workload (TLX: $\chi^2(5) = 21.33$, $p \leq 0.01$), with the lowest and highest median workload recorded for IRT and OT respectively. Post-hoc analysis using the Wilcoxon test showed that significant differences were found between NHF-RT ($Z = -2.981, p = 0.003$) and between OT-IRT ($Z = -3.059, p = 0.002$) i.e., differences were caused by the extreme conditions (NHF and OT). Although IRT lead to the lowest workload, no significant differences were found between ST, UT, IRT and RT as they all had fairly similar median subjective ratings. Contrary to previous research (see Sec. II-C), these results show that three admittance based haptic controllers (i.e., UT, IRT and RT) *decreased* overall workload with respect to the NHF condition. On the other hand, over-tuning the haptic controller, as with OT, significantly increased overall workload compared to NHF.

To better understand the reduction of overall workload for IRT/RT compared to NHF and OT, box plots for the six workload components of the NASA TLX are given in Fig. 29. Here, it can be seen that effort (EF) and frustration (FR) were reported lowest for UT, IRT and RT conditions (EF: $\chi^2(5) = 25.66$, $p \leq 0.01$; FR: $\chi^2(5) = 11.578$, $p \leq 0.05$). This is in sharp contrast to earlier research where haptic cues contributed negatively towards these two workload sources [10]. However, physical load (PL) continued to be higher for the novel tuning approach, and increased with the strength of the haptic controller, a highly significant effect (PL: $\chi^2(5) = 33.41$, $p \leq 0.01$). This may be due to increased control and haptic activity described earlier for all haptic controllers when compared to NHF, see Sec. VI-B3 and VI-B4. Despite this, it is interesting to note that subjective judgment of own performance (PE) was better for haptic conditions, a significant effect (PE: $\chi^2(5) = 13.24$, $p \leq 0.05$), whereas objective dependent measures clearly showed no statistical performance differences between the six conditions. This maybe due to subject interpretation of the significant reduction in the number of collisions for haptic conditions as performance improvements, since collision avoidance was specified as their primary task. Mental load (ML) showed significant improvements for haptic conditions (ML: $\chi^2(5) = 17.23$, $p \leq 0.01$), with the lowest median for UT. No differences between conditions were observed for temporal load (TL) as the task did not require time dependent actions. Post-hoc tests showed that the extreme conditions, NHF and OT, resulted in the significant differences noted above for most workload sources.

Box plots for subjective situational awareness (SA) and haptic feedback acceptance (HA) are given in Fig. 30. For these two indicators, higher subjective ratings imply better SA and HA. A Friedman test showed a highly significant effect of TP on SA, with IRT having the highest median and NHF having the lowest median (SA: $\chi^2(5) = 25.56$, $p \leq 0.01$). Post-hoc tests confirmed that statistical significance was mainly caused by the lower SA of NHF and OT, while no differences were found between the other four haptic conditions. A similar trend was found for HA, with the highest acceptance for IRT and the lowest for OT, a highly significant effect (HA: $\chi^2(4) = 19.12$, $p \leq 0.01$).

The results of the three subjective questionnaires suggests that acceptance of the HCAS increased for the lower strength admittance based haptic controllers, however, over-tuning the controller is found to be more detrimental than providing no haptic support. This strongly supports the conclusion that heuristic tuning, as used in previous studies, can have adverse consequences on user acceptance, an important criteria for wide spread system proliferation.

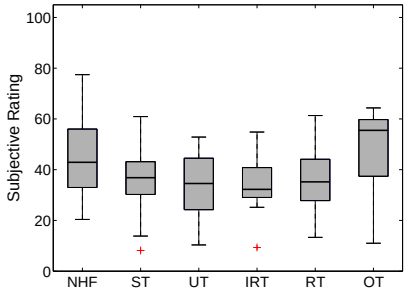

Fig. 28. Medians and interquartile ranges of overall NASA TLX workload score, with outliers (+).

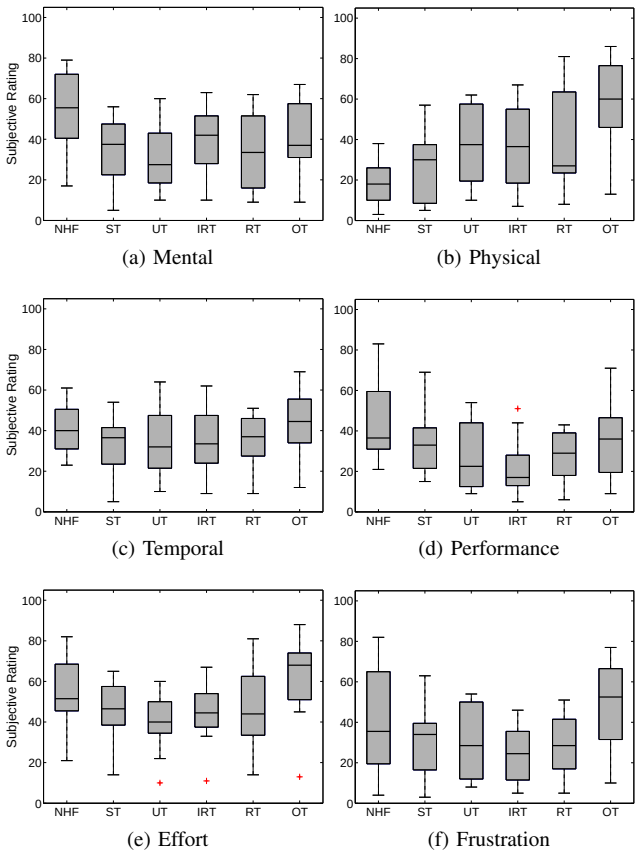

(a) Mental (b) Physical (c) Temporal (d) Performance (e) Effort (f) Frustration

Fig. 29. Medians and interquartile ranges of the NASA TLX workload sources, with outliers (+).

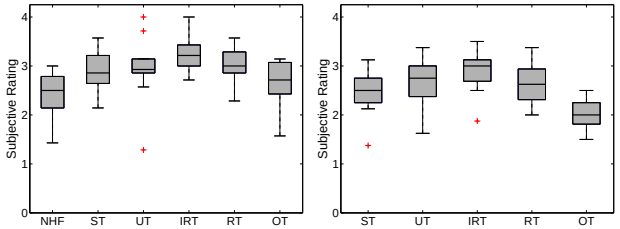

(a) Situational awareness (b) Haptic feedback acceptance

Fig. 30. Medians and interquartile ranges of average situational awareness (SA) and haptic feedback acceptance (HA), with outliers (+).

C. Admittance-Trajectory Relationship Investigation

The admittance-trajectory relationship is analyzed first by considering the mean, or 'overall', admittance per subtask. This is followed by considering admittance variations at 'three points' around the 'beginning', 'middle' and 'end' locations within each subtask, see Fig. 19. The aim of this investigation was to consider additional possibilities of improving the haptic controller tuning law, for instance by taking into account the type of obstacle encountered for the computation of the ideal collision avoidance haptic moment. It should be noted that this section considers only the relatively constant admittance value at 0.5 [Hz] (of the disturbance torque used to measure it) for comparisons between subtasks. This frequency was chosen as the haptic controller used in the tuning validation experiment conditions was also based on admittance measured at 0.5 [Hz].

1) Overall Admittance Comparisons:

Overall longitudinal admittance variations between subtasks can be studied through Fig. 31a. Here it can be clearly seen that subtask 2 caused the lowest admittance, resulting in a highly significant effect of SB on $H_{ADM_{overall_X}}$ (SB: $F_{2.79,30.72} = 46.37, p \leq 0.01$). However, post-hoc analysis revealed no significant differences between other subtasks as they had similar, and relatively high admittance values. These results were surprising as admittance was expected to be the lowest for subtask 3 since this obstacle required subjects to fly the UAV backwards, with visual cues in the opposite direction of motion.

In the lateral direction, subtask 2 once again caused a highly significant effect of SB on $H_{ADM_{overall_Y}}$ (SB: $F_{1.34,14.70} = 13.16, p \leq 0.01$). In this case, subtask 2 induced much higher admittance than for other obstacles, see Fig. 31b. As expected, lowest lateral admittances were found for subtasks 1 and 6 as these two obstacles required subjects to make tight 90^o turns with limited lateral visibility, causing subjects to grip the side-stick tighter to enable more precise control of the UAV. Subjects were also required to perform turns for subtasks 3,4 and 5, thus causing relatively low lateral admittances for these obstacles as well. However, post-hoc tests reported no statistical differences between subtasks (except for subtask 2) as they displayed similar, and relatively low admittance values.

When comparing longitudinal admittance with mean UAV velocity pictured in Fig. 32a, a strong inverse relationship can be established between these two variables. In fact, a

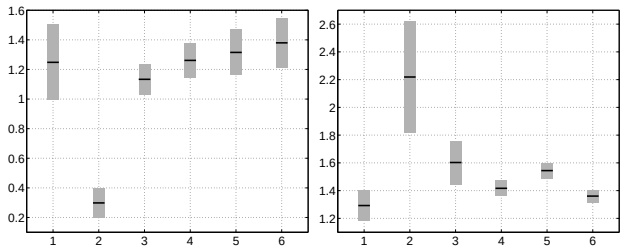

(a) $H_{ADM_{overall_X}}$, rad/Nm (b) $H_{ADM_{overall_Y}}$, rad/Nm

Fig. 31. Means and 95% confidence intervals of overall longitudinal and lateral admittance at 0.5 [Hz]. The numbers 1-6 on the horizontal axis correspond to the subtask number.

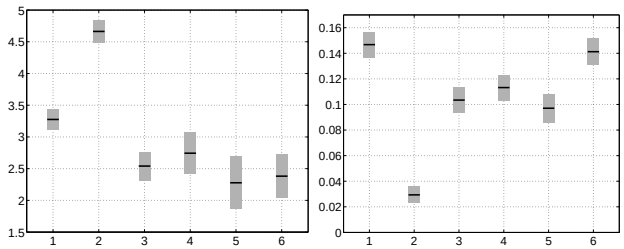

(a) $V_{overall}$, m/s (b) $\dot{\psi}_{overall}$, rad/s

Fig. 32. Means and 95% confidence intervals of overall UAV velocity and yaw rate. The numbers 1-6 on the horizontal axis correspond to the subtask number.

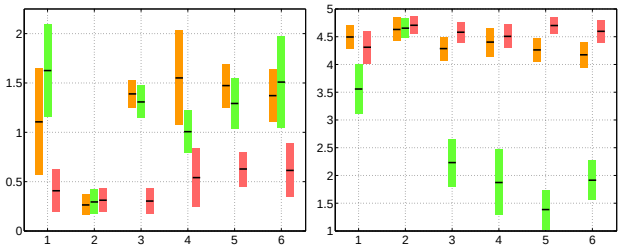

(a) $H_{ADM_{3Point_X}}$, rad/Nm (b) V_{3Point}, m/s

Fig. 33. Means and 95% confidence intervals of longitudinal three point admittance at 0.5 [Hz] and UAV velocity. The numbers 1-6 on the horizontal axis correspond to the subtask number.

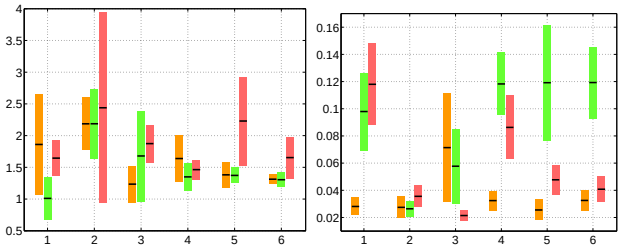

(a) $H_{ADM_{3Point_Y}}$, rad/Nm (b) $\dot{\psi}_{3Point}$, m/s

Fig. 34. Means and 95% confidence intervals of lateral three point admittance at 0.5 [Hz] and UAV yaw rate. The numbers 1-6 on the horizontal axis correspond to the subtask number.

similar inverse relationship can also be found between lateral admittance and UAV yaw rate displayed in Fig. 32b. These inverse relationships explain the admittance trends observed in the longitudinal and lateral directions. To induce high UAV velocities or yaw rates, subjects must apply large bias moments on the side-stick. Large bias moments in turn reduce neuromuscular admittance as shown in Fig. 21. Since trajectory elements trigger subjects to vary UAV velocity and yaw-rate, an indirect relationship between admittance and the trajectory to be flown can be established based on the above discussions.

2) Three-Point Admittance Comparisons:

Variations in longitudinal neuromuscular admittance can be analyzed using Fig. 33a. Subtask was found to have a highly significant effect on $H_{ADM_{3Point_Y}}$, with subtask 2 causing the lowest admittance (SB: $F_{2.97,32.68} = 16.68, p \leq 0.01$). Interestingly, for most subtasks, admittance was found to be the highest in the 'middle', moderate in the 'beginning', and the lowest at the 'end', a highly significant effect of location (LC: $F_{2,22} = 51.09, p \leq 0.01$). Post-hoc tests showed that the greatest significance was found between the 'middle' and 'end' locations. This trend was not followed by subtask 2 for which all locations had very similar low admittances, causing a highly significant two-way interaction (SB×LC: $F_{3.30,36.30} = 4.10, p \leq 0.01S$). Corresponding velocity variations can be studied through Fig. 33b. From this figure, it can be noted that the inverse velocity-longitudinal admittance relationship discussed earlier also explains the trends found between 'three point' admittance and velocity, for which the 'middle' location resulted in the lowest velocity and highest admittance, while the 'end' location displayed the highest velocity and lowest admittance.

In the lateral direction, subtask 6 was found to cause the lowest admittance, see Fig. 34a, resulting in a significant effect of SB on $H_{ADM_{3Point_Y}}$ (SB: $F_{2.13,23,45} = 3.84, p \leq 0.05$). For most subtasks, the 'middle' location was found to cause the lowest admittance, while the highest was found for the 'end' point, a statistically significant effect (LC: $F_{2,22} = 3.64, p \leq 0.05$). No significant two-way interactions were observed between LC and SB in the lateral direction. The correlations between three point lateral admittance and yaw rate, see Fig. 34b, is less evident than in the longitudinal direction. However, for subtasks 4, 5 and 6, the inverse yaw rate-lateral admittance is clearly visible with the highest velocity for the middle location, which also exhibited the lowest admittance. As in the longitudinal direction, a notable exception to this rule is subtask 2 for which no turns were necessary to navigate safely through this obstacle.

VII. Discussion

The primary research goal of this work is to improve current heuristic tuning methods of haptic feedback moments using a systematic approach based on neuromuscular admittance/stiffness of the human arm, to be applied to a haptic collision avoidance system (HCAS) for UAV teleoperation. To further improve this novel tuning method, the secondary research goal is to investigate the admittance-trajectory relationship during a teleoperation task. This section discusses the main results and the conclusions that can be drawn from them in terms of the two aforementioned research goals. Additionally, recommendations for future research are also listed.

A. Neuromuscular Admittance Based Tuning Law Validation

Optimal tuning of haptic cues is difficult as the human arm neuromuscular system (NMS) is highly adaptive. For non-optimal tuning settings, the NMS has been found to vary the relative strengths of its reflexive feedback paths or use muscle co-contraction to stabilize the system and achieve adequate performance. However, an adaptation to non-optimal tuning settings is accompanied with increased user physical workload, as proven by previous experimental investigations of the HCAS where heuristic tuning methods were used. In these experiments, despite considerable improvements in UAV teleoperation safety, users complained that haptic moments felt 'too strong' and were difficult to overrule at times, causing increased frustration over time and negatively influencing user acceptance of the system [10].

To improve user acceptance of the system, whilst simultaneously increasing safety with respect to pure manual control (i.e., with no haptic support), in this research, the haptic controller is tuned to match a so called 'design' neuromuscular admittance (inverse stiffness) setting. In this way, the NMS will adapt to a tuning setting that is based on its own properties, and thus reduce conflicts between the teleoperator and the automation on a neuromuscular level. Of the three

available neuromuscular tuning settings, the relax task (RT) has been chosen as the design point for tuning haptic cues as reflexive feedback paths are suppressed for this setting. In theory this should lead to the lowest physical workload with respect to the other two possible tuning settings i.e., the force (FT) and position (PT) tasks.

To verify the novel tuning procedure, an offline simulation of the HCAS was performed. The simulation included a model of the NMS to study the teleoperator-automation haptic interactions and no visual feedback was provided to the simulated teleoperator. The results of the simulation revealed that the setting of the NMS and haptic controller had a significant impact on the overall response of the system. For all neuromuscular task instructions, the haptic controller tuned to the same stiffness as the NMS model had the best overall response. Additionally, it was found that under-tuning the haptic controller, as for the 'stick tuning' (ST) controller which neglected admittance, led to the highest number of collisions, whilst over-tuned controllers provided highly erratic and unstable haptic feedback. The haptic controller tuned to RT admittance was found to be the best middle ground when considering both absolute response, as well as sensitivity to neuromuscular task instruction. Therefore, the results of the simulation verified the novel tuning procedure, as well as the choice of the relax task as the design point for tuning the haptic controller.

Data from the human-in-the-loop experiment indicates that safety improved drastically, reflected by a reduction in the number of collisions, for the admittance based haptic controllers (UT, IRT, RT and OT) when compared to the stick tuned (ST) controller and the no haptic feedback (NHF) condition. Furthermore, subjective workload and situational awareness (SA) were found to be negatively affected by NHF and OT conditions, while the lower strength admittance based controllers (UT, IRT and RT) produced the best SA and workload. These results suggest that the novel tuning procedure improves user acceptance, particularly for UT, IRT and RT, and are in line with the first hypothesis of the experiment.

An analysis of workload sources discovered that although overall workload decreased for some admittance based controllers, subjective physical load was higher for all haptic feedback conditions when compared to NHF. This contradicting result can be explained by the fact that frustration, effort and mental demand reduced, and subjective judgment of own performance increased when the number of collisions (and therefore collision time penalties) fell for conditions with haptic support. This may have led subjects to weigh other workload sources over physical load, a result significantly different from earlier experiments with the HCAS when providing only moment feedback haptic cues (as in this study).

As expected, OT resulted in the lowest number of collisions and control activity for this controller was the highest in both longitudinal and lateral directions. This combined with the highest subjective physical load resulted in the lowest subjective haptic acceptance (HA) for OT. In fact, all subjective questionnaires indicated that over-tuning haptic cues resulted in lower user acceptance than for the NHF condition. This supports the simulation result that OT, which is indicative of PT tuning, is not an ideal setting for haptic feedback as a consequence of the strong repulsive haptic moments. However, unlike the simulation results, the experiment showed no differences between haptic controllers for the mean risk of collision. This is because subjects were instructed to fly through the middle of waypoints, which were always located at close proximity to obstacles. As a consequence of near constant trajectories (not shown) for each subtask, haptic activity was not found to be higher in the lateral direction for the under-tuned controllers (ST and UT) as concluded from simulation results. To the contrary, in the experiment, haptic activity increased with the strength of the haptic controller for both axes, similar to control activity. These results illustrates the effect of task instructions in human-in-the-loop experiments and therefore partly agrees with the second hypothesis and rejects the third hypothesis.

The control strategy adaptation to meet task instructions is most evident in performance related dependent variables. For instance, the mean UAV velocity and distance to waypoints were statistically indifferent for all experiment conditions. When comparing different obstacles, it was noticed that subjects flew more conservatively, with lower mean velocities and higher distances to waypoints, for difficult obstacles (subtasks 4-6) that caused the most collisions such as to meet the primary instruction of avoiding collisions. This adaptation to achieve constant performance and meet task instructions shows that it is difficult to select an appropriate tuning profile based on performance metrics alone. Another interesting result was the greater appreciation of lateral haptic cues, demonstrated by higher agreement of magnitude and direction of lateral haptic controller accuracy variables. This is likely to be related to the limited lateral visual cues provided, forcing subjects to be more reliant on lateral haptic moments for collision avoidance. Greater variation seen in the magnitude agreement of longitudinal haptic moments, particularly for the difficult subtasks, maybe caused by haptic cues preventing subjects from flying intended trajectories, for instance through the center of waypoints. Hence, goal related conflicts can occur between the teleoperator and the automation as a result of visual feedback of the environment.

When comparing IRT (individually tuned relax task controller) and RT (controller tuned based on the average relax task admittance) in terms of haptic controller accuracy, significant statistical differences were found between these two controllers in the longitudinal direction. However, this result did not translate into valid statistical differences for any of the three subjective questionnaires suggesting that user acceptance is not improved with individual tuning of the haptic controller. Implementing the novel tuning method based on the average admittance of a population of subjects simplifies its commercial application. However, a conclusive test of hypothesis four requires further experimental investigation due to the substantial differences in the measurements used to tune IRT and RT as discussed in Sec. VI-A.

As a final remark, for most dependent variables, no statistical effects were found between IRT/RT and UT (which is representative of FT admittance). Therefore the choice

between FT and RT is dependent on the application under consideration and the consequent control authority made available to the human operator. For applications involving inexperienced users (eg. car driving), a tendency was found in this research for subjects to prefer the smallest haptic cues necessary to complete a given task, and hence the appropriate choice is FT tuning. On the other hand, it is maintained that for professional settings, as for UAV teleoperation, RT tuning presents the best option as it provides the possibility for the teleoperator to increase and decrease his/her admittance with respect to the relax task, allowing for a two-way change in control authority that is not possible for FT.

B. Admittance-Trajectory Relationship Investigation

The admittance-trajectory relationship was investigated, without haptic cues, as the seventh condition of the human-in-the-loop experiment. Note that the comparison between obstacles was performed for admittance identified at 0.5 [Hz] (of the disturbance torque used to measure it).

Overall or mean admittance per subtask was found to be inversely proportional to velocity and yaw rate in the longitudinal and lateral directions respectively. This can be explained as follows. UAV velocity and yaw rate are dependent on the amount of side-stick deflection i.e., bias moment magnitude, applied by the teleoperator. Therefore, high velocities and yaw rates require high bias moments which in turn is known to reduce admittance and vice versa. Note that this inverse relationship is already included in the current implementation of the haptic controller in which instantaneous bias moment magnitude and direction are used to determine the appropriate real time stiffness of the NMS.

In terms of dependence on subtask, except for subtask 2, which was found to be the easiest subtask by subjects as it required no turns, no statistical differences were found between the other obstacles in the longitudinal direction. In the lateral direction, the lowest admittance was found for subtasks 1 and 6, as expected, since these subtasks require sharp 90^o turns with limited lateral visual cues. However, only subtask 2 was once again found to cause any statistical differences in the lateral direction, hence the trends seen for subtasks 1 and 6 are considered inconclusive.

When admittance was investigated for the 'beginning', 'middle' and 'end' points within subtasks, a statistically highly significant effect of location was found along both axes: longitudinal admittance tend to be the highest in the 'middle' as subjects generally slowed down to fly through the center of waypoints, whilst in the lateral direction admittance was the lowest in the 'middle' particularly for subtasks with turns (and therefore high yaw rates). These effects are explained by the admittance-velocity/yaw rate inverse relationship.

Since no explicit relationship could be established between obstacle type and admittance, the fifth hypothesis is rejected. On the other hand, the data establishes a previously unhypothesized relationship between admittance and within obstacle location. It is possible to include this information into the haptic controller tuning law to further optimize the computation of the ideal collision avoidance haptic moment for future implementations of the system.

C. Recommendations for Future Research

The present research aims at improving the teleoperator-automation haptic interaction on a neuromuscular level. The human-in-the-loop experiment results have shown that goal related conflicts between the human and automation are present for the HCAS, even though the system only provides intermittent haptic support when obstacles constitute a risk of collision. To further improve user acceptance of the HCAS, these goal related conflicts also have be minimized. This can be achieved by modulating haptic moments when conflicts are detected. Depending on the specific application, this modulation can either increase haptic support to prevent the human operator from entering a dangerous condition, or it can be modulated to decrease haptic support to preserve human operator's final control authority. It may be possible to achieve the latter option without significant reduction in safety; the present work showed that a reduction of controller strength from IRT to UT was found to cause no significant increases in the number of collisions. If this is the case, it is argued that the latter option is more appropriate for UAV teleoperation, particularly when teleoperators want to fly through waypoints which are close to obstacles.

Telecommunication delays were not modeled in the present study. However, as the haptic controller interpolates real time bias moments to determine the appropriate neuromuscular stiffness for haptic moment computation, communication time delays may cause system instabilities. Therefore, a second topic for further research is to investigate the effects of telecommunication delays on the implementation of the admittance based tuning algorithm. A possible solution to this problem could be the so called 'wave variable transformation' technique which was found by Lam et. al to solve time delay issues for heuristic tuning of the haptic controller [11].

Our final recommendation is to test the HCAS in the presence of wind gusts and turbulence. Such tests are needed to evaluate the effectiveness and robustness of the HCAS for improving safety during these real-life circumstances, as well as to determine additional applications of the system such as collision avoidance from mobile obstacles.

VIII. CONCLUSION

The results of the offline simulation and the human-in-the-loop experiment have found that the novel neuromuscular admittance based tuning algorithm significantly improves teleoperation safety and situational awareness, whilst decreasing operator workload, particularly when comparing the force and relax task controllers with pure manual control and the stick tuned haptic controller. On the other hand, results strongly indicate that over-tuning the haptic controller, as for the position task controller, yields poorer user acceptance than even the case with no haptic support. This indicates the need for systematically tuning haptic feedback moments. Additionally, no significant differences were found between force and relax task controllers, suggesting that the choice between these two tuning options depends on the specific application and the experience of intended users with haptic feedback systems.

Control strategy variations to meet task instructions and achieve constant performance, irrespective of the haptic controller tuning profile, were consistent with previous experimental results. Furthermore, subjects had greater appreciation for lateral haptic cues, while in the longitudinal direction, goal related conflicts were discovered. These conflicts need to be addressed to further improve user acceptance of the system.

The admittance-trajectory investigation revealed no differences between the admittance recorded for different obstacles. However, an inverse relationship between velocity and yaw rate with longitudinal and lateral admittance, receptively, was observed. Moreover, a correlation between admittance and within obstacle location has been established.

REFERENCES

[1] R. E. Weibel and R. J. Hansman, "Safety considerations for operation of unmanned aerial vehicles in the national airspace system," Massachusetts Institute of Technology, Tech. Rep., Nov. 2006.

[2] G. Warwick, "Unmanned community making progress on airspace access," Aug. 2013. [Online]. Available: http://www.aviationweek.com

[3] A. P. Tvaryanas, W. T. Thompson, and S. H. Constable, "U.S. military unmanned aerial vehicle mishaps: Assessment of the role of human factors using human factors analysis and classification system (HFACS)," US Air Force, Tech. Rep., Mar. 2005.

[4] K. W. Williams, "A summary of unmanned aircraft Accident/Incident data: Human factors implications," Federal Aviation Administration, Technical Report DOT/FAA/AM-04/24, Dec. 2004.

[5] N. J. Cooke, "Human factors of remotely operated vehicles," *Proceedings of the Human Factors and Ergonomics Society Annual Meeting*, vol. 50, no. 1, pp. 166–169, Oct. 2006. [Online]. Available: http://pro.sagepub.com/content/50/1/166

[6] J. S. McCarley and C. D. Wickens, "Human factors implications of UAVs in the national airspace," University of Illinois, Aviation Human Factors Division, Savoy, IL, Technical Report AHFD-05-05/FAA-05-01, 2005.

[7] R. Hopcroft, E. Burchat, and J. Vince, "Unmanned aerial vehicles for maritime patrol: Human factors issues," Australian Government Department of Defence, Tech. Rep., May 2006.

[8] H. Boschloo, T. Lam, M. Mulder, and M. van Paassen, "Collision avoidance for a remotely-operated helicopter using haptic feedback," in *2004 IEEE International Conference on Systems, Man and Cybernetics*, vol. 1, 2004, pp. 229 –235 vol.1.

[9] T. Lam, M. Mulder, and M. v. Paassen, "Haptic interface in UAV tele-operation using force-stiffness feedback," in *IEEE International Conference on Systems, Man and Cybernetics, 2009. SMC 2009*, Oct. 2009, pp. 835 –840.

[10] T. M. Lam, M. Mulder, and M. M. (Ren) van Paassen, "Haptic interface for UAV collision avoidance," *The International Journal of Aviation Psychology*, vol. 17, no. 2, pp. 167–195, 2007. [Online]. Available: http://www.tandfonline.com/doi/abs/10.1080/10508410701328649

[11] T. Lam, M. Mulder, and M. M. Van Paassen, "Haptic feedback in uninhabited aerial vehicle teleoperation with time delay," *Journal of guidance, control, and dynamics*, vol. 31, no. 6, pp. 1728–1739, 2008.

[12] T. M. Lam, M. Mulder, M. M. Van Paassen, J. A. Mulder, and F. C. Van Der Helm, "Force-stiffness feedback in uninhabited aerial vehicle teleoperation with time delay," *Journal of Guidance, Control, and Dynamics*, vol. 32, no. 3, pp. 821–835, May 2009.

[13] D. Abbink, D. Cleij, M. Mulder, and M. van Paassen, "The importance of including knowledge of neuromuscular behaviour in haptic shared control," in *2012 IEEE International Conference on Systems, Man, and Cybernetics (SMC)*, Oct. 2012, pp. 3350 –3355.

[14] D. Abbink and M. Mulder, "Neuromuscular analysis as a guideline in designing shared control," *Advances in Haptics*, vol. 109, pp. 499–516, 2010.

[15] J. Smisek, M. van Paassen, M. Mulder, and D. A. Abbink, "Neuromuscular analysis based tuning of haptic shared control assistant for UAV collision avoidance," in *IEEE World Haptics Confrence 2013. WHC 2013*. Daejeon, Korea: IEEE, Apr. 2013. [Online]. Available: http://www.haptics2013.org/index.php

[16] D. A. Abbink, M. Mulder, and E. R. Boer, "Haptic shared control: smoothly shifting control authority?" *Cognition, Technology & Work*, vol. 14, no. 1, pp. 19–28, Mar. 2012. [Online]. Available: http://link.springer.com/article/10.1007/s10111-011-0192-5

[17] M. Mulder, D. A. Abbink, and E. R. Boer, "Sharing control with haptics: Seamless driver support from manual to automatic control," *Human Factors: The Journal of the Human Factors and Ergonomics Society*, May 2012. [Online]. Available: http://hfs.sagepub.com/content/early/2012/05/02/0018720812443984

[18] D. Cleij, "Design of haptic shared control: Analysing driver-controller interaction to improve hapic shared control systems," MSc. Thesis, Delft University of Technology, Delft, Dec. 2011.

[19] R. Parasuraman and V. Riley, "Humans and automation: Use, misuse, disuse, abuse," *Human Factors: The Journal of the Human Factors and Ergonomics Society*, vol. 39, no. 2, pp. 230–253, Jun. 1997. [Online]. Available: http://hfs.sagepub.com/content/39/2/230

[20] T. B. Sheridan, *Humans and Automation: System Design and Research Issues*. New York, NY, USA: John Wiley & Sons, Inc., 2002.

[21] T. Lam, H. Boschloo, M. Mulder, and M. van Paassen, "Artificial force field for haptic feedback in UAV teleoperation," *IEEE Transactions on Systems, Man and Cybernetics, Part A: Systems and Humans*, vol. 39, no. 6, pp. 1316 –1330, Nov. 2009.

[22] B. H. Krogh, "A generalized potential field approach to obstacle avoidance control," Society of Manufactuing Engineers, Dearborn, Michigan, Technical Report MS84-84, 1984.

[23] T. Lam, M. Mulder, and M. van Paassen, "Haptic feedback for UAV tele-operation - force offset and spring load modification," in *IEEE International Conference on Systems, Man and Cybernetics, 2006. SMC '06*, vol. 2, Oct. 2006, pp. 1618 –1623.

[24] D. Abbink, "Neuromuscular analysis of haptic gas pedal feedback during car following," PhD, Delft University of Technology, Delft, 2006.

[25] J. Lasschuit, T. Lam, M. Mulder, M. M. Van Paassen, and D. Abbink, "Measuring and modeling neuromuscular system dynamics for haptic interface design," in *Proceeding of the AIAA Modeling and Simulation Technologies Conference and Exhibit 8 August 2008*. Honolulu, Hawaii: American Institute of Aeronautics and Astronautics, Aug. 2008.

[26] E. De Vlugt, "Identification of spinal reflexes," Ph.D. dissertation, Delft University of Technology, Delft, May 2004.

[27] H. J. Damveld, D. Abbink, M. Mulder, M. Mulder, M. Van Paassen, F. van der Helm, and R. J. Hosman, "Identification of the feedback component of the neuromuscular system in a pitch control task," in *Proceedings of the AIAA Guidance, Navigation, and Control Conference 2 - 5 August 2010, Toronto, Ontario Canada*. Washington D.C.: American Institute of Aeronautics and Astronautics, Aug. 2010, pp. 1–22.

[28] E. de Vlugt, A. C. Schouten, and F. C. van der Helm, "Quantification of intrinsic and reflexive properties during multijoint arm posture," *Journal of Neuroscience Methods*, vol. 155, no. 2, pp. 328–349, Sep. 2006. [Online]. Available: http://www.sciencedirect.com/science/article/pii/S0165027006000549

[29] A. C. Schouten, "Proprioceptive reflexes and neurological disorders," Ph.D. dissertation, Delft University of Technology, Delft, May 2004. [Online]. Available: http://resolver.tudelft.nl/uuid:b34e0469-39eb-4a76-98b0-fb0d29fa06b5

[30] J. Venrooij, D. Abbink, M. Mulder, and M. van Paassen, "A method to measure the relationship between biodynamic feedthrough and neuromuscular admittance," *IEEE Transactions on Systems, Man, and Cybernetics, Part B: Cybernetics*, vol. 41, no. 4, pp. 1158 –1169, Aug. 2011.

[31] E. Sunil, "Tuning of a haptic collision avaoidance system for UAV teleoperation: Preliminary report," Faculty of Aerospace Engineering, TU Delft, Delft, Preliminary, Aug. 2013.

[32] S. G. Hart and L. E. Staveland, "Development of NASA-TLX (task load index): Results of empirical and theoretical research," *Human Mental Workload*, vol. 1, no. 3, pp. 139–183, 1988. [Online]. Available: http://humanfactors.arc.nasa.gov/groups/TLX/downloads/NASA-TLXChapter.pdf

[33] E. Jeannot, C. Kelly, and D. Thompson, "The development of situation awareness measures in ATM systems," *Brussels: Eurocontrol*, 2003.

Part II

PRELIMINARY REPORT

Chapter 1

Introduction

In recent years, interest in Unmanned Aerial Vehicles, or UAVs, has grown significantly. This can be attributed to many factors such as improvements in computing power, global satellite based communication systems, and light weight structures and materials amongst others. In addition, UAVs are highly versatile sensor platforms, capable of performing a wide variety of missions and have been used extensively in the military domain (Weibel & Hansman, 2006). The comparatively low development costs of UAVs has led to numerous new civilian applications including remote-sensing, search and rescue, disaster response and transportation of goods (Sarris, 2001). For instance Delft Dynamics B.V., a spin off from the Faulty of Aerospace Engineering at TU Delft, manufactures the RH2 'Stern' helicopter UAV for law enforcement and fire fighting, see Figure 1-1.

Figure 1-1: RH2 'Stern' UAV helicopter designed and manufactured by Delft Dynamics B.V. is one of many UAVs introduced recently in the civilian market (Delft Dynamics, 2006)

Despite the potential commercial opportunities, in most countries regulations prevent UAV flights over civilian airspace. However new legislation to be proposed in 2015 in the United States (McGarry, 2012), and recent UAV test flights in civilian airspace over Europe (Svitak,

2013), suggests that UAVs are likely to fly alongside manned aircraft in the near future. This calls into question the safety of UAV operations.

Unfortunately, studies have shown that on average UAVs suffer more accidents, or 'mishaps' as their known within the industry, when compared to manned aircraft. For instance in 2005, it was reported by the US military that its 'Predator' UAV had 32 mishaps[1] and the 'Hunter' UAV suffered 55 mishaps per 100,000 flight hours, compared to just one mishap (also per 100,000 flight hours) for its manned aircraft (Tvaryanas, Thompson, & Constable, 2005). Although UAV safety has improved in the recent past (McGarry, 2012), such dire statistics have led to multiple investigations into the source of UAV accidents. For example, Williams (Williams, 2004) categorized the sources of accidents for five UAVs operated by the US military, see Figure 1-2.

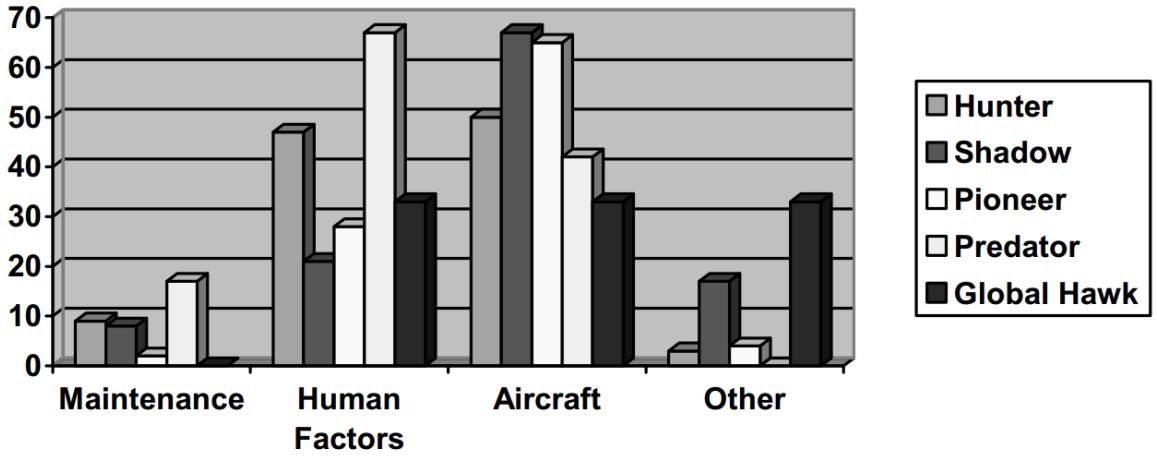

Figure 1-2: Sources of accidents for five UAVs operated by the US millitary (Williams, 2004)

From Figure 1-2, it is quite clear that human factors contribute significantly to the low safety record of UAVs. Here human factors includes aspects such as alerts/alarms and display deficiencies, as well as procedural and skill based errors (Williams, 2004). Although UAVs are 'unmanned aircraft', there is significant human involvement in the planning and operation of UAV missions (Cooke, 2006). UAVs are typically controlled from ground control stations (GCS), see Figure 1-3, which predominantly supply only visual information to the UAV teleoperator. This visual feedback is subject to time delays and has low resolution, contrast and field of view (McCarley & Wickens, 2005). In addition, the physical separation between the aircraft and the teleoperator leads to a lack of auditory, kinesthetic and vestibular sensory inputs (Hopcroft, Burchat, & Vince, 2006). Pilots of manned aircraft are able to integrate these multi-sensory inputs to gain better situational awareness (SA) of the aircraft state and the environment. These shortcomings can overload the visual channel of UAV teleoperators, resulting in situations with poor situational awareness and high workload.

Conventional design philosophy in aeronautics aims at decreasing operator workload and consequent human error by automating critical processess. Humans are meant to a play a 'supervisory' role by which they monitor the status and actions of automation. However, in practice it has been found that automation leaves humans feeling that they are 'out of the

[1]Here a 'mishap' constitutes damage or loss of the vehicle

Figure 1-3: An example ground control station (GCS) used to teleoperate UAVs. Pilots receive only visual feedback of the UAV states. The GCS pictured is manufactured by Aeronautics Ltd.(Aeronautics, 2007).

control loop' and are mere 'spectators' to the actions taken by the automation, particularly when adequate feedback is not provided (Sheridan, 2002). In fact, this can lead to a further reduction of situational awareness. Moreover, automation can cause new problems such as over-reliance and a gradual degradation of manual control skills over time, and in turn may cause human operators to take wrong actions in the event of automation failures (Parasuraman & Riley, 1997). For these reasons, pure automation is not a recommended approach to improve teleoperator situational awareness and UAV safety.

From the above discussion, it is clear that teleoperators need to actively take part in controlling the UAV, and situational awareness can be improved by providing additional information through one of the other human sensory modalities. Over the past decade, the Control and Simulation department of the Faculty of Aerospace Engineering at TU Delft, has been developing a novel control interface which provides kinesthetic or haptic feedback to help teleoperators improve their situational awareness in an obstacle laden environment. In this thesis, this new control interface, which is based on the concept of Haptic Shared Control, is developed further.

1-1 Haptic Shared Control and Previous Research

'Shared Control' is a control paradigm in which an automatic controller and a human operator simultaneously control a process (D. Abbink & Mulder, 2010). In shared control, it is possible to smoothly vary the control authority of the system to prioritize either the human's or the automatic controller's intent (D. A. Abbink, Mulder, & Boer, 2012). By tuning a shared control system to favor manual control, it is possible to reduce operator workload and at the same time improve operator situational awareness, whilst preserving the ability to overrule the automatic controller in the event of failures. Thus shared control has the potential to combine the benefits of both automatic and manual control.

'Haptic Shared Control' (HSC) is a type of shared control where the automatic controller and the human operator share control of a process through force (moment) interactions on a common control interface (e.g. a side-stick in aviation) (Mulder, Abbink, & Boer, 2012). The position of the control interface is the only input to the system, thus the human operator can easily take command of the system (at any time) by applying larger forces than the automatic controller. HSC can be applied to a wide variety of applications, including the teleoperation of robots and the control of vehicles such as aircraft and automobiles, or both. Although HSC is still considered as an emerging technology, uses of it can already be found in the automotive industry, for example in the design of a haptic gas pedal (Mulder et al., 2011).

With respect to the teleoperation of UAVs, a Haptic Collision Avoidance System (HCAS) has been designed by Lam (T. Lam, 2009) using the haptic shared control paradigm. Figure 1-4 below displays the basic working principle of the HCAS. Here, under normal circumstances, the teleoperator manually controls the UAV by applying control torques, known as bias moments, on the side-stick. If the sensor detects obstacles in the environment, an artificial risk field is used to determine the risk i.e., the probability, of collisions based on the relative position and velocity of the UAV. This risk is translated to a haptic moment by a so called 'haptic controller' and is applied on the side-stick, along with the operator bias moments. The operator can decide to either agree or disagree with the haptic feedback provided and the position of the side-stick dictates the final steering commands issued to the UAV.

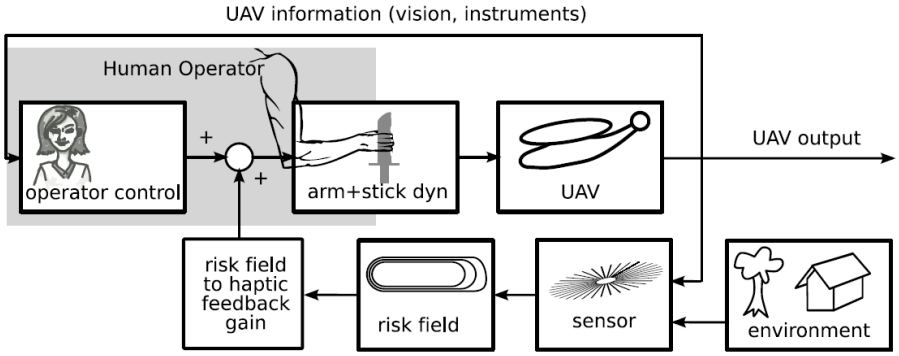

Figure 1-4: Basic working principle of the haptic collision avoidance system (HCAS) for UAV teleoperation (Smisek et al., 2013). The haptic feedback informs the operator about impending collisions with the environment, and suggests a collision avoidance maneuver to steer the UAV safely in an obstacle lade environment.

The usefulness of haptic feedback provided by the HCAS is twofold. First, the presence of haptic feedback informs the teleoperator of potential collisions with the environment. Second, the magnitude and direction of the haptic feedback indicates a collision avoidance steering maneuver that the operator can use to safely navigate around obstacles. This is particularly helpful when visual information from onboard cameras are not in the direction of motion as illustrated by Figure 1-5. Hence, the HCAS can improve the situational awareness of UAV teleoperators for an otherwise purely manual control task (i.e., when no obstacles are detected).

Extensive human-in-the-loop-experiments with different AFF designs (T. M. Lam et al., 2007), varying levels of haptic feedback (T. M. Lam et al., 2009), and haptic feedback in the presence of communication time delays (T. Lam, Mulder, & Van Paassen, 2008) have

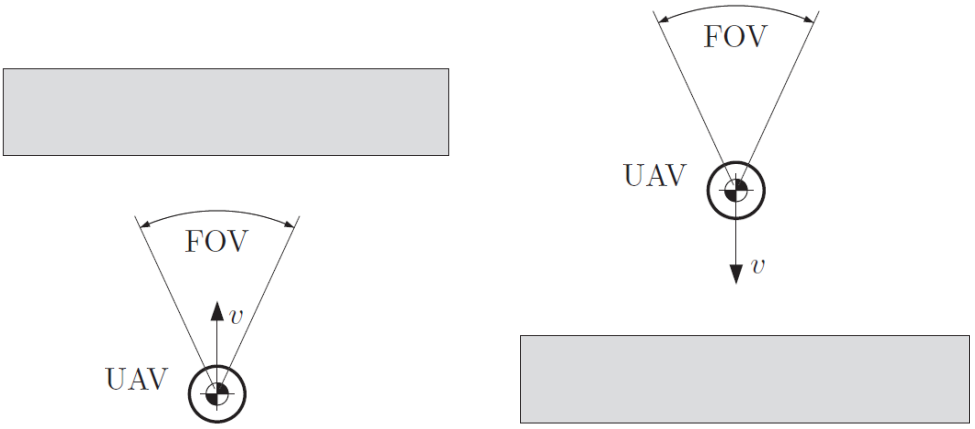

(a) Obstacle in the FOV of the camera (b) Obstacle not in the FOV of the camera

Figure 1-5: The usefulness of haptic feedback is evident when obstacles are not in the field of view (FOV) of the camera (T. Lam, 2009). In this case, the haptic feedback provides the operator with additional situational awareness needed to avoid collisions.

shown that the HCAS significantly improves the safety of UAV teleoperation. However, in all cases, it was found that the haptic feedback increased the control activity and the subjective physical workload of the experiment participants. Moreover, some participants complained that the haptic feedback provided was 'too strong' and was difficult to overrule.

Studies investigating the relationship between the human arm neuromuscular properties and the tuning of HSC systems has revealed that 'trial and error' tuning of the haptic controller, as used by Lam, can result in poor haptic interaction between the automatic controller and the human teleoperator (D. Abbink, Cleij, Mulder, & Paassen, 2012). This poor interaction has been credited to the large adaptability range of the human arm neuromuscular admittance (D. Abbink & Mulder, 2010). Neuromuscular admittance is defined as the ratio between hand position and exerted force. In practice, admittance is equal to the inverse stiffness of the arm-hand system. When the haptic controller is tuned with trial and error, the neuromuscular system adapts its admittance to match that particular tuning, such that the overall system is stable and performance is satisfactory. However, this adaptation can lead to physical discomfort over time, as well as increased frustration with the system (D. Abbink & Mulder, 2010). A possible solution to this problem is to tune the haptic controller to match a so called 'design neuromuscular admittance', where the properties of the neuromuscular system is desirable for the particular control task under consideration (Cleij, 2011).

Recent research by Smisek (Smisek et al., 2013) has been able to experimentally measure neuromuscular admittance in the presence of operator bias moments for the so called 'relax task'. As the name suggests, the relax task is a neuromuscular design point where physical workload is expected to be the least. Furthermore, this research has also shown that admittance is a function of bias moment magnitude and direction. Using the measured admittance data, it is possible to tune the haptic feedback to match the relax task admittance of the neuromuscular system, and in doing so it is hoped to reduce the high operator workload observed in previous experiments. As yet, this novel tuning procedure has neither been verified nor validated.

1-2 Thesis Objectives and Research Questions

This research aims at examining neuromuscular admittance based tuning of haptic shared control systems (HSC). To this end, two distinct research objectives has been defined. The primary research objective can be stated as:

"Make use of experimentally measured neuromuscular admittance data to validate the novel haptic shared control tuning procedure, and the selection of the relax task admittance as the design point for tuning haptic shared control"

The primary thesis objective can be subdivided into the following three research questions:

1. How does the pilot-controller haptic interaction vary depending on the neuromuscular task instruction and the haptic controller setting?
2. How does the novel tuning procedure compare to 'Stick Tuning', and what is the effect of selecting the relax task as the design point for tuning haptic shared control?
3. Is it beneficial to tune haptic feedback on an individual basis, or can it be tuned based on the average admittance of a group of subjects without a significant differences in the overall system response?

As stated in section 1-1, in the novel HSC tuning procedure, the haptic controller is tuned to match a design neuromuscular admittance. In this research, the design neuromuscular admittance corresponds to that of the relax task instruction as there is evidence in previous research that the relax task leads to the least physical workload for the UAV teleoperator (D. Abbink & Mulder, 2010; Cleij, 2011). The other neuromuscular task instructions are the force and position tasks, which have higher and lower admittance, respectively, when compared to the relax task. The 'Stick Tuning' haptic controller neglects neuromuscular admittance and it is used to determine the effect of including neuromuscular admittance in the tuning of HSC. Note that the third research question is of particular commercial interest as it affects the implementation of the tuning procedure for real-life applications.

The secondary thesis objective can be stated as:

"An investigation of the relationship between the adaptation of neuromuscular admittance and the trajectory to be flown"

The research questions pertaining to the secondary thesis objective are listed below:

1. What kind of trajectory element cause neuromuscular admittance to increase and what kind causes it to decrease?
2. Is an increase in admittance accompanied with a decrease in speed?

The purpose of the secondary objective is to investigate additional factors that may affect neuromuscular admittance, and thus further improve the HSC tuning procedure. Whilst this research objective extends the scope of the thesis, it is not considered vital in understanding the relationship between neuromuscular admittance and tuning HSC.

Both the primary and secondary thesis objectives are to be studied in the context of a haptic collision avoidance system (HCAS) for UAV teleoperation. The UAV is modeled as a control augmented helicopter with motion restricted in the horizontal plane i.e., haptic feedback is only provided along the pitch and roll axes. Furthermore, the operator is provided with haptic feedback in the form of force feedback alone. As the focus of this research is purely on neuromuscular admittance based tuning of HSC, no time delays are modeled in UAV teleoperation system.

1-3 Research Approach

A five step approach, split over two phases, is used to meet the thesis objectives and answer the associated research questions, see Figure 1-6. In step one, a comprehensive literature survey is undertaken to gain a sense of the state-of-the-art in the field of haptic shared control (HSC) and neuromuscular admittance based tuning methods. Results from the literature review are used to define the precise topic and scope of the thesis, see section 1-2. The HSC components are modeled in the second step, and an offline simulation is performed to gain initial insights into the primary thesis objective. Should the results of the simulation verify the admittance based tuning procedure, the thesis proceeds to the second phase. Otherwise, a redesign of the tuning algorithm is attempted as it is necessary to ensure that the tuning procedure is theoretically sound before validating it with time-consuming experiments.

The second thesis phase focuses on validating the primary objective, as well as investigating the secondary objective, through a carefully designed human-in-the-loop experiment. In step three, results of the simulation are used to determine experiment hypotheses, and corresponding independent and dependent variables. Furthermore, the experiment is to be implemented in the Human-Machine laboratory (HMI lab) of the Control and Simulation department using the DUECA middleware layer. Once the experiment implementation has been tested with a pilot study, the actual experiment is conducted and results analyzed in step four. Finally in step five, the results of the experiment are considered in the context of the research questions outlined in section 1-2. It is planned to publish the final results of the thesis with either a conference or journal paper.

1-4 Preliminary Thesis Outline

This report presents the results of the Literature Study phase of the thesis, see Figure 1-6. The report starts with an overview of the important literature in the field of haptic shared control and provides a theoretical background for the thesis in chapter 2. In chapter 3, the methodology used to model HSC components are discussed in detail, and the results of the associated offline simulation are presented with respect to the primary thesis objective. Lessons learnt from the simulation are used to propose the design of a two-part human-in-the-loop experiment to validate and investigate the primary and secondary thesis objectives

in chapter 4. Finally, a preliminary conclusion on the thesis objectives and the work that needs to be done to realize the second thesis phase is presented in chapter 5.

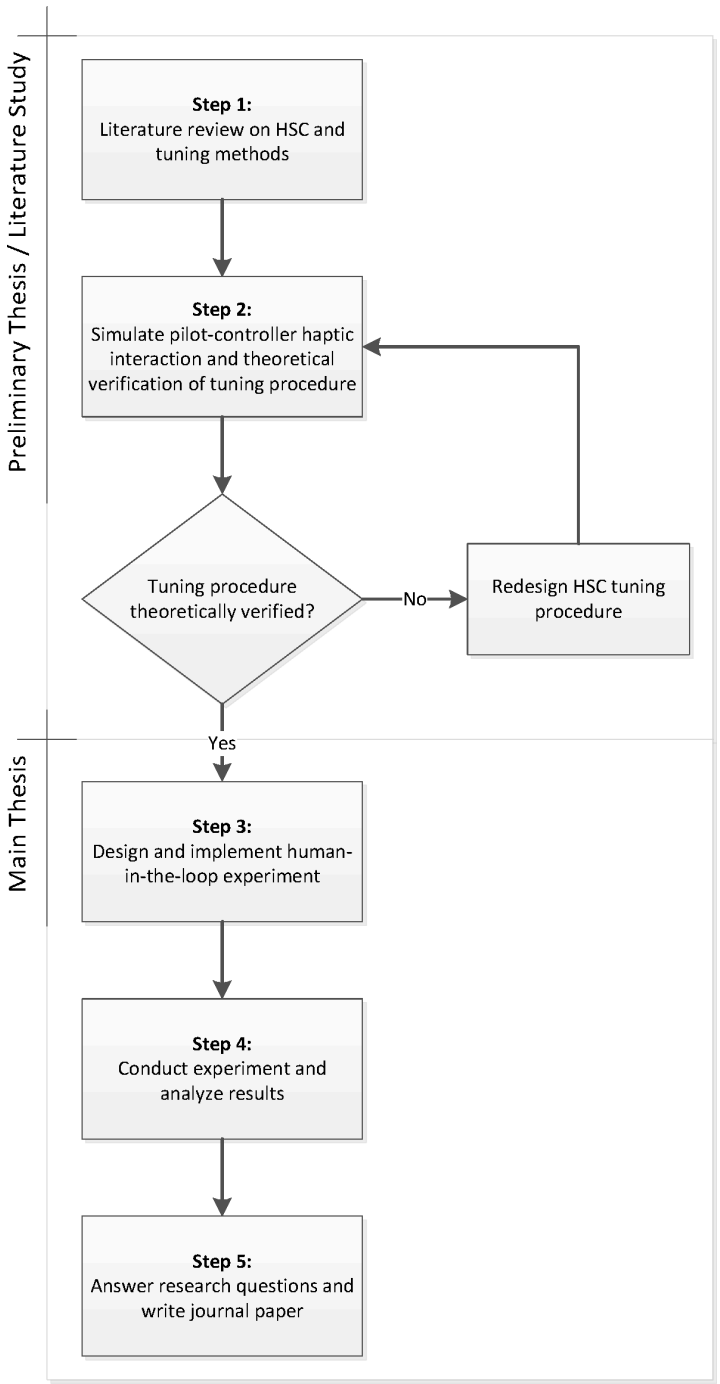

Figure 1-6: Research approach used to meet thesis objectives and answer research questions

Chapter 2

The Design and Tuning of Haptic Shared Control Systems

This chapter summarizes essential literature concerning the design and tuning of haptic shared control systems. It is intended to provide the theoretical backbone necessary for a reader unfamiliar with state-of-the-art research relevant for this thesis, such that he/she is able to follow the work presented in subsequent chapters.

The chapter opens with an introduction into the world of haptic shared control, including a discussion of its architecture, classification and interesting examples in section 2-1. Next in section 2-2, a description of the haptic collision avoidance system for UAV teleoperation is provided as it represents the platform used to answer the underlying research questions of this thesis. Finally in section 2-3, the challenges related to the tuning of haptic shared control systems and a potential method for tackling these challenges are presented.

2-1 Haptic Shared Control: Architecture, Classification and Examples

Haptic shared control (HSC) is a control method that has evolved from the need to address common issues with human-machine interaction. For instance, a well designed haptic shared control system can overcome the problems of misuse, disuse and abuse that is frequently reported for automatic control systems (Parasuraman & Riley, 1997). At the same time, HSC has the potential to reduce workload and improve situational awareness for human operators, thus combining the best of pure manual and pure automatic control systems (D. A. Abbink et al., 2012). In this section, the basic principles of HSC are explained and different classifications and examples commonly found in literature are also discussed.

2-1-1 HSC Architecture

While there are several different types of HSC systems reported in literature, see section 2-1-2, the basic building blocks remain the same. Figure 2-1 below displays a generic block diagram that can be used to describe the important aspects of HSC systems.

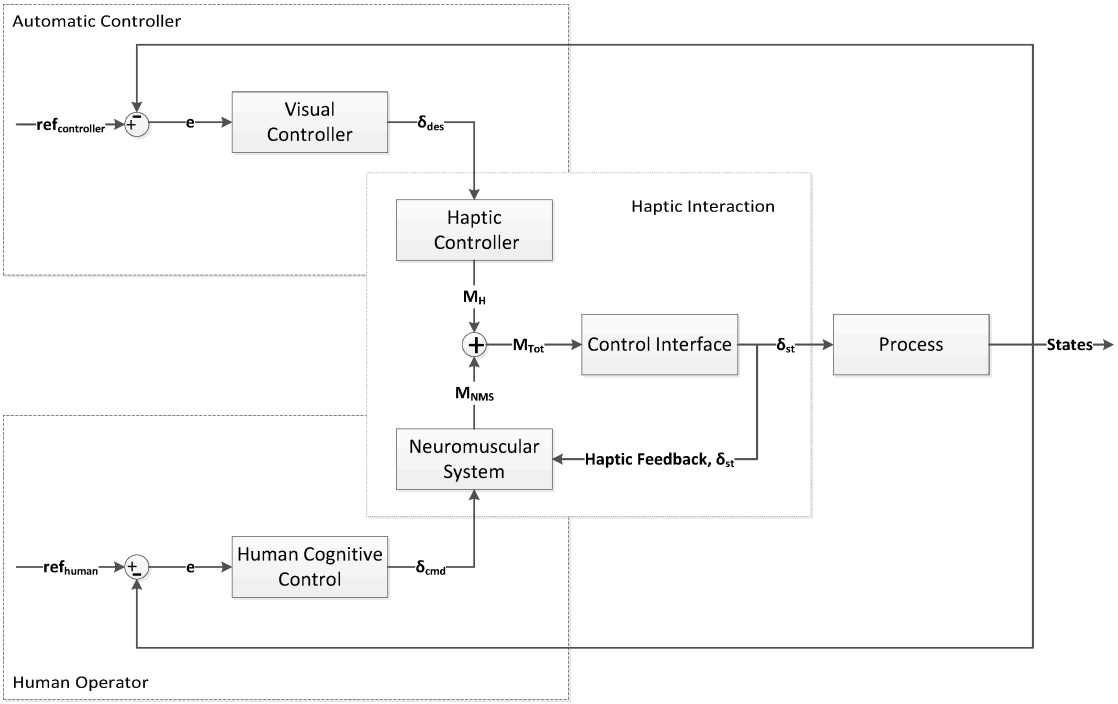

Figure 2-1: Generic haptic shared control architecture, adopted from Abbink and Mulder (D. Abbink & Mulder, 2010)

In HSC systems, an automatic controller (top half of Figure 2-1) and a human operator (bottom half of Figure 2-1) control a process by simultaneously applying moments, M_H and M_{NMS}, on a common control interface. The position of this control interface is the only input to the system (D. Abbink & Mulder, 2010). Therefore, the additional moments that the human operator feels on the control interface provides continuous haptic feedback on the intentions of the automatic controller. As long as the human operator maintains physical contact with the control interface, he/she is actively involved in controlling the system due to the haptic interaction between the human operator neuromuscular system (NMS) and the haptic controller. In fact, the haptic feedback perceived by the human operator is a result of neutral position[1] shifts of the control interface (see inner feedback loop of Figure 2-1), shifts which are caused by the haptic moment, M_H. Furthermore, the human operator can disagree with the actions of the automation as long as the haptic controller is designed to ensure that $M_{H_{max}} < M_{NMS_{max}}$. In this way, the control authority of the system remains firmly with the human operator at all times (Mulder et al., 2012).

[1]The neutral position of a control interface is the position where it is in equilibrium i.e., the position where the sum of all forces acting on the interface is equal to zero.

From the above discussion, it is clear that HSC systems have the potential to solve many of the human factors issues that have been linked with pure automatic systems (Mulder et al., 2012). In HSC, the human operator is not isolated in the decision making process. In fact, there is continuous communication between the human operator and the automatic system through intuitive haptic interactions, and this contributes to the increased situational awareness that is credited with HSC systems (Mulder et al., 2012).

However, to obtain the performance and workload benefits of HSC, conflicts between the automation and the human operator needs to be minimized. This can be achieved by designing the automatic controller to replicate human control strategy and goal (Cleij, 2011). With respect to control strategy, the visual controller has to imitate the cognitive process of determining the appropriate control action based on environmental cues, and the haptic controller has to anticipate the physical interaction between the neuromuscular system and the control interface (D. A. Abbink et al., 2012; Cleij, 2011). These two separate 'mappings' are referred to as 'Visual Control' and 'Haptic Control' respectively and are represented using separate blocks in Figure 2-1.

In literature, several models can be found which describe visual control behavior for various tasks and displays. For instance, Salvucci uses a two point model to explain driver visual control behavior for automobile steering (Salvucci & Gray, 2004). Models of haptic control are also available, for example Van Paassen modeled the pilot arm neuromuscular system to help describe manual control of aircraft with side-sticks (Van Paassen, 1994). However, it is not always clear how these models can be used in the context of HSC. The design and particularly the tuning of the haptic controller i.e., the second mapping of HSC, taking into account neuromuscular behavior, is the focus of this thesis.

2-1-2 Classification and Examples of HSC

Several examples of haptic shared control (HSC) systems can be found in literature. In board terms, these examples can be classified into three different categories. In this subsection, each classification of HSC is discussed with the aid of examples.

Operator Method of Responding to Haptic Feedback

The first classification deals with the way human operators are expected to respond to haptic feedback i.e., whether human operators have to follow or resist the haptic moments to guide a process/system as intended by the automation (Alaimo, Pollini, Bresciani, & Blthoff, 2010). If the human operator is encouraged to follow the haptic guidance on the control interface, it is termed as direct haptic shared control (DHSC). On the other hand, if haptic feedback is presented as disturbance forces which the human operator has to resist, it is called indirect haptic shared control (IHSC).

A good example of DHSC is the haptic gas pedal for automobiles designed by Mulder and Abbink (Mulder et al., 2011). Here, the driver exerts a constant force on the gas pedal indicating his/her desired velocity. Additionally, the driver follows haptic guidance forces acting on the gas pedal such that its position is allowed to vary to maintain a desired separation from a lead vehicle, thus acting as a haptic adaptive cruise control system (Mulder et al.,

2011). The system been implemented by Nissan for its Infinity brand of luxury cars as the 'Distance Control Assist System', see Figure 2-2.

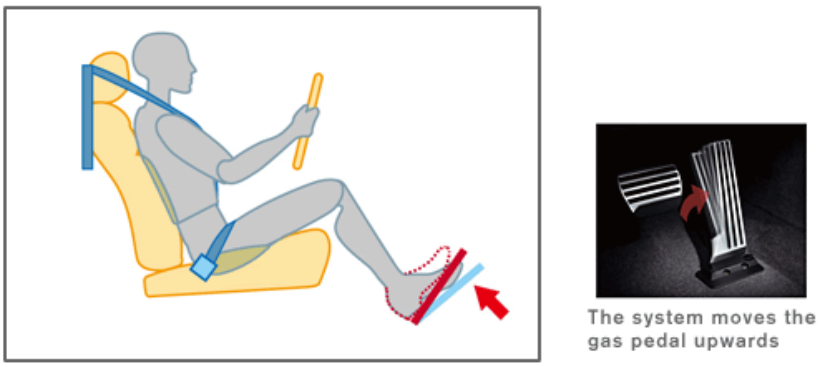

Figure 2-2: Nissan 'Distance Control Assist System' (Nissan, 2006). The system is based on the haptic gas pedal design of Mulder and Abbink (Mulder et al., 2011), and is an example of direct haptic shared control (DHSC).

IHSC has been investigated by de Stigter for its use as a haptic flight director to help pilots of manned aircraft in the approach phase of landing (Stigter et al., 2007). Here the traditional visual flight director command bars are augmented with haptic cues on a side-stick. The system works by shifting the neutral position of the side-stick in the opposite direction of the aircraft trajectory error. These shifts in neutral position are sensed as disturbances by the pilot, and appropriate control inputs can be applied by centering the side-stick and thus resisting the neutral position shifts. Additional manual control inputs can be imposed on the system by moving the stick away from the center position. The detailed working principle of the haptic flight director is presented graphically in Figure 2-3.

Research by Alaimo comparing DHSC to IHSC for phugoid[2] suppression of a manned aircraft suggests that initial performance for untrained subjects is better for IHSC (Alaimo et al., 2010). However, the situation is reversed after a few training runs, and the performance of DHSC is significantly better (Alaimo et al., 2010). Furthermore, Abbink argues that IHSC may degrade the internal mental model of human operators as the intentions of the automation are not directly visible (D. A. Abbink et al., 2012). Although no experimental evidence is provided for this argument, Abbink stresses the need for additional studies analyzing the long term effects of HSC (D. A. Abbink et al., 2012).

Level of Haptic Assistance

The second classification of HSC systems deals with the level of haptic assistance provided, which in turn is closely related to the goals of the automation and the human operator. If the goals of the human operator and the automation match, then often a high level of haptic feedback is provided, aimed at guiding the human operator along a predefined 'optimal trajectory' (D. A. Abbink et al., 2012). This approach is illustrated by the haptic steering wheel designed and tested by Griffiths and Gillespie (Griffiths & Gillespie, 2005). Here the

[2]The phugoid is one of the longitudinal eigenmotions of aircraft and is characterized by a continuous exchange of airspeed and altitude, accompanied with constantly varying pitch angles.

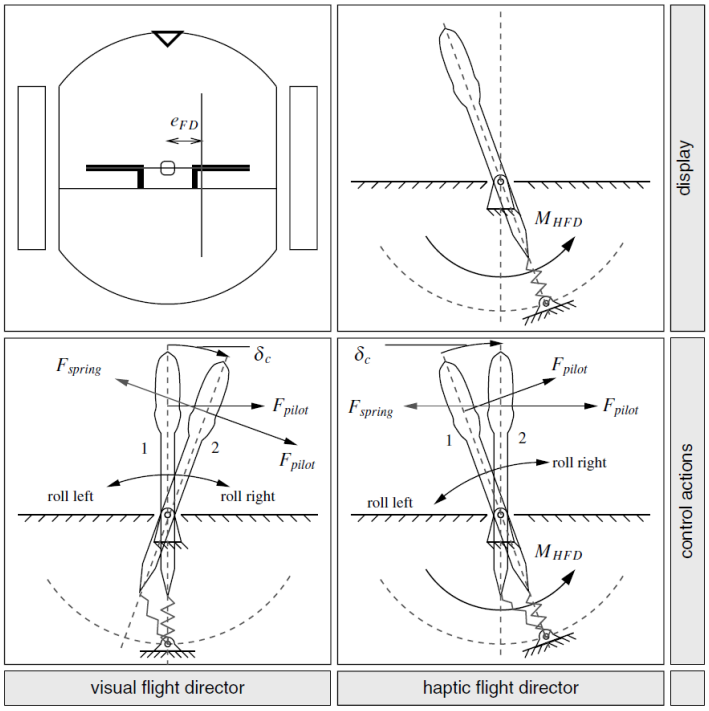

Figure 2-3: Basic working principle of the haptic flight director (Stigter et al., 2007), an example of indirect haptic shared control (IHSC). Note that the spring restoring force, F_{spring}, directed to the non-central neutral position constitutes the haptic feedback felt by the pilot (bottom right).

automation acts like a 'copilot' applying haptic moments on a 'motorized steering wheel' to *pull* the driver back to the road centerline when deviations occur. Experimental analysis using the apparatus pictured in Figure 2-4 showed that lane following performance was increased by an impressive 30% whilst simultaneously reducing visual demand by 29% when compared to manual control.

If the human operator and the automation have (intentionally) different goals, a low level of haptic feedback is provided to assist the human in performing an otherwise purely manual control task. These low level haptic cues are usually present to ensure safe operation of a system. For instance, the haptic flight envelope protection systems applied in the DLR flying helicopter simulator (FHS) supply 'counter forces' on a haptic collective should control inputs exceed rotor blade or powertrain structural limits (Grnhagen et al., 2010). These 'counter forces' define the operational boundaries of the helicopter and is used to *push* the pilot away from impending limits, and additionally indicate the appropriate load alleviation control action (both magnitude and direction). In the FHS, such a system has been implemented to protect the gearbox from excessive torques during take-offs and the rotor from large bending moments during slope landings, as well as to prevent vortex ring states (VRS)[3] at low altitudes. The basic architecture used in the FHS for these haptic protection systems is pictured in Figure 2-5.

[3]Vortex ring state (VRS) causes recirculation to develop around the rotor at low forward velocities and high rates of decent. VRS often occurs at low altitudes and results in poor controllability of the helicopter, thus leading to fatal accidents.

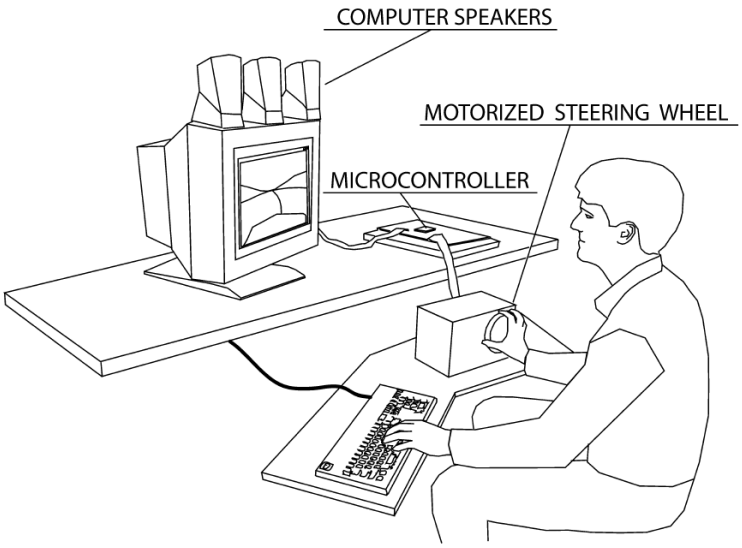

Figure 2-4: Haptic steering wheel used to guide drivers along a road centerline designed by Griffiths and Gillespie (Griffiths & Gillespie, 2005). It is an example of a high level haptic shared control system which guides human operators along a predefined optimal trajectory.

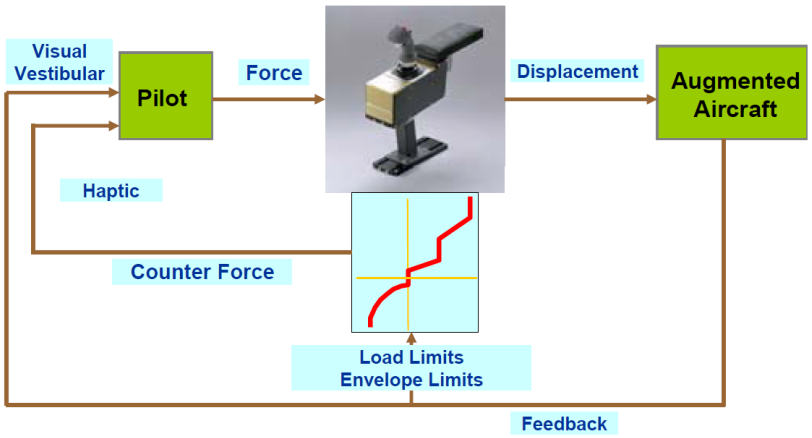

Figure 2-5: The flight envelope protection system developed by von Grnhagen is a representative low level haptic shared control system (Grnhagen et al., 2010). This type of HSC provides haptic cues only when critical system limits are detected and aims at improving system safety during manual control tasks.

Nature of Haptic Feedback

The third and final classification of HSC concerns the nature of haptic feedback cues. Up to this point, only examples of pure force feedback systems have been described. However, most active control interfaces, such as control loaded side-sticks, have the ability to modify its stiffness' in addition to applying haptic forces to the human operator. This property can be used to combine force feedback (FF) and stiffness feedback (SF) to so called 'stiffness-force' (SFF) and 'force-stiffness' feedback (FSF) systems (T. M. Lam et al., 2009). SFF and FSF can be best explained by first considering FF and SF separately. Note for simplicity, the control interface considered in the following discussion is a control loaded side-stick with stiffness k_{st}.

In FF systems, see Figure 2-6(a), the haptic force, F_f, shifts the neutral position of the side-stick from the origin to point A (T. M. Lam et al., 2009). As explained in section 2-1-1, this neutral position shift is perceived as haptic feedback by the human operator. However, frequent changes in the side-stick neutral position has been experimentally linked to increased physical workload (T. Lam, Boschloo, et al., 2009). To tackle this problem, in SF systems the automation modifies only the stiffness of the side-stick to provide haptic feedback to the human operator, k_s in Figure 2-6(b). In this way the neutral position of the side-stick remains permanently at the origin. However, a downside to this method is that the magnitude of the haptic feedback sensed by the human operator is directly proportional to the stick deflection initiated by the human operator him/herself, see Figure 2-6(b). For many applications, the resulting low control authority of the automation is not sufficient for safe operations.

To combine the best of FF and SF, Lam proposed the 'stiffness-force' (SFF) feedback system in which the automation modifies the stiffness of the side-stick and additionally provides 'reduced' haptic forces (T. Lam, Mulder, & Paassen, 2006). Despite the anticipated benefits, experimental evidence showed that there was not much difference between the safety of FF and SFF systems (T. Lam et al., 2006). This is because the SF component of SFF has the negative effect of further reducing the neutral position shift from point A to point B, see Figure 2-6(c). Thus SFF also reduces the control authority of the automation.

To compensate for this issue, Abbink and Mulder suggested that an additional force offset has to be provided to restore the neutral position shift to point A, see Figure 2-6(d). The magnitude of this force offset, F_s', is based on the instantaneous SF (D. A. Abbink & Mulder, 2009). This revised method, dubbed 'force-stiffness' (FSF) feedback, was found by Lam to significantly improve safety when compared to FF (T. M. Lam et al., 2009).

2-2 Haptic Collision Avoidance System for UAV Teleoperation

As stated in chapter 1, the haptic collision avoidance system (HCAS) is designed to help teleoperators avoid obstacles and thereby improve the safety of UAVs, especially in urban environments. The HCAS is of particular interest to this thesis as it is used as the framework for testing a novel haptic controller tuning law. Therefore in this section, the functionality of the HCAS is described. Based on previous experimental results, the need for a new tuning law to further improve user acceptance of the system is also discussed.

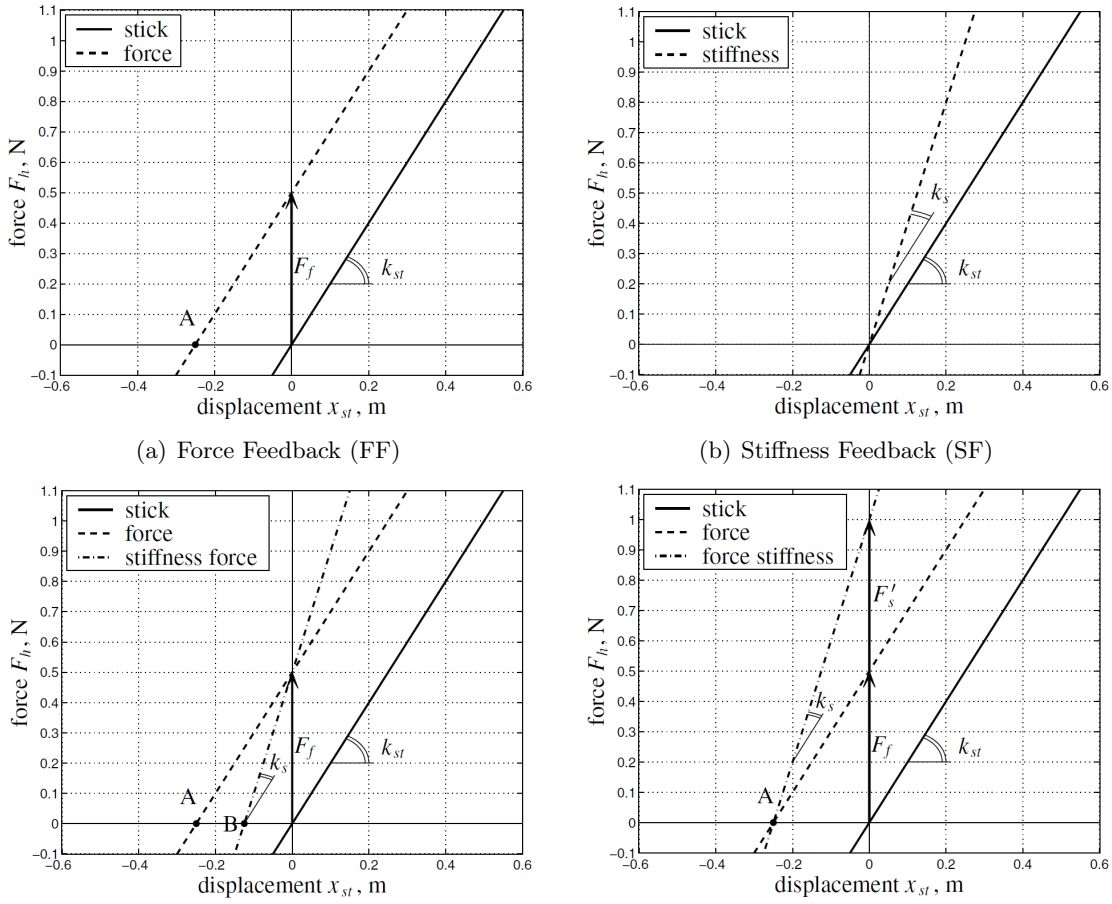

(a) Force Feedback (FF)

(b) Stiffness Feedback (SF)

(c) Stiffness-Force Feedback (SFF)

(d) Force-Stiffness Feedback (FSF)

Figure 2-6: Force-displacement relations for different variations in the nature of haptic feedback (T. M. Lam et al., 2009)

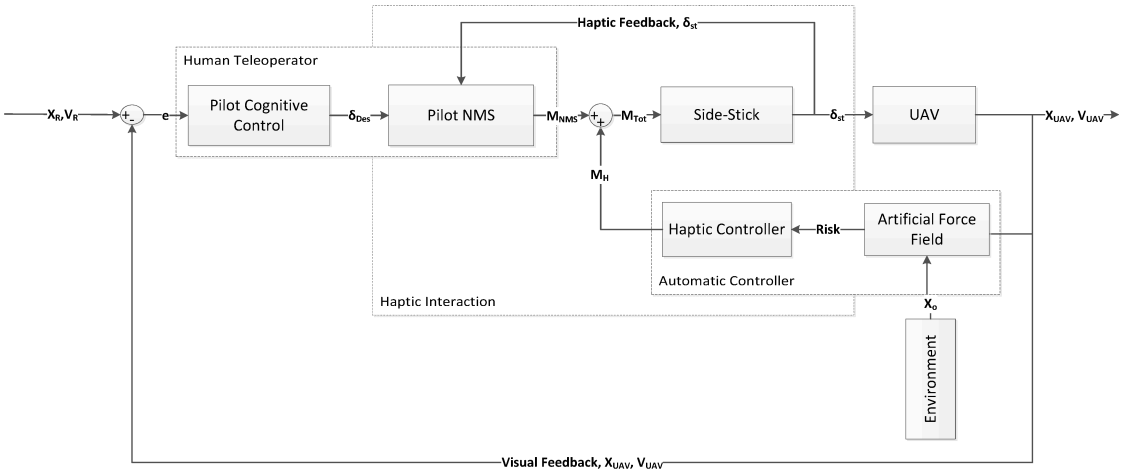

Figure 2-7: Haptic collision avoidance system architecture adopted from Lam (T. Lam, 2009)

2-2-1 HCAS Architecture

Boschloo (Boschloo et al., 2004) and Lam (T. Lam, Boschloo, Mulder, Paassen, & Helm, 2004), the original designers of the haptic collision avoidance system (HCAS), aimed at increasing the safety and performance of UAV teleoperation, whilst concurrently reducing teleoperator workload and improving his/her situational awareness. To meet these conflicting requirements, a system to help teleoperators avoid collisions, particularly when obstacles are not in their visual field of view (FOV), was designed based on the principles of haptic shared control (see section 2-1 for details on HSC). The architecture of this system is depicted in Figure 2-7.

In Figure 2-7, it can be seen that the UAV teleoperator is provided with an outer visual feedback loop and an inner haptic feedback loop. Similar to the generic HSC block diagram pictured in Figure 2-1, haptic feedback is provided by an automatic controller which consists of two separate 'mappings'. For the HCAS, the visual control function i.e., the first mapping of HSC, is performed by a so called 'artificial force field'. The artificial force field, see section 2-2-2, scans the environment for obstacles and computes the risk of collisions. This risk is converted to a haptic moment, M_H, by the 'haptic controller' which constitutes the second mapping of HSC. M_H and M_{NMS}, the moment generated by the teleoperator neuromuscular system (NMS), acts together on the side-stick, and its resulting position is the only input to the UAV. This distinct characteristic of HSC systems ensures that the teleoperator can always overrule the automation. The haptic feedback perceived by the teleoperator is a result of shifts in side-stick neutral position, which in turn is caused by M_H. Note that in Figure 2-7 only force feedback haptic cues are supplied by the automation as it is the only haptic configuration studied in this thesis. Also communication delays are not considered.

Based on the above description, and the classification of HSC systems discussed in section 2-1-2, it is clear that the HCAS provides a low level of haptic assistance. The sole goal of the automation in the HCAS is to improve the safety of UAV teleoperation by assisting the teleoperator in detecting and avoiding obstacles. Therefore, when no obstacles are detected by the artificial force field, no haptic feedback is provided and the teleoperator is responsible for manual control of the UAV. Additionally, the HCAS can be categorized as an example of direct haptic shared control (DHSC). This is because the haptic moment, M_H, is designed to encourage the teleoperator to follow the commands of the automation to fulfill the collision avoidance function.

2-2-2 Artificial Force Field

The purpose of the artificial force field (AFF) is to detect obstacle around the UAV and to compute the corresponding risk of collision (Boschloo et al., 2004). For this reason, they are also known as artificial risk fields. The risk computed by the AFF is analogous to the probability of collision and it is therefore a value between 0and 1, with 1 indicating a certain collision with the environment.

The basic working principle of an AFF is illustrated graphically in Figure 2-8. The AFF moves with the UAV and obstacles are detected only if they lie within the area scanned by the AFF. Subsequently, the AFF computes the risk of collision based on the relative position

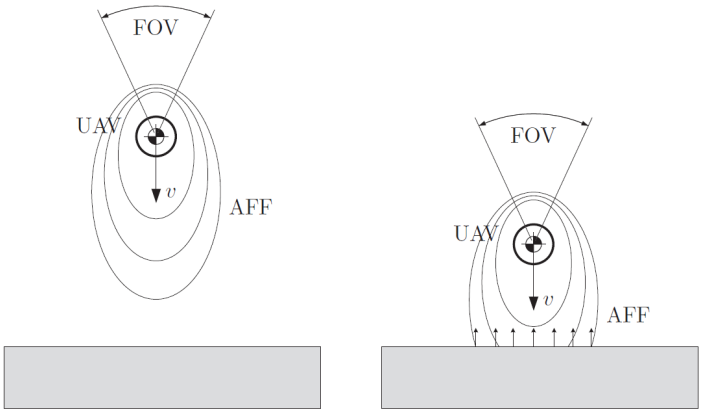

Figure 2-8: Basic working principle of the artificial force field (AFF) (T. Lam, 2009). Only obstacles within the geometry of the field are detected.

of the obstacle to the UAV. This risk is translated to repulsive haptic forces (small arrows in Figure 2-8) by the haptic controller to guide the teleoperator away from danger.

The shape and size of an AFF are two important properties which determine its ability to detect obstacles. Boschloo designed two different AFFs of varying shape and size specifically for generating haptic feedback cues called the basic risk field (BRF)[4] and the parametric risk field (PRF) (Boschloo et al., 2004). Based on offline simulations, Boschloo concluded that the PRF was better suited for UAV teleoperation as it led to fewer collisions and was more stable than the BRF (Boschloo et al., 2004). A human-in-the-loop experiment conducted by Lam validated these observations. Additionally it was found that the PRF resulted in smaller haptic forces that build up closer to obstacles, thus allowing for higher UAV velocities (T. M. Lam et al., 2007). For these reasons, the PRF was selected for the HCAS and the rest of this subsection will focus on it.

As the name suggests, the shape and size of the parametric risk field are dependent on a number of parameters. Furthermore, the shape and size of the PRF are proportional to the instantaneous velocity, $\mathbf{v}$, and inversely proportional to the UAV maximum deceleration, a_{max}, see Figure 2-9. If the UAV is not moving, the PRF scans a relatively small circular region around the UAV as in Figure 2-9a. To provide sufficient time for the teleoperator to react to haptic feedback forces, the PRF extends in the direction of motion as in Figure 2-9b, especially at higher velocities. In addition, the field extends slightly behind the UAV such that objects can be detected if the accidentally UAV drifts backwards.

Figure 2-10 displays the parameters and zones of the PRF. Here the parameters r_{pz}, the radius of a circular protection zone around the UAV, and d_{min}, the distance between zone 1 and zone 2 at stand still, are constants. Parameters d_{stop} and d_{ahead} are responsible for extending the size of the PRF when the UAV is moving and are defined through equations 2-1 and 2-2 respectively. These two equations are derived from simple kinematic relations for rigid body motion (Boschloo et al., 2004). From Figure 2-10 and equations 2-1 and 2-2, it is clear that the PRF geometry is completely defined by constant parameters r_{pz}, d_{min}, t_{ahead} and a_{max}, and the instantaneous velocity $\mathbf{v}$. The constant parameters were refined through simulations

[4]The BRF is a type of generalized potential field (GPF) designed for land robot obstacle avoidance (Krogh, 1984).

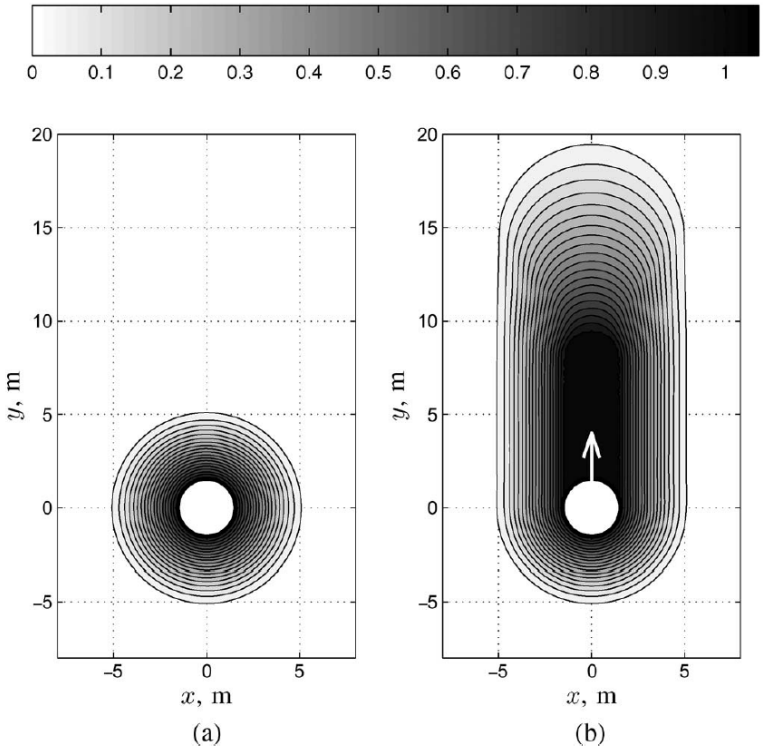

Figure 2-9: The parametric risk field (PRF) adjusts its shape and size based on the instantaneous velocity and maximum UAV deceleration (T. Lam, Boschloo, et al., 2009). The field is circular when $\mathbf{v} = 0$ (a) and extends in the direction of motion (b). The color-bar indicates the risk of collision.

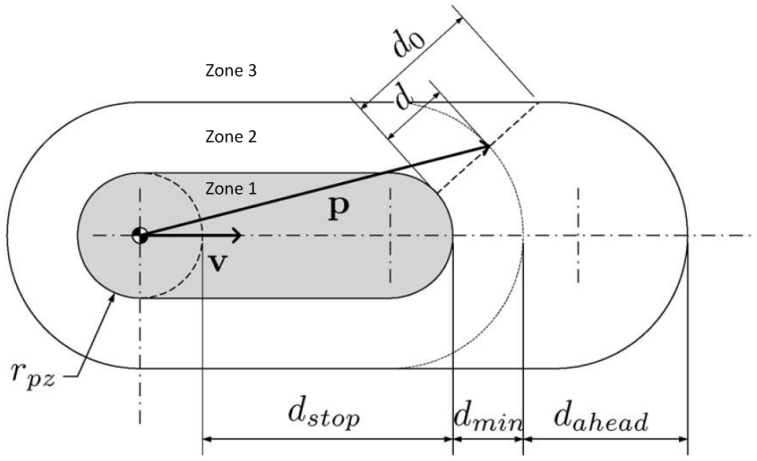

Figure 2-10: Variables used to describe the shape of the parametric risk field (PRF) (Boschloo et al., 2004).

by Lam for the UAV model used in this thesis and are listed in Table 2-1 (T. Lam, Boschloo, et al., 2009).

$$d_{stop} = \frac{|\mathbf{v}|^2}{2a_{max}} \tag{2-1}$$

$$d_{ahead} = |\mathbf{v}|\, t_{ahead} \tag{2-2}$$

Table 2-1: Heuristically optimized constant parameters that define the geometry of the parametric risk field (PRF)

	Parameter	Value	Description
1	r_{pz}	1.5	Radius of protection zone [m]
2	d_{min}	1.5	Distance between zone 1 and zone 2 [m]
3	t_{ahead}	2	Maximum available reaction time [s]
4	a_{max}	1	Maximum UAV deceleration $[m/s^2]$

As stated earlier, the risk of collision is computed based on the relative distance between the UAV and an obstacle. For the PRF, the risk is computed differently depending on the zone in which the obstacle is detected, see equation 2-3. Note that for zone 2, the risk is computed using a shifted cosine function. This function ensures that there is a smooth transition in the risk between the zones, thus making sure that there are no sudden changes in the corresponding haptic forces (T. M. Lam et al., 2007). To evaluate the shifted cosine function at a point p, distances d and d_0 need to computed and are defined in Figure 2-10.

$$risk\,(\mathbf{p},\mathbf{v}) = \begin{cases} 1 & \text{if } \mathbf{p} \text{ in Zone 1} \\ \cos\left(\frac{d}{d_0}\cdot 180^o + 180^o\right) + 1 & \text{if } \mathbf{p} \text{ in Zone 2} \\ 0 & \text{if } \mathbf{p} \text{ in Zone 3} \end{cases} \tag{2-3}$$

The PRF can also be used to compute a collision avoidance vector. The magnitude of this vector is simply equal to the risk magnitude computed using equation 2.3. The direction of the vector is defined from the obstacle to the UAV. If multiple obstacles are detected, the final collision avoidance vector can be computed using a so called 'max-min' method. In this method the largest and smallest avoidance risk vectors are summed vectorially. According to Boschloo, this method does not suffer from either over or underestimating the final collision avoidance vector of summing or averaging methods (Boschloo et al., 2004).

2-2-3 Previous Experimental Results

The HCAS has been tested extensively by Lam in multiple human-in-the-loop experiments where the teleoperator subjects was required to perform a reconnaissance task in an obstacle laden urban environment. In each experiment, modifications over the basic HCAS described in section 2-2-1 were tested. These included the testing of:

1. Multiple artificial force fields (T. M. Lam et al., 2007)
2. Multiple haptic feedback configurations: force feedback, 'stiffness-force' feedback and 'force-stiffness' feedback (T. Lam et al., 2006)
3. 'Wave variables' to counteract communication time delays (T. Lam et al., 2008; T. M. Lam et al., 2009)

In all experiments, it was found that haptic feedback considerably improved the safety of teleoperation when compared to manual control. In Figure 2-11 the number of collisions for different artificial force fields are plotted for all experiment subjects. Here 'NHF' stand for no haptic feedback representing pure manual control. GPF (i.e., BRF) and PRF are two types of artificial force fields introduced in section 2-2-2. It is clear from the figure that the number of collisions decreases significantly with haptic feedback. Improvements in teleoperator performance, measured in terms of time spent within a critical distance to obstacles, was also reported.

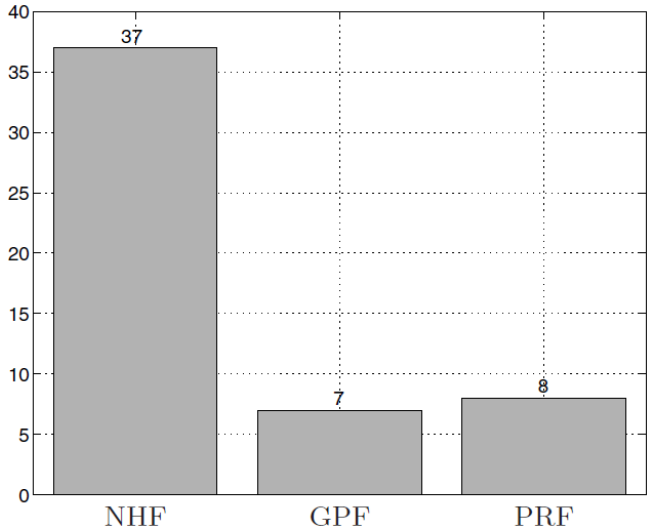

Figure 2-11: Total number of collisions for all experiment subjects (T. M. Lam et al., 2007). Here 'NHF' stand for no haptic feedback, 'GPF' and 'PRF' are haptic feedback configurations based on different artificial force fields. Haptic feedback significantly reduces the number of collisions and thereby improves the safety of UAV teleoperation.

However, in most cases, the overall subjective workload measured using the NASA Task Load Index (TLX) was greater with haptic feedback[5]. Figure 2-12 shows box plots for the various components of the NASA TLX for same experiment as depicted in Figure 2.11. Lam attributes the increased overall workload (Figure 2-12a) for haptic feedback configurations to increased physical workload (Figure 2-12c) and frustration(Figure 2-12g) (T. M. Lam et al., 2007). Furthermore, some subjects reported that haptic forces were 'too strong' making it difficult to overrule the automation (T. M. Lam et al., 2007). In his final experiment, Lam combined the above mentioned three improvements and changed the experiment procedure slightly to include a 60 second time penalty for each collision (T. M. Lam et al., 2009).

[5]see section 4-2-5 for details on the NASA TLX.

Since the NHF configuration resulted in the most number of collisions, the frustration and the overall subjective workload was slightly lower for haptic feedback configurations when compared to manual control. However, even in this case, the subjective physical workload and measured control activity continued to be much higher for haptic feedback.

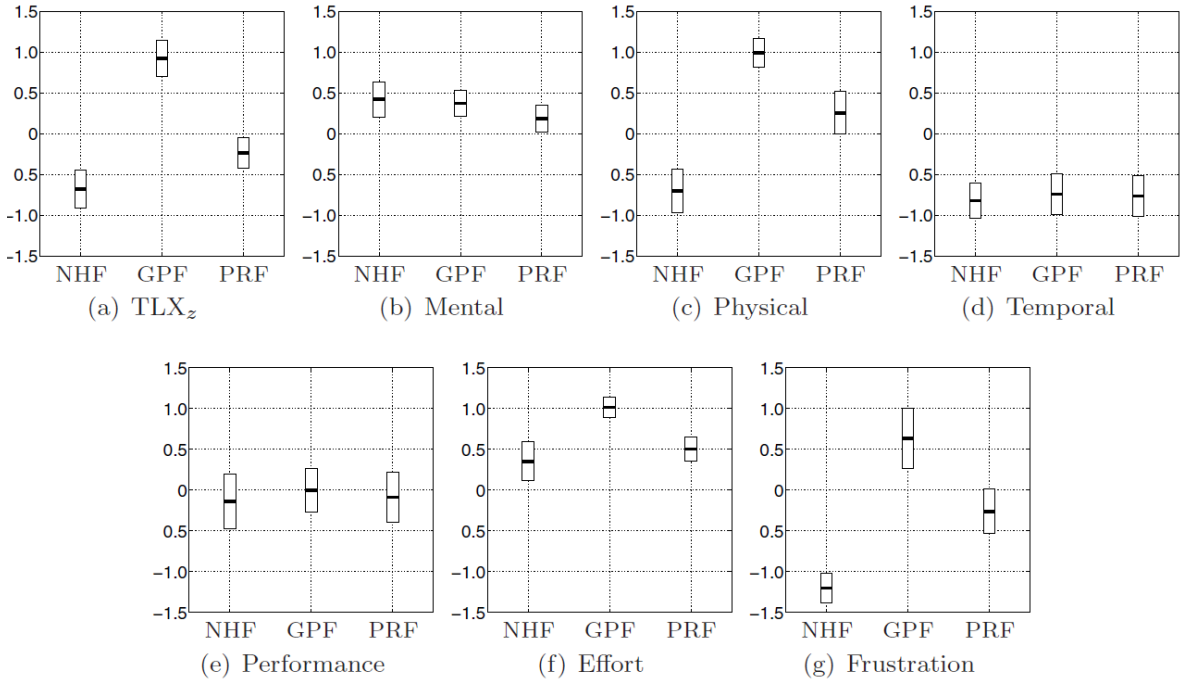

Figure 2-12: Mean and 95% confidence intervals of the NASA TLX subjective workload scores for the six workload sources (T. M. Lam et al., 2007). Haptic feedback configurations result in higher overall Z score due to increased physical workload and frustration.

The underlying root cause for the increased physical workload reported in previous experiments can be understood by considering the tuning procedure used for the haptic controller. Equation 2-4 shows that the haptic moment, M_H, is computed as the product of a haptic gain, K_H, and the risk vector magnitude, $\left\|\vec{R}\right\|$. In essence, the form of the haptic control law corresponds to that of a proportional controller in which the haptic gain, K_H, has to be optimized.

$$M_H = K_H \cdot \left\|\vec{R}\right\| \tag{2-4}$$

Due to the complex human-machine interactions involved, optimization of K_H in a control theoretic manner was deemed to be too difficult (T. Lam, Mulder, & Paassen, 2009). Instead, K_H was tuned using a 'trial and error' process, and in doing so Lam accepted that a tradeoff had to be made between safety and workload. As safety of teleoperation was given a higher priority in the initial design process, the haptic controller was 'overturned' using a 'high' value for K_H. This 'high' value of K_H resulted in forces perceived as being 'too strong', leading to increased physical workload and higher frustration levels over time.

To reduce physical workload and improve safety at the same time, it is proposed that a 'human centered' approach has to be taken when tuning the haptic controller (D. A. Abbink et al.,

2012). Lam himself recognized that taking into account the neuromuscular behavior of the human arm to haptic forces may improve user acceptance of the system (T. Lam, Mulder, & Paassen, 2009). In the following section, a new method to tune the haptic controller based on these ideas is proposed.

2-3 Tuning Haptic Feedback

In this section, a novel haptic controller tuning procedure that is based on models and measurements of the neuromuscular system is introduced. It is expected that by taking into account the neuromuscular response when designing haptic feedback forces, the high physical workload and frustration levels reported for 'trial and error' tuning can be reduced, see section 2-2-3. The section begins by describing the components and properties of the human arm neuromuscular system relevant to the tuning procedure, followed by the derivation of the tuning procedure itself. The section concludes by describing a method to measure neuromuscular admittance, an important property that is needed for the tuning procedure.

2-3-1 Human Arm Neuromuscular System

The neuromuscular system (NMS) is organized and consists of components that resembles a closed loop feedback control system, see Figure 2-13. It is capable of voluntary movements and rejecting (or following) external moments at the same time (D. Abbink, 2006).

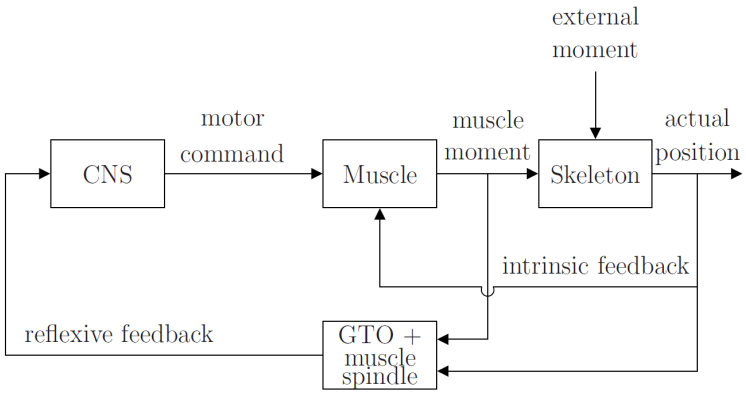

Figure 2-13: Closed loop block diagram of the neuromuscular system (NMS) (Lasschuit et al., 2008). The system resembles a classic feedback control system.

In Figure 2-13, the central nervous system acts as the controller/compensator of the system and consists of the brain and spinal cord. The CNS determines appropriate motor commands based on feedback from sensors, as well as goal directed feed-forward control signals originating from so called 'higher brain centers[6]' (D. Abbink, 2006). These motor commands travel along nerves to the muscles via electrochemical processes. The muscles act as actuators and produce moments based on the 'level of activation', which in turn determines its spring-damper properties(Lasschuit et al., 2008). Muscle moments are transmitted via tendons to

[6]Higher brain centers are areas of the brain responsible for cognitive thought processes.

skeletal bones and can either cause or restrict motion of the skeleton. The function of the skeleton is to provide a rigid structure for the NMS components, and its mass and inertia properties also affects the kinematics of the system (Lasschuit et al., 2008).

Proprioceptive[7] sensors located within the muscles and the tendons detect the state of the NMS. The important sensors are the muscle spindles, which detects muscle stretch and stretch rates, and the Golgi tendon organ (GTO), which measures muscle forces, thus constituting separate position and force feedback loops. Information collected by the muscle spindles and the GTO are sent for processing to the brain, but also to so called 'α-motoneurons' located within the spinal cord (D. Abbink, 2006). The later allows for fast subconscious spinal reflexes which accounts for the faster reaction times associated with the NMS ($\leq$ 40ms) when compared to other senses such as the visual system ($\approx$ 200ms) (D. Abbink, 2006). A mathematical model of the NMS developed by de Vlugt(Vlugt et al., 2006) is used for the offline simulation described in the next chapter, see section 3-2-2 for more details.

With respect to the tuning of the haptic controller, an important dynamic property of the NMS is its endpoint admittance. Endpoint admittance is defined as the "causal relationship between force (input) and hand position (output)" (D. Abbink, 2006). It can be "thought of as a measure of the displacement that a force causes" (D. Abbink, 2006). Therefore in practical terms, admittance is equal to the inverse stiffness of the system. Research has shown that admittance is dependent on the magnitude and the direction of voluntary feed-forward or 'bias' moments commanded by the CNS. Furthermore, admittance is found to be higher along the lateral (roll) axis of the human arm when compared to the longitudinal (pitch) axis (Lasschuit et al., 2008). This is because more mass has to be rotated when performing a longitudinal motion, which correspondingly requires more force/moment.

The endpoint admittance can be varied over a large range of values by the modulating the stiffness and damping parameters of the muscles. This can be achieved through two different physiological mechanisms (Lasschuit et al., 2008). The first mechanism involves the adjustment of the relative strengths of the aforementioned reflexive feedback paths. Greater position feedback from the muscle spindles results in low admittance. On the other hand, larger force feedback from the GTO results in high admittance. At a setting where both feedback paths are suppressed, admittance is characterized mainly by relatively constant intrinsic muscle stiffness and damping values, caused by a constant level of muscle activation (Lasschuit et al., 2008). The second mechanism entails co-contraction of muscle pairs resulting in high admittance, and it often is used to reject external disturbance moments (D. Abbink, 2006). When comparing the two mechanisms, reflexive feedback is more energy efficient process, leading to lower physical workload (D. Abbink, 2006).

Using the two above mentioned mechanisms, humans can be instructed to respond to haptic forces in three distinct ways (D. A. Abbink et al., 2012):

1. Resist haptic forces using muscle co-contraction and position feedback (muscle spindle) dominated reflexive activity

2. Amplify and actively follow haptic forces with force feedback (GTO) dominated reflexive activity

[7]Proprioception is the body's inherent sense of motion and orientation.

3. Do not react to haptic forces by suppressing all reflexive activity and using only the intrinsic feedback path

These three different instructions are called position, force and relax tasks respectively. Each task instruction and its associated qualitative admittance and stiffness are listed in Table 2-2. Note that although admittance is listed as 'high' or 'medium' or 'low' in Table 2-2, in reality the numerical admittance value for the position task is significantly lower than for the other two tasks.

Table 2-2: Description and relative admittance/stiffness of the three neuromuscular task instructions

Task	Admittance	Stiffness	Description
Position	Low	High	Resist haptic forces and maintain position of control interface
Relax	Medium	Medium	Do not react to haptic forces and follow motion of control interface
Force	High	Low	Amplify and actively follow haptic forces and give way to the motion of the control interface

2-3-2 Neuromuscular Admittance Based Tuning Paradigm

As stated in section 2-3-1, the neuromuscular system (NMS) is highly adaptive and it is able to vary its admittance over a large range of values, see Figure 2-14. Experimental evidence has shown that the NMS adapts its admittance to match the particular tuning setting of the haptic controller in an effort to maintain stability and adequate performance (Cleij, 2011; D. Abbink et al., 2012). This adaptation makes the response of a HSC system rather insensitive to the tuning of the haptic forces, thus making it difficult to determine the optimal tuning setting for the haptic controller (D. Abbink et al., 2012; Smisek et al., 2013). However, an adaptation to a non-optimal tuning setting has been found to lead to increased physical workload and frustration over time. These effects were reported for the 'trial and error' tuning method using by Lam for the haptic collision avoidance system (HCAS), see section 2-2-3.

A possible solution to this problem is to tune the haptic controller to match a so called 'design' neuromuscular admittance/stiffness setting (D. Abbink & Mulder, 2010; Smisek et al., 2013). In this way, the NMS will adapt to a tuning setting that is based on its own properties, and thus possibly reducing conflicts between the human operator and the automation on a neuromuscular level. This is approach illustrated in equation 2-5 for the HCAS:

$$M_H = \underbrace{[K_{NMS} + K_{st}]}_{combined\ system\ stiffness} \cdot \vec{R} \tag{2-5}$$

Here, K_{NMS} is the design neuromuscular stiffness and K_{st} is the stiffness of the control interface, in this case a side-stick. When comparing equations 2-4 and 2-5, the main difference

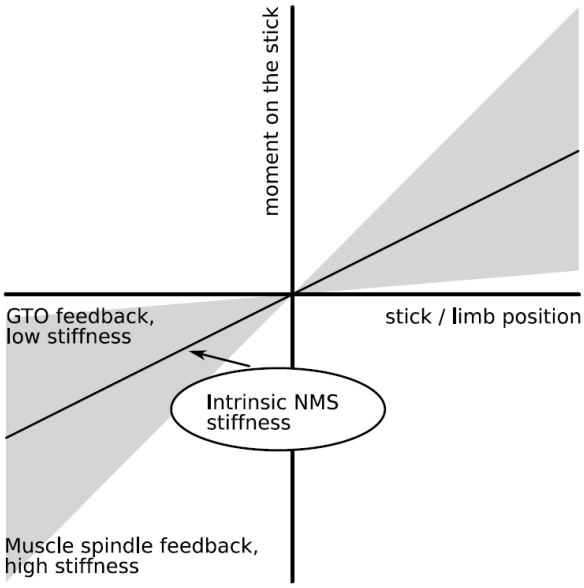

Figure 2-14: Large adaptability range of neuromuscular stiffness (Smisek et al., 2013). Note that the linear representations in this figure are for illustrative purposes only.

in the new approach is that the haptic moment, M_H, is computed based on the 'combined' stiffness of the NMS and the side-stick. The rationale behind this new tuning paradigm can be better understood by considering Figure 2-15. To realize the optimal deflection of the stick-hand combination, the haptic controller must supply a force/moment that corresponds to the combined stiffness of the system i.e., the sum of the stiffness' of the NMS and side-stick.

In theory any admittance/stiffness setting of the NMS can be chosen as the design point. However as explained in section 2-3-1, in practice humans respond to haptic cues in three distinct ways called the position, force and relax tasks. Each of these tasks are characterized by different, but constant admittance/stiffness values at low frequencies of the disturbance signal (see Table 2-2). This makes it possible to select one of the tasks as the design point and to include neuromuscular stiffness as a simple gain in the haptic controller tuning law, just as in equation 2-4.

In this thesis, the relax task stiffness is selected as the design point for tuning the haptic controller. This is primarily because when performing the relax task, reflexive feedback paths of the muscle spindles and GTO are suppressed, and the properties of the NMS are mainly dependent on its intrinsic (and relatively constant) mass-spring-damper parameters, see section 2-3-1. In addition, this leads to the lowest physical activity when compared to the other tasks, thus the relax task is aligned with the goal of reducing physical workload for HSC systems.

Some researchers suggest the force task stiffness as the ideal design point as it requires human operators to be actively part of the control task, thus improving their situational awareness (D. Abbink et al., 2012). Although this is a valid argument, experimental evidence has shown that some subjects find it difficult to perform the force task, and low frequency coherence[8] of the admittance measurements tend to be higher for the relax task (Lasschuit et al.,

[8]Coherence is a measure of linearity. A high coherence value indicates high linearity which is advantageous

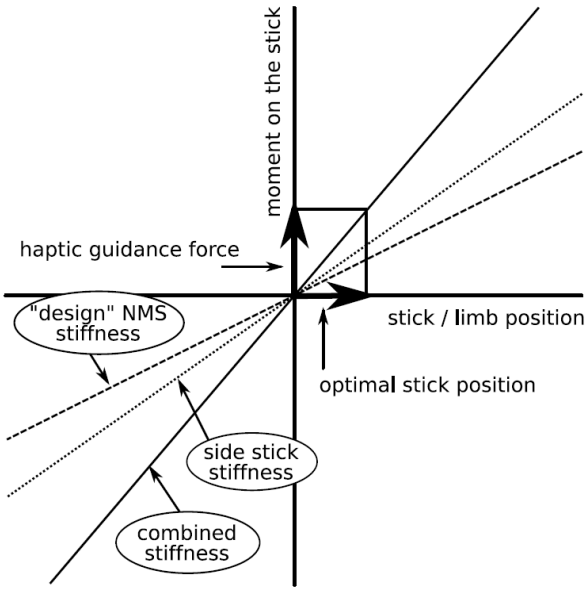

Figure 2-15: Rationale behind the novel tuning procedure (Smisek et al., 2013). Here it is proposed that a haptic moment corresponding to the combined system stiffness i.e., stiffness of stick + design neuromuscular stiffness, has to be provided by the haptic controller to obtain the desired stick deflection.

2008; De Vlugt, 2004).

It is commonly accepted that the position task stiffness should not be chosen as the design point as the task is performed using muscle spindle reflexive feedback and through co-contraction of muscle pairs. These two physiological mechanisms are energy inefficient and therefore would lead to increased physical workload (Lasschuit et al., 2008). Also, since the position task stiffness corresponds to the highest stiffness capability of the NMS, see Figure 2-14, tuning a controller to the position task would make it difficult for human operators to overrule the automation (Smisek et al., 2013).

As a final remark, admittance was found to be dependent on the magnitude and direction of the operator feed-forward bias moment, M_{NMS}. Therefore the haptic controller tuning law given by equation 2-4 has to be defined separately for the X and Y axes:

$$M_{H_X} = [K_{NMS_X}(M_{NMS_X}) + K_{st}] \cdot \vec{R}_X \tag{2-6}$$

$$M_{H_Y} = [K_{NMS_Y}(M_{NMS_Y}) + K_{st}] \cdot \vec{R}_Y \tag{2-7}$$

To be able to implement equations 2-6 and 2-7 in the HCAS, numerical values for the relax task admittance has to be determined. In the following section, the method used by Smisek to measure admittance in the presence of bias forces is explained.

as admittance can then be considered equivalent to a constant gain.

2-3-3 Experimental Measurement of Neuromuscular Admittance

Neuromuscular admittance is defined as the ratio between hand position and exerted force and it is a measure of the displacement that a force causes (D. Abbink, 2006). Admittance can be determined experimentally using small stochastic torque disturbances, T_{dist}, on the control interface to excite the NMS, and by measuring resultant hand displacements, δ_{st}, and handling moments, M_{NMS}. The method is analogous to determining the stiffness of a joystick by qualitatively measuring displacements caused by random torques applied on it.

The torque disturbance is designed in the frequency domain as a stochastic multi-sine signal that contains power at logarithmically spaced frequencies. Typically, the signal contains frequencies up to 25Hz as most neuromuscular dynamics occur below 20Hz (De Vlugt, 2004). The phase of the sine components are randomized to ensure an unpredictable signal that cannot be anticipated by experiment subjects (D. Abbink, 2006). The admittance along the longitudinal (pitch) and lateral (roll) hand axes can be measured simultaneously by applying two different disturbance torques which are separated in the frequency domain (Damveld et al., 2010). In this way the response to each disturbance can be separated when identifying admittance from the experiment data.

Research has shown that admittance measured using the above method is dependent on the bandwidth of the disturbance torques. Admittance measured using low bandwidth signals tend to be significantly lower than with wide bandwidth signals (Mugge, Abbink, & Helm, 2007). It is suspected that wide bandwidth signals suppress reflexive activity and this in turn affects the measured admittance at low frequencies. Since dynamics related to motion-control are prevalent at frequencies below the eigen-frequency of the NMS, low frequency characteristics are very important (Mugge et al., 2007). The Reduced Power Method developed by Mugge et al. tackles this issue by using a wide bandwidth signal which reduces power at high frequencies (Mugge et al., 2007). Thus high frequency dynamics can be captured without affecting the control behavior at low frequencies.

Using experimental data, admittance can be estimated at the frequencies of the disturbance torque, f_{dist}, by computing the cross-spectral density between T_{dist} and δ_{st}, and the cross-spectral density between T_{dist} and M_{NMS} (Lasschuit et al., 2008):

$$\hat{H}_{adm}\left(f_{dist}\right) = \frac{\hat{S}_{T_{dist}-\delta_{st}}\left(f_{dist}\right)}{\hat{S}_{T_{dist}-M_{NMS}}\left(f_{dist}\right)} \tag{2-8}$$

Note that equation 2-8 has to be evaluated separately along the longitudinal and lateral directions to estimate the admittance along these two axes.

A human-in-the-loop experiment was conducted by Smisek to measure the relax task admittance to implement the novel haptic controller tuning laws given by equations 2-6and 2-7. When manually controlling a UAV, a teleoperator applies voluntary feed-forward 'bias' moments on the side-stick, hence relax task admittance has to be measured in the presence of bias moments (Smisek et al., 2013). However, these bias moments make it difficult for an operator to intentionally suppress his/her neural reflexes, a distinct characteristic of the relax task. In fact, the bias moments actually represent a force task that is being performed by the teleoperator to manually control the UAV.

To be able to measure relax task admittance whilst performing a force task, neural reflexes have to be artificially suppressed. To achieve this, Smisek designed a wide bandwidth disturbance torque. The disturbance torque is based on the Reduced Power Method mentioned above, but the full power spectrum of the signal has been made wider in an attempt to suppress reflexes (Smisek et al., 2013). Figure 2-16 displays the disturbance torque in the frequency and time domains, in both the longitudinal (pitch) and lateral (roll) directions.

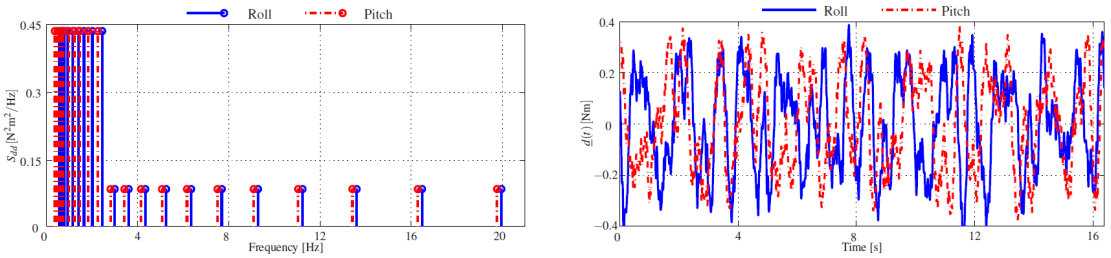

(a) Frequency domain representation

(b) Time domain realization for 1 period

Figure 2-16: Frequency and time domain representations of the wide bandwidth disturbance torque (Smisek et al., 2013). The disturbance torque is designed to suppress reflexive activity and thereby measure relax task stiffness when performing a force task.

The human-in-the-loop experiment was conducted in the Human-Machine Lab of the Control and simulation department of the faculty of Aerospace Engineering at TU Delft. Ten right-handed subjects were recruited for the experiment, and had to perform bias moments of three different magnitudes (0Nm, 0.7Nm & 1.4Nm), and six different directions ($0^o, 45^o, 90^o, 135^o, 180^o$&$270^o$), resulting in a total of 13 conditions, see Figure 2-17. For the central condition C1, subjects were required to perform a relax task in addition to a force task to check whether the wide bandwidth disturbance torque suppressed reflexes in reality.

Figure 2-18 displays the measured force task admittance for all conditions of one subject using a so called 'admittance ellipse'. Here the lengths of the major and minor axes indicates the admittance along the lateral and longitudinal axes respectively, at a disturbance torque frequency of 0.7Hz. The central condition ellipses for the force and relax tasks overlap indicating that the admittance measured for both tasks are equal. This suggests that the wide bandwidth disturbance torque succeeded in suppressing reflexive activity. It is therefore assumed that reflexes were also suppressed for the other conditions and admittance data from these conditions can be used to optimize haptic cues for the HCAS (Smisek et al., 2013). Additionally, Figure 2-18 shows that the admittance along the longitudinal axes is lower than for the lateral axes, an effect that has been reported by other literature, see section 2-3-1.

The experimental admittance data averaged over all subjects is used to verify the novel tuning procedure in chapter 3 through an offline simulation, and subsequently to validate it with a human-in-the- loop experiment described in chapter 4.

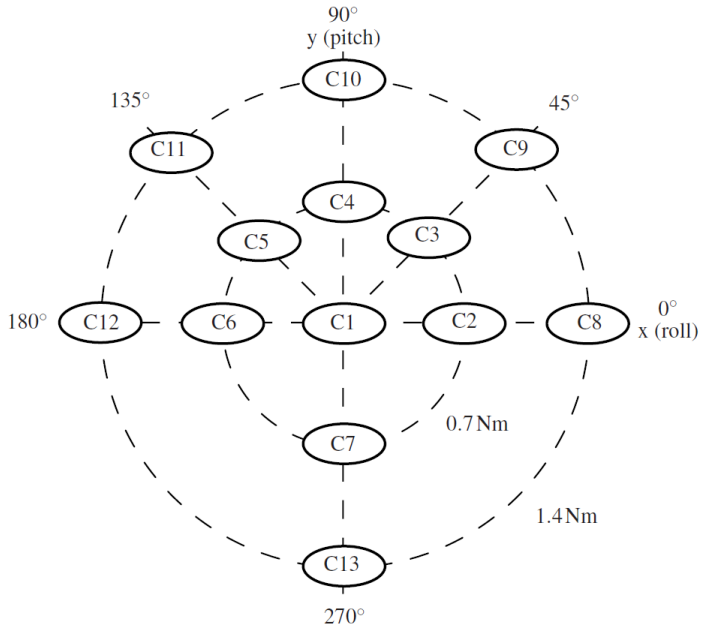

Figure 2-17: Thirteen bias moment conditions of the experiment (Smisek et al., 2013). Note that relax and force task admittances were measured for the central condition C1.

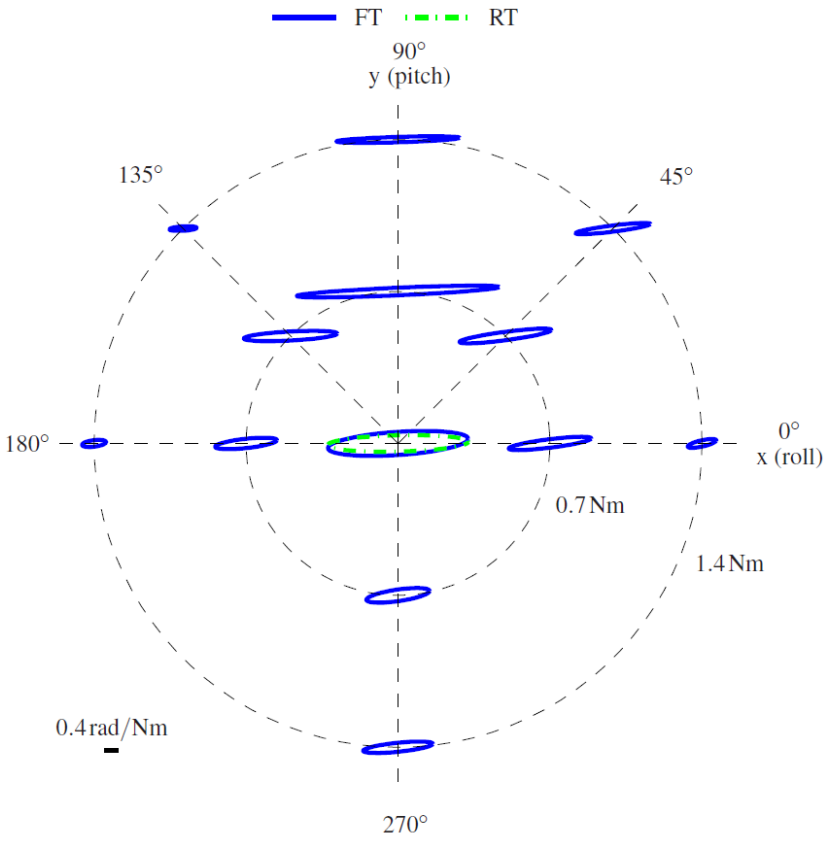

Figure 2-18: Admittance ellipse displaying longitudinal and lateral admittances for one subject at $f_{dist} = 0.7Hz$ (Smisek et al., 2013). Note that the relax task and the force task admittances are equal for the central condition. This means that reflexive activity has been suppressed by the wide bandwidth disturbance torque and thus relax task admittance can be considered equal to that of the force task for all conditions.

Chapter 3

Modeling and Simulating Pilot-Controller Haptic Interaction

From the literature review presented in chapter 2, it is clear that the pilot-controller haptic interaction is central to the optimal tuning of haptic shared control (HSC) systems. Therefore, it is necessary to analyze how variations in the pilot neuromuscular system (NMS) and different tuning profiles of the haptic controller affect the total system response. In addition, an initial verification of the tuning procedure proposed by Smisek (Smisek et al., 2013), see section 2-3-2, is required before validating it with a human-in-the-loop experiment. For these reasons, in this chapter, the pilot-controller haptic interaction is investigated on a theoretical level through offline Simulink simulations, and the results of the simulation form the basis for the experiment proposal presented in chapter 4.

The chapter begins by discussing the main scientific goals of the simulation as well as the resulting simulation architecture. This is followed in section 3-2 with detailed descriptions of the simulation components, in particular that of the haptic collision avoidance system (HCAS). In section 3-3, the specific conditions of the simulation and the evaluation criteria for the haptic interaction are presented. The chapter concludes with the results of the simulation, and their analysis in section 3-4.

3-1 Simulation Goals and Overall Architecture

As stated in section 2-1-1, Abbink (D. Abbink et al., 2012) and Cleij (Cleij, 2011) argue that haptic shared controlled systems can be decomposed into two mappings for both the pilot and the haptic shared controller. The first mapping considers the cognitive process of selecting the desired steering angle based on environmental cues, and is referred to as visual control. The second mapping involves the translation of these desired steering angles to haptic guidance forces on the control inceptor, known as haptic control.

The tuning of this haptic interaction between the pilot NMS and the haptic controller i.e., the tuning of the second mapping, is the topic of this thesis, and thus also corresponds to the scientific goals of the simulation. The simulation goals can be stated more specifically as:

1. An investigation of the sensitivity of the total haptic collision avoidance system (HCAS) to varying pilot NMS and haptic controller settings[1] and,
2. A verification of the NMS admittance based tuning procedure of the haptic controller using experimentally compiled admittance data by Smisek (Smisek et al., 2013).

To comply with the simulation goals listed above, the visual feedback pilots receive in reality i.e., the first mapping of HSC for the pilot, has to be suppressed in the simulation. By doing so, the simulated pilot has to rely solely on haptic feedback to avoid obstacles in the environment, thus isolating the effects of the second mapping when analyzing the results of the simulation. These considerations result in the overall simulation architecture displayed in Figure 3-1.

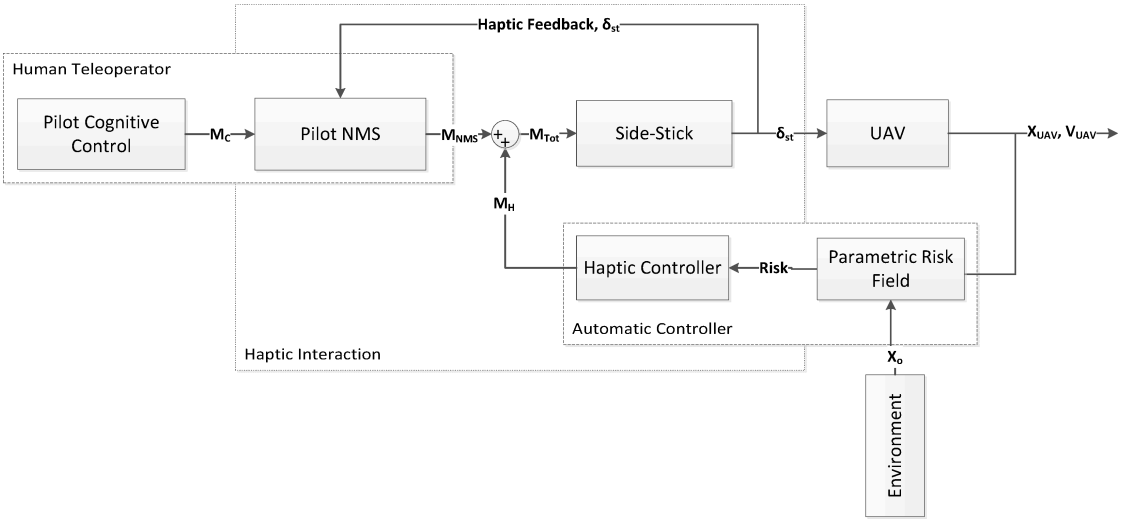

Figure 3-1: Overall simulation architecture. This scheme is similar to reality, however, the visual feedback loop to the pilot is deliberately removed to ensure that only the second mapping of HSC is modeled.

As can be seen from Figure 3-1, the input to the simulation is the so called 'pilot cognitive control' block. This block computes the constant control moment, M_c, necessary to maintain a predetermined fixed velocity and yaw rate in the absence of haptic feedback. In the feed-forward direction, other simulation components include the pilot NMS, side-stick and UAV dynamics.

The simulation architecture contains two feedback paths. The first feedback path contains two elements, the parametric risk field (PRF) and the haptic controller, which together comprises the haptic collision avoidance system (HCAS). The PRF computes the risk of obstacle

[1]Here, the settings of the NMS and haptic controller corresponds to that of the force, relax and position task instructions commonly used in haptic research, see section 2-3-1 for more detail.

collisions based on the relative position and velocity of the UAV to the surrounding environment. The risk of collision is converted to a haptic moment, M_H, that is applied on the side-stick by the haptic controller. The second feedback path constitutes the haptic feedback experienced by the pilot NMS due to differences between the expected and actual stick position, δ_{st}. Further details of all the simulation components pictured in Figure 3-1 are described in section 3-2.

3-2 Modeling Simulation Components

In this section, detailed descriptions of the simulation components and their associated models are elaborated on. Furthermore, whenever appropriate, details of the Simulink implementation of the models are also presented. Figure 3-2 below depicts the complete simulation architecture as implemented in the Simulink file `tuning_simulation.mdl`.

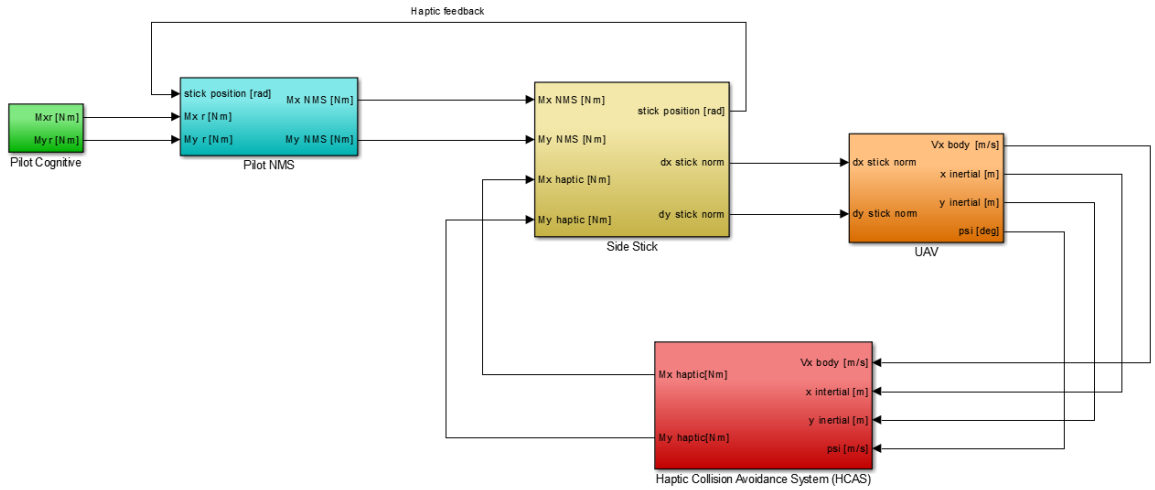

Figure 3-2: Simulink implementation of the simulation architecture. The implementation has the same basic structure as the architecture illustrated in Figure 3-1. Note that the HCAS block contains both the parametric risk field (PRF) and the haptic controller.

3-2-1 Pilot Cognitive Control

The 'Pilot Cognitive Control' block forms the input or forcing function of the simulation and can be thought of as a simple simulated pilot. As mentioned in section 3-1, the simulated pilot does not receive visual feedback of the UAV states or the environment and therefore has to rely solely on haptic feedback to avoid obstacles. In fact, the 'Pilot Cognitive Control' block represents the open loop control inputs necessary to maintain the constant desired body velocity and yaw rate in an obstacle free environment.

The simplified simulated pilot is modeled by assuming that the pilot has a perfect internal representation of the side-stick and UAV dynamics (see section 3-2-3). Based on this assumption, the longitudinal, $\delta_{X'}$, and lateral, $\delta_{Y'}$, stick deflections needed to maintain the desired body velocity, $V_{X'_{des}}$, and yaw rate, $\dot{\psi}_{des}$, are given by Eqs. 3-1 and 3-2 respectively. From

the required stick deflections, the final outputs of the 'Pilot Cognitive Control' block, the required stick moments, $M_{C_{X'}}$ and $M_{C_{Y'}}$, can be computed using Eqs. 3-3 and 3-4.

$$\delta_{X'} = \frac{V_{X'_{des}}}{V_{max}} \cdot \delta_{X'_{max}} \tag{3-1}$$

$$\delta_{Y'} = \frac{\dot{\psi}_{des}}{\dot{\psi}_{max}} \cdot \delta_{Y'_{max}} \tag{3-2}$$

$$M_{C_{X'}} = \delta_{X'} \cdot K_{st} \tag{3-3}$$

$$M_{C_{Y'}} = \delta_{Y'} \cdot K_{st} \tag{3-4}$$

Here V_{max} is the maximum UAV velocity in m/s, $\dot{\psi}_{max}$ is the maximum UAV yaw rate in rad/s, $\delta_{X'_{max}}$ is the maximum longitudinal stick deflection in rad, $\delta_{Y'_{max}}$ is the maximum lateral stick deflection in rad and K_{st} is the stick spring stiffness in Nm/rad. The values of these parameters are given in section 3-2-3 where the stick and UAV dynamics are explained further. Note that parameters with the subscript ' are defined in the rotating body reference frame.

As the control strategy of the simplified simulated pilot remains constant in time, the 'Pilot Cognitive Control' is implemented in Simulink using 'Constant' blocks with values corresponding to $M_{c_{X'}}$ and $M_{c_{Y'}}$ given by Eqs. 3-3 and 3-4 respectively. It should be noted that if no haptic moments were to be supplied by the HCAS, $M_{c_{X'}}$ and $M_{c_{Y'}}$ would cause the UAV to travel with the constant desired body velocity and yaw rate.

3-2-2 Pilot Neuromuscular Model

The pilot neuromuscular model simulates the dynamics of the muscles and skeletal bones of the human arm and hand. A model developed by de Vlugt is used in the simulation (Vlugt et al., 2006). By varying the model parameters, it is possible to simulate the pilot's response to the three haptic task instructions i.e., the force, relax and position tasks. In this subsection, a brief overview of the model as well as minor modifications necessary for its implementation in the simulation will be discussed.

Figure 3-3 displays the block diagram of the pilot NMS model used in the simulation. The muscle buildup of the commanded moment, M_C, is given by the 'Activation Dynamics' block. The arm inertia is modeled by the 'Inertia' block, and the intrinsic muscle stiffness and damping are described by the 'Intrinsic Feedback' block. The 'Grip Dynamics' block simulates the spring-damper characteristics of the hand tissue in contact with the side-stick. It is important to note that the actual side-stick position, δ_{st}, comprises the simulated haptic feedback to the NMS model. The side-stick position is in turn affected by the output of the NMS, M_{NMS}, and the haptic feedback moment, M_H, from the haptic controller.

When comparing Figure 3-3 and the model introduced by de Vlugt, it can be seen that there are two main differences. The first difference originates from the constant activation of the muscles in the simulation due to the constant control strategy employed by the simplified simulated pilot (see section 3-2-1). Since reflexive muscle action is a result of non-constant muscle activation (Lasschuit et al., 2008), the reflexive feedback paths of the muscle spindles

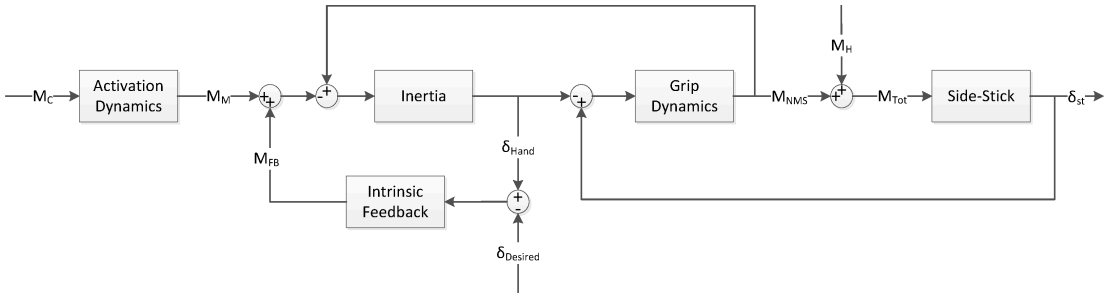

Figure 3-3: Pilot neuromuscular system model used in the simulation adopted from de Vlugt (Vlugt et al., 2006). Note that reflexive feedback paths have been neglected and that intrinsic feedback is centered around the desired hand deflection.

and GTO are neglected in the simulation. The second difference between the two NMS models is that the intrinsic feedback moment, M_{FB}, is centered around the desired hand deflection, $\delta_{Desired}$, and not around the actual hand deflection, δ_{Hand}[2]. This is of particular importance when the simulation is run at non-zero initial velocities and/or yaw rates, implying non-zero initial hand deflections.

Equations 3-5 to 3-8 below describe the dynamics of the model components pictured in Figure 3-3:

$$H_{activation}(s) = \frac{M_M}{M_C} = \frac{1}{\frac{1}{\omega_0^2}s^2 + \frac{2\beta}{\omega_0}s + 1} \tag{3-5}$$

$$H_{intertia}(s) = \frac{\delta_{hand}}{M_{NMS} - M_M - M_{FB}} = \frac{1}{I_i s^2} \tag{3-6}$$

$$H_{intrinsic}(s) = \frac{M_{FB}}{\delta_{Hand} - \delta_{Desired}} = B_i s + K_i \tag{3-7}$$

$$H_{grip}(s) = \frac{M_{NMS}}{\delta_{st} - \delta_{Hand}} = B_g s + K_g \tag{3-8}$$

Here 's' is the laplace operator, ω_0 is the natural frequency of the muscles and equals 2.2 Hz (13.82 rad/s) (Schouten, 2004), and β is the damping ratio of the muscles and equals $\sqrt{2}/2$. The inertia of the arm, I_i, as well as the stiffness(Nms^2/rad) and damping (Nms/rad) of the intrinsic feedback, K_i and B_i, and grip dynamics, K_g and B_g, were measured experimentally by Lasschuit (Lasschuit et al., 2008) for the relax task neuromuscular task instruction and are given by equations 3-10 to 3-13. Note that subscripts 'p' and 'r' represent the pitch and roll parameters respectively.

[2]The desired hand deflection is equal to the desired side-stick deflection, equations 3-1 and 3-2, due to the physical connection between the hand and the side-stick.

$$I_i = \begin{bmatrix} I_{i_p} & 0 \\ 0 & I_{i_r} \end{bmatrix} = \begin{bmatrix} 0.0147 & 0 \\ 0 & 0.0077 \end{bmatrix} \tag{3-9}$$

$$K_i = \begin{bmatrix} K_{i_p} & 0 \\ 0 & K_{i_r} \end{bmatrix} = \begin{bmatrix} 9.2034 & 0 \\ 0 & 1.2050 \end{bmatrix} \tag{3-10}$$

$$B_i = \begin{bmatrix} B_{i_p} & 0 \\ 0 & B_{i_r} \end{bmatrix} = \begin{bmatrix} 0.5052 & 0 \\ 0 & 0.0574 \end{bmatrix} \tag{3-11}$$

$$K_g = \begin{bmatrix} K_{g_p} & 0 \\ 0 & K_{g_r} \end{bmatrix} = \begin{bmatrix} 298.4789 & 0 \\ 0 & 163.2491 \end{bmatrix} \tag{3-12}$$

$$B_g = \begin{bmatrix} B_{g_p} & 0 \\ 0 & B_{g_r} \end{bmatrix} = \begin{bmatrix} 2.5046 & 0 \\ 0 & 2.0268 \end{bmatrix} \tag{3-13}$$

To simulate the NMS model for the force and position neuromuscular task instructions, the stiffness and damping parameters[3] of the relax task, given by equations 3-11 to 3-13, are multiplied by a gain of 0.5 and 7.0 respectively.The rationale behind this method is explained in section 3-2-5.

As a final note, the Simulink implementation of the NMS model is separated in the longitudinal and lateral directions to take into account the differences between the model parameters along the two directions.

3-2-3 Side-Stick and UAV dynamics

The side-stick and UAV dynamics modeled in the simulation are identical to those used by Lam (T. Lam, Mulder, & Paassen, 2009) (T. Lam, 2009) (T. Lam, Mulder, Paassen, & Helm, 2005), however a brief overview of the important characteristics of both these components are discussed in this sub-section.

The moments exerted by the pilot NMS, M_{NMS}, and the haptic controller, M_H, are applied on the side-stick, and the resultant position of the side-stick is the sole input to the UAV dynamics, see Figures 3-1 and 3-2. Although Lam used a second order mass-spring-damper system to represent the side-stick dynamics, a simple linear spring model is used here to represent the side-stick in the simulation, see equation 3-14. This linear spring model is equivalent to the more complex second order dynamics at the low signal frequencies that are experienced in the simulation.

$$\delta_{st} = \frac{M_{Tot}}{K_{st}} \tag{3-14}$$

[3]Note that the arm inertia remains constant for all three neuromuscular task instructions.

In equation 3-14, K_{st} is the stiffness of the side-stick and equals 2.0 Nm/rad in both the longitudinal and lateral directions. The maximum side-stick deflection in the longitudinal direction, $\delta_{X'_{max}}$, is simulated to equal 0.35 rad. In the lateral direction, the maximum deflection of the stick, $\delta_{Y'_{max}}$, is limited to 0.40 rad. These values correspond to the actual physical limitations of the side-stick used to determine NMS admittance by Smisek (Smisek et al., 2013).

The UAV is modeled as a control augmented helicopter with easy-to-control dynamics in the horizontal plane[4]. Positive longitudinal side-stick inputs are mapped to velocity commands along the positive body X' axis, whereas positive lateral side-stick inputs correspond to counter-clockwise yaw rate commands around the body Z'-axis, and are described through Eqs. 3-15 and 3-16 respectively.

$$H_{X'_{UAV}}(s) = \frac{V_{X'}}{\delta_{X'}} = \frac{1}{(0.3s+1)(0.18s+1)} \tag{3-15}$$

$$H_{Y'_{UAV}}(s) = \frac{\dot{\psi}}{\delta_{Y'}} = \frac{1}{(0.2s+1)} \tag{3-16}$$

In equations Eqs. 3-15 and 3-16, 's' is the Laplace operator. In addition to the above dynamics, the UAV has a maximum velocity, V_{max}, and acceleration, a_{max}, of 5.0 m/s and 1.0 m/s^2 in the longitudinal direction, and a maximum yaw rate, $\dot{\psi}_{max}$, and acceleration, $\ddot{\psi}_{max}$, of 0.32 rad/s and 2.0 rad/s^2 in the lateral direction. Figure 3-4(a) displays the rotating body reference frame along which UAV commands are defined and Figure 3-4(b) shows the relationship between side-stick inputs and UAV motion.

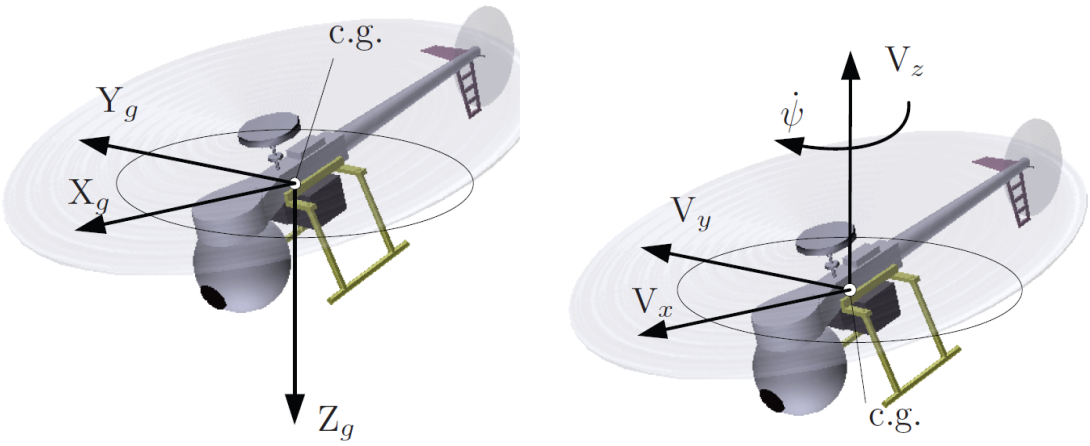

(a) Rotating body reference frame

(b) UAV commands and corresponding motion

Figure 3-4: UAV model used in the simulation (T. Lam, Mulder, & Paassen, 2009)

A block diagram description of the complete UAV dynamics is displayed in Figure 3-5. The blocks 'Cartesian to Polar' and 'Polar to Cartesian' compute the transformations needed to move from the inputs ($V_{X'}$, ψ) defined in the rotating body frame to the UAV sates ($\dot{x}$, $\dot{y}$)

[4]The simulation, as well as this thesis, only considers motion of the UAV along the horizontal plane. It is assumed that the altitude of the UAV is held constant by an altitude hold control augmentation system.

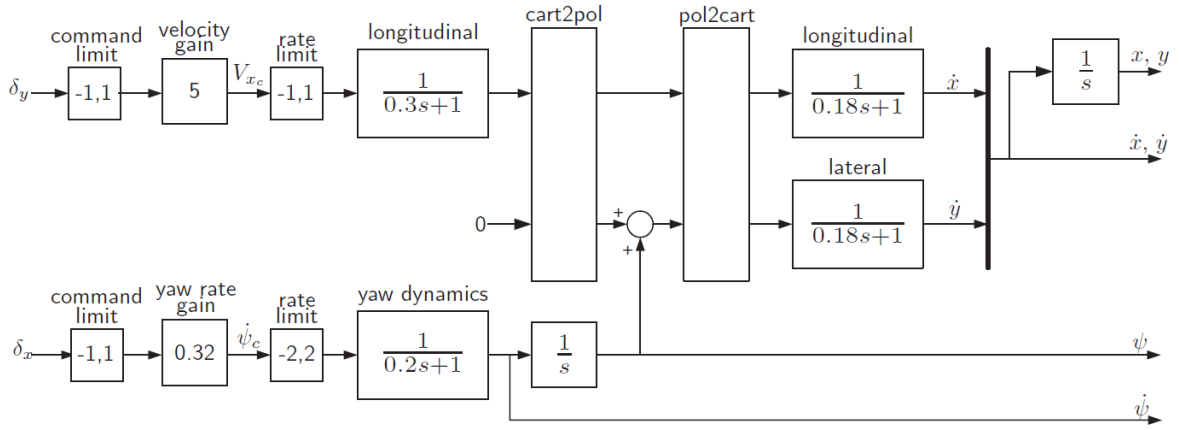

Figure 3-5: Block diagram of the complete UAV Dynamics (T. Lam, Mulder, & Paassen, 2009). The Simulink implementation of the UAV dynamics is identical to this scheme.

defined in the inertial reference frame. The Cartesian to Polar transformation is given by Eqs. 3-17 and 3-18 and its inverse is given by Eqs.3-19 and 3-20 (Stewart, 2007).

$$V_{X'}{}^2 = \dot{x}^2 + \dot{y}^2 \tag{3-17}$$

$$\psi = \arctan(\dot{y}, \dot{x}) \tag{3-18}$$

$$\dot{x} = V_{X'} \cdot \cos\psi \tag{3-19}$$

$$\dot{y} = V_{X'} \cdot \sin\psi \tag{3-20}$$

The inertial velocities ($\dot{x}$,$\dot{y}$) obtained after the reference frame transformations are subsequently integrated to obtain the inertial positions (x,y). It should be noted that normalized side-stick positions are used as inputs to the 'UAV' block. Normalized side-stick positions can be easily computed by dividing the actual side-stick positions by the physical side-stick limits.

3-2-4 Parametric Risk Field

The Parametric Risk Field (PRF) is one of two components that make up the Haptic Collision Avoidance System (HCAS). The PRF is a type of Artificial Force Field (AFF) that scans the environment around the UAV and computes the risk i.e., the probability $E[0,1]$, of collisions with surrounding obstacles. For this reason, the PRF can be thought of as the (automated) visual controller in the HCAS architecture. This sub-section is divided into two parts. In the first part, the sensor model used to detect obstacles is explained. In the second part, the mathematical steps needed to implement the PRF and the sensor model are discussed in detail.

LiDAR Based Sensor Model

To detect obstacles in the virtual environment of the simulation, a simulated sensor model is needed. The sensor model used in the simulation works similarly to Light Detection And

Ranging, commonly known as LiDAR. In LiDAR, a single rotating ray of light is used to detect objects by measuring the time taken for the emitted ray to return to the sensor after being reflected by objects. One of the important properties of LiDAR is that only objects in direct Line of Sight (LoS) to the light ray can be detected. This same property is exhibited by the simulated sensor, however, instead of using a single rotating ray, several rays with a fixed angular resolution are used to scan 360^o degrees around the UAV to detect all surrounding objects simultaneously. Figure 3-6 displays the working principle of the simulated sensor.

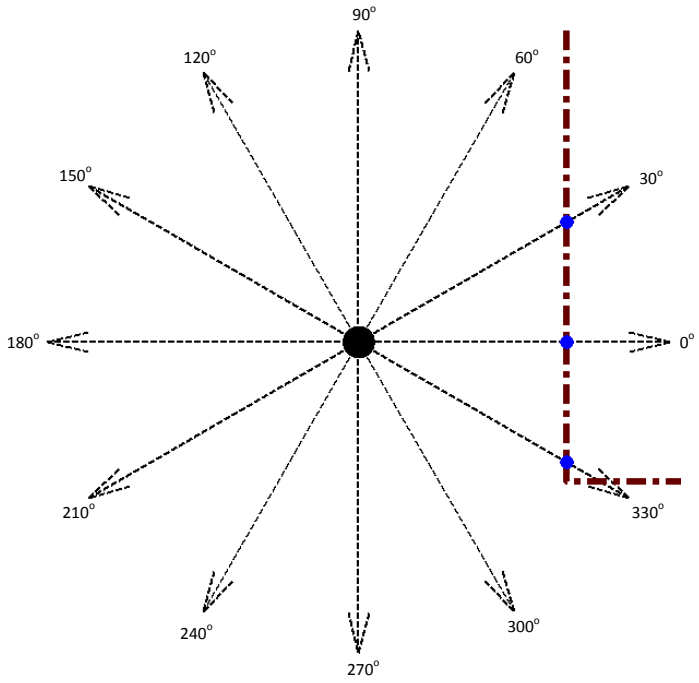

Figure 3-6: LiDAR based simulated sensor model. Intersections between the sensor rays and the object are displayed as blue dots representing the 'discrete' obstacles detected by the sensor.

Due to the fixed angular spacing between the sensor rays, continuous objects such as the 'L' shaped wall (brown dot-dashed line) pictured in Figure 3-6 are detected as a number of discrete objects (blue dots). Furthermore, for the ray at 330^o, only the closest part of the wall is detected, preserving the LoS property of LiDAR. This is important as it ensures that only the risk of collision with the closest obstacle along a sensor ray is computed. In the simulation, a sensor with an angular resolution of 3^o (resulting in 120 sensor rays) and a range of 50 meters is used.

Once obstacles around the UAV are detected, the risk of collisions between the UAV and the obstacles can be computed. This is done by mapping the PRF onto the sensor rays such that the geometry of the PRF is discretized along each sensor ray. This is made clearer in Figure 3-7 where the discretization of the PRF boundary locations along a single sensor ray (at 7.5^o) is pictured. By comparing the distances along a ray to the boundaries of zone 1, R_1, and zone 2, R_2, to the distance of the discrete obstacle, R_O, the risk of collision for each ray can be computed using the PRF equations introduced in section 2-2-2.

It is important to note that the PRF geometry is dependent on a number of parameters including the instantaneous velocity, V, of the UAV. Therefore it is necessary to re-compute the locations of the PRF zone boundaries along each sensor ray at every simulation time step. For more details regarding the variation of the PRF geometry with velocity, including the governing equations, see section 2-2-2.

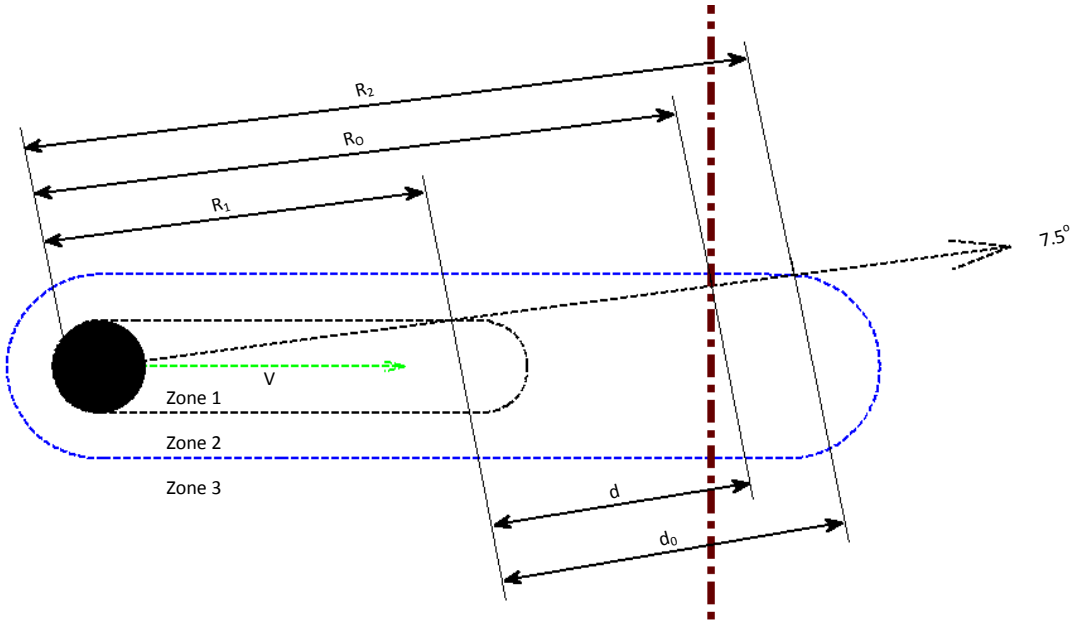

Figure 3-7: Discretization of the Parametric Risk Field geometry along a sensor ray. The risk of collision for a particular ray can be computed by comparing the distances to the zone boundaries, R_1 and R_2, to the distance of the 'discrete' obstacle, R_O.

Mathematical Implementation of the Parametric Risk Field

The mathematical implementation of the PRF and the sensor model can be divided into seven steps listed below:

1. Discrete sensor model implementation
2. Determination of Parametric Risk Field boundary locations along each sensor ray
3. Rotation of sensor ray definitions to match UAV heading
4. Detection and ranging of obstacles along each sensor ray
5. Computation of 'discrete' obstacle risk for each sensor ray
6. Computation of risk vector in inertial reference frame
7. Projection of final collision avoidance risk vector along body reference frame axes

Step 1: Discrete sensor model implementation

As stated earlier, the sensor model consists of several rays with a constant angular resolution. The angular resolution of the sensor, β, is dependent on the number of rays, n_{rays}, through the following relation:

$$\beta = \frac{360^o}{n_{rays}} \tag{3-21}$$

Each sensor ray is identified/defined by its heading, ψ_{ray}, in the body reference frame, see Figure 3-6. In the simulation, a sensor with $\beta = 3^o$ (n_{rays} =120) and a range, d_{ray}, of 50 meters is used. Mathematically each sensor ray can be represented as a vector line equation, $\vec{V}_{ray}$:

$$\vec{V}_{ray} = \vec{P}_{UAV} + t \cdot \left(\vec{P}_{UAV} - \vec{P}_{ray_{end}}\right) \tag{3-22}$$

Here $\vec{P}_{UAV}$ is the position vector of the UAV, which is also equal to the position vector of the start of all sensor rays. $\vec{P}_{ray_{end}}$ is the position vector of the (arrow) end of a sensor ray and is given by equation 3-23 below:

$$\vec{P}_{ray_{end}} = \vec{P}_{UAV} + d_{rays} \cdot \begin{bmatrix} \cos(\psi_{ray}) \\ \sin(\psi_{ray}) \end{bmatrix} \tag{3-23}$$

By ensuring that the variable t E[0,1], it is possible to ensure that the physical range of the ray, d_{ray}, is not exceeded when using equation 3-22.

Step 2: Determination of Parametric Risk Field boundary locations along each sensor ray

To map the PRF geometry onto the sensor rays, it is necessary to determine the distance to the boundaries of zone 1, R_1, and zone 2, R_2, along each ray, see Figure 3-7. Due to the circular shape of the PRF zones, R_1 and R_2 are dependent on the heading angle of each ray, ψ_{ray}. In fact, there are five different cases of ψ_{ray} which determine R_1 and R_2:

1. $\psi_{ray} = 0^o$
2. $0^o < \psi_{ray} < \theta$
3. $\theta \leq \psi_{ray} < 90^o$
4. $90^o \leq \psi_{ray} \leq 180^o$
5. $180^o < \psi_{ray} < 360^o$

Here θ for zone 1 and 2 are given by equations 3-24 and 3-25 respectively and can be visualized in Figure 3-8.

$$\theta_1 = \arctan\left[\frac{r_{pz}}{d_{stop}}\right] \tag{3-24}$$

$$\theta_2 = \arctan\left[\frac{r_{pz} + d_{min}}{d_{stop} + d_{ahead}}\right] \tag{3-25}$$

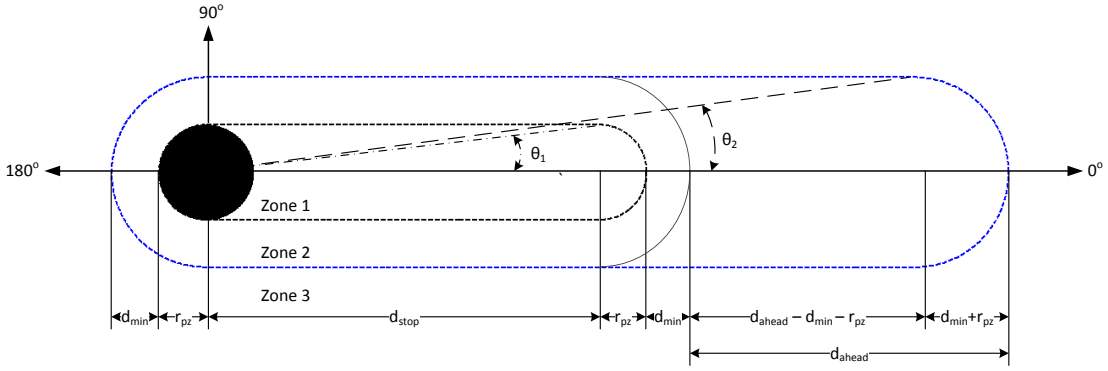

Figure 3-8: Determination of Parametric Risk Field boundary locations along each sensor ray

The equations to determine R_1 and R_2 for all five cases are presented in Table 3-1. These equations are derived using simple geometric relations from Figure 3-8. Note that R_1 and R_2 for case 5 is simply that of cases 1-4 in reverse. This is because the PRF is symmetric along the inertial X axis ($\psi = 0^o$).

Table 3-1: Equations to determine zone boundary distances, R_1 and R_2, for a particular ray, for each of the five cases

Case	Condition	Zone 1	Zone 2
1	$\psi_{ray} = 0^o$	$R_1 = r_{pz} + d_{stop}$	$R_1 = r_{pz} + d_{stop} + d_{min} + d_{ahead}$
2	$0^o < \psi_{ray} < \theta$	$\alpha_1 = \arcsin\left[\frac{d_{stop}\sin(\psi_{ray})}{r_{pz}}\right]$ $\gamma_1 = 180^o - \psi_{ray} - \alpha_1$ $R_1 = r_{pz}\left[\frac{\sin(\gamma_1)}{\sin(\psi_{ray})}\right]$	$\alpha_2 = \arcsin\left[\frac{(d_{stop}+d_{ahead})\sin(\psi_{ray})}{r_{pz}+d_{min}}\right]$ $\gamma_2 = 180^o - \psi_{ray} - \alpha_2$ $R_2 = (r_{pz} + d_{min})\left[\frac{\sin(\gamma_1)}{\sin(\psi_{ray})}\right]$
3	$\theta \leq \psi_{ray} < 90^o$	$R_1 = \frac{r_{pz}}{\sin(\psi_{ray})}$	$R_2 = \frac{r_{pz}+d_{min}}{\sin(\psi_{ray})}$
4	$90^o \leq \psi_{ray} \leq 180^o$	$R_1 = r_{pz}$	$R_2 = r_{pz} + d_{min}$
5	$180^o < \psi_{ray} < 360^o$	$R_{1(180^o-360^o)} = R_{1(180^o-0^o)}$	$R_{2(180^o-360^o)} = R_{2(180^o-0^o)}$

As a final note, R_1 and R_2 are calculated in this step assuming that $\psi_{UAV} = 0$. In step 3, the modification necessary to compute R_1 and R_2 for $\psi_{UAV} \neq 0$ is given.

Step 3: Rotation of sensor ray definitions to match UAV heading

The ray definitions described in step 1, ψ_{ray}, must be rotated to take into account the heading of the UAV, ψ_{UAV}, so that the PRF geometry is aligned with the UAV velocity vector, $V_{X'}$. This can be visualized in Figure 3-9. In this figure, the two sensor rays shown are rotated by ψ_{UAV}, however, it can also be seen that this ray definition rotation does not affect the zone boundary distances along a particular sensor ray. The ray definition rotation can be described mathematically through equation 3-26.

$$\psi_{ray,rotated} = \psi_{ray} + \psi_{UAV} \tag{3-26}$$

It is theoretically possible to take into account the heading of the UAV, ψ_{UAV}, when defining the ray definitions in step 1. However it is easier to visualize the five cases for computing the zone boundary distances along a particular ray if $\psi_{UAV} = 0$ (see step 2). Equation 3-27 can be used to ensure that the rotated ray definitions, $\psi_{ray,rotated}$, lie in the interval $0^o - 360^o$:

$$\psi_{ray,adjusted} = \psi_{ray,rotated} - \left[floor \left(\frac{\psi_{ray,rotated}}{360^o} \right) \cdot 360^o \right] \tag{3-27}$$

Here the function 'Floor' rounds the quotient of the fraction $\frac{\psi_{ray,rotated}}{360^o}$ down to the nearest integer.

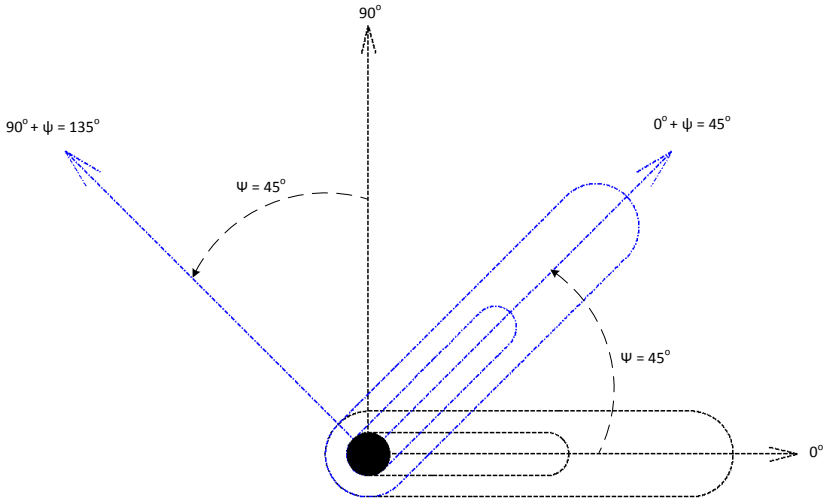

Figure 3-9: Rotation of sensor ray definitions to take into account UAV heading, ψ

Step 4: Detection and ranging of obstacles along each sensor ray

The location of a 'discrete' obstacle along a particular sensor ray can be computed by finding the intersection point of the sensor ray and obstacle vector line equations, see Figure 3-7. In step 1, the vector line equation of a sensor ray is given by equation 3-22. Similarly, the vector line equation of an obstacle line segment is given by equation 3-28.

$$\vec{V}_{obs} = \vec{P}_{obs_{start}} + r \cdot \left(\vec{P}_{obs_{start}} - \vec{P}_{obs_{end}} \right) \tag{3-28}$$

By equating equations 3-22 and 3-28, and solving the resulting simultaneous equation, the position vector, $\vec{P_D}$, of a discrete obstacle along a particular sensor ray can be computed. The distance between the discrete obstacle and the UAV, R_O, can then be computed using equation 3-29:

$$R_O = \left\| \vec{P}_{UAV} - \vec{P}_D \right\| \tag{3-29}$$

When using the methodology described in this step, two additional factors must be taken into account. Firstly, when computing $\vec{P_D}$ by simultaneously solving equations 3-22 and 3-28, it is important to ensure that the variables 't' and 'r' both have a value between 0 and 1. This is to make sure that the physical dimensions of the sensor rays and obstacle line segments are taken into account when detecting obstacles in the environment. Secondly, to maintain the LoS property of LiDAR, the intersection between all ray-obstacle combinations have to be computed. The final location of a discrete obstacle on a particular sensor ray is the intersection point, $\vec{P_D}$, with the smallest distance from the UAV.

Step 5: Computation of 'discrete' obstacle risk for each sensor ray

The risk of collision for each sensor ray, R_{ray}, can be determined by comparing the location of a ray's 'discrete' obstacle, R_O, to its zone boundary locations, R_1 and R_2. Table 3-2 summarizes how this position comparison can be translated to a risk value based on the PRF equations defined by Boschloo (Boschloo et al., 2004) and Lam (T. Lam, Boschloo, et al., 2009).

Table 3-2: Determination of the collision risk for each sensor ray based on the location of a 'discrete' obstacle within the PRF

Case	Condition	Obstacle Zone	Risk
1	$R_O \leq R_1$	1	$R_{ray} = 1$
2	$R_1 < R_O \leq R_2$	2	$R_{ray} = \cos\left(\frac{d}{d_0} \cdot 180^o + 180^o\right) + 1$
3	$R_O > R_2$	3	$R_{ray} = 0$

As can be seen from Table 3-2, to compute the risk of obstacles in zone 2, two additional distances are needed to evaluate the shifted cosine function, d and d_0. These two distances are defined by equations 3-30 and 3-31 respectively and can be visualized in Figure 3-7.

$$d = |R_O - R_1| \tag{3-30}$$

$$d_0 = |R_2 - R_1| \tag{3-31}$$

Step 6: Computation of risk vector in inertial reference frame

In addition to calculating the scalar risk value, R_{ray}, it is also necessary to compute the risk vector for each sensor ray, $\vec{R}_{ray}$. $\vec{R}_{ray}$ for a particular sensor ray can be computed easily by multiplying its negative unit vector[5], $-\hat{V}_{ray}$, and scalar risk value, R_{ray}, see equation 3-32.

$$\vec{R}_{ray} = \underbrace{-\hat{V}_{ray}}_{direction} \cdot \underbrace{R_{ray}}_{magnitude} \tag{3-32}$$

The final collision avoidance risk vector components along the inertial X and Y axes, $\vec{R}_X$ and $\vec{R}_Y$, can then be found by combining the risk vectors for all rays using the Max-Min method. In the Max-Min method, the largest and smallest X and Y components of all the risk vectors (in the inertial frame) are summed as can be seen in equations 3-33 and 3-34. Here the subscript i indicates that the 'Max' and 'Min' functions apply to the risk vectors of all sensor rays.

$$\vec{R}_X = Max\left(\vec{R}_{ray_{X,i}}\right) + Min\left(\vec{R}_{ray_{X,i}}\right) \tag{3-33}$$

$$\vec{R}_Y = Max\left(\vec{R}_{ray_{Y,i}}\right) + Min\left(\vec{R}_{ray_{Y,i}}\right) \tag{3-34}$$

$\vec{R}_X$ and $\vec{R}_X$ can be summed vectorially to compute the the final collision avoidance risk vector, $\vec{R}$, in the inertial reference frame:

$$\vec{R} = \vec{R}_X + \vec{R}_Y \tag{3-35}$$

$\vec{R}$ can be visualized as the solid red arrow in Figure 3-10. Due to the summation used to compute $\vec{R}$, it is necessary to ensure that $\left|\vec{R}\right| \leq 1$ such that the risk/probability of collision is always less than or equal to 1. .

Step 7: Projection of final collision avoidance risk vector along body reference frame axes

As inputs to the UAV are given in the rotating body reference frame (see section 3-2-3), the risk vector $\vec{R}$ computed in step 6 has to be projected along the rotating body axes, X' and Y'. The rotating body reference frame is simply the inertial reference frame X and Y axes rotated around the inertial Z axis by the heading angle of the UAV, ψ_{UAV}. Therefore, unit vectors along X' and Y', $\hat{x'}$ and $\hat{y'}$, can be found by rotating unit vectors along X and Y, $\hat{x}$ and $\hat{y}$, with the rotation matrix Θ:

$$\hat{x'} = \Theta \cdot \hat{x} = \begin{bmatrix} \cos(\psi_{UAV}) & -sin(\psi_{UAV}) \\ \sin(\psi_{UAV}) & \cos(\psi_{UAV}) \end{bmatrix} \cdot \begin{bmatrix} 1 \\ 0 \end{bmatrix} = \begin{bmatrix} \cos(\psi_{UAV}) \\ \sin(\psi_{UAV}) \end{bmatrix} \tag{3-36}$$

[5]The negative sign is necessary because risk vectors are directed in the opposite direction to sensor rays.

$$\hat{y'} = \Theta \cdot \hat{y} = \begin{bmatrix} \cos(\psi_{UAV}) & -sin(\psi_{UAV}) \\ \sin(\psi_{UAV}) & \cos(\psi_{UAV}) \end{bmatrix} \cdot \begin{bmatrix} 0 \\ 1 \end{bmatrix} = \begin{bmatrix} -sin(\psi_{UAV}) \\ \cos(\psi_{UAV}) \end{bmatrix} \tag{3-37}$$

As with the rest of the simulation, counter-clockwise rotations of ψ_{UAV} are considered positive. Using the above definitions of $\hat{x'}$ and $\hat{y'}$, the projection of $\vec{R}$ along X' and Y' can be calculated using equations 3-38 and 3-39 respectively. Here $\bullet$ represents the scalar product of two vectors.

$$\vec{R}_{X'} = proj_{\hat{x'}} R_X = \frac{\vec{R}_X \bullet \hat{x'}}{\left\|\hat{x'}\right\|} \hat{x'} \tag{3-38}$$

$$\vec{R}_{Y'} = proj_{\hat{y'}} R_Y = \frac{\vec{R}_Y \bullet \hat{y'}}{\left\|\hat{y'}\right\|} \hat{y'} \tag{3-39}$$

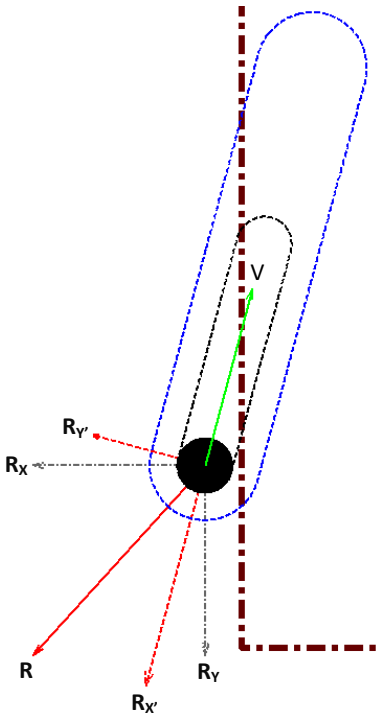

Figure 3-10: Final risk vector along body (red dashed arrows) and inertial axes (gray dashed arrows). The direction and magnitude of $R_{X'}$ and $R_{Y'}$ is a direct indication of how the UAV has to be steered to avoid obstacles.

The differences between the inertial reference frame (gray dashed arrows) and the rotating body reference frame (red dashed arrows) components of $\vec{R}$ can be clearly seen in Figure 3-10. The direction of $\vec{R}_{X'}$ and $\vec{R}_{Y'}$ with respect to X' and Y' can be determined by comparing

the signs (positive or negative) of the components of $\vec{R}_{X'}$ and $\vec{R}_{Y'}$ with those of $\hat{x'}$ and $\hat{y'}$. If the signs match, then $\vec{R}_{X'}$ and $\vec{R}_{Y'}$ are directed along the positive X' and Y' axes. The 'Parametric Risk Field' block in the Simulink simulation outputs the magnitude together with the sign of the body frame risk vector, $\pm \left\| \vec{R}_{X'} \right\|$ and $\pm \left\| \vec{R}_{Y'} \right\|$, and this is a direct indication of how much and in which direction the UAV has to be steered to avoid all detected obstacles.

Simulink implementation of PRF

It is important to note that all seven steps have to be repeated at each time step of the simulation. The PRF is implemented in Simulink using the 'Embedded Matlab Function' block. The 'Embedded Matlab Function' block compiles code in the 'C' programming language when the simulation is run, and therefore the code runs much faster than if the 'Interpreted Matlab Function' block were to be used. To use the 'Embedded Matlab Function' block, it is necessary to install an appropriate 'C' language compiler depending on the operating system of the computer used for running simulations.

3-2-5 Haptic Controller

The haptic controller is the second component of the HCAS and it also constitutes the 'second mapping' of HSC. It receives the magnitude and sign of the collision avoidance risk vector components along the rotating body reference frame axes from the parametric risk field: $\pm \left\| \vec{R_{X'}} \right\|$ and $\pm \left\| \vec{R_{Y'}} \right\|$ (see section 3-2-4). Based on this information, it computes the corresponding haptic moments, $M_{H_{X'}}$ and $M_{H_{Y'}}$, that needs to be applied on the side-stick to steer the UAV away from obstacles in the environment.

As stated earlier in section 2-3-2, the tuning of the haptic moments, $M_{H_{X'}}$ and $M_{H_{Y'}}$, has to take into account the 'combined' stiffness of the pilot arm NMS and the side-stick. Using this tuning paradigm, $M_{H_{X'}}$ and $M_{H_{Y'}}$ are computed through the following haptic controller 'tuning laws':

$$M_{H_{X'}} = \pm \left\| \vec{R_{X'}} \right\| \cdot \left(K_{NMS_{X'}} + K_{st} \right) \tag{3-40}$$

$$M_{H_{Y'}} = \pm \left\| \vec{R_{Y'}} \right\| \cdot \left(K_{NMS_{Y'}} + K_{st} \right) \tag{3-41}$$

Here $K_{NMS_{X'}}$ and $K_{NMS_{Y'}}$ are the stiffness' of the arm NMS in Nm/rad for the longitudinal and lateral directions respectively, and K_{st} is the stiffness of the stick (2.0 Nm/rad in both directions). Previous research by Smisek (Smisek et al., 2013) has shown that $K_{NMS_{X'}}$ and $K_{NMS_{Y'}}$ are both dependent on the magnitudes of the pilot bias moments, $M_{C_{X'}}$ and $M_{C_{Y'}}$. Pilot bias moments are moments resulting from the manual control inputs of the pilot to fly the UAV in a desired manner (for instance to a desired target position and/or velocity). Therefore, the tuning laws given by equations 3-40 an 3-41 shows that the haptic moments supplied by the haptic controller, $M_{H_{X'}}$ and $M_{H_{Y'}}$, take into account the risk of collision but also also the constantly changing manual control inputs of the pilot.

In this simulation however, the values of $M_{C_{X'}}$ and $M_{C_{Y'}}$ remain constant due to the constant control strategy employed by the simulated pilot model, see equations 3-3 and 3-3 in

section 3-2-1. Using the average neuromuscular admittance of the ten subjects measured by Smisek (Smisek et al., 2013), corresponding values of $K_{NMS_{X'}}$ and $K_{NMS_{Y'}}$ for the relax task haptic controller were found at a disturbance signal frequency of $0.5Hz$. These values, together with corresponding values of M_{C_X} and M_{C_Y}, as well as the desired pilot control strategy, are displayed in Table 3-3 (for more details on the simulation intitial conditions, see section 3-3-1).

Table 3-3: Experimentally determined NMS stiffness of the relax task, $K_{NMS_{RT}}$, for the conditions used in the simulation

	Pilot Strategy	M_C $[Nm]$	$K_{NMS_{RT}}$ $[Nm/rad]$
X'	$V_{des} = 5.0m/s$	0.7	5.051
Y'	$\dot{\psi}_{des} = 0.0rad/s$	0.0	0.455

To be able to simulate pilot-controller haptic interaction for the three haptic controllers, the values of $K_{NMS_{X'}}$ and $K_{NMS_{Y'}}$ for the force and position task haptic controllers also needs to be determined. By consulting other published literature where stiffness/admittance measurements of the human arm were taken (Venrooij, Abbink, Mulder, & Paassen, 2011) (Damveld et al., 2010), it was found that the NMS stiffness for the force and position tasks were approximately 0.5 and 7 times that of the relax task:

$$K_{NMS_{FT}} = G_{FT} \cdot K_{NMS_{RT}} = 0.5 \cdot K_{NMS_{RT}} \tag{3-42}$$

$$K_{NMS_{PT}} = G_{PT} \cdot K_{NMS_{RT}} = 7.0 \cdot K_{NMS_{RT}} \tag{3-43}$$

'Gains' G_{FT} and G_{PT} are applied both in the longitudinal and lateral directions, and are also used to determine the NMS model parameters for the force and position task instructions from those of the relax task instruction, see equations 3-11 to 3-13 in section 3-2-2. The haptic controller, like the parametric risk field, is implemented in Simulink using the 'Embedded Matlab Function' block.

3-2-6 Environment

The final simulation component to be discussed is the virtual environment of the simulation. Due to the constant control strategy of the simplified pilot model used, the 'Pilot Cognitive Control' block can only steer the UAV with a constant body velocity and yaw rate, see section 3-2-1. Therefore, it is the environment that is responsible for triggering the haptic feedback cues which indirectly guides the UAV from the starting location to the target point. For these reasons, the geometry of the environment is of critical importance when studying the pilot-controller haptic interaction using the simulation.

Figure 3-11 displays the 'tunnel' shaped obstacle which is used as the virtual simulation environment. Haptic feedback moments are generated if the UAV gets too close to the tunnel wall, and in this way the UAV is guided from its initial position (blue circle) to the target position (green star). The black solid line in Figure 3-11 indicates a typical path that is followed by the UAV. To further perturb the motion of the UAV, a 30^o turn (to force a

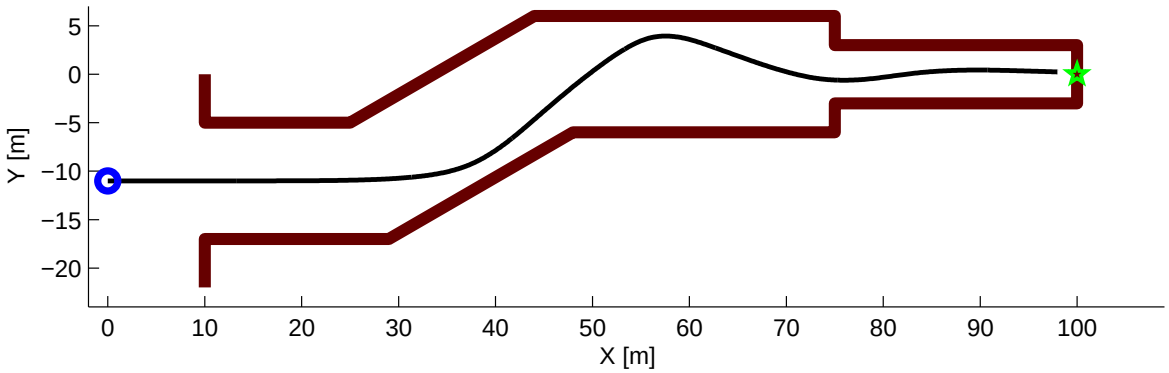

Figure 3-11: Geometry of the 'tunnel' like obstacle used to simulate the virtual environment of the simulation. The shape of the tunnel triggers the haptic feedback that guides the UAV from the initial position (blue circle) to the target position (green star).

'chicane' like maneuver), a sudden change in the tunnel diameter from $12r_{pz}$ to $8r_{pz}$, and a dead-end (to stop the UAV completely) are included in the geometry of the tunnel. These additional elements of the obstacle cause variations in the haptic feedback that is generated.

The obstacle is implemented in Simulink as a matrix containing the corner point coordinates of the tunnel line segments. The parametric risk field algorithm outlined in section 3-2-4, converts this obstacle definition to a set of vector line equations which describe the tunnel geometry, see equation 3-28. To aid in visualizing the motion of the UAV during the simulation, a Simulink animation of the UAV and the tunnel obstacle is created through modifications of a '6DOF Animation' block. Here the UAV helicopter and the tunnel are represented as 'patch' graphical elements, see Figure 3-12.

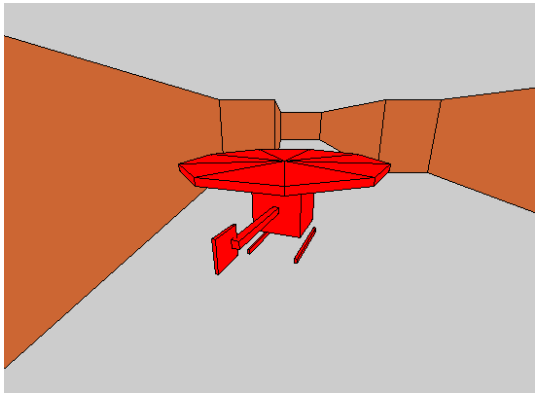

Figure 3-12: Six degree of freedom animation portraying the UAV motion and its relative position to the tunnel walls. The animation presents a graphic representation of the haptic collision avoidance system (HCAS) as the simulation progresses.

3-3 Simulation Setup and Conditions

The initial conditions, as well as the independent and dependent variables necessary to achieve the goals of the simulation are presented in this section.

3-3-1 Initial Conditions and Simulink Model Configuration

The initial conditions of the simulation are listed in Table 3-4 below. Here the pilot-controller haptic interaction gains, G_{NMS} and $G_{controller}$, allow for the modification of the NMS model parameters and the haptic controller setting to reflect that of the force, relax and position task instructions in relation to the relax task[6]. Note that a gain of '0' can be used to simulate the so called 'No NMS' and 'Stick Tuning' simulation conditions, see section 3-3-2 for more details.

Table 3-4: Initial conditions of the simulation

Pilot Cognitive Control	V_{des}	5.0 [m/s]	Desired velociy along body X' axis
	$\dot{\psi}_{des}$	0.0 [rad/s]	Desired yaw rate around body Z' axis
UAV Location and Heading	X_{UAV}	0.0 [m]	Initial UAV location along inertial X axis
	Y_{UAV}	-11.0 [m]	Initial UAV location along inertial Y axis
	ψ_{UAV}	0.0 $[rad]$	Initial UAV heading around inertial Z axis
Haptic Gain	G_{NMS}	0.0 / 0.5 / 1.0 / 7.0	Gain to select pilot NMS parameter values
	$G_{controller}$	0.0 / 0.5 / 1.0 / 7.0	Gain to select haptic controller setting

The simulation is propagated with a discrete time step of $dt = 0.05s$ using the Runge-Kutta integration method (solver 'ODE4' in Simulink). This time step was chosen as a compromise between simulation accuracy and speed. Two different stopping criteria are used to automatically stop the simulation if:

1. $V_{X'} \leq 0.1m/s$
2. $X_{UAV} \geq 100m$

The first criterion is an indication that the UAV has (nearly) stopped to safely avoid collisions with obstacles in the environment. As stated in section 3-3-3, the distance from the final UAV position to the target point is a measure of the performance of a particular haptic controller tuning setting. The second criterion is related to the location of the target point at 100 meters on the inertial X axis, see Figure 3-11. If the final UAV X position is equal to or greater than 100 meters, the UAV has either collided with the dead-end of the tunnel or has flown outside the tunnel obstacle all together. This is in an indication that the haptic feedback provided, and thus the tuning of the haptic controller, was insufficient to slow down the UAV adequately.

[6]Both G_{NMS} and $G_{controller}$ are equal to '1' for the relax task, see section 3-2-5 for the rationale behind this approach.

The initial conditions listed in Table 3-4, and the remaining parameters of the simulation components described in section 3-2, are initialized through the `model_config.m` Matlab script. This script is automatically executed when the Simulink simulation is run.

3-3-2 Simulation Independent Variables and Conditions

The neuromuscular task instruction and the setting of the haptic controller comprise the two main types of independent variable of the simulation. Twelve simulation conditions arising from different combinations of the two independent variables makes it possible to investigate the effect of each independent variable on the pilot-controller haptic interaction. The twelve conditions, as well as the 'Baseline' condition, are defined in Table 3-5 below:

Table 3-5: Simulation conditions arising from different combinations of the two types of independent variables: Neuromuscular Task Instruction & Haptic Controller Setting

Condition	Neuromuscular Task	Haptic Controller	Symbol
C1	Force Task	Force Task	$NMS_{FT}HC_{FT}$
C2		Relax Task	$NMS_{FT}HC_{RT}$
C3		Position Task	$NMS_{FT}HC_{PT}$
C4		Stick Tuning	$NMS_{FT}HC_{ST}$
C5	Relax Task	Force Task	$NMS_{RT}HC_{FT}$
C6		Relax Task	$NMS_{RT}HC_{RT}$
C7		Position Task	$NMS_{RT}HC_{PT}$
C8		Stick Tuning	$NMS_{RT}HC_{ST}$
C9	Position Task	Force Task	$NMS_{PT}HC_{FT}$
C10		Relax Task	$NMS_{PT}HC_{RT}$
C11		Position Task	$NMS_{PT}HC_{PT}$
C12		Stick Tuning	$NMS_{PT}HC_{ST}$
Baseline	No NMS	Stick Tuning	$NMS_{B}HC_{ST}$

In Table 3-5, the force, relax and position neuromuscular task instructions and haptic controller settings are modeled in sections 3-2-2 and 3-2-5 respectively. The 'Stick Tuning' haptic controller considers only the stick stiffness, K_{st}, when computing the haptic feedback moments, $M_{H_{X'}}$ and $M_{H_{Y'}}$. By comparing the 'Stick Tuning' haptic controller with haptic controllers that take into account the combined stiffness of the arm NMS and side-stick, the neuromuscular admittance based tuning paradigm proposed by Smisek (Smisek et al., 2013) can be verified.

The 'Baseline' condition is used to enable a fair comparison between the twelve simulation conditions. In the 'Baseline' condition, the entire NMS model and the haptic feedback path in Figure 3-1 are neglected, and the outputs of the 'Pilot Cognitive Control' block are fed directly into the side-stick. Since 'No NMS' is modeled, the haptic controller for this condition is tuned using the 'Stick Tuning' profile described in the previous paragraph. In effect the 'Baseline' condition simulates a quasi-automatic collision avoidance system where there is no

physical interaction between the pilot NMS and the side-stick. More information of how the 'Baseline' is used in the results analysis is detailed in section 3-3-3.

3-3-3 Simulation Dependent Variables

The dependent variables used to evaluate the pilot-controller haptic interaction in terms of performance, control activity, safety and haptic controller accuracy are listed in Table 3-6. Here 'RMS' stands for Root Mean Square error and 'STD' is the standard deviation. The control activity and haptic controller accuracy variables are computed separately along the body X' and Y' axes. The haptic controller accuracy is a measure of how well the controller predicted the moments generated by the NMS. Note that smaller values of the dependent variables indicate better performance, lower control activity, higher safety and better controller accuracy of the total system.

Table 3-6: Dependent variables of the simulation

Performance	$RMS_{V_{X'}}$	Root mean square error of body velocity relative to Baseline [%]
	$STD_{V_{X'}}$	Standard deviation of body velocity relative to Baseline [%]
	d_{target}	Distance to target relative to Baseline [%]
Control Activity	$STD_{\delta_{st}}$	Standard deviation of stick deflection relative to Baseline [%]
	$STD_{\dot{\delta}_{st}}$	Standard deviation of stick deflection rate relative to Baseline [%]
	$CR_{\delta_{st}}$	Control reversal of stick deflection relative to Baseline [%]
Safety	$\overline{d}_{obstacle}$	Mean distance to obstacle relative to Baseline [%]
	$n_{collisions}$	Number of collisions
Haptic Controller Accuracy	$RMS_{(\lvert M_H \rvert - \lvert M_{NMS} \rvert)}$	RMS error between the absolute haptic moment and the absolute NMS moment [Nm]

For some simulation conditions, it was found that the UAV continues to fly outside the tunnel after a collision with the tunnel wall. As safety of UAV teleoperation is of prime importance, and because no haptic feedback is generated when flying outside the tunnel, the dependent variables are computed only up to the first collision point. However, this procedure results in unfair comparisons of the dependent variables as it is possible for the distance traveled before the first collision to be significantly different between simulation conditions. For example, it is unfair to compare a condition where the UAV traveled only 30 meters before a collision to a condition where the UAV traveled without collisions.

To allow for a fairer comparison between simulation conditions, for a particular simulation condition the dependent variables are calculated relative to the same distance traveled by

the Baseline condition up to the first collision. For instance, if the UAV traveled 30 meters before colliding with the tunnel wall, the dependent variables for that condition are computed relative to the baseline results till 30 meters. Note that this baseline comparison is not possible for $n_{collsions}$ and $RMS_{(|M_H|-|M_{NMS}|)}$ as the Baseline simulation has no collisions and no NMS model. For these two variables, the actual values are used for comparison.

3-4 Results and Analysis

As stated in section 3-1 the purpose of the simulation is to investigate the pilot-controller haptic interaction under varying pilot neuromuscular system and haptic controller settings, as well as to verify the novel haptic feedback tuning algorithm. In this section, the data obtained from the simulation is presented and analyzed in terms of these two simulation goals. To this end, this section is divided into three parts. First the overall results of the simulation are considered. This is followed by an in depth analysis of the four haptic controllers for the 'relaxed' neuromuscular task instruction. Finally, the results are discussed in terms of the research questions mentioned in section 1-2.

3-4-1 Overall Simulation Results

In this subsection, the results of all twelve simulation conditions are presented. The conditions are compared qualitatively in terms of the trajectories flown, and quantitatively through the simulation dependent variables (see section 3-3-3).

Qualitative Results Comparison

By visually inspecting the trajectories flown by the UAV, it is possible to qualitatively analyze the effects of the two independent variables, neuromuscular task instruction and haptic controller tuning, on the overall system response. Figure 3-13 displays the trajectories for all twelve simulation conditions categorized according to the neuromuscular task instruction.

When comparing the trajectories pictured in Figure 3-13, there is a very clear difference between the three neuromuscular task instructions after $X = 35$ meters[7]. For the force task, the trajectories of all four haptic controllers are very similar. The trajectories for the relax task are similar up to $X = 50$ meters, after which HC_{FT} and HC_{NT} are more oscillatory than HC_{RT} and HC_{PT}. In contrast, the trajectories, as well as final the UAV positions, are very different for the position task. In essence, as the stiffness of the NMS increases from force to position task, there is greater variation in the trajectories flown by the four haptic controllers.

A second observation from Figure 3-13 is when the haptic controller is tuned to a lower stiffness than that of the NMS model, the UAV is not able to safely navigate through the tunnel obstacle without collisions. This is most evident in Figure 3-13(c) for the position task where three of the four haptic controllers are under-tuned, and are not even able to tackle

[7]Note that before $X = 35$ meters, the trajectories of all the conditions are very similar due to the low haptic feedback moments supplied in this region.

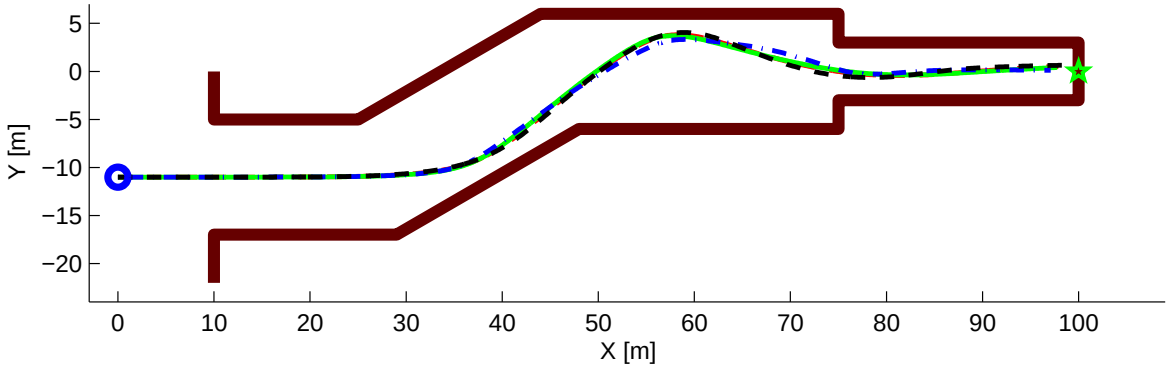

(a) Force task neuromuscular setting

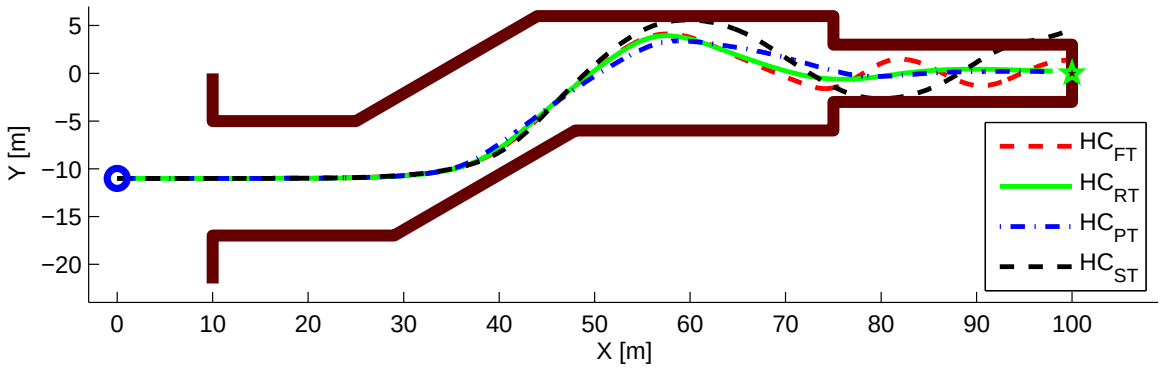

(b) Relax task neuromuscular setting

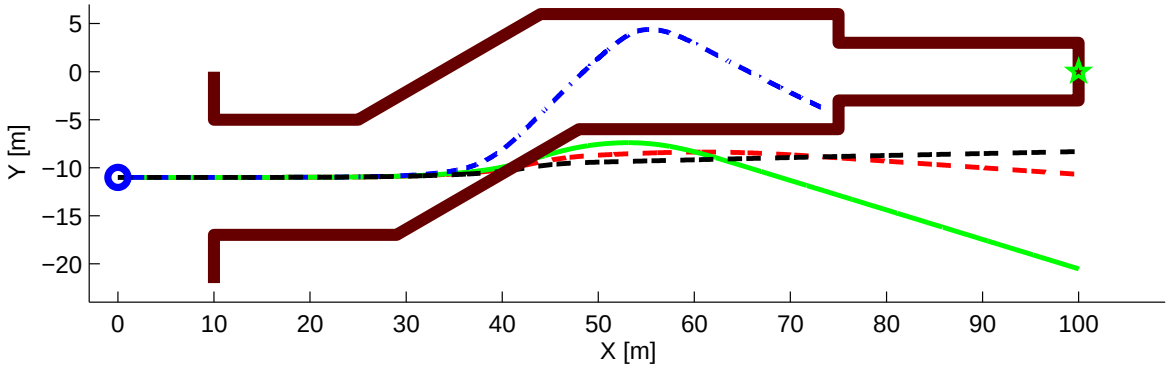

(c) Position task neuromuscular setting

Figure 3-13: Trajectories flown by the four haptic controllers for each neuromuscular task instruction. The blue circle and the green star represent the starting and target locations respectively.

the first turn. In fact for this case, even HC_{PT} is not able to fly through the entire tunnel, suggesting that the position task is not the optimal design point for tuning haptic feedback.

As a final remark on Figure 3-13, note that out of the four haptic controllers, the 'Stick Tuning' haptic controller, HC_{ST}, collides with the obstacle for all three neuromuscular task instructions. Moreover, the safety of this controller gets progressively worse as the stiffness of the NMS increases. This is an initial indication that the neuromuscular stiffness should be taken into account when tuning the haptic controller.

Quantitative Results Comparison

For each simulation condition, a 'Combined Score', S_C, can be computed as a summation of the simulation dependent variables. The combined score makes it easier to quantify the differences between the simulation conditions through a single numerical value, see equation 3-44.

$$S_C = RMS_{V_{X'}} + STD_{V_{X'}} + d_{target} + STD_{\delta_{st}} + STD_{\dot{\delta}_{st}} + CR_{\delta_{st}} + \overline{d}_{obstacle} + 100\ n_{collisions} + 100\ RMS_{(M_H - M_{NMS})} \tag{3-44}$$

Here the number of collisions, $n_{collisions}$, and the haptic controller accuracy, $RMS_{(|M_H|-|M_{NMS}|)}$, are each multiplied by a gain of 100. This is done to ensure that their values are in the same range as the other dependent variables which are in turn computed as a percentage of the baseline condition, see section 3-3-3 for more details. Similar to the individual dependent variables, smaller values of the combined score indicates a better overall system response. Figure 3-14 displays a bar chart of the combined scores of all twelve simulation conditions categorized according to the neuromuscular task instruction.

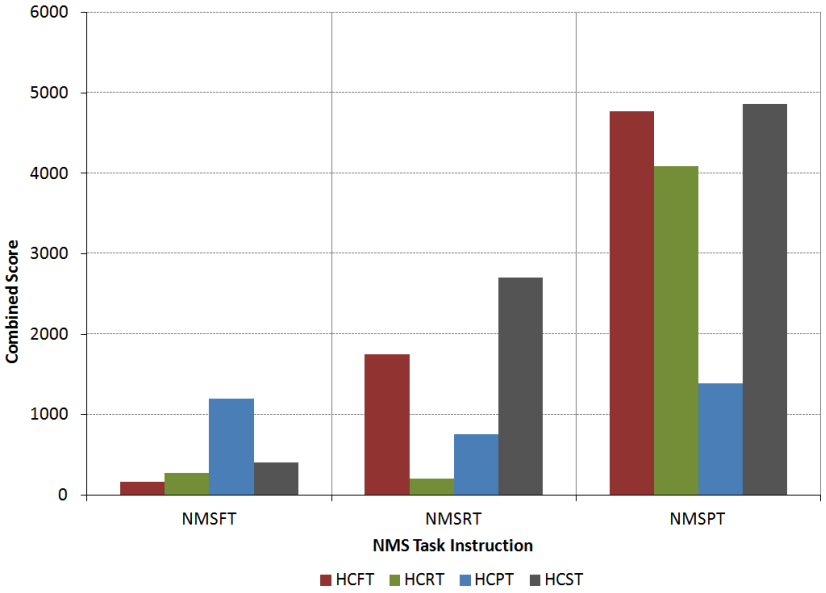

Figure 3-14: Combined scores for all four haptic controllers for each neuromuscular task instruction

From Figure 3-14, it can be seen that for a particular neuromuscular task instruction, the haptic controller tuned to the same stiffness has the lowest combined score, and therefore the best overall response. For instance, the best overall response for all conditions is for the HC_{FT} controller when tuned for the force task. This result agrees with those found experimentally by Cleij (Cleij, 2011) for passive control tasks[8], and it also verifies the concept of taking into account the 'combined' system stiffness in tuning the haptic controller as proposed by Smisek (Smisek et al., 2013).

Figure 3-14 also confirms several of the initial qualitative observations made earlier. Most importantly, it can be noted that for a particular task instruction, the value of the combined score increases significantly when the haptic controller is under-tuned as opposed to an over-tuned controller. This is clearly evident in the relax task where the combined score of the HC_{FT} controller (1750) is almost two and a half times that of the HC_{PT} controller (760), indicating a greater degradation of the overall system response with an under-tuned controller. Furthermore, it is clear from Figure 3-14 that all four controllers perform the worst for the position task. This agrees with the qualitative analysis mentioned earlier that the position task should not be selected as the design point for tuning the haptic controller.

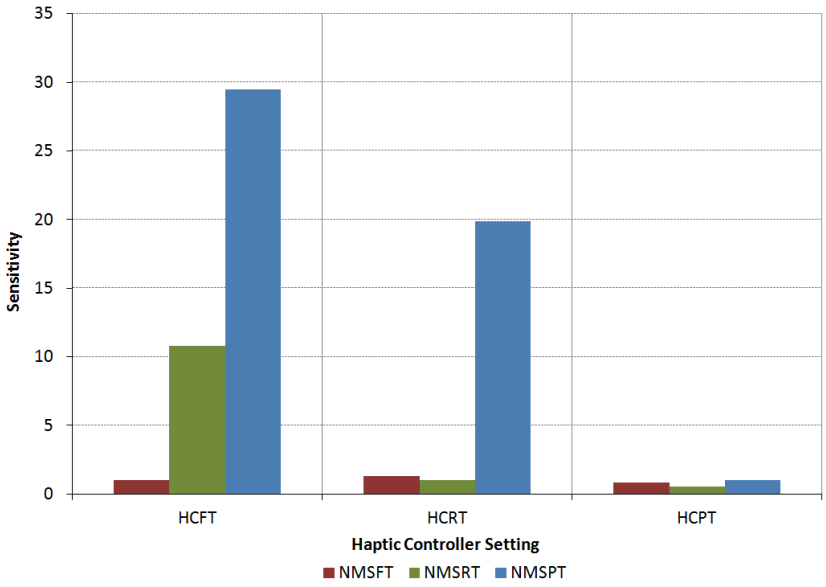

Figure 3-15: Sensitivity of each haptic controller to variations in the neuromuscular task instruction. A large value indicates a high controller sensitivity.

In addition to comparing the system responses of the four haptic controllers for a particular neuromuscular task instruction, it is also necessary to consider the sensitivity of each controller to changes in the operator NMS task/stiffness. This is because in reality the haptic controller will be tuned to a single neuromuscular design stiffness, and the operator will vary his/her actual neuromuscular stiffness depending on whether he/she agrees or disagrees with the controller actions. For this reason, the sensitivity of each controller is computed as the change in the combined score when the neuromuscular task is varied to an off-design point and is pictured in Figure 3-15. Here a large value indicates high sensitivity.

[8]As the visual control of the simplified pilot model used in the simulation is constant over time, the pilot control can be considered passive.

It is clear from Figure 3-15 that the HC_{PT} controller has the lowest sensitivity of all the controllers. This is to be expected as for this controller, the NMS needs to exert large moments to prevent overshoots of the UAV for all three neuromuscular task instructions. On the other hand, the HC_{FT} controller, which was found to have the best overall response from Figure 3-14, is also the most sensitive to changes in neuromuscular stiffness. The HC_{RT} controller is less sensitive when compared to the HC_{FT} controller, and it is an ideal middle ground when considering both the actual system response and the controller sensitivity.

3-4-2 'Relaxed' Neuromuscular System Results

Preceding research by Smisek (Smisek et al., 2013) selects the relax task neuromuscular stiffness as the design point for tuning the haptic controller. Therefore in this subsection, a detailed analysis of the system response to all four haptic controllers for the 'relaxed' NMS is presented. For the relax task it should be noted that the HC_{RT} controller is tuned to the same stiffness as the NMS model, whereas HC_{ST} and HC_{FT} are the under-tuned controllers, and HC_{PT} is the over-tuned controller.

Just as with the previous subsection, data from the simulation is analyzed both qualitatively and quantitatively to gain a better understanding of the total system response.

Qualitative Results Analysis

The effect of haptic feedback on the trajectory and velocity changes of the UAV for all four haptic controllers can be analyzed qualitatively using Figure 3-16. Here, the black solid line represents the trajectory of the UAV, and the red arrows indicate the magnitude and direction of the haptic collision avoidance moments supplied per second. Additionally, the UAV protection zone per second is depicted as black dashed circles, and the spacing between the circles can be used to infer velocity changes of the UAV.

From Figure 3-16, it is clear that the under-tuned controllers, HC_{ST} and HC_{FT}, follow more erratic trajectories, and as a result are more susceptible to collisions. This same behavior was noted earlier in section 3-4-1. In addition, the under-tuned controllers seem to apply relatively large lateral haptic moments at close proximity to obstacles. On the other hand, when the haptic controller is tuned to the same stiffness as the NMS as for HC_{RT}, or is over-tuned as in the case of HC_{PT}, the UAV appears to decelerate quicker and at greater distances from obstacles. Furthermore, haptic moments supplied tend to be aligned along the UAV trajectory (but in the opposite direction) with less lateral moments.

These differences can be explained by considering the haptic controller tuning laws described in section 3-2-4. For convenience, the general form of the tuning law is given below:

$$\|M_H\| = \underbrace{\left\|\vec{R}\right\|}_{RiskMagnitude} \cdot \underbrace{(K_{NMS} + K_{st})}_{CombinedSystemStiffness} \tag{3-45}$$

Here the magnitude of the haptic moment, $\|M_H\|$, is the product of the risk of collision, which is a value between zero and one, and the combined system stiffness, assumed to be a different constant for each controller in the simulation (see section 3-2-4). Thus in essence the risk

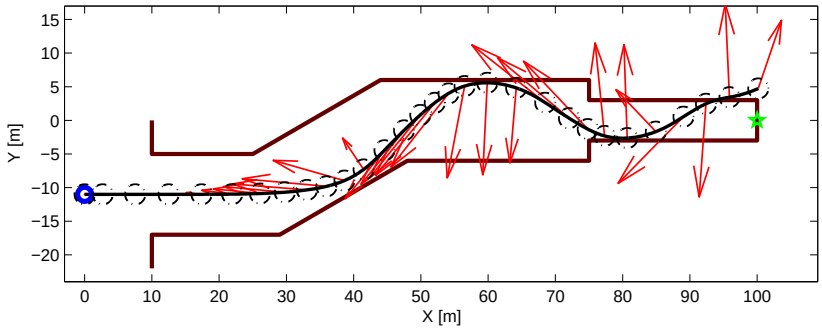

(a) HC_{ST}

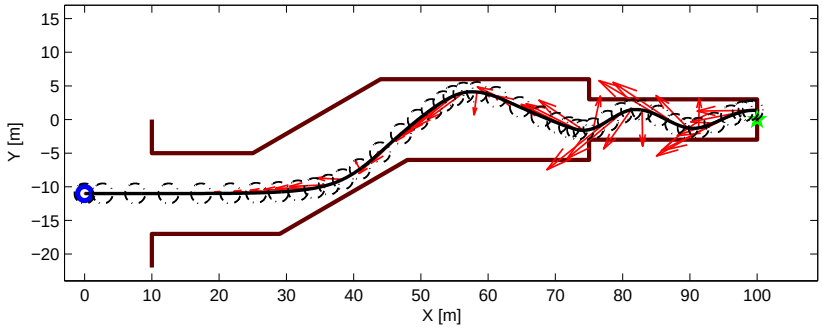

(b) HC_{FT}

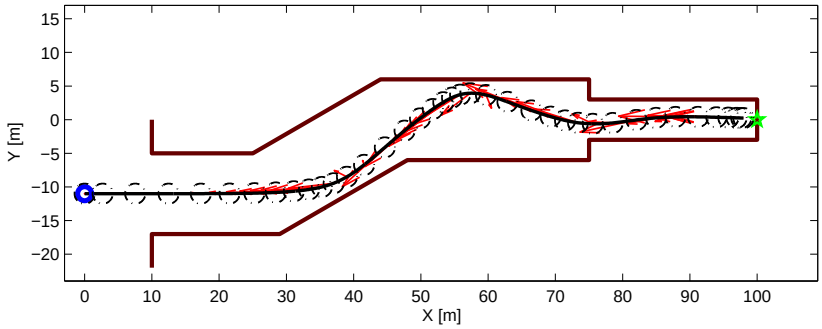

(c) HC_{RT}

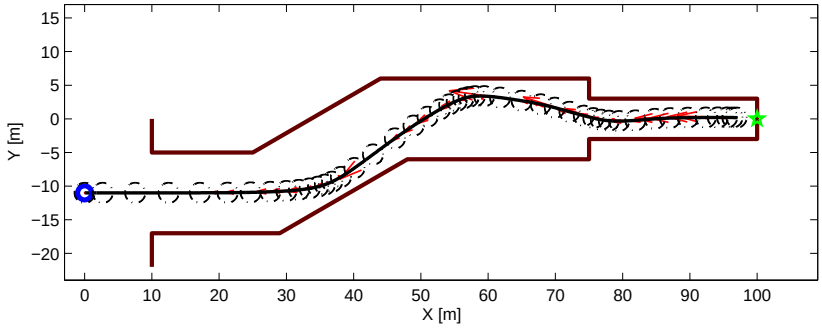

(d) HC_{PT}

Figure 3-16: Trajectories (black solid lines), haptic feedback per second (red arrows) and UAV protection zone per second (dashed black circles) of the four haptic controllers for NMS_{RT}

magnitude scales the combined system stiffness and the maximum haptic moment that can be supplied is numerically equal to the combined system stiffness.

For the under-tuned controllers, the combined system stiffness is under estimated. Therefore, adequate haptic collision avoidance moments are generated only when the UAV is relatively close to obstacles such that the risk of collision is relatively high. This insufficient deceleration of the UAV longitudinal velocity requires high lateral haptic moments to induce large heading changes in an attempt to steer the UAV away from danger. However for both HC_{ST} and HC_{FT}, the delayed haptic guidance results in a number of collisions and oscillatory UAV motion.

The situation appears to improve considerably when the haptic controller over estimates the actual neuromuscular stiffness as for HC_{PT}. For this controller, it can be seen in Figure 3-16 that longitudinal haptic moments build up in magnitude from larger distances to obstacles. This causes the UAV to decelerate to a very low longitudinal velocity at close proximity to the tunnel walls, and thus requires only small lateral haptic moments to steer it safely without collisions. When the controller is tuned to match the stiffness of the NMS as with HC_{RT}, a mixture of the two control strategies seems to be used, but with a greater emphasis on longitudinal velocity reduction. However, to gain a better understanding of the differences between these two controllers, a quantitative analysis of the simulation data is needed.

Quantitative Results Analysis

A quantitative results analysis is possible by comparing the simulation dependent variables discussed in section 3-3-3. The dependent variables can be categorized into four categories: performance, control activity, safety and haptic controller accuracy. It should be noted that most dependent variables are computed only up to the first collision point. In addition they are given relative to the same distance traveled by the baseline condition and thus only a ranking between the controllers is possible. The symbol 'RTB' is used to indicate this in the subsequent text. For two dependent variables, the number of collisions, $n_{collisions}$, and the haptic controller accuracy, $RMS_{(|M_H|-|M_{NMS}|)}$, actual values are used for comparison.

Table 3-7 displays the performance related dependent variables of all four haptic controllers. It is clear that for all three dependent variables, the HC_{RT} controller, which is tuned to match the stiffness of the NMS, has the lowest numerical values and therefore performs the best. HC_{FT} is the second best controller for the velocity related dependent variables, but as this controller experiences a collision at $X = 75$ meters, the second best controller for the distance to target measure, d_{target}, is HC_{PT}. As expected the HC_{ST} controller performs the worst in all cases.

In the qualitative results analysis, it was stated that one of the primary reasons for the poor performance of the under-tuned controllers was due to the delay and insufficient reduction of longitudinal velocity when approaching obstacles. This can be clearly visualized in Figure 3-17 where the longitudinal velocity of the UAV is plotted. As the haptic feedback strength increases from HC_{ST} to HC_{PT}, the UAV decelerates (slightly) earlier, faster (greater slope) and to a (much) lower obstacle approach velocity. However, despite this general trend, the deceleration/acceleration (slope) of HC_{RT} and HC_{FT} are very similar up to the collision point of HC_{FT}. Another interesting conclusion that can be drawn from Figure 3-17 is that although the under-tuned controllers can safely navigate the first turn with a lower reduction

of velocity, the consequent trajectory makes it impossible for them to avoid collisions later on in the tunnel.

Table 3-7: Performance related simulation dependent variables computed relative to baseline condition (RTB) for NMS_{RT}

	HC_{ST}	HC_{FT}	HC_{RT}	HC_{PT}
$RMS_{V_{X'}}$ RTB [%]	10.11	1.59	0.81	8.99
$STD_{V_{X'}}$ RTB [%]	18.15	3.24	0.35	5.19
d_{target} RTB [%]	1872.28	1014.20	10.71	27.49
Combined Score	1900.54	1019.02	11.87	41.68

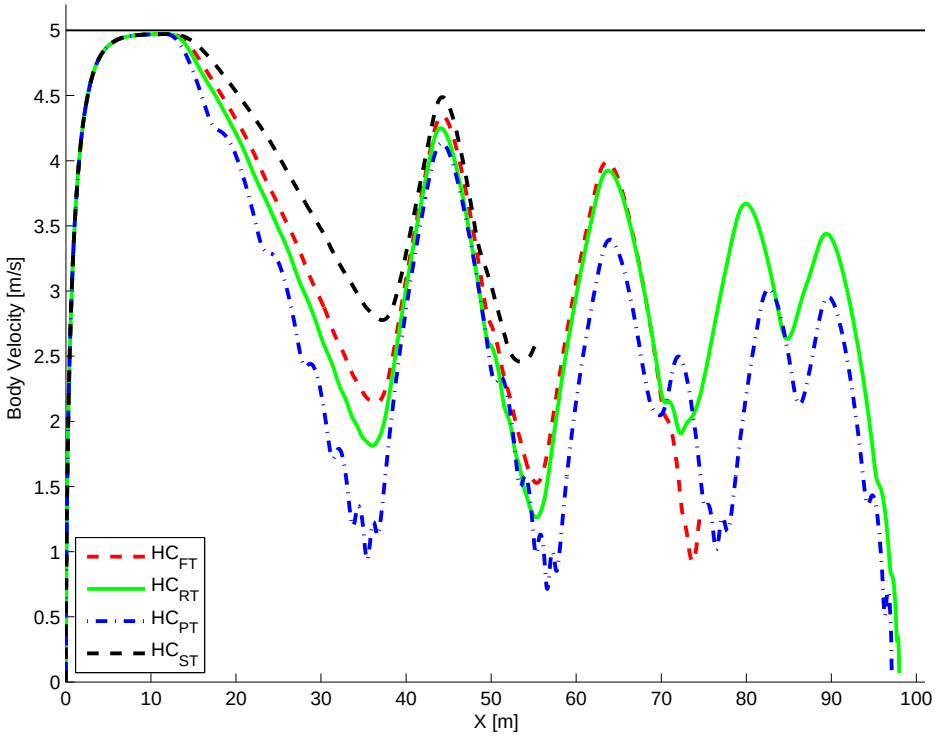

Figure 3-17: UAV longitudinal velocity variation of the four haptic controllers for NMS_{RT}. The black horizontal line indicates the desired velocity of the pilot.

The control activity related dependent variables are computed separately along the body longitudinal, X', and lateral, Y', axes and are displayed in Table 3-8. Although HC_{RT} has the lowest combined score, when inspecting the individual dependent variables, it can be seen that HC_{FT} has the lowest numerical value for all three longitudinal measures. In fact, when comparing the normalized stick deflections in Figure 3-18, it is clear that HC_{RT} and HC_{PT} have greater deflections along the longitudinal direction, and HC_{ST} and HC_{FT} have greater deflections along the lateral direction. This is evidence for the qualitative control behavior noted earlier that adequately and over-tuned controllers avoid obstacles through velocity changes, and under-tuned controllers mainly through heading changes.

It is interesting to find that the HC_{PT} controller has the highest control activity. Particularly in the longitudinal direction, see Figure 3-18(a), HC_{PT} is highly erratic and the stick is deflected with extreme magnitudes together with a very high deflection rate. This behavior would be very uncomfortable to the pilot leading to frustration and distrust in the haptic feedback and thus should be avoided.

Table 3-8: Control activity related simulation dependent variables computed relative to baseline condition (RTB) for NMS_{RT}

	HC_{ST}	HC_{FT}	HC_{RT}	HC_{PT}
$STD_{\delta_{st_{X'}}}$ RTB [%]	33.72	1.65	8.44	80.06
$STD_{\delta_{st_{Y'}}}$ RTB [%]	103.83	73.43	24.30	13.55
$STD_{\dot{\delta}_{st_{X'}}}$ RTB [%]	33.67	6.28	18.52	351.07
$STD_{\dot{\delta}_{st_{Y'}}}$ RTB [%]	194.76	88.41	34.59	108.55
$CR_{\delta_{st_{X'}}}$ RTB [%]	54.55	34.48	41.03	69.23
$CR_{\delta_{st_{Y'}}}$ RTB [%]	0.00	46.15	5.45	29.09
Combined Score	420.53	250.41	132.33	651.54

Safety of the UAV is measured as the number of collisions, $n_{collisions}$, and the mean distance to obstacles, $\overline{d}_{obstacle}$. In terms of these two dependent variables, it can be seen from Table 3-9 that the safety of HC_{RT} is the highest. Due to the collisions of the under-tuned controllers, HC_{PT} has the second highest safety.

To help visualize the safety of UAV teleoperation in the simulation, Figure 3-19(a) displays the minimum distance to obstacles and Figure 3-19(b) shows the corresponding risk magnitude. As expected, when the minimum distance to obstacles decreases, the risk magnitude increases and vice versa. However, it is interesting to note that although the minimum distance to obstacles are quite similar for all four haptic controllers, there are significant differences in terms of the risk magnitude, even when considering only up to the first collision of HC_{ST}. This suggests that the haptic feedback provided is very sensitive to the trajectory flown by each haptic controller.

Table 3-9: Safety related simulation dependent variables computed relative to baseline condition (RTB) for NMS_{RT}

	HC_{ST}	HC_{FT}	HC_{RT}	HC_{PT}
$\overline{d}_{obstacle}$ RTB [%]	3.23	1.59	0.11	4.26
$n_{collisions}$	3.00	4.00	0.00	0.00
Combined Score	303.23	401.59	0.11	4.26

Figures 3-20 and 3-21 shows the moment exerted by the NMS, M_{NMS}, the moment applied

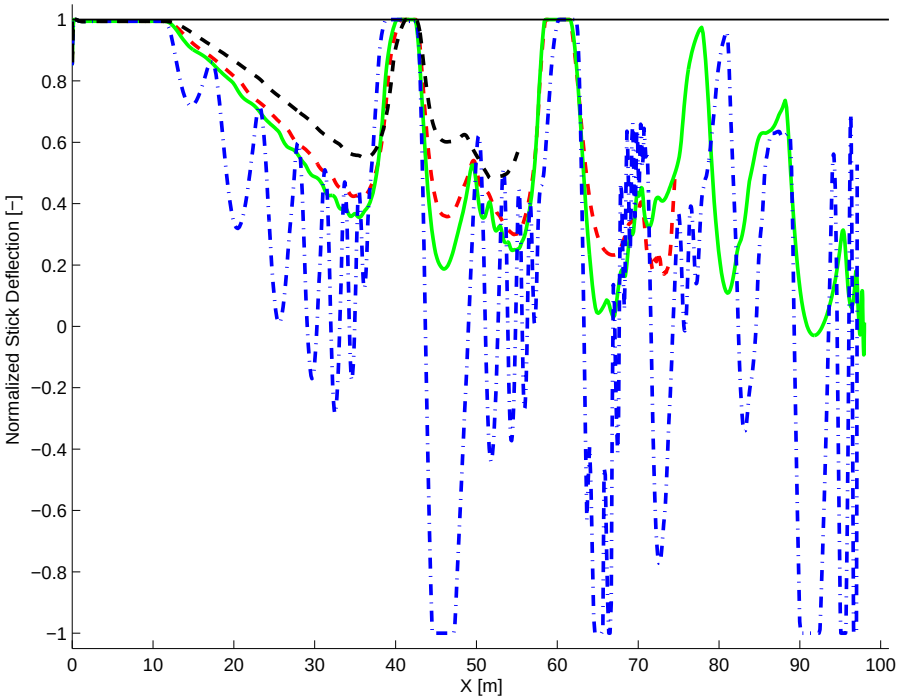

(a) Longitudinal

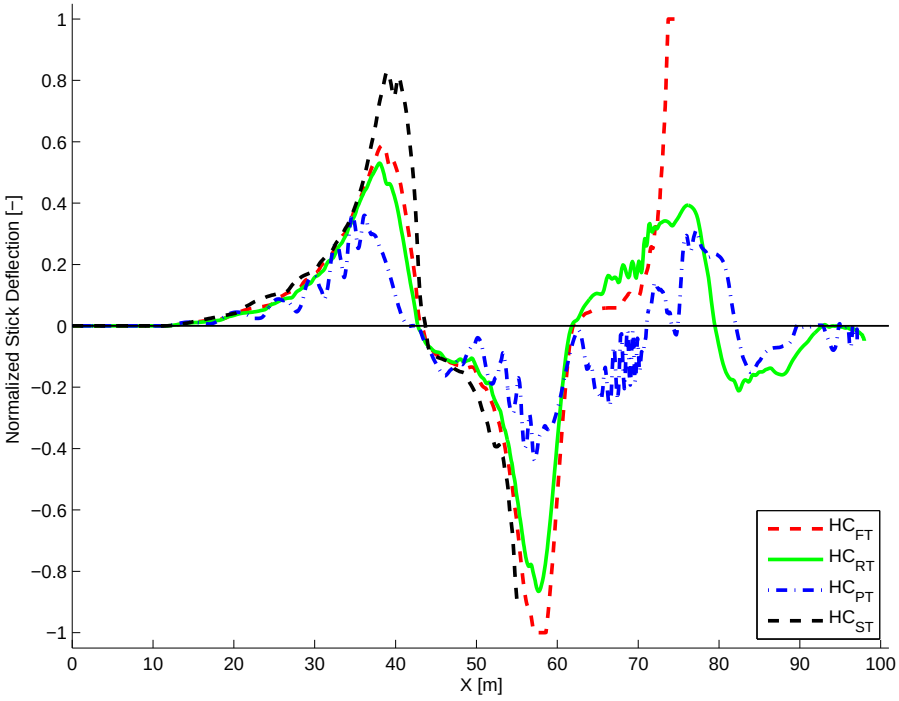

(b) Lateral

Figure 3-18: Normalized stick deflection of the four haptic controllers for NMS_{RT}. The black horizontal lines represent the deflections necessary to maintain the desired velocity and yaw rate of the pilot.

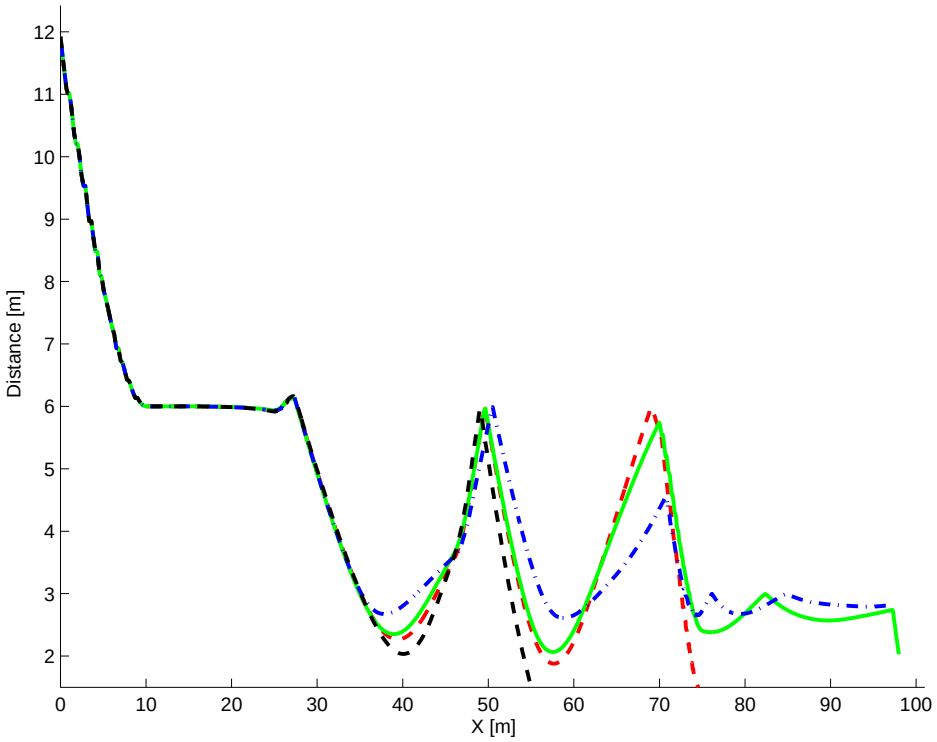

(a) Distance to obstacles

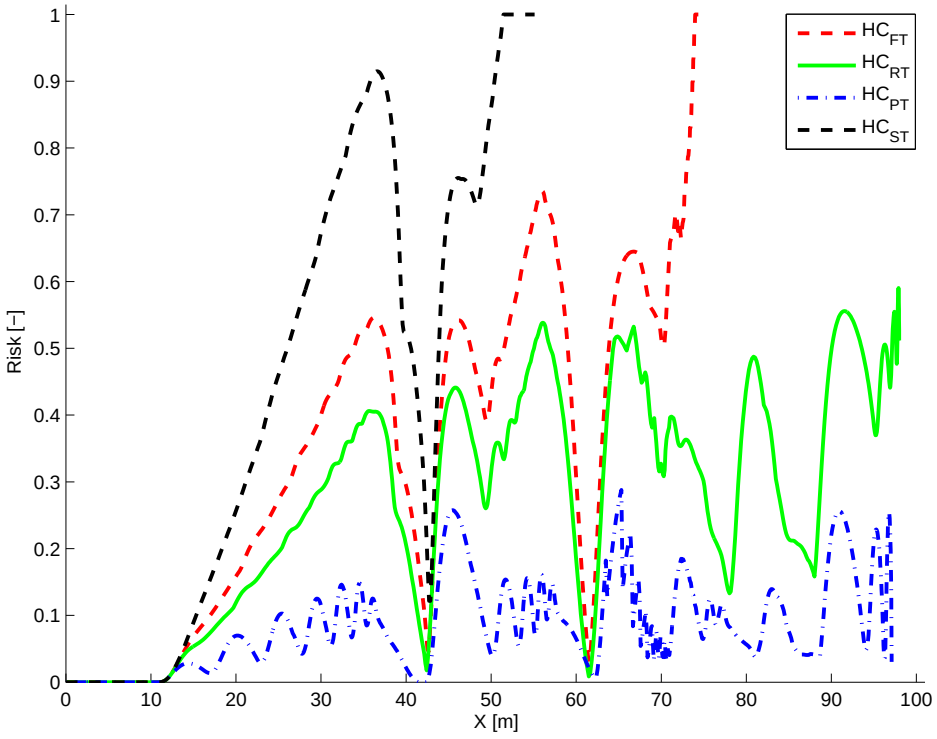

(b) Risk vector magnitude

Figure 3-19: Safety comparison of the four haptic controllers for NMS_{RT}

by the haptic controller, M_H, and the difference between the absolute values of these two moments, $|M_H| - |M_{NMS}|$, in the longitudinal and lateral directions respectively.

Initially the NMS exerts the constant moments that are required to achieve the desired velocity and yaw rate. However, when the UAV is too close to obstacles, haptic moments are supplied to reduce the velocity and steer the UAV away from collisions. Due to the haptic feedback applied on the NMS, see Figure 3-1, and because the visual control loop of the pilot is suppressed in the simulation, the NMS tries to counteract the haptic moments on the side-stick and recover to the desired velocity and yaw rate. This is done by exerting 'extra' neuromuscular moments that are applied in the opposite direction to the haptic moments. This is why the traces of M_{NMS} and M_H appear to be opposites of each other in Figures 3-20 and 3-21.

Whilst this apparent reluctance of the neuromuscular model in the simulation is expected to be different in reality, this property can be used to help assess the quality of the four different haptic controllers. When the difference between the absolute values of M_H and M_{NMS} is small, less additional haptic moment is required to make sure that the UAV is steered as intended by the haptic controller. Thus when $|M_H| - |M_{NMS}|$ is closer to zero, the haptic controller better predicts the NMS moments. The plots of $|M_H| - |M_{NMS}|$ are given in the third subfigure of Figures 3-20 and 3-21. The dependent variable 'haptic controller accuracy' is the root mean square value of this plot, see Table 3-10.

Table 3-10: Haptic controller accuracy for NMS_{RT}

	HC_{ST}	HC_{FT}	HC_{RT}	HC_{PT}
$RMS_{\left(\lvert M_{H_{X'}}\rvert - \lvert M_{NMS_{X'}}\rvert\right)}$ [Nm]	0.53	0.43	0.39	0.45
$RMS_{\left(\lvert M_{H_{Y'}}\rvert - \lvert M_{NMS_{Y'}}\rvert\right)}$ [Nm]	0.27	0.36	0.23	0.15
Combined Score	80.88	78.83	61.78	60.01

On consulting Table 3-10, it is clear that the haptic controller accuracy for HC_{RT} is the best for the longitudinal direction, but in the lateral direction, HC_{PT} is better. This lower value for HC_{PT} in the lateral direction may be explained by its control strategy of predominantly controlling the UAV through velocity changes. However it is clear from Figures 3-20 and 3-21 that in both the longitudinal and lateral directions, HC_{PT} provides highly oscillatory haptic moments, resulting in highly oscillatory neuromuscular moments.
Based on the argumentation given in the previous paragraph, the large oscillations maybe due to its over estimation of the neuromuscular stiffness, resulting in excess additional moments applied by HC_{RT} to force its will on the NMS. As stated earlier, erratic haptic moments should be avoided as they cause irritation and discomfort to the pilot.

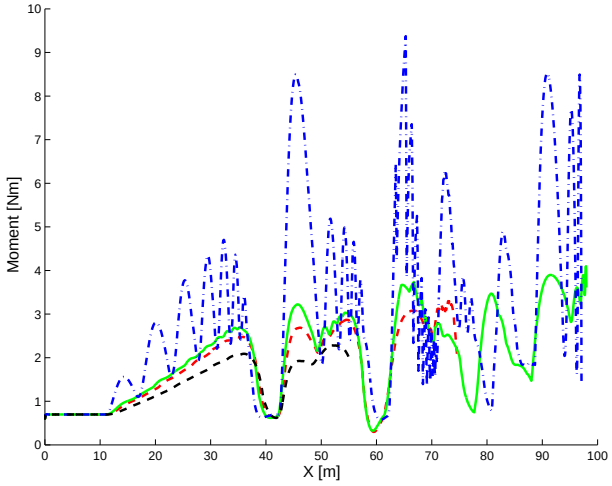

(a) $M_{NMS_{X'}}$

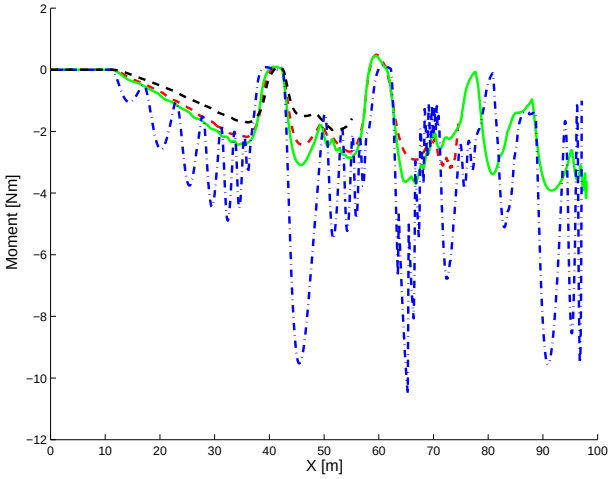

(b) $M_{H_{X'}}$

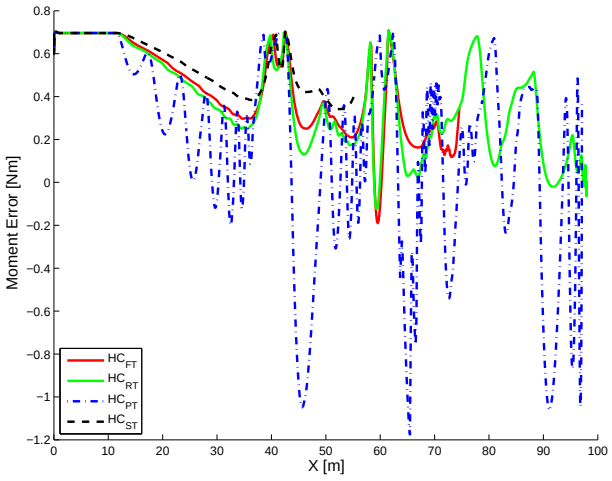

(c) $\left(|M_{H_{X'}}| - |M_{NMS_{X'}}|\right)$

Figure 3-20: Longitudinal moment comparisons of the four haptic controllers for NMS_{RT}

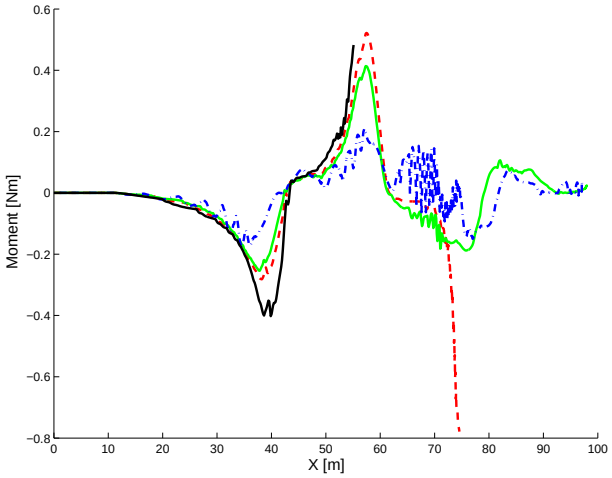

(a) $M_{NMS_{Y'}}$

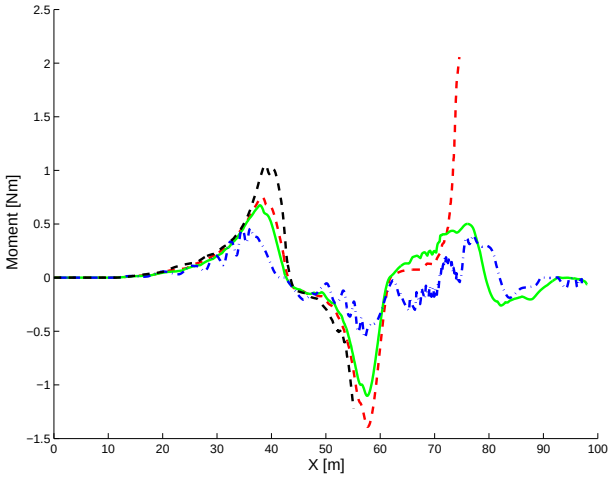

(b) $M_{H_{Y'}}$

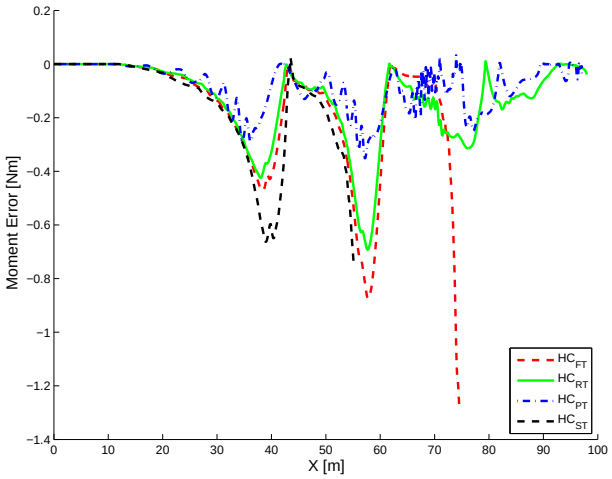

(c) $\left(\left|M_{H_{Y'}}\right| - \left|M_{NMS_{X'}}\right|\right)$

Figure 3-21: Lateral moment comparisons of the four haptic controllers for NMS_{RT}

3-4-3 Results Discussion and Conclusions

In this subsection, the main results of the simulation are used to provide initial insights into the first two research questions pertaining to the primary thesis objective introduced in section 1-2.

How does the pilot-controller haptic interaction vary depending on the neuromuscular task instruction and the haptic controller setting?

Based on the overall results of the simulation presented in section 3-4-1, there is clear evidence that both the neuromuscular task instruction and the haptic controller setting have significant impacts on the overall system response. The impact of the neuromuscular task instruction is most noticeable in the trajectories followed by the UAV. As the stiffness of the NMS increases from force to position task, there is greater variation in the trajectories flown by the four haptic controllers. The opposite trend is found for the sensitivity of the haptic controllers. HC_{PT} is least sensitive to changes in neuromuscular task instruction, whilst HC_{FT} is most sensitive. The sensitivity of HC_{RT} lies between the other two controllers. In fact, for HC_{RT} there is very little difference between the relax task and force task responses.

When analyzing the response of the four haptic controllers to the relax task in section 3-4-2, a trend is found for the control strategy exhibited by the controllers. The under-tuned controllers for this task, HC_{ST} and HC_{FT}, seem to apply relatively large lateral haptic moments at close proximity to obstacles in an effort to avoid them with heading changes. However, this control strategy leads to erratic trajectories and collisions. On the other hand, the over-tuned controller, HC_{PT}, applies longitudinal haptic moments at comparatively large distances from obstacles. In this way, the UAV decelerates to a very low velocity near obstacles such that only small lateral haptic moments are necessary to avoid all collisions safely. HC_{RT}, which is the controller tuned to match the stiffness of the NMS for the relax task, was found to use a combination of these two control strategies, leading to the best performance, safety and control activity.

How does the novel tuning procedure compare to 'Stick Tuning', and what is the effect of selecting the relax task as the design point for tuning haptic shared control?

For all three neuromuscular task instructions, the haptic controller tuned to the same stiffness as the NMS model has the best overall response. When neuromuscular stiffness was neglected as with the 'Stick Tuning' HC_{ST} controller, the overall response of the system degraded, leading to multiple collisions for all neuromuscular task instructions. Additionally, it was found that under-tuning the haptic controller led to collisions, whilst over-tuned controllers provided highly erratic and unstable haptic feedback. These results are an initial indication that the haptic controller should be designed to take into account the combined stiffness of the NMS and side-stick, and thus verifies the novel tuning procedure proposed by Smisek (Smisek et al., 2013).

Out of the four haptic controllers, HC_{FT} had the best overall response (for the force task), and is closely followed by HC_{RT} (for the relax task). However as stated earlier, HC_{FT} is very sensitive to changes in neuromuscular task instruction when compared with HC_{RT}. Hence,

HC_{RT} is a good middle ground when considering both the absolute response, as well as sensitivity to neuromuscular task instruction.

Preceding research by Smisek (Smisek et al., 2013) selects the relax task stiffness of the NMS as the design point for tuning the haptic controller. This is because the relax task requires the lowest physical effort due to the suppression of reflexive neuromuscular activity. Since reflexive feedback paths of the Golgi Tendon Organ (GTO) and the muscle spindles are not included in the NMS model used in the simulation, this property could not be verified. A human-in-the-loop experiment is needed to compare the physical activity induced by the different haptic controllers.

Chapter 4

Human-In-The-Loop Experiment Proposal

The results of the offline simulation presented in chapter 3 provides initial insights into the pilot-controller haptic interaction and verifies the novel haptic controller tuning procedure. However, the simulation differs from reality due to assumptions made in modeling the simulation components, particularly those of the pilot cognitive control and the neuromuscular system. In addition, several research questions discussed in chapter 1 can only be answered based on the results of a human-in-the-loop experiment which replicates UAV teleoperation. In this chapter, the design of such an experiment is proposed.

The chapter starts by presenting the experiment goals and critical differences from the simulation in section 4-1. This is followed in section 4-2 by a detailed discussion of the proposed experiment, including the experiment hypothesis, procedure, independent and dependent variables.

4-1 Experiment Goals and Differences from Simulation

The three goals of the experiment are listed below:

1. Validate the novel neuromuscular admittance based tuning procedure with visual and haptic feedback
2. Investigate whether it is beneficial to tune the haptic controller to suit individual subjects
3. Investigate the relationship between neuromuscular admittance and trajectory to be flown without haptic feedback

The first two goals are related to the primary thesis objective whilst the third goal pertains to the secondary thesis objective. The rest of this section focuses on key differences between the experiment and the simulation.

The most important difference from the simulation is the availability of visual information of the environment in the experiment. It is planned to provide a three-dimensional 'outside' camera view, as well as a two-dimensional navigation display to replicate the visual cues typically provided to UAV teleoperators in reality. Although the experiment focuses on the effect of different haptic tuning profiles on UAV teleoperation, the visual feedback provided makes it possible for the pilot to use his/her cognitive ability to actively navigate the UAV around obstacles to the target location. In this way, the visual and haptic control loops i.e., the two mappings of haptic shared control, are taken into account in the experiment.

Preceding research by Smisek revealed that the neuromuscular stiffness of the human arm is dependent on the magnitude and direction of the pilot bias moments (Smisek et al., 2013). Due to the constant control strategy of the pilot model in the simulation, the haptic controller was tuned to only take into account the neuromuscular stiffness corresponding to the constant bias moments along the X' and Y' body axes. However, the visual cues provided, and the different obstacles in the virtual environment (see section 4-2-3) are expected to cause the magnitude of the bias moments to vary continuously in the experiment. Therefore, it is planned to use a two-dimensional nearest neighbor interpolation of the neuromuscular data measured by Smisek (Smisek et al., 2013) to tune the haptic controller in the experiment based on the instantaneous bias moment magnitude and direction.

The final difference between the simulation and the experiment concerns the neuromuscular task instruction. In the simulation, the neuromuscular task performed by the simulated pilot could easily be varied between force, relax and position tasks by changing the NMS model parameters. However, the focus of the experiment is to analyze how the dependent variables (see section 4-2-5) are affected by the different haptic tuning profiles (see section 4-2-4), and to measure admittance itself. Furthermore, if the haptic collision avoidance system (HCAS) is to be made commercially available, it is unreasonable to expect pilots to always respond to haptic feedback in the same manner. Hence, subjects are free to respond to the haptic feedback provided in any way they wish on a neuromuscular level.

4-2 Experiment Design

A two-part experiment is needed to fulfill the three experiment goals outlined in section 4-1. Part one addresses the first two experiment goals and deals with the tuning of the haptic controller (i.e., the primary thesis objective). The second part concerns the third experiment goal where the relationship between trajectory and neuromuscular admittance is examined (i.e., the secondary thesis objective).

Dividing the experiment into two parts provides additional flexibility in scheduling subjects as well as reducing subject boredom and physical strain. Furthermore, as the subject task varies between the experiment parts, clearer instructions can be provided and is likely to reduce subject confusion. In this section, detailed descriptions of the design of both experiment parts are presented.

4-2-1 Subjects and Task Instruction

A total of twelve right-handed[1] subjects are needed for the human-in-the loop experiment, and each subject performs both experiment parts (preferably on two separate days). It is planned to recruit graduate students of the faculty of Aerospace Engineering at TU Delft as subjects. Approval from the *Human Research Ethics Committee* of TU Delft, as well as informed consent from each potential subject will be sought before conducting the experiment.

For both experiment parts, subjects have to perform an active remote-sensing task through an obstacle laden environment in which they have to fly from waypoint to waypoint. As safety of teleoperation is of prime importance, subjects are instructed to avoid collisions with the environment. If a collisions occurs, a loud beep is sounded and a twenty second time penalty is applied during which the experiment is paused. After the penalty, the UAV is repositioned to the start of the sub-task (see section 4-2-3) where the collision occurred and the experiment is continued. Furthermore, subjects are asked to choose and maintain a constant arm-hand orientation and grip. Below, specific subject tasks and instructions for the two experiment parts are discussed separately.

Experiment part one

For part one of the experiment, subjects initially perform an admittance identification measurement, similar to the experiment conducted by Smisek (Smisek et al., 2013), to compute their individual relax task admittance. This data is used to tune one of the haptic controllers to suit their individual neuromuscular properties. During the identification run, subjects are instructed to apply bias moments of three different magnitudes (0N, 0.7N and 1.4N) and six different directions (0^o, 45^o,90^o, 135^o, 180^o and 270^o) in the presence of a wide bandwidth disturbance signal. This disturbance signal is designed to suppress reflexive neuromuscular activity and thus measure relax task admittance/stiffness whilst performing a force task.

After the identification measurement, subjects perform the remote sensing task described earlier. Subjects are provided with haptic moments on a control loaded side-stick to help avoid obstacles in the environment. Subjects are free to respond to the haptic moments in any way they wish on a neuromuscular level. Furthermore, they are instructed to fly as fast as possible and as close to the center of waypoints as possible. This is because the average velocity and the minimum distance to waypoints are used as metrics for comparing different haptic controllers (see section 4-2-5).After each experiment condition, subjects fill in NASA TLX and Eurocontrol SASHA questionnaires to measure workload and situational awareness respectively.

Experiment part two

Subjects are not provided with haptic feedback for the second part of the experiment. Instead, low power disturbance torques are applied on the side-stick to measure the neuromuscular admittance of the subject as he/she flies from waypoint to waypoint. Unlike the first experiment part, subjects are free to fly as fast as they feel comfortable and are not required to fly through the center of waypoints.

[1] Only right-handed subjects can take part in the experiment as the side-stick and arm rest are mounted to the right of the aircraft seat in the Human-Machine Interaction lab where experiments are to be conducted.

4-2-2 Apparatus

The fixed base flight simulator in the Human-Machine Interaction lab (HMI Lab) of the faculty of Aerospace Engineering at TU Delft is to be used to conduct the experiments. Figure 4-1 below displays the apparatus in the HMI lab which are to be used in the experiment. Here the subject is seated in a fully adjustable aircraft chair (1), with an electro-hydraulic side-stick and arm rest (2) mounted on the right side. Visual feedback is provided by three displays. An 18 inch vertically oriented LCD screen with a resolution of 1280×1024 at 60Hz is used for the navigation display(3). The adjacent horizontally oriented LCD screen (with the same specifications) is used during the admittance identification measurements. An onboard camera view (4) is projected onto a white wall 2.9 meters in front of the subject with a resolution of 1024×768 at 60Hz. The camera view of the 'outside world' has a field of view of 60^o horizontally and 45^o vertically.

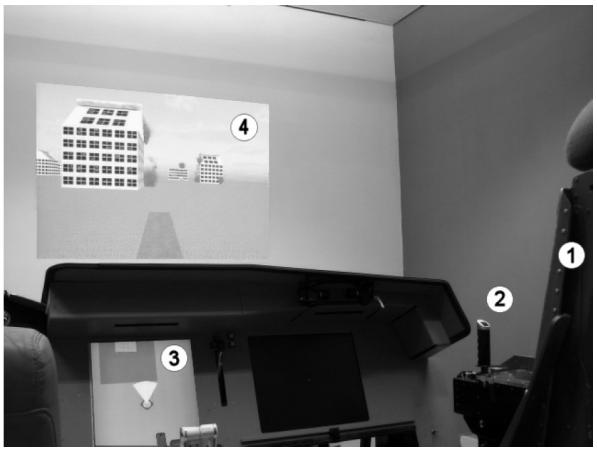

Figure 4-1: Human-Machine Interaction lab with aircraft chair (1), hydraulic side-stick (2), navigation display (3) and onboard camera view (4) (T. Lam, 2009)

The electro-hydraulic side-stick displayed in Figure 4-2 is used for manual control of the UAV and to provide haptic collision avoidance moments. Second order dynamics with an inertia $I_{st} = 0.02\ kgm^2$, a damping coefficient $B_{st} = 0.2\ Nmsrad^{-1}$, and a spring constant $K_{st} = 2.0\ Nmrad^{-1}$ are simulated on the stick. These values match those used by Smisek for neuromuscular admittance identification (Smisek et al., 2013). Furthermore, stick motion is to be limited to 0.35 rad and 0.40 rad in the longitudinal and lateral directions respectively.

The UAV teleoperation simulation code developed by Lam (T. Lam, 2009) using the DUECA middleware layer, in the C++ programming language, is to be modified and used for the experiment. It is anticipated that the implementation of the novel haptic controller tuning algorithm, including the nearest neighbor interpolation discussed in section 4-1, will constitute the majority of changes that need to be made.Finally, the UAV dynamics and parametric risk field parameters are the same as used in the simulation, see sections 3-2-3 and 3-2-4 for more details.

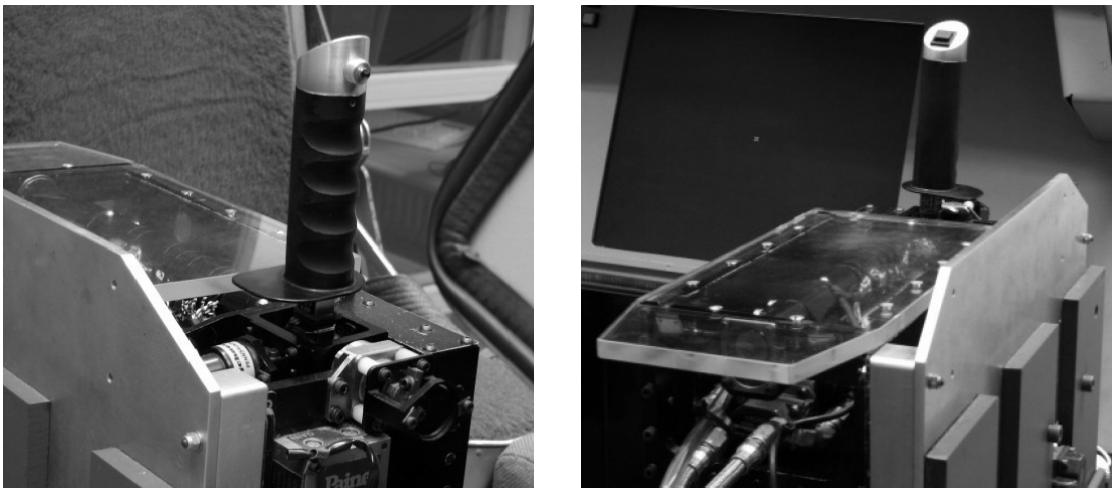

(a) Front (b) Rear

Figure 4-2: Electro-hydraulic side-stick to be used in the experiment (T. Lam, 2009)

4-2-3 Trajectories

The trajectories used in the experiment are the same as those designed by Lam for previous UAV teleoperation experiments (T. Lam, 2009). The virtual environment for the remote sensing task consists of six different obstacles termed as 'subtasks', see Figure 4-3. Here the red star represents waypoints, and the black arrows indicate the UAV reset locations and orientations after a collision. In the three-dimensional camera view, subtasks are pictured as buildings and waypoints as smoke plumes. The smoke plumes are intended to reduce visibility near obstacles.

Each subtask is designed to provoke a different control behavior. For instance, in subtask 3 the subject is required to hover and fly backwards into the building until a stop sign is visible (asterisk). Since the camera view is in the opposite direction of motion, the subject has to rely heavily on haptic feedback to complete the maneuver without collisions.

Three so called 'sectors' are created with the six subtasks in a random order. The three sectors are placed next to each other to obtain a trajectory, see Figure 4-4. Thus a trajectory is made of three repetitions of each subtask and is expected to take approximately six minutes to complete without collisions. To prevent boredom and learning of the trajectories, 6 different trajectories are designed by placing sectors in a different order.

4-2-4 Independent Variables

Two categories of independent variables are defined for the experiment. The first category is concerned with the tuning profile, TP, of the haptic controller, HC. In total six different tuning profiles are tested in the experiment and are listed in Table 4-1 below.

In Table 4-1, tuning profiles TP3 to TP6 take into account the neuromuscular stiffness of the human arm for the force, relax and position tasks. Although TP4 and TP5 are both tuned to match the relax task stiffness, TP4 is based on the average stiffness of 10 subjects from

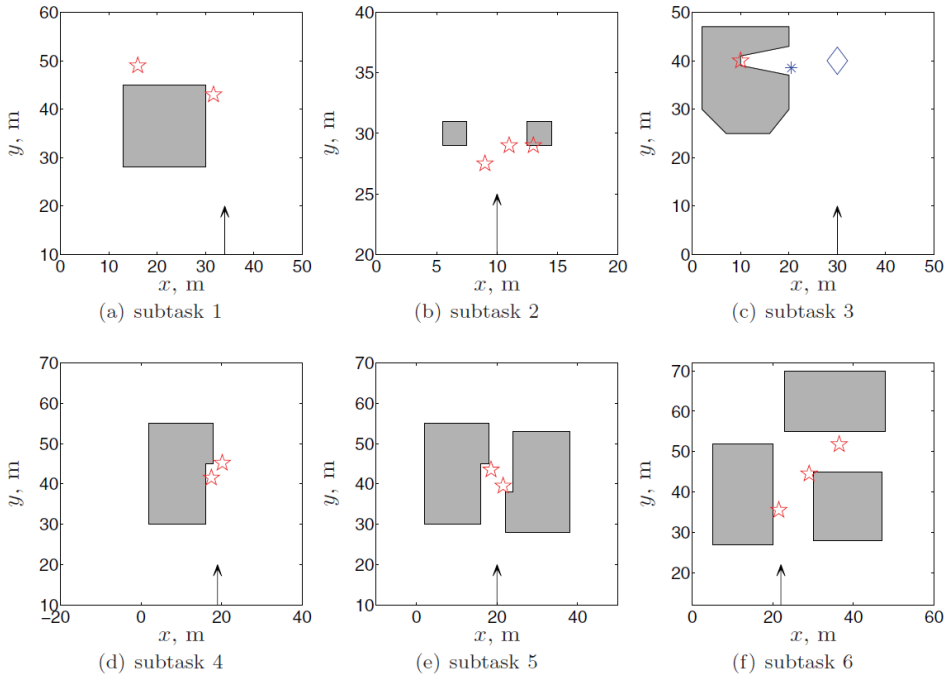

Figure 4-3: Six obstacles or 'subtasks' used in the experiment (T. Lam, 2009). Waypoints are pictured as red stars, and the UAV reset location and orientation after a collision are indicated with black arrows.

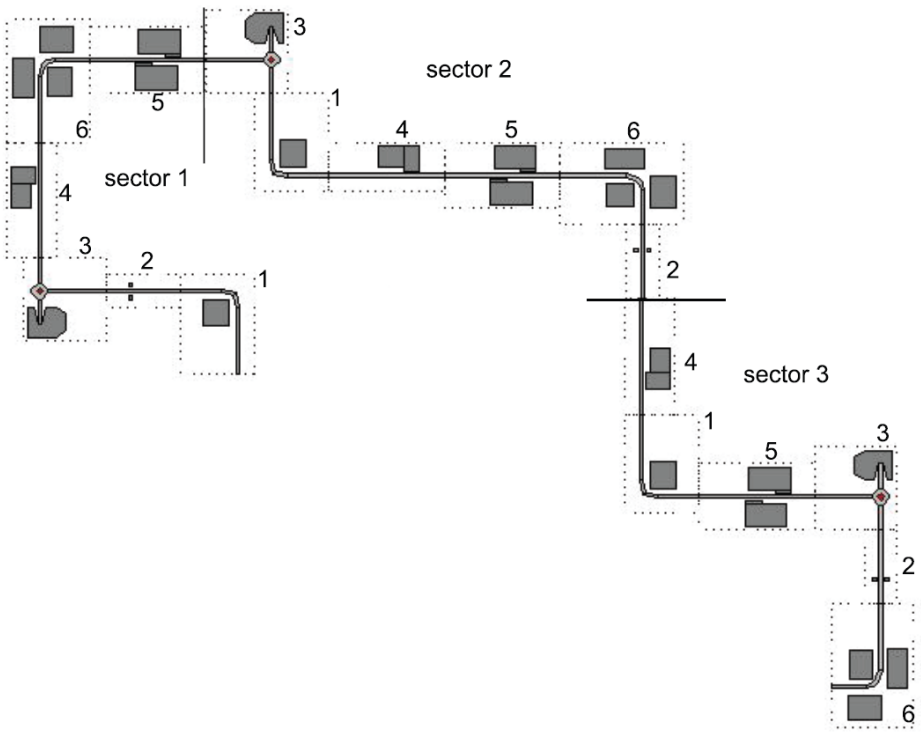

Figure 4-4: An example trajectory consisting of three sectors, with six subtasks each (T. Lam, 2009)

Table 4-1: List of haptic controller tuning profiles to be tested in the experiment

Tuning Profile	Symbol	Description
TP1	HC_{NHF}	No haptic feedback. Pure manual control of UAV.
TP2	HC_{ST}	HC tuned to match only stick stiffness
TP3	HC_{FT}	HC tuned to match force task stiffness
TP4	HC_{RT_A}	HC tuned to match relax task stiffness (average tuning)
TP5	HC_{RT_I}	HC tuned to match relax task stiffness (individual tuning)
TP6	HC_{PT}	HC tuned to match position task stiffness

previous research (Smisek et al., 2013), whilst TP5 is tuned to match the stiffness of each subject participating in this experiment. By comparing the results of these two conditions, it can be determined whether it is worthwhile to tune the haptic controller to suit individual subjects. Just as in the simulation, the stiffness data for the (average) relax task is multiplied by a gain of 0.5 and 7.0 to obtain the stiffness of the force and position tasks respectively. See section 3-2-5 for the rationale behind this approach.

The second category of independent variables are the six subtasks, ST, which make up the obstacles for the remote sensing task, see section 4-2-3 for more details.

4-2-5 Dependent Variables

The dependent variables used to compare different haptic controller tuning profiles can be divided into six categories: performance, control activity, haptic activity, safety, haptic controller accuracy and subjective questionnaires. The neuromuscular admittance is the only dependent variable computed for experiment part two. A complete list of dependent variables is listed in Table 4-2. Here 'RMS' stands for root mean square, 'STD' is the standard deviation and 'SGN' is the sign of a variable (positive/negative).

It can be seen from Table 4-2 that most of the dependent variables are self explanatory and were also used to analyze the results of the simulation, see section 3-3-3. However, a few variables need additional clarification. A sign comparison of the haptic moment, M_H, and the neuromuscular moment, M_{NMS}, is used to determine whether the pilot agrees or disagrees with the actions of the haptic controller. Furthermore, the frequency response functions (FRF) of admittance along the longitudinal (pitch) and lateral (roll) axes, H_{adm_P} and H_{adm_R}, are computed using the method described in section 2-3-3.

Subjective workload and situational awareness are measured using the NASA TLX (Hart & Staveland, 1988) and Eurocontrol SASHA (Jeannot, Kelly, & Thompson, 2003) questionnaires respectively. In the NASA TLX (task load index), workload is defined as the weighted average of 6 subscales: mental demand, physical demand, temporal demand, overall performance, frustration level and effort. Subjects first determine the weight of each subscale by selecting the subscale that had a greater contribution to workload from pairs of subscales. In the second step, each subscale is scored from 0 to 100. The higher the resulting weighted average,

Table 4-2: Dependent variables of the experiment

Performance	$\overline{V}$	Mean body velocity [m/s]
	STD_V	Standard deviation of body velocity [m/s]
	d_{wp}	Minimum distance to waypoints [m]
	$t_{elapsed}$	Time elapsed [s]
Control Activity	$\overline{M}_{NMS}$	Mean NMS moment [Nm]
	$STD_{M_{NMS}}$	Standard deviation of NMS moment [Nm]
	$CR_{\delta_{st}}$	Control Reversal of stick (¿2 degrees) [-]
Haptic Activity	$\overline{M}_H$	Mean haptic moment [Nm]
	STD_{M_H}	Standard deviation of haptic moment [Nm]
Safety	$n_{collisions}$	Number of collisions [-]
	$\overline{d}_{obstacle}$	Average distance to obstacle [m]
Haptic Controller Accuracy	$RMS_{(M_H - M_{NMS})}$	RMS error between the haptic moment and the NMS moment [Nm]
	$SGN_{M_H \ \& \ M_{NMS}}$	Sign comparison of haptic and NMS moments [-]
Subjective	NASA TLX	Subjective workload assessment
	Eurocontrol SASHA	Subjective situational awareness questionnaire
Admittance	H_{adm_P}	FRF of longitudinal/pitch admittance
	H_{adm_R}	FRF of lateral/roll admittance

the higher the subjective workload. In the Eurocontrol SASHA, subjects are asked to rate questions relating to situational awareness on a 7 point scale. The simple average of all questions is taken as a measure of situational awareness, with higher scores indicating better situational awareness. The questions are not standardized, and have to be designed separately for each control task. However, the authors of the method have laid out specific guidelines for the design of questions.

Since the arrangement of subtasks varies from run to run, the dependent variables will be computed per subtask. For the same reason, the data obtained from the experiment will be interpolated over distance (and not time) to ensure fair comparisons between the different haptic controllers. Needless to add, data from multiple runs of the same condition, for a particular subject, will be averaged to reduce noise in the data before the dependent variables are computed.

4-2-6 Hypotheses

The hypotheses of the experiment are in part based on the results of the offline simulation described in chapter 3, and in part based on results from previous research. The five hypotheses of the experiment are listed below:

1. Safety and situational awareness are expected to increase, and workload is expected to decrease when the haptic controller is tuned to take into account the combined system stiffness of the NMS and side-stick when compared to a controller which is tuned to only the stick stiffness.

2. It is anticipated that the controller tuned to the position task stiffness i.e., the over tuned controller, will result in the least number of collisions and the lowest mean risk value. However, this increased safety is expected to come at the cost of increased control activity, particularly when compared to the under tuned controllers (stick tuning and force task controllers). Despite the improvements in safety, the increased control activity and accompanying increased physical effort are likely to lead to the lowest subjective acceptance for the over tuned controller.

3. Under tuned controllers are likely to cause greater lateral control activity and comparatively higher mean risk values. On the other hand, over tuned controllers are expected to have greater longitudinal control activity, as well as lower mean risk values . This is based on the simulation results which showed that under tuned controllers avoided obstacles mainly through heading changes at close range to obstacles, and over tuned controllers avoided obstacles through velocity changes at larger distances from obstacles. The relax task controller, is expected to induce a combination of both control strategies.

4. Individual tuning is likely to improve haptic controller accuracy and reduce subjective physical workload, however this is not expected to be a highly significant effect.

5. Neuromuscular admittance is expected to increase when the operator is subjected to trajectory elements that limit visibility and force a reduction of velocity

The first four hypotheses are related to part one of the experiment and is concerned with the tuning of the haptic controller. The fifth hypothesis is related to the second experiment part and considers the effect of trajectory on neuromuscular admittance variations.

4-2-7 Procedure

The procedure is different for the two experiment parts and are discussed separately below:

Experiment part one

Part one of the experiment begins with the relax task admittance identification measurement. Subjects are allowed to train multiple times to familiarize themselves with the disturbance signal and their control task. Subsequently, all fourteen conditions of the identification experiment are performed. Each condition lasts 60 seconds, and is repeated twice. The data from the identification experiment is used to tune one of the haptic controllers of the remote sensing task to match the neuromuscular properties of a particular subject. It is expected that the entire identification measurement lasts approximately one hour (with breaks).

The remote sensing task begins with separate briefing and training sessions. Once the subjects has experienced all 6 different haptic controller tuning profiles, the measurement runs commence. At the end of a particular run, subjects are informed of their performance and control activity in terms of their average velocity, $\overline{V}$, and mean neuromuscular moment, $\overline{M}_{NMS}$. Each condition, i.e., haptic controller tuning profiles, is repeated until two consecutive runs have similar performance and control activity. Only the data from these two runs are used for analysis. Once all runs for a particular condition has been completed, the subject has to fill in the NASA TLX and Eurocontrol SASHA subjective questionnaires. The conditions are presented in a random order and the subjects are not informed which condition they are flying. It is expected that all six conditions take approximately three hours and thirty minutes to complete with breaks, and thus the total duration of the first experiment part is four hours and thirty minutes.

Experiment part two

In the second experiment part, subjects are not provided with haptic feedback, instead disturbance moments are added to the side-stick to measure their admittance. Subjects are allowed to train until he/she has become accustomed to flying with the disturbance moments. Subjects then fly all six different trajectories once during which data needed to compute admittance is logged. The second experiment part is shorter and is expected to take around one hour and thirty minutes to complete.

During both experiment parts, subjects are encouraged to take breaks between experiment conditions to alleviate physical strain. For the same reason, subjects are encouraged to schedule the two experiment parts on separate days. It is estimated that ten working days are needed to complete the experiment for twelve subjects.

Chapter 5

Conclusion

In this preliminary report, the results of the Literature Study phase of the MSc thesis are presented. This thesis examines neuromuscular admittance based tuning of haptic shared control systems. The primary thesis objective is to validate a novel haptic controller tuning law which takes into account the response of the neuromuscular system to haptic cues and thereby improve user acceptance of haptic shared control systems. To further improve the tuning algorithm, the secondary thesis objective is to investigate the relationship between neuromuscular admittance and the trajectory to be flown.

A haptic collision avoidance system (HCAS) for UAV teleoperation is used as a framework to accomplish the primary and secondary thesis objectives. The HCAS system was designed by Lam and Boschloo to improve the safety of UAV teleoperation. The system provides additional haptic feedback forces to help teleoperators steer the UAV away from obstacles. Previous experimental investigations using a 'trial and error' method for tuning the haptic controller revealed that haptic feedback significantly improved performance, but at the cost of increased physical workload.

Tuning of haptic shared control systems is difficult because the human neuromuscular system (NMS) is highly adaptive. For a non-optimal tuning setting, the NMS will vary the relative strengths of its reflexive feedback paths or use muscle co-contraction to stabilize the system and achieve adequate performance. This adaptation to a non-optimal tuning setting is accompanied with increased user physical workload and frustration over time. To overcome this problem, in this thesis the haptic controller is tuned to match a so called 'design' neuromuscular admittance (inverse stiffness) setting. In this way, the NMS will adapt to a tuning setting that is based on its own properties, and thus reduce conflicts between the teleoperator and the automation on a neuromuscular level. The relax task stiffness has been chosen as the design point as reflexive feedback paths are suppressed during this task. In theory this should reduce the high physical workload commonly reported for haptic shared control systems.

To verify the novel tuning procedure, an offline simulation of the HCAS was performed. In the simulation, the visual feedback loop was intentionally neglected such that the results could be analyzed in terms of the haptic tuning procedure alone. The simulation included a model

of the NMS to study the pilot-controller haptic interactions. The results of the simulation revealed that the setting of the NMS and haptic controller had a significant impact on the overall response of the system. For all neuromuscular task instructions, the haptic controller tuned to the same stiffness as the NMS model had the best overall response. Additionally, it was found that under-tuning the haptic controller led to collisions, whilst over-tuned controllers provided highly erratic and unstable haptic feedback. The haptic controller tuned to the relax task stiffness was found to be the best middle ground when considering both the absolute response, as well as sensitivity to neuromuscular task instruction. Therefore, the results of the simulation verified the novel tuning procedure, and the choice of the relax task as the design point for tuning the haptic controller.

In the next phase of the thesis, a human-in-the-loop experiment will be conducted to validate the new tuning procedure and to investigate the secondary thesis objective. The experiment will be performed in the Human-Machine Lab at the Control and Simulation department of the faculty of Aerospace Engineering at TU Delft. Subjects will be required to perform a remote sensing task in an urban obstacle laden environment. To limit subject fatigue, the experiment will divided into two parts, with each part investigating a separate thesis objective. Each part has six independent variables and therefore it is planned to recruit twelve subjects. The dependent variables for the first experiment part will include subjective workload and situational awareness metrics, in addition to performance, control activity, safety and haptic interaction measures. During the second experiment part, haptic feedback will not be provided. Instead a wide bandwidth disturbance torque based on the Reduced Power Method will be applied on the side-stick to measure neuromuscular admittance. The majority of work required to set up the experiment involves modifying existing code to match the conditions of the experiment. At present, it is planned to conduct the experiment in the month of September 2013.

Part III

EXPERIMENT APPENDICES

Appendix A

Experiment Subject Details

A total of twelve right-handed male subjects took part in the human-in-the-loop experiments. All subjects participated in both experiment sessions. Table A-1 lists details of the experiment subjects.

Table A-1: Experiment Subject Details

ID	**Age [Years]**	**Height [m]**	**Weight[kg]**	**BMI** $[kg/m^2]$
1	24	1.87	88	25.17
2	23	1.69	66	23.11
3	23	1.80	65	20.06
4	23	1.85	70	20.45
5	23	1.90	82	22.71
6	24	1.95	73	19.20
7	23	1.93	83	22.28
8	23	1.77	74	23.62
9	23	1.82	70	21.13
10	25	1.82	81	24.45
11	23	1.72	60	20.28
12	24	1.84	75	22.15
Mean	23.42	1.83	73.92	22.05
Median	23	1.83	73.50	22.22
Standard Deviation	0.67	0.08	8.34	1.86

Appendix B

Call for Participants

Subjects for the human-in-the-loop experiment were recruited from the graduate student population of the Faculty of Aerospace Engineering at TU Delft. Participation was voluntary and no financial compensation was offered. The following page provides the literature used to advertise the experiment.

Call for Participants

Tuning of a Haptic Collision Avoidance System for UAV Teleoperation

Experiment Dates: Monday, 23rd of September - Friday, the 4th of October

Number of Sessions: 2

Experiment Duration: Session A - 1.5 hours, Session B - 4.0 hours

Experiment Location: HMI Lab (room 0.37, ground floor), Faculty of Aerospace Engineering.

Choose time slots here: Session A http://doodle.com/rntz5rfb9ua3nr2f

Session B http://doodle.com/mvs2cba9bwsxnyhm

Contact: Emmanuel Sunil - e.sunil@student.tudelft.nl

Haptic collision avoidance system:
To improve the safety of unmanned aerial vehicles (UAVs), the Control and Simulation department has developed a new control interface which provides haptic (force-feedback) cues to help teleoperators steer away from potential collisions.

Present research:
In this research, the system is further optimized by taking into account the human neuromuscular system's response to haptic feedback cues. To test this novel tuning algorithm, a two part experiment has been designed:

1. Session A: Neuromuscular admittance measurement
2. Session B: Haptic feedback assessment during a simulated remote sensing task in an obstacle laden urban environment

Please note:

- If interested, please sign up for both experiment sessions. Sign up for session A first, and session B on a later date.
- An experiment briefing with more details will be emailed to you after signing up for both sessions
- Right-handed participants are preferred due to lab constraints
- No flying or driving experience necessary
- Participation is voluntary and no monetary compensation is offered

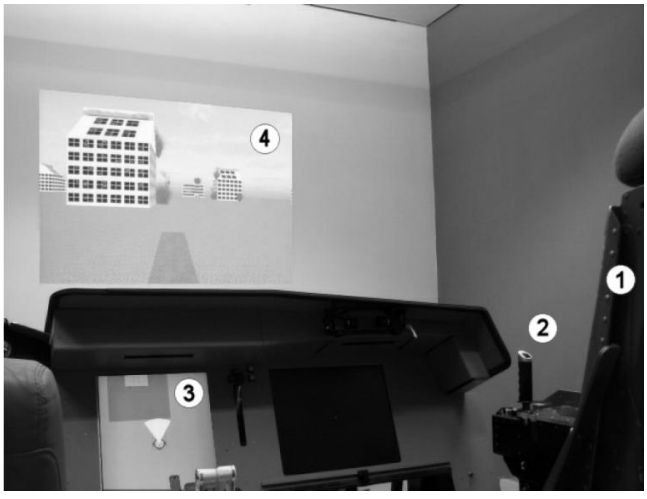

HMI lab with aircraft chair (1), side-stick (2), navigation display (3) and onboard camera view (4)

Appendix C

Experiment Briefing

The experiment briefing sent to subjects prior to the experiment is included in the following pages.

Tuning of a Haptic Collision Avoidance System for UAV Teleoperation

Experiment Briefing

1 Introduction

The goal of this research is to validate a novel tuning algorithm for haptic feedback systems which makes use of neuromuscular models and measurements. The new method is to be validated in the context of a haptic collision avoidance system (HCAS) for UAV teleoperation[1]. To this is end, a two part experiment has been designed:

1. Experiment A: Neuromuscular admittance measurement
2. Experiment B: Haptic feedback assessment

This document serves as a pre-experiment briefing, and contains details on the two experiment parts, including participant tasks, experiment conditions and procedures.

2 Experiment A: Admittance Measurement

The essential dynamics of the neuromuscular system can be determined by measuring it's end-point admittance. Endpoint admittance is defined as the ratio between force (input) and position (output). In experiment A, the neuromuscular admittance of the participant is measured through an abstract control task.

Task: Your task is to **apply forces of pre-determined magnitudes and directions on the side-stick in the presence of small disturbance torques**. The disturbance torques are used to measure your neuromuscular admittance. In this experiment, two distinct 'settings' of your neuromuscular system will be determined. These settings are named the 'force task' and 'relax task', and can be measured by **reacting to the disturbance torques in two different ways**:

- Force task: "Actively give way to the disturbance torques" (i.e., do not resist them, but try to follow the disturbance torques).
- Relax task: "Relax your muscles and do not react to the disturbance torques."

[1] More information about the HCAS can be found in section 5

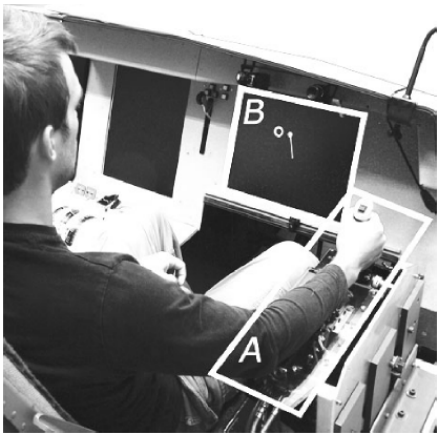

(a) Experiment A task

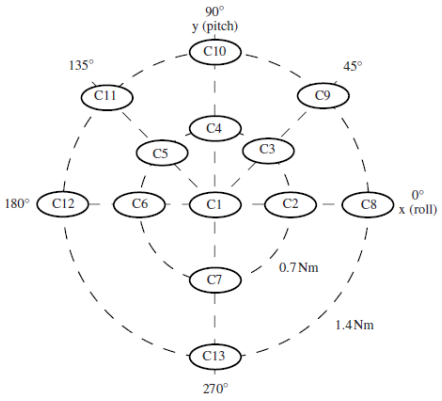

(b) Experiment A conditions

Figure 1: Experiment A setup

An on-screen visualization will help you apply the appropriate 'bias' forces. Here, participants must apply forces to position a pendulum shaped object within a larger circular shape, see Figure 1(a). **To obtain uniform and comparable data, it is important that you hold the stick with constant orientation and grip for all experiment conditions.**

Conditions: To gain a complete model of your neuromuscular dynamics, thirteen conditions of varying bias force amplitudes and directions are evaluated, see Figure 1(b). For the central condition C1, participants will be required to perform both the force and relax tasks. For the remaining conditions, participants are only required to perform the force task.

Procedure: The experiment commences with multiple training runs to allow participants to familiarize themselves with the control task. Subsequently, the actual measurement runs will be performed. Each condition pictured in Figure 1(b) will be performed once and lasts 60 seconds (containing three periods of the disturbance torque). The conditions will be presented in a random order. Frequent breaks will be taken frequently to avoid fatigue, and at least once every three conditions. It is expected that experiment A will take approximately 1 hour and 30 minutes, including training, breaks and the pre-experiment briefing.

3 Experiment B: Haptic Feedback Assessment

The novel haptic tuning procedure will be tested in experiment B. This experiment part simulates a remote sensing scenario in an obstacle laden urban environment.

Task: Your tasks, in order of priority, are to fly a control augmented UAV helicopter:

1. **Without colliding with any obstacles**
2. **As close as possible to the center of waypoints**
3. **As fast as possible**

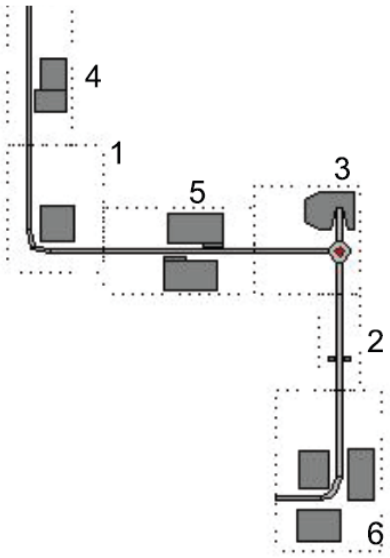

Figure 2: An example trajectory consisting of six different obstacles arranged randomly

Trajectories are composed of six different obstacles arranged randomly, see Figure 2 for an example trajectory. A trajectory is expected to take around two minutes and thirty seconds to complete (without collisions). Visual feedback will be provided by two displays: the onboard camera image is projected onto the wall in front of you, and a navigation display is shown on an LCD screen. Waypoints are shown as smoke plumes on both displays and are located in close proximity to obstacles. The smoke plumes will partly cover buildings to make visual information incomplete. Every collision results in a 20 second time penalty during which the simulation is paused and a beeping sound is played. **To obtain uniform and comparable data, it is important that you hold the stick with constant orientation and grip for all experiment conditions.**

Conditions: A total of seven different conditions will be evaluated, with each condition corresponding to a different level of haptic feedback. In one of the conditions, small disturbance torques are applied on the side-stick to measure your neuromuscular admittance whilst performing the remote sensing task.

Procedure: Each condition is preceded by at least one training run to familiarize yourself with the level of haptic feedback provided. Conditions are repeated four times. Conditions are presented in a random order and you will not be informed which condition you are attempting. At the end of a particular condition, subjects are requested to fill in workload and situational awareness questionnaires. Participants are encouraged to take at least one break at the end of each condition to reduce fatigue. The total duration of experiment B, including breaks, questionnaires, training and the pre-experiment briefing is expected to be four hours.

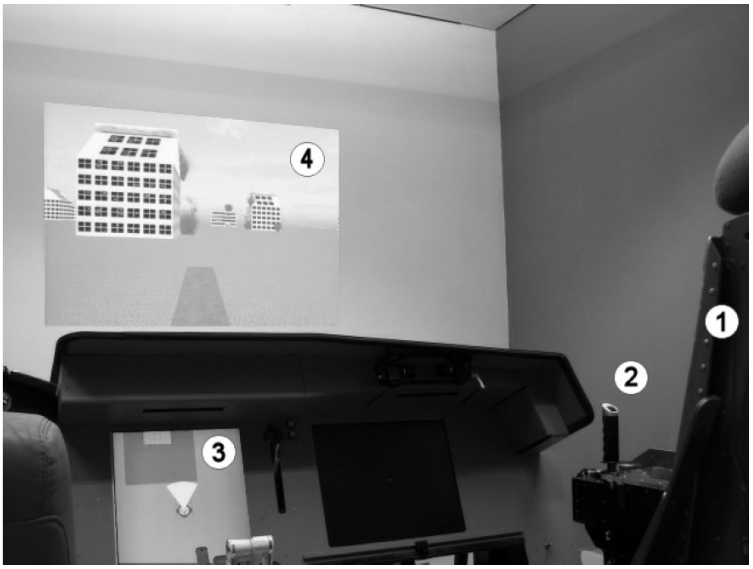

Figure 3: Human-Machine Interaction lab with aircraft chair (1), hydraulic side-stick (2), navigation display (3) and onboard camera view (4)

4 Apparatus

The fixed base flight simulator in the Human-Machine Interaction lab (HMI Lab) of the faculty of Aerospace Engineering at TU Delft is to be used to conduct the experiments. The lab is located in room 0.37 on the ground floor (next to the C&S coffee corner). Here participants are seated on a fully adjustable aircraft chair and control the UAV via a hydraulic control loaded side-stick mounted on the right hand side. The stick pitch axis controls the UAV velocity and the roll axis controls UAV yaw rate. UAV altitude is held constant by an autopilot system. It is important that participants **choose and maintain a constant arm-hand orientation and grip**. Figure 3 displays the apparatus in the HMI lab which are to be used in the experiment, including the onboard camera view and navigation displays.

5 Background

At present, UAVs are typically controlled from ground control stations (GCS) which predominantly supplies only visual information to the UAV teleoperator. This visual feedback has low resolution, contrast and field of view. Additionally, the physical separation between the aircraft and the teleoperator leads to a lack of auditory, kinesthetic and vestibular sensory inputs. Pilots of manned aircraft are able to integrate these multi-sensory inputs to gain better situational awareness (SA) of the aircraft state and the environment. These shortcomings can overload the visual channel of UAV teleoperators, resulting in situations with poor situational awareness and high workload.

In an attempt to overcome these issues and to improve UAV safety in obstacle laden environments, a new control interface has been developed which provides haptic or force feedback

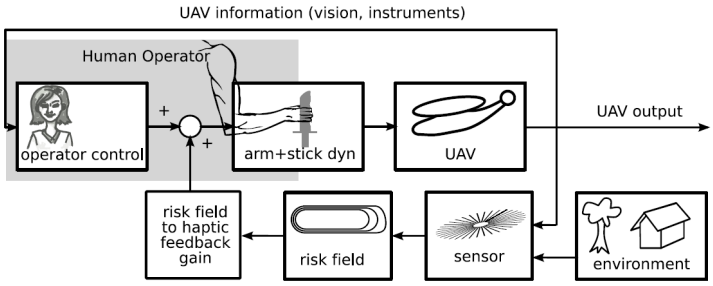

Figure 4: Basic working principle of the haptic collision avoidance system (HCAS)

to steer teleoperators away from potential conflicts. This haptic collision avoidance system (HCAS) makes use of an 'artificial force field' to compute the risk or probability of collisions to detected obstacles in the environment. This risk is translated to a haptic moment by a so called 'haptic controller' and is applied on the aircraft side-stick. Figure 4 depicts the basic working principle of the HCAS. In past research, haptic feedback has been found to be particularly useful when obstacles are not directly visible on the video feed transmitted from onboard cameras.

6 Experiment Scheduling and Contact Details

The experiment is to be conducted between Monday the 23^{rd} of September and Friday the 4^{th} of October. Participants can indicate their preferred time slots for the two experiment parts on the experiment Doodle web-pages.

- Experiment A: http://doodle.com/rntz5rfb9ua3nr2f
- Experiment B: http://doodle.com/mvs2cba9bwsxnyhm

It is important that participants sign up for experiment A first, and experiment B on a later date. This is because data collected during experiment A is used in experiment B. As lab availability is limited, we kindly request participants to be present at the scheduled time. If you would like to change your time slot or cancel your participation, please inform us by email at least one day in advance.

If have any questions or would like more information concerning the experiment setup, please contact Emmanuel Sunil.
Email: e.sunil@student.tudelft.nl Phone: 0642477580.

Thank you for participating in this research!

Appendix D

Subjective Questionnaires

Questionnaires were used to measure subjective workload, situational awareness and haptic feedback acceptance after each hapitc feedback configuration. Workload was measured using a software version of the NASA Task Load Index (TLX) that was downloaded from `http://www.playgraph.com/2009/blog-2/nasa-tlx`. Situational awareness and haptic feedback acceptance were recorded by means of two questionnaires, based on the Eurocontrol SASHA method. The following pages contain paper versions of the three subjective questionnaires.

NASA Task Load Index (TLX) rating sheet

Subject: Tunnel: Run:

Step 1 Sources of load

☐ Mental demand	☐ Physical demand
☐ Mental demand	☐ Temporal demand
☐ Mental demand	☐ Performance
☐ Mental demand	☐ Effort
☐ Mental demand	☐ Frustration level
☐ Physical demand	☐ Temporal demand
☐ Physical demand	☐ Performance
☐ Physical demand	☐ Effort
☐ Physical demand	☐ Frustration level
☐ Temporal demand	☐ Performance
☐ Temporal demand	☐ Effort
☐ Temporal demand	☐ Frustration level
☐ Performance	☐ Effort
☐ Performance	☐ Frustration level
☐ Effort	☐ Frustration level

Step 2 Magnitude of load

Mental demand

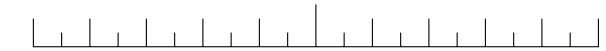

Low High

Physical demand

Low High

Temporal demand

Low High

Performance

Good Poor

Effort

Low High

Frustration level

Low High

NASA TLX rating descriptions		
Title	**Endpoints**	**Description**
Mental demand	Low, High	How much mental and perceptual activity was required? (e.g. thinking, deciding, calculating, remembering, looking, searching, etc.) Was the task easy or demanding, simple or complex, exacting or forgiving?
Physical demand	Low, High	How much physical activity was required (e.g. pushing, pulling, turning, controlling, activating, etc.)? Was the task easy or demanding, slow or brisk, slack or strenuous, restful or laborous?
Temporal demand	Low, High	How much time pressure did you feel due to the rate or pace at which the tasks or task elements occured? Was the pace slow and leisurely or rapid and frantic?
Effort	Low, High	How hard did you have to work (mentally or physically) to accomplish your level of performance?
Performance	Good, Poor	How successful do you think you were in accomplishing the goals of the task set by the experimenter (or yourself)? How satisfied were you with your performance in accomplishing these goals?
Frustration Level	Low, High	How insecure, discouraged, irritated, stressed and annoyed versus secure, gratified, content, relaxed and complacent did you feel during the task?

Situational Awareness Questionnaire

Name: .....

Date: .....

Scenario: .....

1. I knew where I was and where I had to go next (I felt aware of my surroundings)

☐	☐	☐	☐	☐
Never		Sometimes		Always

2. I had enough time to plan and execute a path through the center of waypoints (smoke plumes)

☐	☐	☐	☐	☐
Never		Sometimes		Always

3. I was able to judge the distance to obstacles easily

☐	☐	☐	☐	☐
Never		Sometimes		Always

4. I was able to judge the severity of a dangerous situation easily

☐	☐	☐	☐	☐
Never		Sometimes		Always

5. I was surprised by obstacles outside my visual field of view

☐	☐	☐	☐	☐
Never		Sometimes		Always

6. I was surprised by the visual and/or haptic feedback that I received

☐	☐	☐	☐	☐
Never		Sometimes		Always

7. I would rate my overall situational awareness during this experiment condition as

☐	☐	☐	☐	☐
Poor		Average		Excellent

Haptic Feedback Questionnaire

1. How useful was the haptic feedback in helping you :
   a) be aware of obstacles?

☐	☐	☐	☐	☐
Not Useful		Moderately Useful		Extremely Useful

   b) judge the severity of a situation?

☐	☐	☐	☐	☐
Not Useful		Moderately Useful		Extremely Useful

   c) avoid collisions with obstacles?

☐	☐	☐	☐	☐
Not Useful		Moderately Useful		Extremely Useful

2. How often did you have to counteract haptic feedback forces? (Did you understand/agree with the intensions of the haptic feedback?)

☐	☐	☐	☐	☐
Never		Sometimes		Always

3. How comfortable was it to control the UAV with haptic feedback?

☐	☐	☐	☐	☐
Uncomfortable		Moderately Comfortable		Very Comfortable

4. Did you ever find the haptic feedback distracting from achieving your primary goal of avoiding obstacles?

☐	☐	☐	☐	☐
Never		Sometimes		Always

5. Did you feel that the haptic feedback could help you during a dangerous situation that you did not foresee?

☐	☐	☐	☐	☐
Never		Sometimes		Always

6. What did you think about the strength of the haptic feedback provided?

☐	☐	☐	☐	☐
Very Weak		Just Right		Too Strong

Appendix E

Ethics Committee Forms

Before the human-in-the-loop experiments were conducted, permission from the TU Delft Human Research Ethics Committee was sought. The following pages contain the two filled-out forms needed to gain ethics approval from the committee.

Research Ethics Checklist

1. Complete this checklist before you start your research study.
2. Send/give the completed and signed form to the Human Research Ethics Committee HREC@tudelft.nl
3. Keep a copy for your records.

Important note concerning question 1

Note that research involving participants who are in a dependent or unequal relationship with the researcher or research supervisor (e.g., the researcher's or research supervisor's students or staff) may be regarded as a vulnerable group.[1] If your study involves such participants, it is essential that you safeguard against possible adverse consequences of this situation (e.g., allowing a student's failure to complete their participation to your satisfaction to affect your evaluation of their coursework). This can be achieved by ensuring that participants remain anonymous to the individuals concerned (e.g., you do not seek names of students taking part in your study). If such safeguards are in place, or the research does not involve other potentially vulnerable groups or individuals unable to give informed consent, it is appropriate to check the NO box for question 1.

[1] Children, mentally challenged, historically discriminated-against, etc.

Delft University of Technology
ETHICS REVIEW CHECKLIST FOR STAFF AND PhD RESEARCH

This checklist should be completed for every research study that involves human participants. Before completing it please refer to the Central Committee on Research Involving Human Subjects (CCMO) http://www.ccmo-online.nl/main.asp?pid=1&taal=1 This checklist must be completed fully and submitted before potential participants are approached to take part in your research study.

Project title: Tuning of a Haptic Collision Avoidance System for UAV Teleoperation

Name(s) of researcher(s): E. Sunil (1544136)

Name of supervisor (if applicable): ir. J. Smisek, dr.ir. M. M. van Paassen, prof.dr.ir. M. Mulder

	Yes	No
1. Does the study involve participants who are particularly vulnerable or unable to give informed consent? (e.g., children, people with learning difficulties, patients, people receiving counselling, people living in care or nursing homes, people recruited through self-help groups)	☐	■
2. Will it be necessary for participants to take part in the study without their knowledge and consent at the time? (e.g., covert observation of people in non-public places)	☐	■
3. Will the study involve actively deceiving the participants? (e.g., will participants be deliberately falsely informed, will information be withheld from them or will they be misled in such a way that they are likely to object or show unease when debriefed about the study)	☐	■
4. Will the study involve discussion or collection of information on sensitive topics? (e.g., sexual activity, drug use, mental health)	☐	■
5. Will drugs, placebos, or other substances (e.g., drinks, foods, food or drink constituents, dietary supplements) be administered to the study participants?	☐	■
6. Will blood or tissue samples be obtained from participants?	☐	■
7. Is pain or more than mild discomfort likely to result from the study?	☐	■
8. Does the study risk causing psychological stress or anxiety or other harm or negative consequences beyond that normally encountered by the participants in their life outside research?	☐	■
9. Will financial inducement (other than reasonable expenses and compensation for time) be offered to participants?	☐	■
10. Will the study involve recruitment of patients or staff through the TU Delft, or working at a TU Delft site?	☐	■
11. Will the experiment collect and store videos, pictures, or other identifiable data of human subjects? a. If "yes", you have to ensure that collected data is safeguarded physically and will not be accessible to anyone outside the study. Furthermore, the data has to be de-identified if possible and has to be destroyed after a scientifically appropriate period of time.	☐	■

12. Will the experiment involve the use of devices that are not "CE" certified? ■ □

b. If "yes", was the device built in-house? ■ □

i. If "yes", was it inspected and certified safe by a safety expert at TU Delft? (please provide records of the inspection) □ ■

ii. If "no", was it inspected by some other, qualified authority in safety and approved? (please provide records of the inspection) □ ■

13. Has or will this research be submitted to a research ethics committee other than this one? (if so, please provide details) □ ■

Name of Committee:

Date of submission:

Submission or approval number (if known):

If you have answered NO to all questions above (excluding sub-questions) above (i.e., a more detailed submission to an ethics committee is not required), please very briefly (100-200 words) summarise your research, stating the question for the research, who will participate, the number of participants to be tested and the methods to be used.

Write or type your summary here:

The goal of the experiment is to investigate neuromuscular admittance based tuning of haptic feedback systems in the context of a collision avoidance system for unmanned aerial vehicles (UAV).

The experiment consists of two parts. In the first part, subjects perform an abstract control task designed to measure their neuromuscular admittance. Admittance is measured using small disturbance torques on the side-stick. In the second experiment part, subjects perform a simulated remote sensing task of a teleoperated UAV in an obstacle laden urban environment. During this experiment subjects will be provided with varying levels of haptic feedback forces. Subject performance, workload and situational awareness will be evaluated during the second experiment part to analyze the effects of haptic feedback. To prevent physical fatigue, the two experiment parts are to be performed on separate days. Furthermore, subjects will be encouraged to take breaks whenever they feel tired.

It is planned to recruit twelve right-handed subjects from the student population of Aerospace Engineering for this experiment. Potential subjects will be briefed well ahead of the experiment and participation is entirely voluntary. Furthermore, participants are free to withdraw at any time during the experiment if they should choose to do so. No financial compensation will be offered for participation.

The experiment will be conducted in the Human-Machine Interaction (HMI Lab)[2] of the faculty of Aerospace Engineering, see Figure 1. The lab consists of a fixed base aircraft/automobile simulator and can be used as a platform for control task and visual perception research. The main apparatus of interest is a control loaded hydraulic side-stick which subjects are to use to control the UAV, see Figure 2. This side-stick has passed ARBO inspections to check for its electrical , hydraulic and general safety. However no safety records declaring the safe use of the stick exists. This is because the safety officer in charge of inspecting the scientific facilities of the TU Delft does not have the authority to provide safety certifications. Despite this, it should be noted that the stick has been used for many research projects in the past without incident.

[2] http://www.lr.tudelft.nl/en/organisation/departments/control-and-operations/control-and-simulation/facilities/human-machine-laboratory/

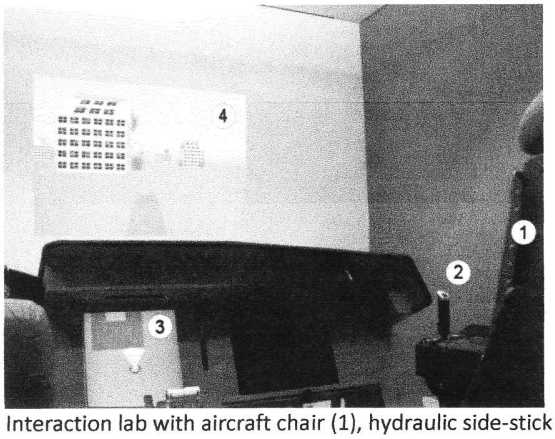

Figure 1: Human-Machine Interaction lab with aircraft chair (1), hydraulic side-stick (2), navigation display (3) and onboard camera view (4)


Figure 2: Hydraulic side-stick of HMI lab

Send the completed and signed form to dr. David Koepsell, Chair, Human Research Ethics Committee: HREC@tudelft.nl, TBM-Faculty, Values and Technology, 5 Jaffalaan rm. B4.250

If you have answered 'NO' to all questions you can proceed with your study.
If you have answered 'YES' to **any of the questions above**, you will need to submit an application for ethics approval, including sample consent documents to this committee.
To submit your research proposal for consideration by the Human Subjects Research Ethics Committee, use the ethics approval application form available on Blackboard. This Committee meets monthly during term time, and less frequently out of term time.

Signature(s) of researcher(s):

E.Sunil
10/09/13

Signature research supervisor (if applicable):

M. M. van Paassen
10/09/13

Research Ethics Application

Please fill in the checklist first if you have not done so already. Please complete this form digitally and send it the Ethics Committee.

Date of Submission:10-9-2013

Project Title: Tuning of a Haptic Collision Avoidance System for UAV Teleoperation

Name(s) of researcher(s): E. Sunil (1544136)

Name of supervisor (if applicable): ir. J. Smisek, dr.ir. M. M. van Paassen, prof.dr.ir. M. Mulder

Contact Information

Department: Aerospace Engineering

Telephone number: +(0)642477580 (E.Sunil)

E-mail address: e.sunil@student.tudelft.nl

Contact information of external partners (if applicable):

Research

R.1. What is the research question? Please indicate what scientific contributions you expect from the research.
Research question: Is it beneficial to include neuromuscular admittance in the tuning of haptic shared control systems?
Scientific Contributions: Experimental validation of a new tuning method aimed at reducing user workload and improving situational awareness for users of haptic shared control systems

R.2. What will the research conducted be a part of?
☐Bachelor's thesis
■Master's thesis
☐PhD thesis
☐Research shills training
Other, namely:

R.3. What type of research is involved?
☐Questionnaire
☐Observation
■Experiment
Other, namely:

R.4. Where will the research be conducted?
☐Online
■At the university
☐Off-campus / non-university setting:
Other, namely:

R.5. On what type of variable is the research based?
Neuromuscular admittance is measured offline using disturbance torques of small amplitude on the control stick and by measuring the resulting stick deflections and handling moments.
Performance is measured in terms of the number of collisions, minimum distance to waypoints and time to complete task. Workload and situational awareness are to be measured using the well known NASA Task Load Index (TLX) and Eurocontrol SASHA questionnaires respectively.

R.6. If the research is experimental, what is the nature of the experimental manipulation?
In the first experiment part, neuromuscular admittance is measured. Subjects have to apply forces of pre-determined magnitudes and directions on the side-stick in the presence of small disturbance torques.
In the second experiment part, seven different tuning profiles of the haptic controller are tested.

R.7. Why is the research socially important? What benefits may result from the study?
Haptic shared control has been proven to improve the safety and user situational awareness of many control tasks. However current heuristic tuning methods have been found to increase user physical workload. In this research, a human centred tuning approach taking into account neuromuscular properties for the tuning process is validated. It is expected that the new method will reduce physical workload and thereby improve user acceptance of haptic shared control systems, particularly in its application for UAV teleoperation.

R.8. Are any external partners involved in the experiment? If so, please name them and describe the way they are involved in the experiment.
No external partners.

Participants

Pa.1. What is the number of participants needed? Please specify a minimum and maximum.
Minimum: 12
Maximum: 14

Pa.2.a. Does the study involve participants who are particularly vulnerable or unable to give informed consent? *(e.g., children, people with learning difficulties, patients, people receiving counselling, people living in care or nursing homes, people recruited through self-help groups)*
No, only participants capable of giving informed consent will take part in the study. Fellow students from the faculty of Aerospace Engineering will be recruited as subjects. Anyone approached has the right to refuse and withdraw participation without reason.

Pa.2.b. If yes and unable to give informed consent, has permission been received from caretakers/parents?
Not applicable.

Pa.3. Will the participants (or legal guardian) give written permission for the research with an 'Informed Consent' form that states the nature of the research, its duration, the risk, and any difficulties involved? If no, please explain.
Participants will be provided with a detailed experiment briefing. This experiment briefing is attached to this application form. Just prior to taking part in the experiment, participants will be re-informed about the experiment and written informed consent form is to be signed before participation can continue.

Pa.4. Are the participants, outside the context of the research, in a dependent or subordinate position to the investigator (such as own children or students)? If yes, please explain.
No, participants are not in a dependent or subordinate position with respect to the investigator.

Pa.5. How much time in total (maximum) will a participant have to spend on the activities of the study?
Participants will spend approximately 5.5 hours on the experiment.

Pa.6. Will the participants have to take part in multiple sessions? Please specify how many and how long each session will take.
Yes, the experiment is split into two sessions. The first session is 1.5 hours and the second session is 4 hours.

Pa.7. What will the participants be asked to do?
In the first session participants will first have to complete an abstract control task where they will be asked to apply bias forces of varying magnitudes and directions on the control stick.

In the second session, haptic feedback will be provided and participants will be instructed to fly as fast as possible whilst avoiding collisions with the environment. Subjects are free to react to the seven different haptic feedback profiles as they please. At the end of each condition participants will be asked to fill in the NASA TLX and Eurocontrol SASHA questionnaires to measure subjective workload and situational awareness respectively.

Pa.8. Will participants be instructed to act differently than normal or be subject to certain actions which are not normal? *(e.g. subject to stress inducing methods)*
No, participants are free to act as they wish to the experiment conditions. In fact their natural reactions to the experiment conditions are of prime interest to this study. To simulate collisions with obstacles, the experiment will be paused for 20 seconds (for every collision).

Pa.9. What are the possible (reasonably foreseeable) risks for the participants? Please list the possible harms if any.
No foreseeable risks to the participants are anticipated.

Pa.10. Will extra precautions be taken to protect the participants? If yes, please explain.
All collected data will be kept anonymous. Any arising physical fatigue due to sitting in a fixed position for a prolonged period is to be mitigated by taking frequent breaks, at least once every half an hour.

Pa.11. Are there any positive consequences for a participant by taking part in the research? If yes, please explain.
No. However, negative consequences are also not foreseen. No monetary compensation is offered.

Pa.12. Will the participants (or their parents/primary caretakers) be fully informed about the nature of the study? If no, please explain why and state if they will receive all information after participating.
Participants will receive a briefing prior to the experiment. This briefing informs the participants the nature of their task, experiment conditions and procedures (see attached briefing). During the experiment a number of conditions will be evaluated. Participants will not be informed apriori about the next condition to prevent goal related behaviour. Additionally, experiment conditions will be randomized. At the end of the experiment, any questions that the participants have will be answered.

Pa.13. Will it be made clear to the participants that they can withdraw their cooperation at any time?
Yes, during the pre-experiment briefing participants will be told that they have the right to withdraw participation at any time without reason.

Pa.14. Where can participants go with their questions about the research and how are they notified of this?
Participants can personally contact my supervisors or myself by email, phone, or even request a face-to-face meeting. Contact details will be indicated in the pre-experiment briefing.

Pa.15. Will the participants receive a reward?
☐Travel expenses
☐Compensation per hour
■Nothing
Other, namely:

Pa.16. How will participants be recruited?
An email with the pre-experiment briefing will be sent out to the students of Aerospace Engineering. If they would like to participate, they can indicate their preferred time slot on a Doodle web-page.

Privacy

Pr.1. Are the research data made anonymous? If no, please explain.
All collected data will be anonymous and data will classified by a numerical participant id.

Pr.2. Will directly identifiable data (such as name, address, telephone number, and so on) be kept longer than 6 months? If yes, will the participants give written permission to store their information for longer than 6 months?
Directly identifiable data will be deleted within 2/3 months of the experiment when it is planned to complete the experiment analysis.

Pr.3. Who will have access to the data which will be collected?
Only my supervisors and myself will have direct access to the raw data collected.

Pr.4. Will the participants have access to their own data? If no, please explain.
Should participants request a copy of their raw data files, this can be provided. Participants will be invited to a presentation summarizing the main conclusions from the experiment.

Pr.5. Will covert methods be used? *(e.g. participants are filmed without them knowing)*
No covert methods will be used.

Pr.6. Will any human tissue and/or biological samples be collected? *(e.g. urine)*
No human tissue will be collected.

Documents

Please attach the following documents to the application:

- Text used for ads (to find participants);
- Text used for debriefings;
- Form of informed consent for participants;
- Form of consent for other agencies when the research is conducted at a location (such as a hospital or school).

Appendix F

Haptic Controller Parameters

Section F-1 lists each individual subject's haptic controller parameters i.e., neuromuscular relax task stiffnesss, for the thirteen bias moment conditions pictured in Fig. F-1. These parameters were used to tune a haptic controller suited to match each subject's neuromuscular system for the 'IRT' experiment condition. Additionally, the mean controller parameters, also for the relax task, for ten subjects from an earlier experiment conducted by Smisek et al. are presented in section F-2 (Smisek et al., 2013). These average controller parameters were used for the experiment conditions 'RT', 'UT' ($UT = 0.5 \times RT$) and 'OT' ($OT = 2 \times RT$).

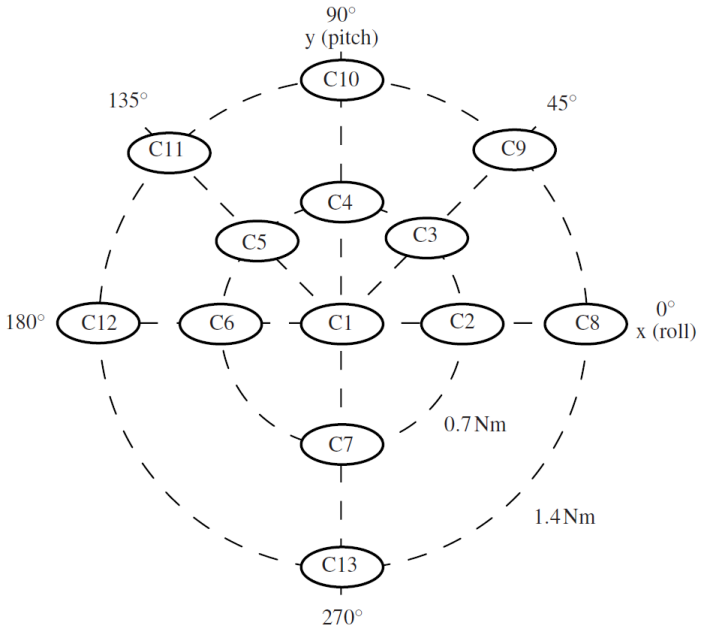

Figure F-1: Thirteen bias moment conditions of the experiment (Smisek et al., 2013). Note that relax and force task admittances were measured for the central condition C1.

F-1 Individual Controller Parameters

Table F-1: Longitudinal individual controller parameters [Nm/rad] for the 'relax task'

Subject ID	0N	0.7N						1.4N					
	0°	0°	45°	90°	135°	180°	270°	0°	45°	90°	135°	180°	270°
1	1.23	2.58	2.33	2.04	2.56	1.34	1.75	1.87	2.13	1.66	1.58	1.78	2.65
2	1.00	0.71	1.27	1.19	1.60	1.40	1.33	1.09	0.85	1.25	1.25	1.05	3.17
3	1.00	0.86	0.99	1.00	0.95	0.96	1.21	1.09	1.25	1.23	1.43	1.31	1.24
4	0.93	0.76	0.80	0.73	0.82	0.76	0.94	0.88	1.18	0.84	1.01	1.10	0.76
5	1.25	1.61	1.52	1.45	1.11	1.80	1.54	2.09	1.57	1.47	1.58	1.97	1.36
6	1.12	1.07	1.09	1.31	1.14	1.24	1.31	1.32	1.63	1.34	1.33	1.34	1.22
7	1.11	1.45	1.27	1.31	1.35	1.26	1.20	1.31	1.23	1.27	1.30	1.29	1.89
8	1.20	1.17	1.48	1.41	1.27	1.29	1.39	1.28	1.30	1.35	1.25	1.23	1.18
9	1.02	1.18	0.95	1.22	1.20	1.06	1.13	1.28	1.03	1.16	1.06	0.97	1.04
10	0.70	1.29	0.56	1.24	0.85	0.85	1.90	0.84	0.84	1.47	1.46	1.49	0.38
11	0.90	0.66	0.98	1.03	0.89	0.92	0.81	0.73	0.81	1.12	0.93	1.02	0.93
12	0.82	1.04	0.87	1.23	0.85	0.82	0.90	1.23	0.91	0.84	0.87	0.97	1.50
Mean	**1.02**	**1.20**	**1.18**	**1.26**	**1.22**	**1.14**	**1.28**	**1.25**	**1.23**	**1.25**	**1.25**	**1.29**	**1.44**

Table F-2: Lateral individual controller parameters [Nm/rad] for the 'relax task'

Subject ID	0N	0.7N						1.4N					
	0°	0°	45°	90°	135°	180°	270°	0°	45°	90°	135°	180°	270°
1	0.82	1.07	0.96	0.91	0.89	0.90	0.93	1.19	1.06	0.97	1.07	1.08	1.19
2	0.87	0.92	0.97	1.06	0.92	0.96	0.86	0.91	1.03	0.84	0.91	0.80	0.76
3	0.90	0.77	0.81	0.96	0.91	0.92	1.01	0.67	0.92	0.88	0.94	0.97	1.00
4	0.89	1.11	0.97	0.93	0.90	0.94	0.89	0.67	0.92	0.88	0.94	0.97	1.00
5	0.78	1.11	1.22	0.97	0.95	1.05	1.12	1.26	1.03	1.05	1.09	1.07	1.01
6	0.94	1.14	1.04	0.89	0.96	0.88	1.11	0.91	1.39	1.12	1.04	0.85	0.97
7	0.85	1.04	0.95	0.85	1.06	1.21	1.02	1.07	1.05	1.03	1.03	1.02	1.12
8	0.89	1.46	1.51	1.12	1.19	1.36	1.22	1.23	1.28	1.30	1.26	1.37	1.16
9	0.85	0.93	1.02	0.99	0.75	0.80	0.85	1.24	0.75	0.90	1.03	0.94	1.01
10	1.11	1.38	0.91	1.75	1.12	0.52	1.33	5.03	0.89	1.51	1.09	1.33	1.11
11	0.93	0.79	0.99	0.89	0.90	0.90	0.85	0.66	0.87	0.89	0.81	0.93	0.90
12	0.96	0.82	0.88	0.97	0.94	0.84	0.85	0.97	0.88	0.82	0.98	0.97	0.98
Mean	**0.90**	**1.05**	**1.02**	**1.02**	**0.96**	**0.94**	**1.00**	**1.32**	**1.01**	**1.01**	**1.02**	**1.02**	**1.02**

F-2 Average Controller Parameters From Smisek et al.

Table F-3: Average controller parameters [Nm/rad] of ten subjects from Smisek et al. (Smisek et al., 2013) for the 'relax task'

	0N	0.7N						1.4N					
	0°	0°	45°	90°	135°	180°	270°	0°	45°	90°	135°	180°	270°
Longitudinal	1.53	4.36	4.37	5.42	5.00	4.94	4.48	6.60	5.60	7.18	8.45	5.96	5.68
Lateral	0.46	0.53	0.62	0.48	0.65	0.48	0.64	0.59	0.70	0.72	0.87	1.65	0.63

Appendix G

Neuromuscular Admittance Based Tuning Method Graphs

In this appendix, time traces of the raw data used to compute the dependent variables of the neuromuscular admittance based tuning method validation experiment for subject number two (for trajectory number two) are presented. Raw data plots are displayed separately for each subtask (obstacle) and are categorized into six sections: trajectory, safety, performance, control activity, haptic activity and haptic controller accuracy.

G-1 Trajectory

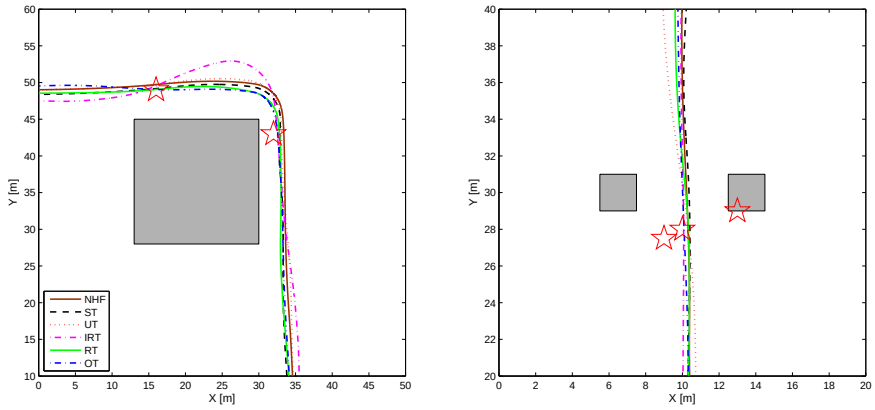

(a) Subtask 1

(b) Subtask 2

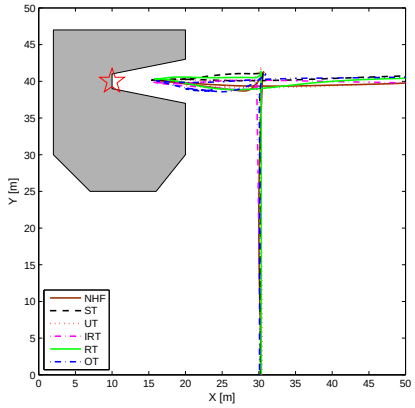

(c) Subtask 3

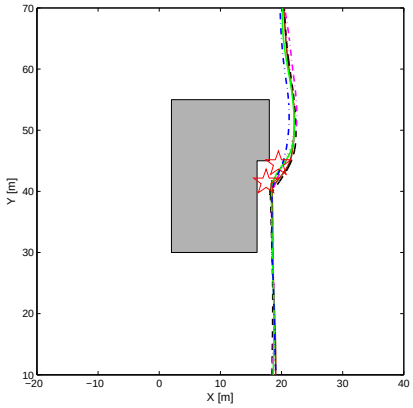

(d) Subtask 4

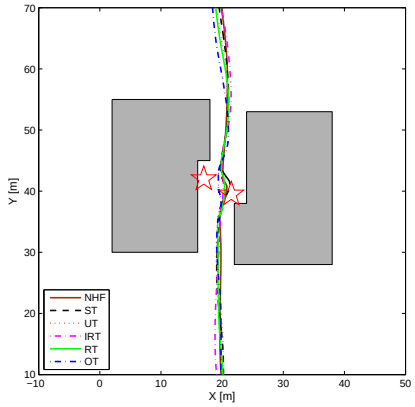

(e) Subtask 5

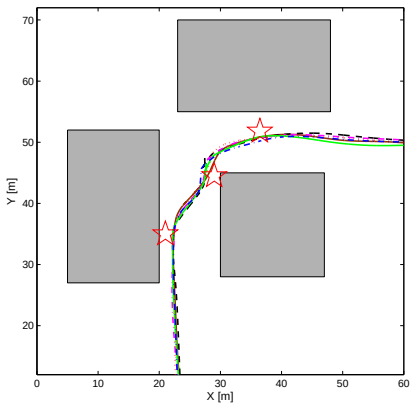

(f) Subtask 6

Figure G-1: UAV Trajectories

G-2 Safety

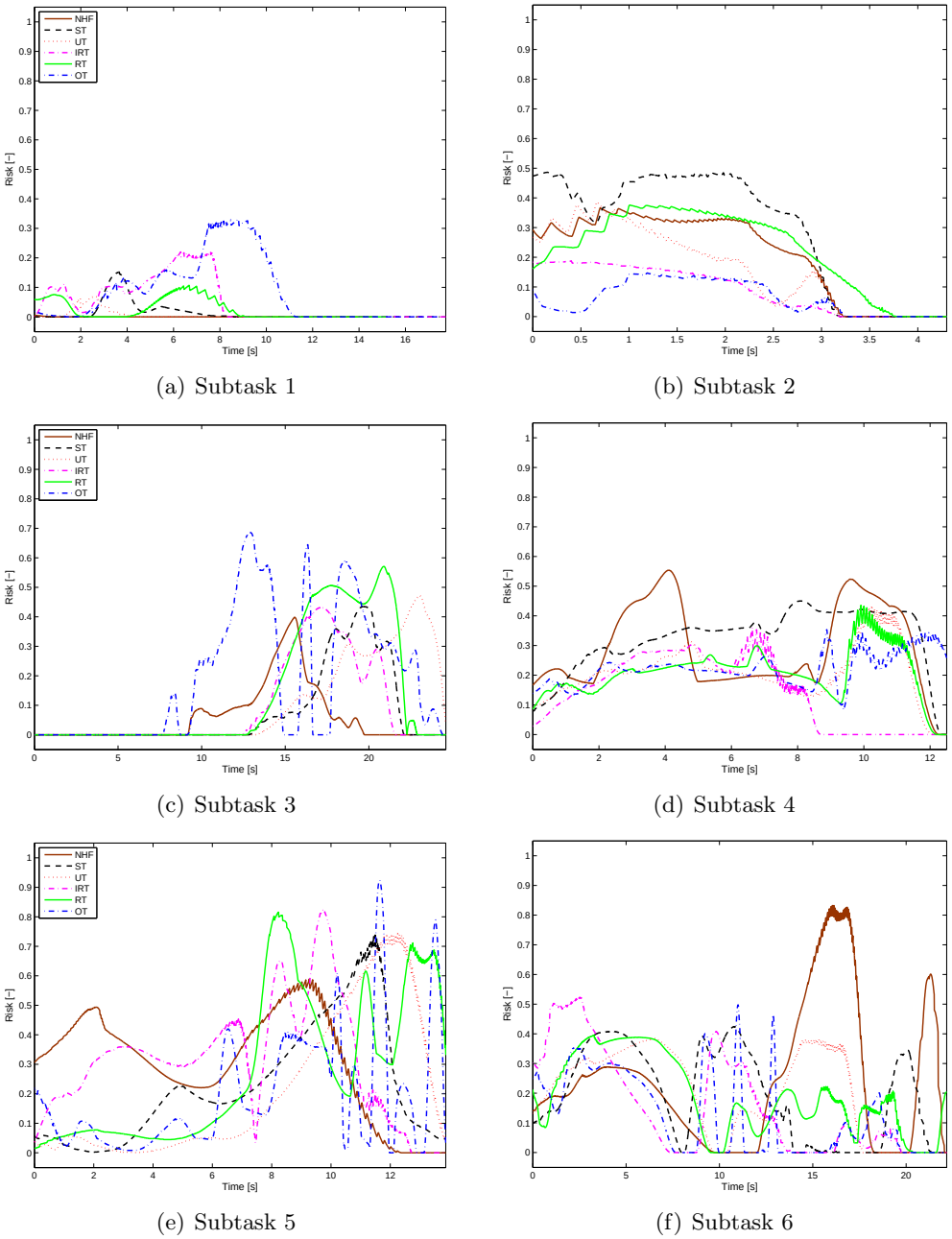

(a) Subtask 1

(b) Subtask 2

(c) Subtask 3

(d) Subtask 4

(e) Subtask 5

(f) Subtask 6

Figure G-2: Resultant risk vector magnitude

G-3 Performance

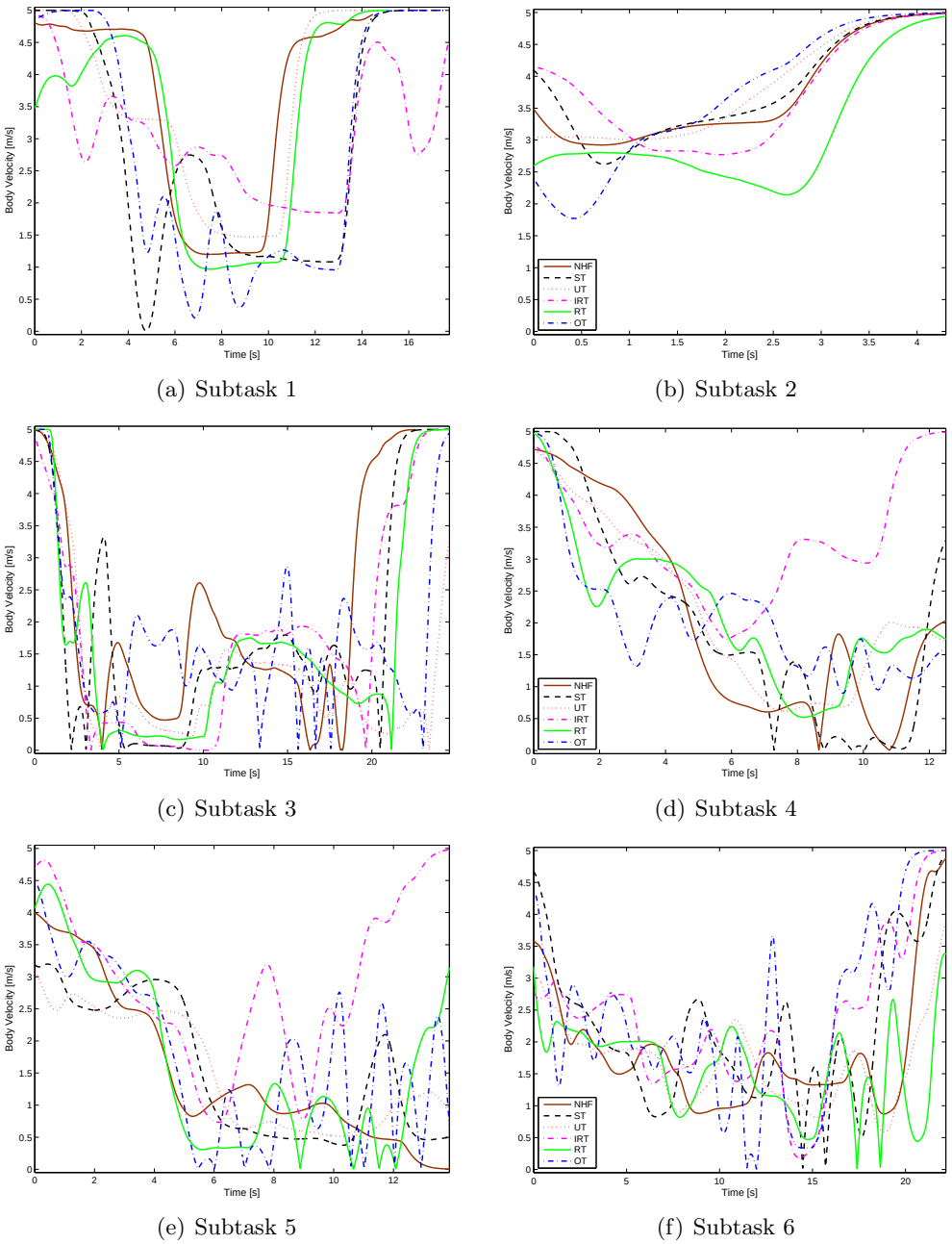

(a) Subtask 1

(b) Subtask 2

(c) Subtask 3

(d) Subtask 4

(e) Subtask 5

(f) Subtask 6

Figure G-3: Resultant UAV velocity

G-4 Control Activity

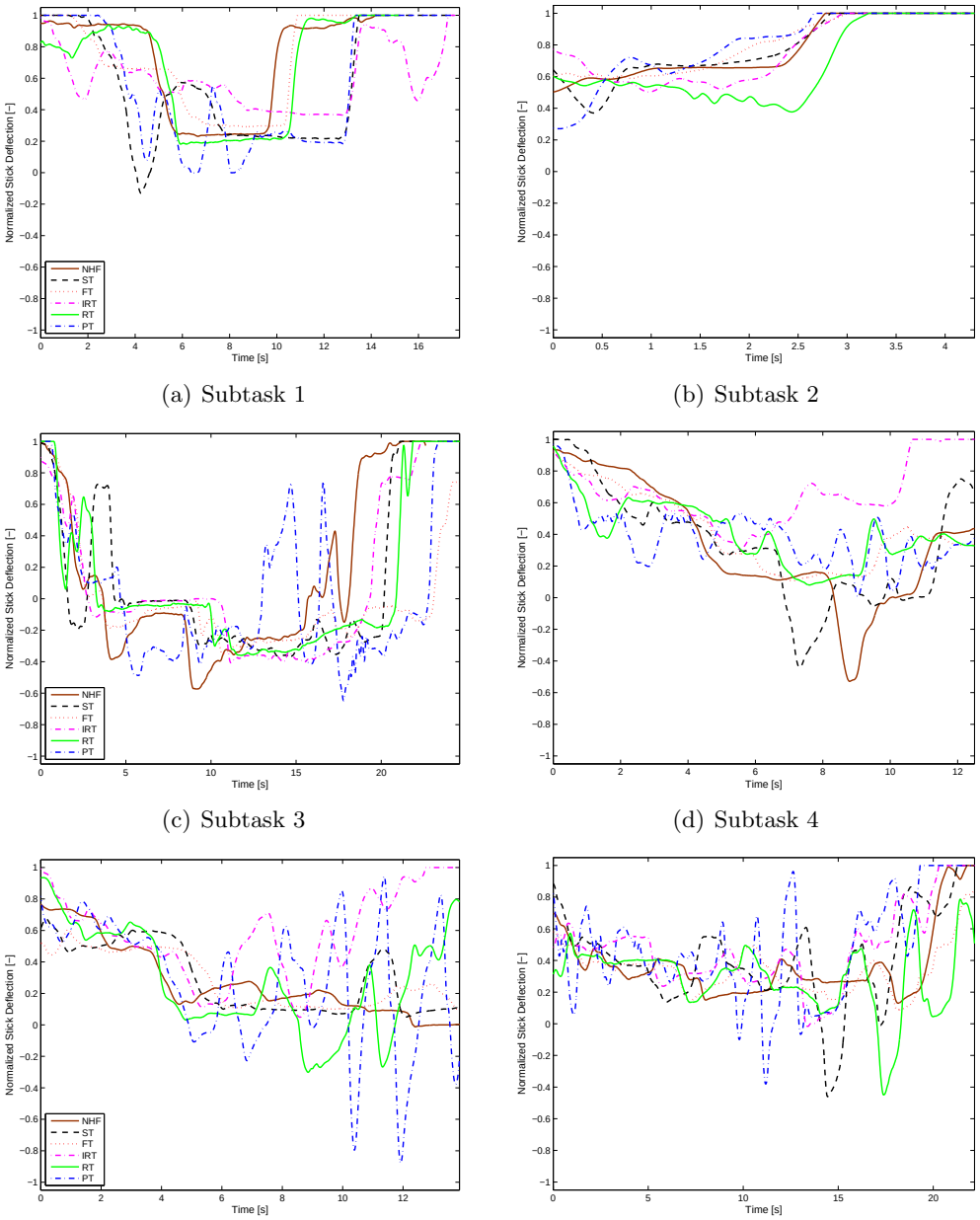

(a) Subtask 1

(b) Subtask 2

(c) Subtask 3

(d) Subtask 4

(e) Subtask 5

(f) Subtask 6

Figure G-4: Normalized longitudinal side-stick deflection

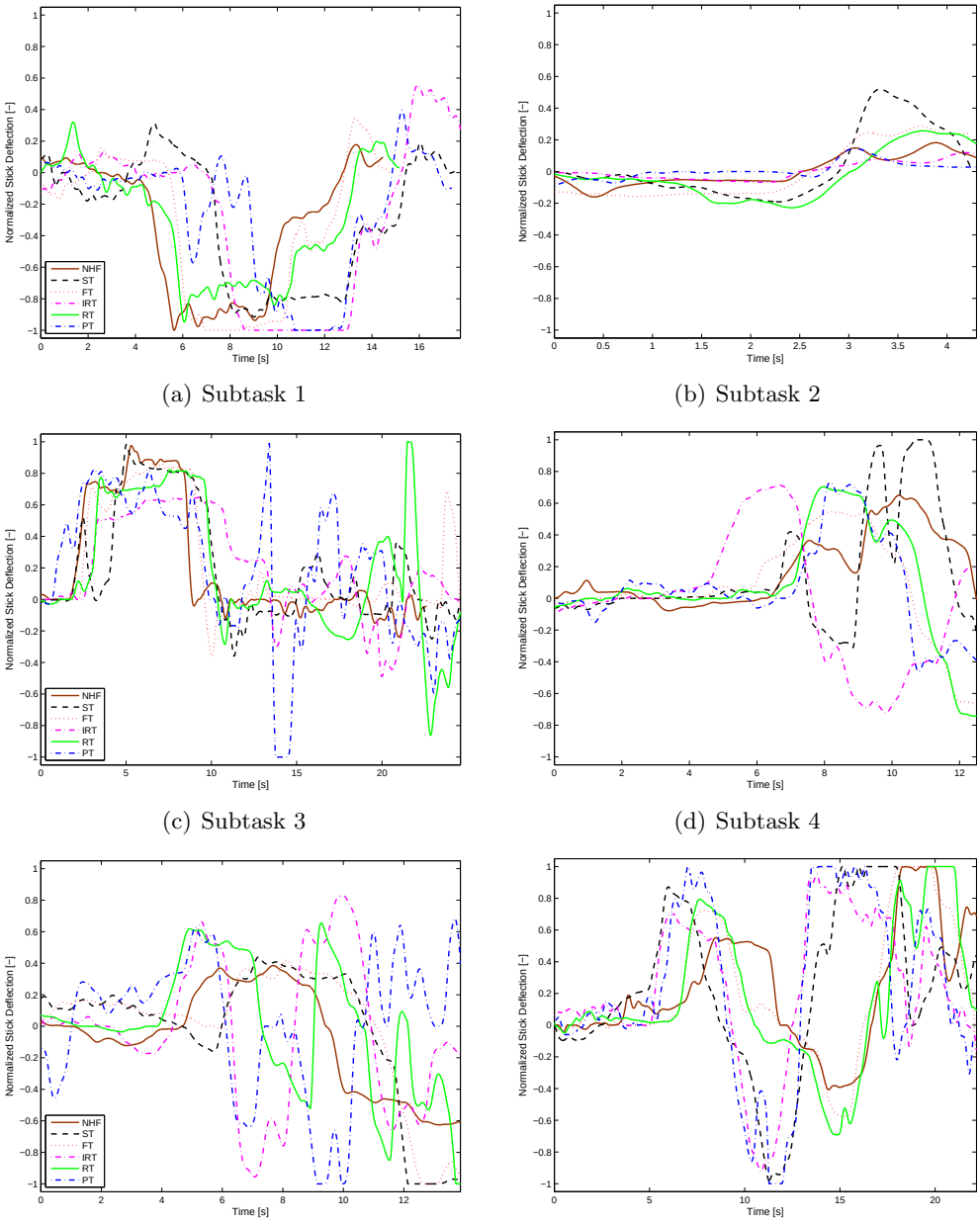

(a) Subtask 1

(b) Subtask 2

(c) Subtask 3

(d) Subtask 4

(e) Subtask 5

(f) Subtask 6

Figure G-5: Normalized lateral side-stick deflection

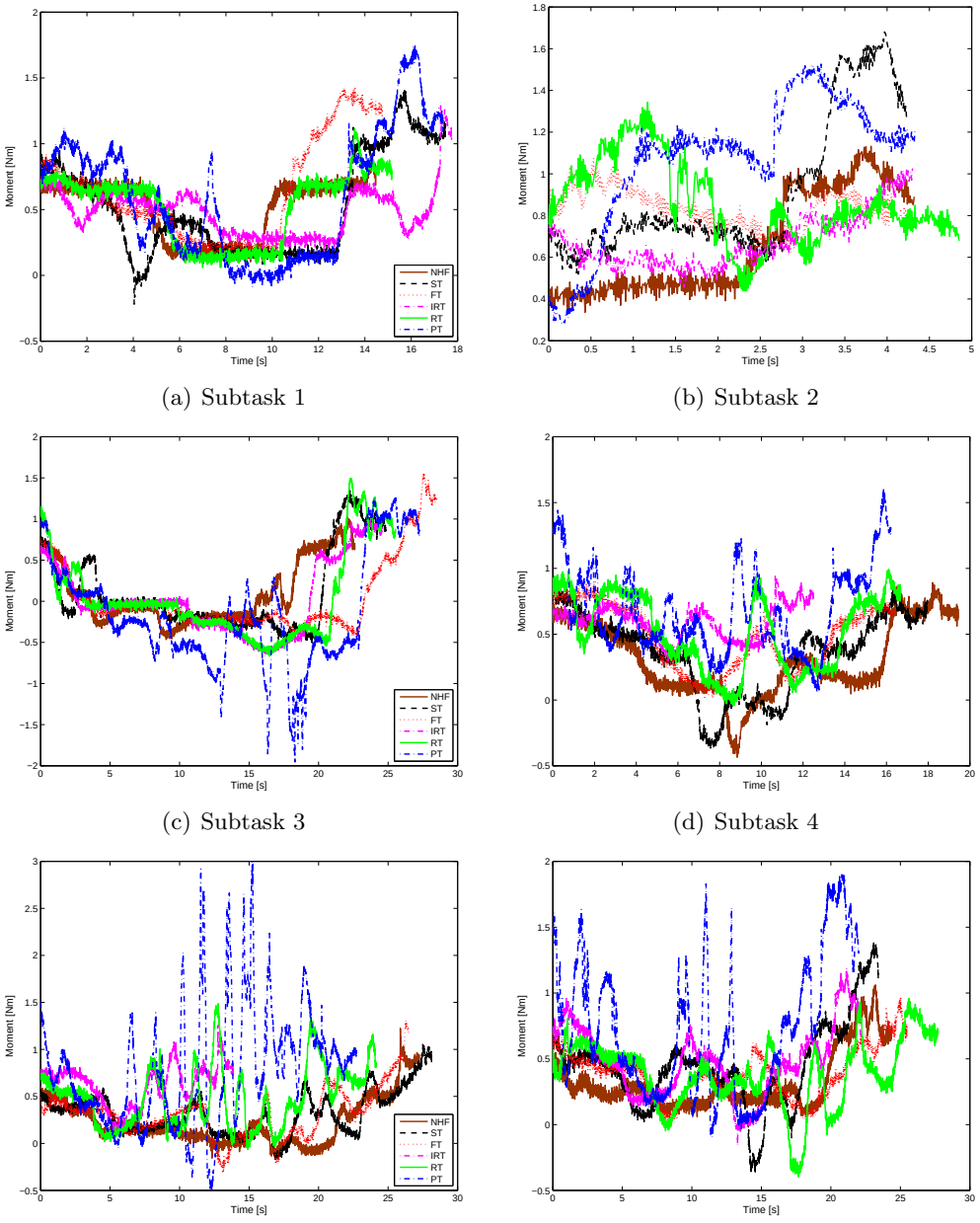

(a) Subtask 1

(b) Subtask 2

(c) Subtask 3

(d) Subtask 4

(e) Subtask 5

(f) Subtask 6

Figure G-6: Longitudinal neuromuscular/bias moment, M_{NMS_X}

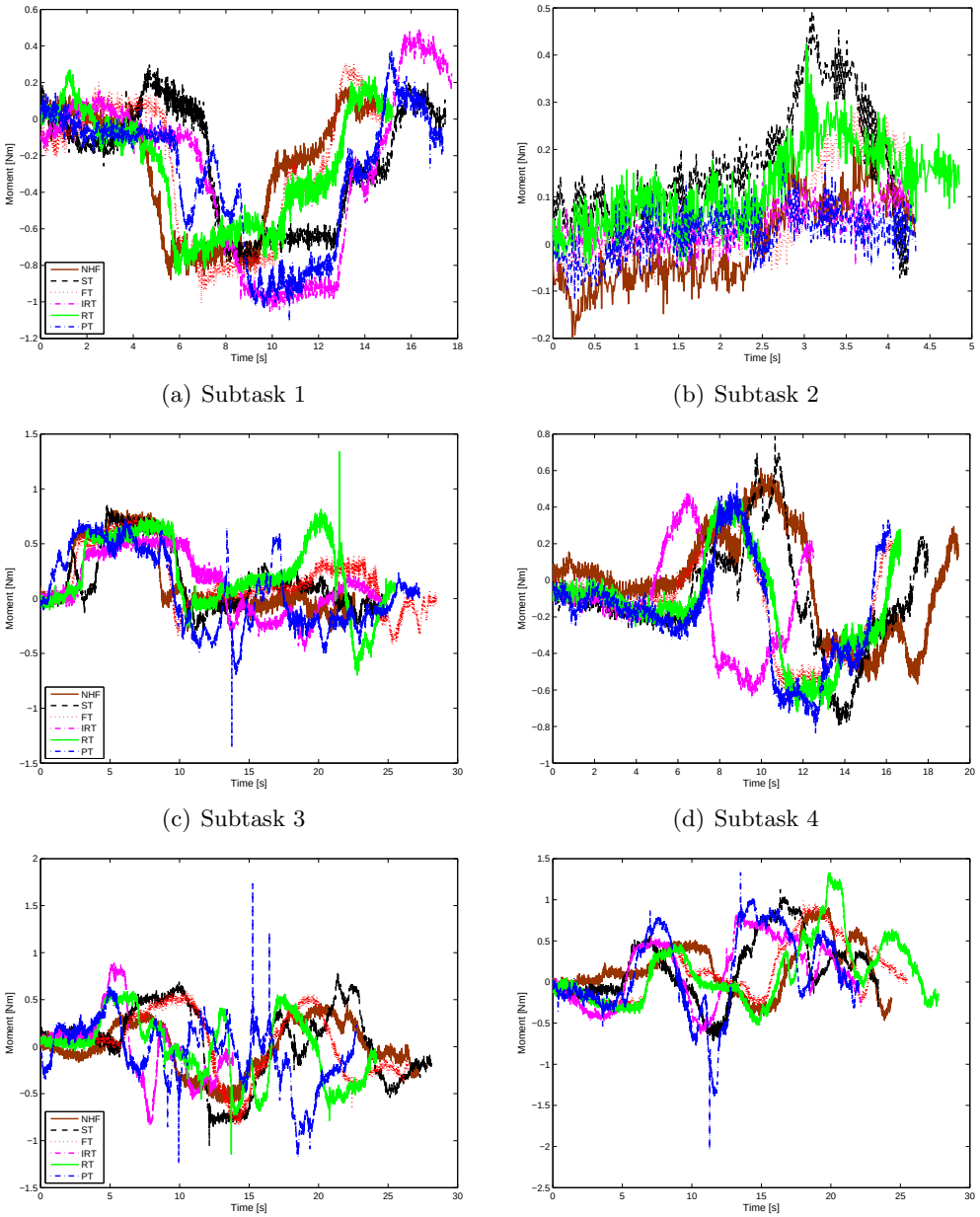

(a) Subtask 1

(b) Subtask 2

(c) Subtask 3

(d) Subtask 4

(e) Subtask 5

(f) Subtask 6

Figure G-7: Lateral neuromuscular/bias moment, M_{NMS_Y}

G-5 Haptic Activity

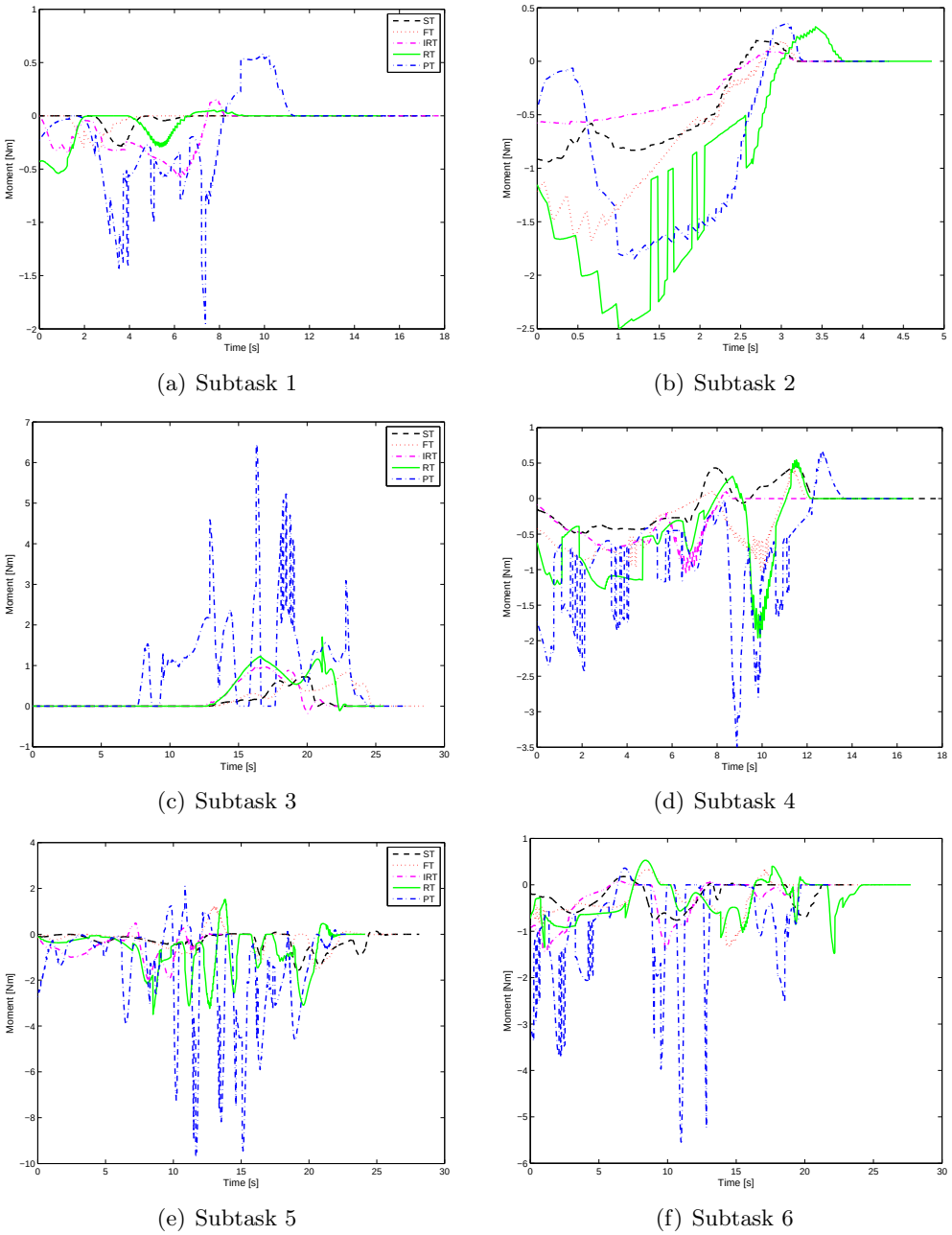

(a) Subtask 1

(b) Subtask 2

(c) Subtask 3

(d) Subtask 4

(e) Subtask 5

(f) Subtask 6

Figure G-8: Longitudinal haptic collision avoidance moment, M_{H_X}

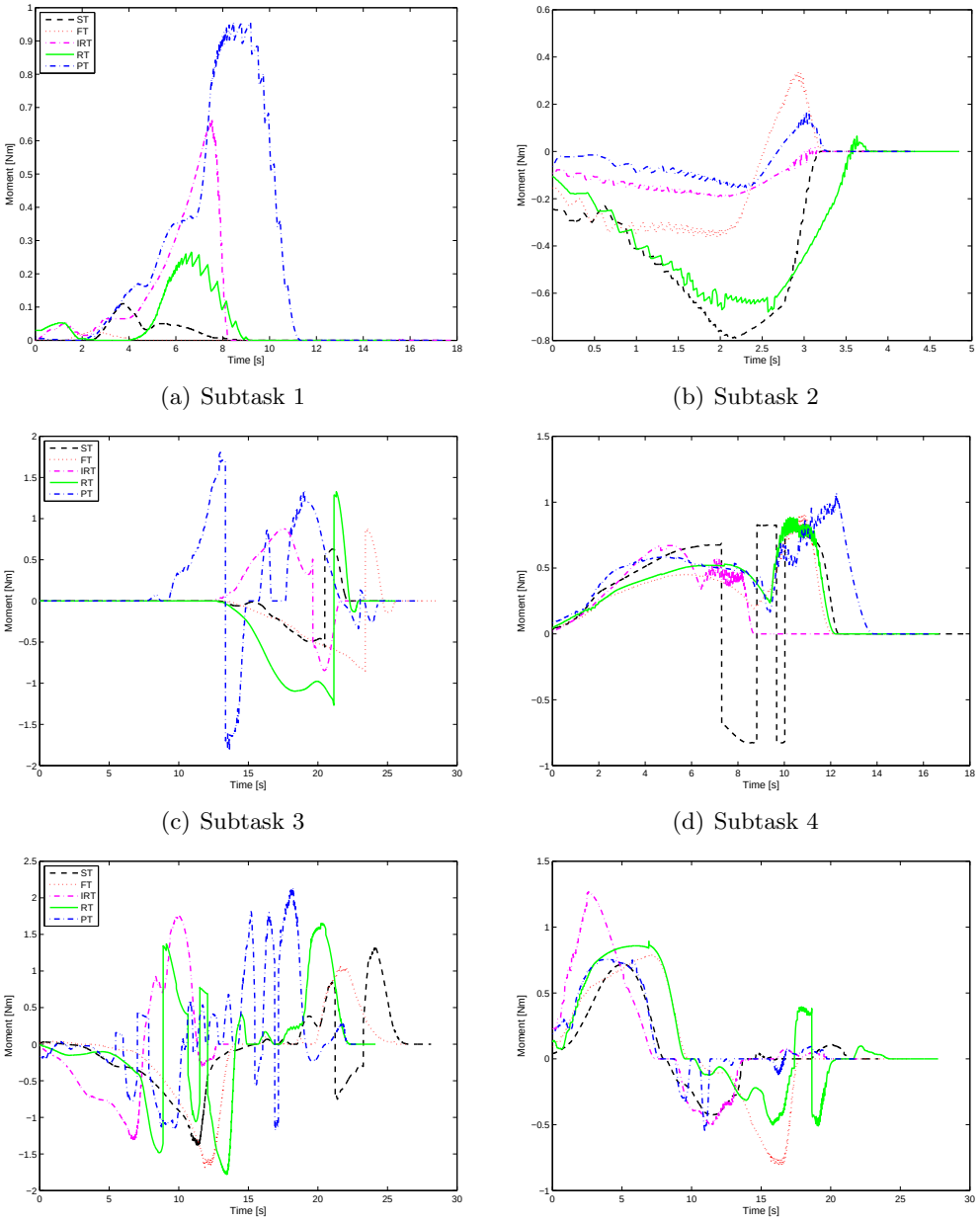

(a) Subtask 1

(b) Subtask 2

(c) Subtask 3

(d) Subtask 4

(e) Subtask 5

(f) Subtask 6

Figure G-9: Lateral haptic collision avoidance moment, M_{H_Y}

G-6 Haptic Controller Accuracy

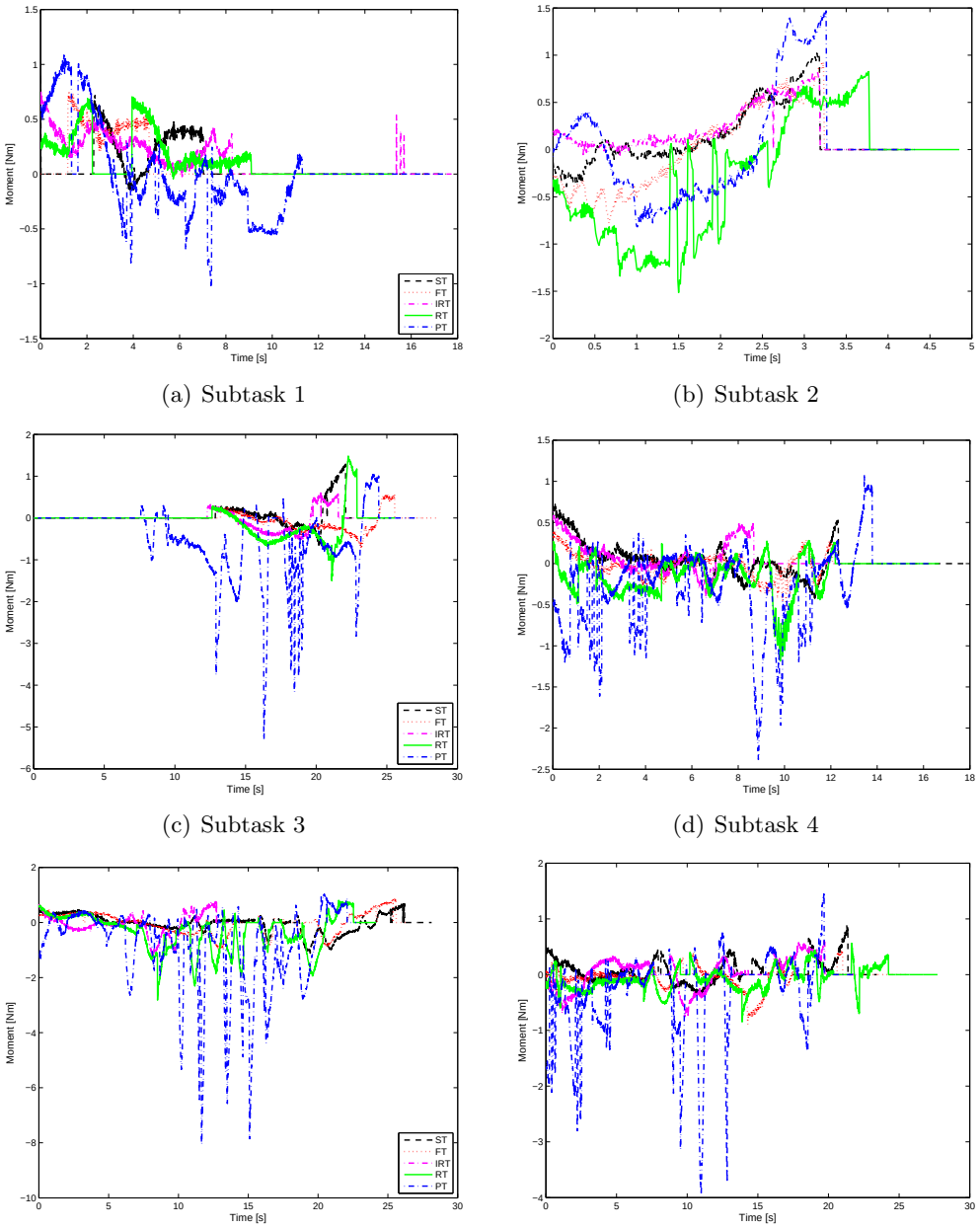

(a) Subtask 1

(b) Subtask 2

(c) Subtask 3

(d) Subtask 4

(e) Subtask 5

(f) Subtask 6

Figure G-10: Longitudinal haptic controller accuracy, $(|M_{H_X}| - |M_{NMS_X}|)$

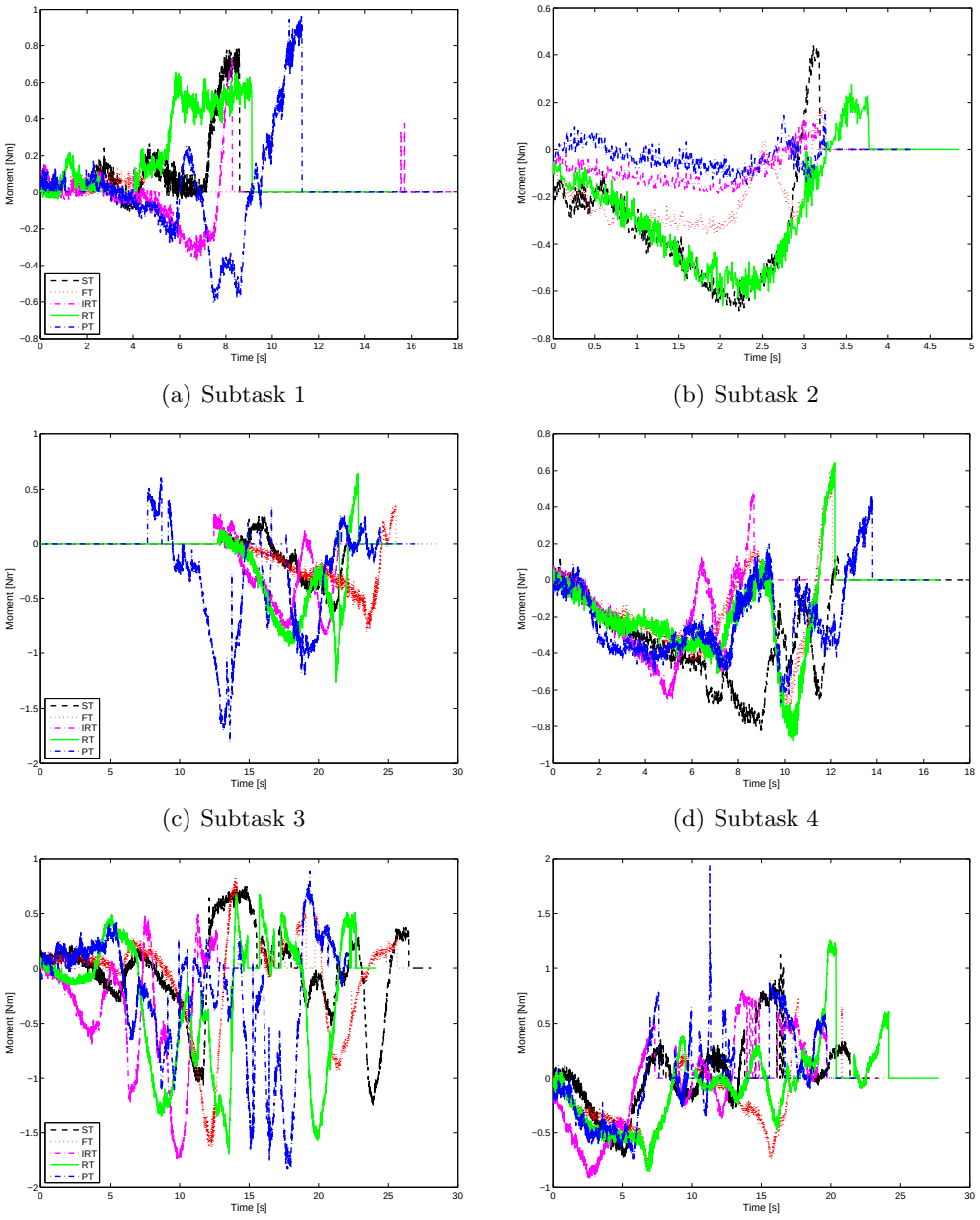

(a) Subtask 1

(b) Subtask 2

(c) Subtask 3

(d) Subtask 4

(e) Subtask 5

(f) Subtask 6

Figure G-11: Lateral haptic controller accuracy, $(|M_{H_Y}| - |M_{NMS_Y}|)$

Appendix H

Admittance-Trajectory Relationship Graphs

In this appendix, (magnitude) Bode plots used to quantify the admittance-trajectory relationship are given. First, the 'overall' or mean admittance for each subtask is presented in section H-1. In section H-2, admittance Bode plots for 'three points' around the 'beginning', 'middle' and 'end' points of each subtask are given to investigate the within obstacle variations of admittance. Note that Hx represents admittance in the longitudinal direction, and Hy represents admittance in the lateral direction.

H-1 'Overall' Admittance

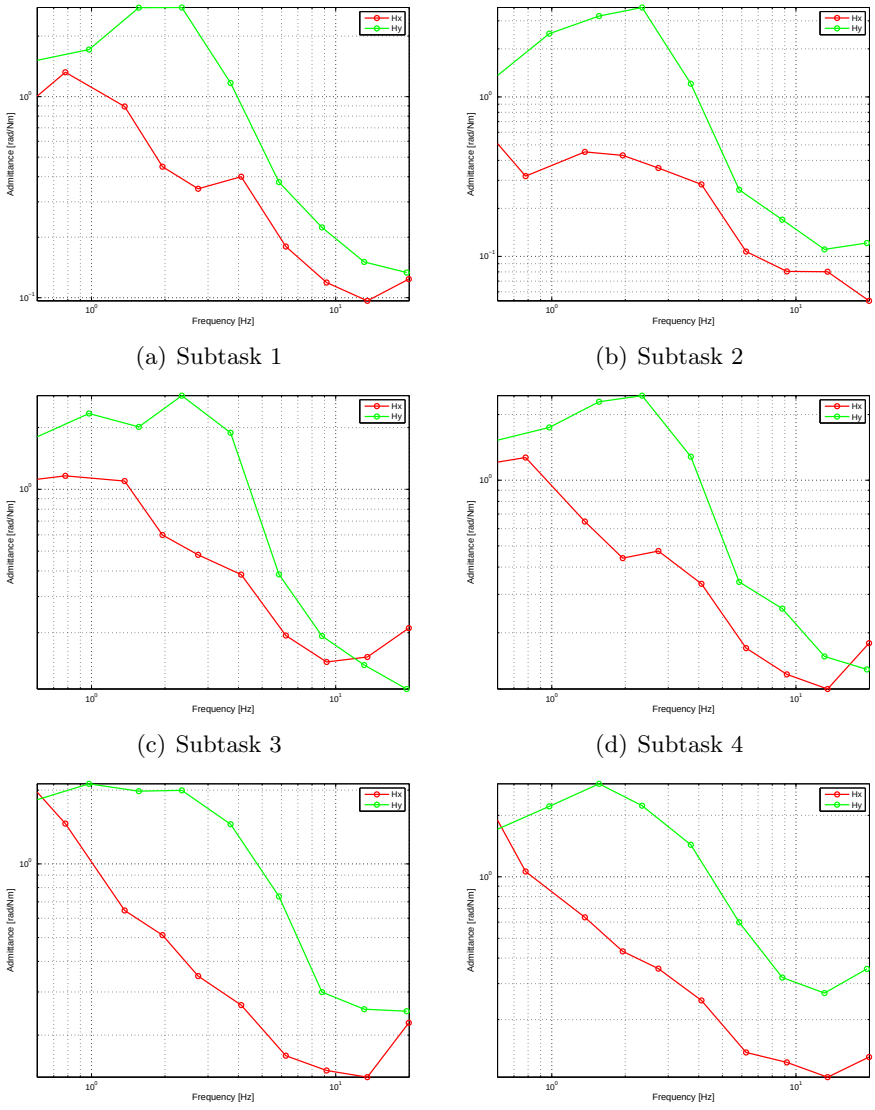

(a) Subtask 1

(b) Subtask 2

(c) Subtask 3

(d) Subtask 4

(e) Subtask 5

(f) Subtask 6

Figure H-1: 'Overall'/Mean admittance per obstacle

H-2 'Three Point' Admittance

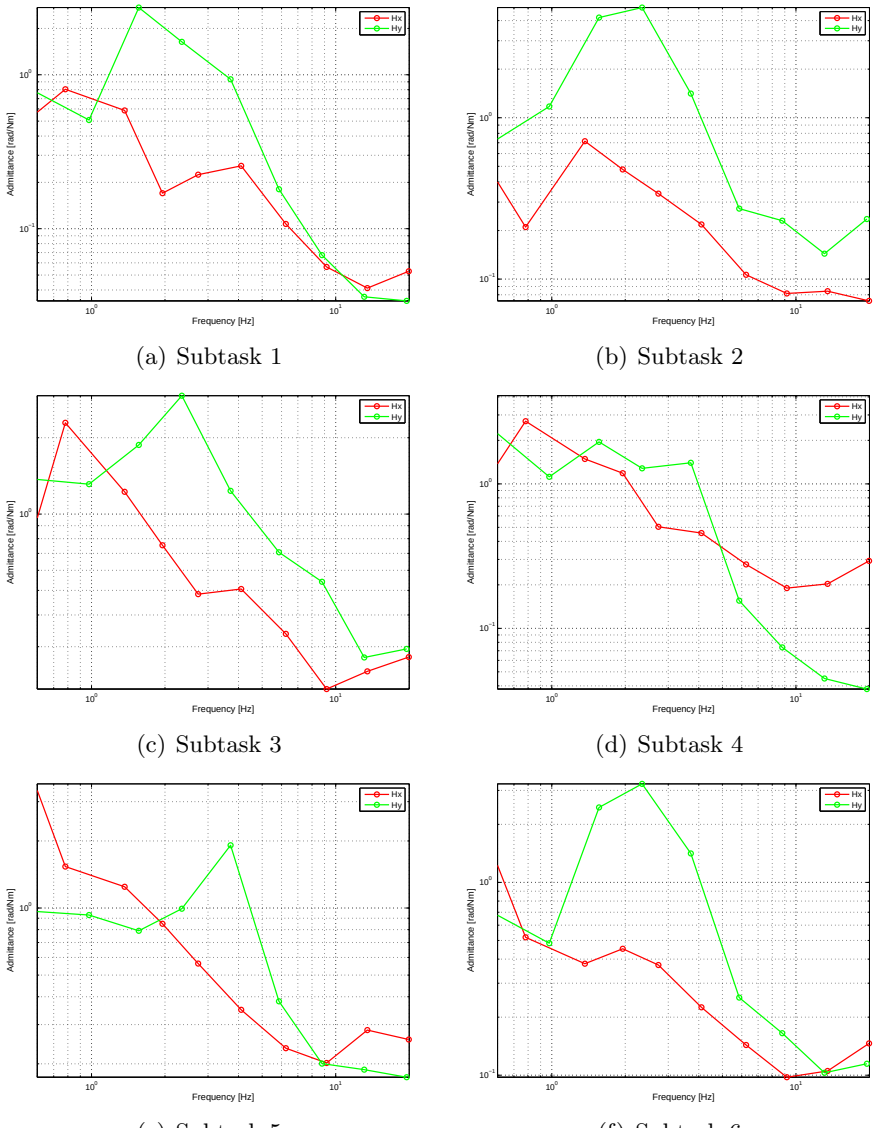

(a) Subtask 1

(b) Subtask 2

(c) Subtask 3

(d) Subtask 4

(e) Subtask 5

(f) Subtask 6

Figure H-2: Admittance for 0.5 second interval around the 'Beginning' point per obstacle

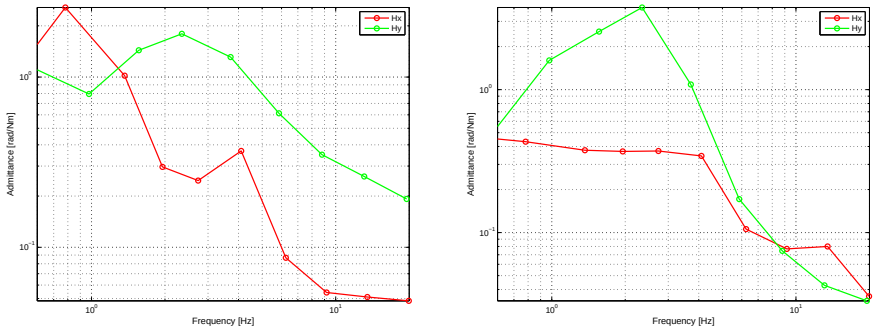

(a) Subtask 1

(b) Subtask 2

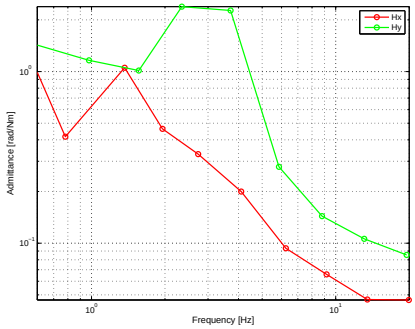

(c) Subtask 3

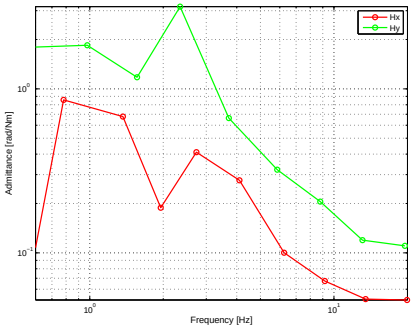

(d) Subtask 4

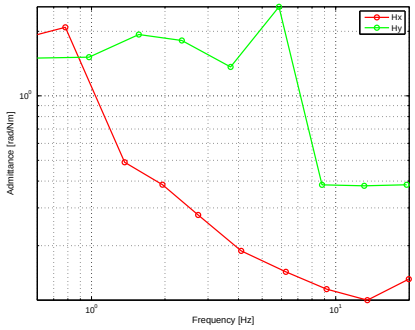

(e) Subtask 5

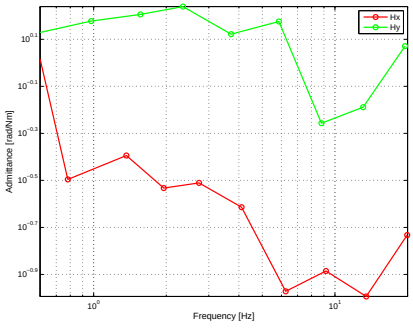

(f) Subtask 6

Figure H-3: Admittance for 0.5 second interval around the 'Middle' point per obstacle

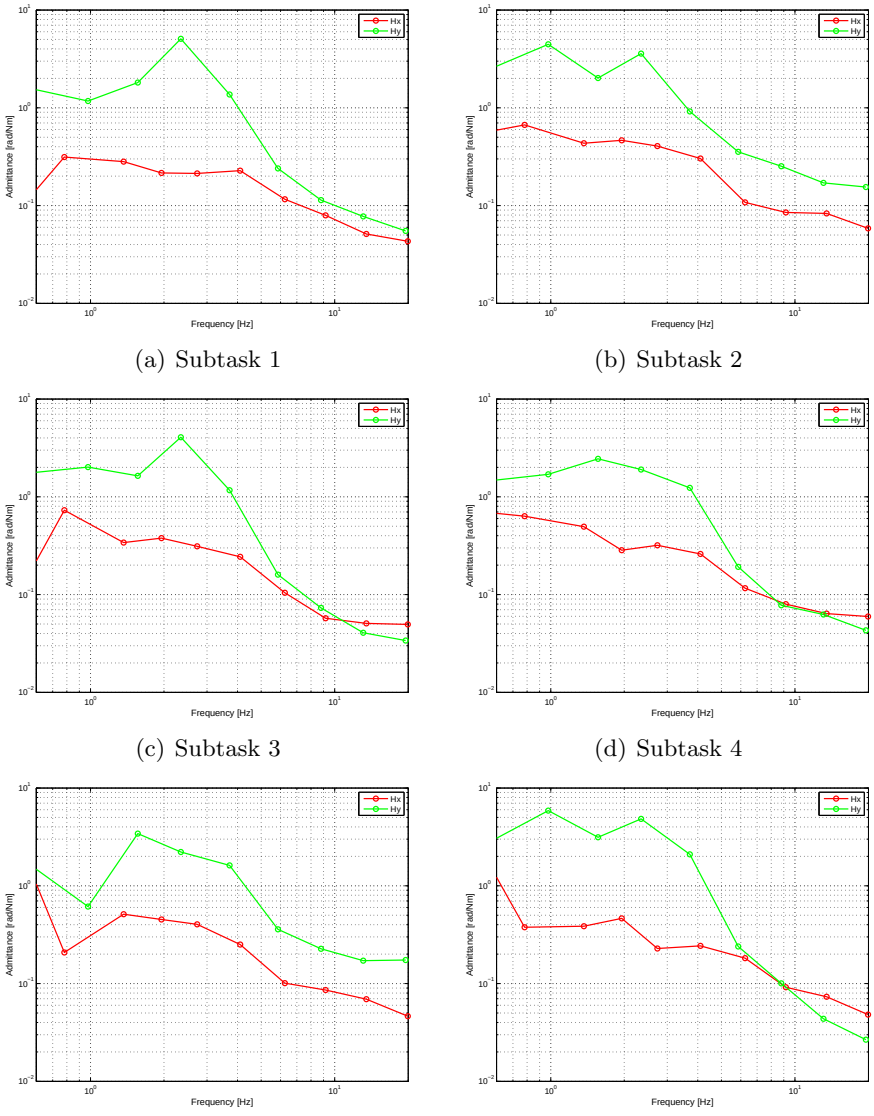

(a) Subtask 1

(b) Subtask 2

(c) Subtask 3

(d) Subtask 4

(e) Subtask 5

(f) Subtask 6

Figure H-4: Admittance for 0.5 second interval around the 'End' point per obstacle

Bibliography

Abbink, D. (2006). *Neuromuscular analysis of haptic gas pedal feedback during car following.* PhD, Delft University of Technology, Delft.

Abbink, D., Cleij, D., Mulder, M., & Paassen, M. van. (2012, October). The importance of including knowledge of neuromuscular behaviour in haptic shared control. In *2012 IEEE international conference on systems, man, and cybernetics (SMC)* (pp. 3350 –3355).

Abbink, D., & Mulder, M. (2010). Neuromuscular analysis as a guideline in designing shared control. *Advances in Haptics*, *109*, 499–516.

Abbink, D. A., & Mulder, M. (2009). Exploring the dimensions of haptic feedback support in manual control. *Journal of Computing and Information Science in Engineering*, *9*(1), 011006. Available from `http://link.aip.org/link/?CIS/9/011006/1`

Abbink, D. A., Mulder, M., & Boer, E. R. (2012, March). Haptic shared control: smoothly shifting control authority? *Cognition, Technology & Work*, *14*(1), 19–28. Available from `http://link.springer.com/article/10.1007/s10111-011-0192-5`

Aeronautics, L. (2007). *GCS C4I system.* Available from `http://www.aeronautics-sys.com/`

Alaimo, S., Pollini, L., Bresciani, J., & Blthoff, H. (2010, September). A comparison of direct and indirect haptic aiding for remotely piloted vehicles. In *2010 IEEE RO-MAN* (pp. 506 –512).

Boschloo, H., Lam, T., Mulder, M., & Paassen, M. van. (2004). Collision avoidance for a remotely-operated helicopter using haptic feedback. In *2004 IEEE international conference on systems, man and cybernetics* (Vol. 1, pp. 229 –235 vol.1).

Cleij, D. (2011). *Design of haptic shared control: Analysing driver-controller interaction to improve hapic shared control systems.* MSc. thesis, Delft University of Technology, Delft.

Cooke, N. J. (2006, October). Human factors of remotely operated vehicles. *Proceedings of the Human Factors and Ergonomics Society Annual Meeting*, *50*(1), 166–169. Available from `http://pro.sagepub.com/content/50/1/166`

Damveld, H. J., Abbink, D., Mulder, M., Mulder, M., Van Paassen, M., Helm, F. van der, et al. (2010, August). Identification of the feedback component of the neuromuscular system in a pitch control task. In *Proceedings of the AIAA guidance, navigation, and*

control conference 2 - 5 august 2010, toronto, ontario canada (pp. 1–22). Washington D.C.: American Institute of Aeronautics and Astronautics.

Delft Dynamics, B. (2006). *RH2 'Stern' robot helicopter* [Commercial]. Available from `http://www.delftdynamics.nl/`

De Vlugt, E. (2004). *Identification of spinal reflexes*. Unpublished doctoral dissertation, Delft University of Technology, Delft.

Griffiths, P. G., & Gillespie, R. B. (2005, September). Sharing control between humans and automation using haptic interface: Primary and secondary task performance benefits. *Human Factors: The Journal of the Human Factors and Ergonomics Society*, *47*(3), 574–590. Available from `http://hfs.sagepub.com/content/47/3/574`

Grnhagen, W. von, Mllhuser, M., Abildgaard, M., & Lantzsch, R. (2010, September). Active inceptors in FHS for pilot assitance systems. In *Proceedings of the 36th european rotorcraft forum,*. Paris: European Rotorcraft Forum.

Hart, S. G., & Staveland, L. E. (1988). Development of NASA-TLX (task load index): Results of empirical and theoretical research. *Human Mental Workload*, *1*(3), 139–183. Available from `http://humanfactors.arc.nasa.gov/groups/TLX/downloads/NASA-TLXChapter.pdf`

Hopcroft, R., Burchat, E., & Vince, J. (2006, May). *Unmanned aerial vehicles for maritime patrol: Human factors issues* (Tech. Rep.). Australian Government Department of Defence.

Jeannot, E., Kelly, C., & Thompson, D. (2003). The development of situation awareness measures in ATM systems. *Brussels: Eurocontrol*.

Krogh, B. H. (1984). *A generalized potential field approach to obstacle avoidance control* (Technical Report No. MS84-84). Dearborn, Michigan: Society of Manufactuing Engineers.

Lam, T. (2009). *Haptic interface for UAV teleoperation*. Unpublished doctoral dissertation, Delft University of Technology, Delft. (ISBN: 9789090241999)

Lam, T., Boschloo, H., Mulder, M., & Paassen, M. van. (2009, November). Artificial force field for haptic feedback in UAV teleoperation. *IEEE Transactions on Systems, Man and Cybernetics, Part A: Systems and Humans*, *39*(6), 1316 –1330.

Lam, T., Boschloo, H., Mulder, M., Paassen, M. van, & Helm, F. van der. (2004, October). Effect of haptic feedback in a trajectory following task with an unmanned aerial vehicle. In *2004 IEEE international conference on systems, man and cybernetics* (Vol. 3, pp. 2500 – 2506 vol.3).

Lam, T., Mulder, M., & Paassen, M. van. (2006, October). Haptic feedback for UAV teleoperation - force offset and spring load modification. In *IEEE international conference on systems, man and cybernetics, 2006. SMC '06* (Vol. 2, pp. 1618 –1623).

Lam, T., Mulder, M., Paassen, M. van, & Helm, F. van der. (2005, October). Tele-operating a UAV using haptics - modeling the neuromuscular system. In *2005 IEEE international conference on systems, man and cybernetics* (Vol. 3, pp. 2695 – 2700 Vol. 3).

Lam, T., Mulder, M., & Paassen, M. v. (2009, October). Haptic interface in UAV teleoperation using force-stiffness feedback. In *IEEE international conference on systems, man and cybernetics, 2009. SMC 2009* (pp. 835 –840).

Lam, T., Mulder, M., & Van Paassen, M. M. (2008). Haptic feedback in uninhabited aerial vehicle teleoperation with time delay. *Journal of guidance, control, and dynamics*, *31*(6), 1728–1739.

Lam, T. M., Mulder, M., & Paassen, M. M. (Ren) van. (2007). Haptic interface for UAV collision avoidance. *The International Journal of Aviation Psychology*, *17*(2), 167–195. Available from http://www.tandfonline.com/doi/abs/10.1080/10508410701328649

Lam, T. M., Mulder, M., Van Paassen, M. M., Mulder, J. A., & Van Der Helm, F. C. (2009, May). Force-stiffness feedback in uninhabited aerial vehicle teleoperation with time delay. *Journal of Guidance, Control, and Dynamics*, *32*(3), 821–835.

Lasschuit, J., Lam, T., Mulder, M., Van Paassen, M. M., & Abbink, D. (2008, August). Measuring and modeling neuromuscular system dynamics for haptic interface design. In *Proceeding of the AIAA modeling and simulation technologies conference and exhibit 8 august 2008.* Honolulu, Hawaii: American Institute of Aeronautics and Astronautics.

McCarley, J. S., & Wickens, C. D. (2005). *Human factors implications of UAVs in the national airspace* (Technical Report No. AHFD-05-05/FAA-05-01). Savoy, IL: University of Illinois, Aviation Human Factors Division.

McGarry, B. (2012, June). *Drones most accident-prone U.S. air force craft: BGOV barometer.* Available from http://www.bloomberg.com/

Mugge, W., Abbink, D., & Helm, F. van der. (2007, June). Reduced power method: how to evoke low-bandwidth behaviour while estimating full-bandwidth dynamics. In *IEEE 10th international conference on rehabilitation robotics, 2007. ICORR 2007* (pp. 575 –581).

Mulder, M., Abbink, D., Van Paassen, M., & Mulder, M. (2011). Design of a haptic gas pedal for active car-following support. *IEEE Transactions on Intelligent Transportation Systems*, *12*(1), 268–279.

Mulder, M., Abbink, D. A., & Boer, E. R. (2012, May). Sharing control with haptics: Seamless driver support from manual to automatic control. *Human Factors: The Journal of the Human Factors and Ergonomics Society*. Available from http://hfs.sagepub.com/content/early/2012/05/02/0018720812443984

Nissan. (2006). *Distance control assist system.* Available from /EN/TECHNOLOGY/OVERVIEW/dcas.html

Parasuraman, R., & Riley, V. (1997, June). Humans and automation: Use, misuse, disuse, abuse. *Human Factors: The Journal of the Human Factors and Ergonomics Society*, *39*(2), 230–253. Available from http://hfs.sagepub.com/content/39/2/230

Salvucci, D. D., & Gray, R. (2004). A two-point visual control model of steering. *Perception*, *33*(10), 1233–1248. (WOS:000226521000008)

Sarris, Z. (2001, June). Survey of UAV applications in civil markets. In *Proceedings of the 9th IEEE mediterranean conference on control and automation.*

Schouten, A. C. (2004). *Proprioceptive reflexes and neurological disorders.* Unpublished doctoral dissertation, Delft University of Technology, Delft. Available from http://resolver.tudelft.nl/uuid:b34e0469-39eb-4a76-98b0-fb0d29fa06b5

Sheridan, T. B. (2002). *Humans and automation: System design and research issues.* New York, NY, USA: John Wiley & Sons, Inc.

Smisek, J., Paassen, M. van, Mulder, M., & Abbink, D. A. (2013, April). Neuromuscular analysis based tuning of haptic shared control assistant for UAV collision avoidance. In *IEEE world haptics confrence 2013. WHC 2013.* Daejeon, Korea: IEEE. Available from http://www.haptics2013.org/index.php

Stewart, J. (2007). *Calculus: Early transcendentals* (6th ed.). Cengage Learning.

Stigter, S. de, Mulder, M., & Van Paassen, M. M. (2007, January). Design and evaluation of a haptic flight director. *Journal of Guidance, Navigation and Control*, *30*(1).

Svitak, A. (2013, April). *Europe demos heron UAV in civil air space.* Available from `http://www.aviationweek.com`

Tvaryanas, A. P., Thompson, W. T., & Constable, S. H. (2005, March). *U.S. military unmanned aerial vehicle mishaps: Assessment of the role of human factors using human factors analysis and classification system (HFACS)* (Tech. Rep.). US Air Force.

Van Paassen, M. M. (1994). *Biophysics in aircraft control: a model of the neuromuscular system of the pilot's arm.* Unpublished doctoral dissertation. Available from `http://resolver.tudelft.nl/uuid:1bf5f5b6-95da-4d70-84f9-571cdabb5b0d`

Venrooij, J., Abbink, D., Mulder, M., & Paassen, M. van. (2011, August). A method to measure the relationship between biodynamic feedthrough and neuromuscular admittance. *IEEE Transactions on Systems, Man, and Cybernetics, Part B: Cybernetics*, *41*(4), 1158 –1169.

Vlugt, E. de, Schouten, A. C., & Helm, F. C. van der. (2006, September). Quantification of intrinsic and reflexive properties during multijoint arm posture. *Journal of Neuroscience Methods*, *155*(2), 328–349. Available from `http://www.sciencedirect.com/science/article/pii/S0165027006000549`

Weibel, R. E., & Hansman, R. J. (2006, November). *Safety considerations for operation of unmanned aerial vehicles in the national airspace system* (Tech. Rep.). Massachusetts Institute of Technology.

Williams, K. W. (2004, December). *A summary of unmanned aircraft Accident/Incident data: Human factors implications* (Technical Report No. DOT/FAA/AM-04/24). Federal Aviation Administration.